Faculdade de Engenharia da Universidade do Porto

Sonic Anemometer and Atmospheric Flows over Complex Terrain

Luís Manuel Frölén Ribeiro
(Mestre em Engenharia Mecânica)

Resumo

O objectivo desta tese é o estudo e aplicação de anemómetros sónicos no âmbito da energia eólica para caracterização dos campos médio e turbulento do escoamento sobre terreno complexo. São explorados os resultados de medições com anemómetros sónicos em quatro situações distintas: terreno plano com elevada rugosidade e evapo-transpiração; túnel aerodinâmico; e duas situações de terreno complexo na Ilha da Madeira, terreno costeiro e montanhoso.

A variabilidade das medições dos dois primeiros momentos estatísticos é explorada no caso do terreno plano onde instrumentos de 3 fabricantes, NUW do NCAR, modelo CSAT-3 da Campbell Scientific Inc., e modelo HS da Gill Solent Instruments, num escoamento com gradientes térmicos e evapo-transpiração elevados. Verificou-se dos primeiros momentos estatísticos da velocidade e temperatura uma correlação entre instrumentos de 0.99 e dos segundos momentos correlações que variavam de 92 a 99%, em concordância com resultados obtidos sobre outro tipo de terreno. O instrumento cujo desempenho se pode classificar como superior foi o Campbell (modelo CSI-3). No entanto, para efeitos de estudos do recurso eólico e turbulência atmosférica para fins energéticos as diferenças entre instrumentos são desprezáveis.

Quantificou-se em túnel aerodinâmico a distorção (*transducer shadow effect*) de um anemómetro sónico Metek (modelo USA-1) para velocidades entre os 4 e 16 ms^{-1}, todas as direcções e inclinação com o escoamento a variar entre $\pm 25°$. Os resultados indicaram a existência de zonas de desaceleração e aceleração do escoamento a variar de -12 a +5%. As distorções foram corrigidas para um máximo de $\pm 0.1\%$ depois de aplicada uma matriz de correcção que contabilizava a direcção e ângulo do escoamento. As medições de temperatura não eram afectadas.

Medições com dois anemómetros, copos e sónico (NRG modelo 40 e Metek modelo USA-1), foram efectuadas no cimo de uma turbina eólica, em terreno complexo, para investigar as possíveis causas do seu mau funcionamento. Dado o carácter transiente do campo médio de velocidades recorreu-se a técnicas espectrais, transformadas de ôndula e análise de quadrante para análise das medições, que foram confrontados favoravelmente com resultados de simulações computacionais que indicavam a presença de vórtices com periodicidade de 2.5-min na vizinhança da turbina. As medições confirmaram a existência de vórtices com

uma diferença em periodicidade de 14% relativamente às simulações indicando também a existência de estruturas coerentes como *sweeps* e *ejections* com componentes verticais a exceder os 20 ms^{-1}. As medições da velocidade média com anemómetros de copos foram superiores em 3.2% e as médias temporais de 10 minutos são reveladas como uma limitação da metodologia actual para avaliação do recurso eólico.

Os mesmos anemómetros foram usados no segundo caso de escoamentos sobre terreno complexo, agora a 40 m do solo no planalto do Paul da Serra, Ilha da Madeira, a 1500 m de altitude. Mostrou-se que as componentes verticais eram reduzidas apesar da torre de medição estar a poucos metros de uma encosta. Comparações entre anemómetros mostraram que a velocidade média medida pelo sónico era inferior em 1% relativamente ao anemómetro de copos e que a intensidade de turbulência medida pelo sónico era superior em 11%. A análise da turbulência indicou que o escoamento tinha características de um escoamento sobre terreno plano, com *it*, $\sigma(v)/\sigma(u)$ e $\sigma(w)/\sigma(u)$ respectivamente com 8, 91 e 60%. Análise aos dados de outras estações do Paúl, afastadas de 2 a 5 km, indicaram efeitos induzidos pelo terreno que desviavam o escoamento quer para ventos de nordeste como de sudoeste (115 a 72°). Verificou-se que os níveis de turbulência neste local não comprometem o funcionamento de aerogeradores.

Abstract

The objective of this thesis was the study and application of sonic anemometers in turbulent flows over complex terrain for wind energy purposes. The results from sonic anemometer measurements under 4 different situations were explored: flat terrain with large evapotranspiration, wind tunnel, and two complex terrain sites at Madeira Island, coastal and mountain.

For the flat terrain case we compared the variability of 1st and 2nd statistical moments of sonic anemometers from 3 manufacturers: NUW from NCAR, model CSAT-3 from Campbell Scientific Inc., and model HS from Gill Solent Instruments, in a flow with large evapotranspiration and temperature gradients. Mean correlations for wind velocity and temperature 1st moments were 99% while 2nd moments correlations varied from 92 to 99% in agreement with results on different terrains. The instrument whose performance could be classified as superior was Campbell (model CSI-3). However, for the purpose of wind resource assessment studies instrument differences are negligible.

The transducer shadow effect of a Metek (model USA-1) sonic anemometer was quantified in wind tunnel for velocities from 4 to 16 ms^{-1}, all azimuth angles and flow inclination of $\pm 25^{\circ}$. The results showed deceleration and acceleration areas from -12 to +5%. Instruments deviations were reduced to a maximum of $\pm 0.1\%$ after applying a correction matrix for a given direction and inclination of the flow. Temperature measurements were not affected.

Cup and sonic anemometer measurements (NRG model 40 and Metek USA-1) were made on a wind turbine nacelle, in complex terrain, to investigate the possible reasons for its performance below expected. Due to large transient characteristics of the mean flow, we recur to spectral, wavelet and quadrant analyses of the measurements, that were favorably confronted against computer simulations that indicated the existence of vortices with periodicity of 2.5-min in the vicinity of the turbine. The measurements validated a periodicity difference of 14% in the results and showed also the existence of coherent events such as sweeps and ejections with vertical components in excess of 20 ms^{-1}. Cup anemometer mean velocity measurements were 3.2% higher against sonic and limitations of the standard wind resource assessment based on 10 minute averaging intervals were revealed due to low resolution.

The same anemometers were used in the second complex terrain case, now at 40 m above ground level on the Paul da Serra plateau, Madeira Island, at 1500 m altitude. It was showed that vertical components were reduced in spite of the tower location, few meters from a cliff. Cup anemometer mean velocity was 1% higher against sonic while turbulence intensity was 11% higher for sonic against cup anemometer. The analysis of turbulence showed that the flow was close to a flat terrain case, with *it*, $\sigma(v)/\sigma(u)$ and $\sigma(w)/\sigma(u)$ respectively 8, 91 and 60%. Data analysis from other stations of Paúl located from 2 to 5 km apart showed that terrain induced effects shifted the flow in one station for northeast and southwest winds (115 a 72°). Turbulent intensity at all 4 stations on the plateau was within wind turbine design values.

Résumé

Le principal objectif de cette thèse est l'étude ainsi que l'application des anémomètres soniques pour des écoulements turbulents dans des terrains complexes, ceci est dans le contexte de l'énergie éolienne. Les résultats de mesures sont explorés à l'aide des anémomètres soniques dans quatre situations distinctes : terrain plat avec rugosité élevée et évapotranspiration ; tunnel aérodynamique ; et deux situations de terrains complexes dans l'Île de Madère, terrain côtier et montagneux.

La variabilité des mesures des deux premiers moments statistiques est explorée dans le cas du terrain plat où les instruments de 3 fabricants : NUW de NCAR, modèle CSAT-3 du Campbell Scientific Incorporation, et modèle HS du Gill Solent Instruments, sont comparés à la même hauteur et avec une séparation spatiale qui ne dépasse pas les 9 m pour un écoulement à gradients thermiques et à évapotranspiration élevées. Les premiers moments statistiques de la vitesse et de la température montrent une corrélation entre les instruments de 99% et les seconds moments une corrélation qui variait de 92% à 99% de concordance avec les résultats sur d'autres types de terrains. L'instrument dont la performance qui peut être classer comme la meilleur a été celui de Campbell (modèle CSI-3). Néanmoins, pour des effets d'études des ressources éoliennes et de la turbulence atmosphérique pour des buts énergétiques, la différence des résultats de mesure entre les instruments sont insignifiantes.

On a quantifié, dans un tunnel aérodynamique, la déformation *transducer shadow effect* d'un anémomètre sonique Metek (modèle USA-1) pour des vitesses entre 4 et 16 ms^{-1}, dans toutes les directions, et une inclinaison avec la direction de l'écoulement qui varie entre $\pm 25°$. Les résultats ont indiqués l'existence de zones de décélération et d'accélération de l'écoulement qui varient de -12 jusqu'a + 5%. Les variations ont été corrigées pour un maximum de $\pm 0.1\%$ après avoir appliqué une matrice de correction qui comptabilisait la direction et l'angle de l'écoulement. On a remarqué que les mesures de température n'étaient pas affectées. La connaissance de ces instruments a rendu possible la réalisation des mesures de turbulence sur des terrains complexe avec une certaine confiance.

Les mesures avec les deux anémomètres, gobelets et sonique (NRG modèle 40 et Metek modèle USA-1), ont été effectuées au niveau de la hauteur d'une turbine éolienne sur terrain complexe pour chercher les causes responsables de son mauvais fonctionnement.

Compte tenu du caractère passager et non stationnaire du champ moyen des vitesses, on a utilisé des techniques spectrales, ondulette et d'analyse de quadrant. Les résultats des mesures ont été aussi confrontés à des résultats de simulations indépendantes, qui indiquaient la présence de tourbillon avec une périodicité de 2.5-min dans les proximités de l'aérogénérateur. Les mesures ont confirmé l'existence de ces tourbillons, avec une différence de périodicité de l'ordre de 14%, à l'égard des simulations numériques, indiquant aussi l'existence de structures cohérentes comme les *sweeps* et les *ejections* avec des composantes verticales qui dépassent les 20 ms^{-1}. Les mesures avec les anémomètres de gobelets sont surestimées de 3.2% et les moyennes temporaires de 10 minutes apparaissent comme une limitation de la méthodologie actuelle pour l'évaluation de ressources éoliennes.

Les mêmes anémomètres ont été utilisés dans le second cas de l'écoulement sur terrain complexe, maintenant à 40 m du sol sur le plateau du Paúl da Serra, Île de Madère, à 1500 m de hauteur. On a vérifié que les composantes verticales étaient réduites malgré la proximité entre la tour de mesure et les précipices. Des comparaisons entre anémomètres ont montrés que la vitesse moyenne mesurée par le sonique était surestimée de 1% dans le cas de l'anémomètre de gobelets et que l'intensité de la turbulence était surestimée, par le sonique, de 11%. L'analyse de la turbulence a indiqué que l'écoulement était similaire à un écoulement sur terrain plat, avec *it*, $\sigma(v)/\sigma(u)$ et $\sigma(w)/\sigma(u)$ respectivement avec 8, 91 et 60%. L'analyse des données d'autres postes du Paúl, éloignés de 2 a 5 km, indique que les effets induits par le terrain déviaient l'écoulement pour le cas des vents de nord-est et celui du sud-ouest (115 à 72°). Il s'est avéré que les niveaux de turbulence dans ce lieu ne compromettent pas le fonctionnement de l'aérogénérateur.

Acknowledgments

Several people have been responsible for making this dissertation possible, they have been:

José Manuel Laginha Mestre Palma who supervised, supported and believed in my work. Thanks for keeping high standards and avoiding shortcuts.

Steve Oncley who hosted me in the States for 6 months at NCAR and integrated me into OASIS and EBEX projects, and for the fruitful discussions on instrumentation and turbulence measurements.

Roland Vogt an EBEX partner who hosted me in Basel and invited to a sonic calibration competition at Zürich.

Thomas Foken for the fruitful discussions in the micrometeorological problems and by including my contributes in EBEX.

Álvaro Henrique Rodrigues who was always supportive throughout the years that lasted this thesis and invited me to participate in the measurements made in Madeira.

Fernando Aristides de Castro and Alexandre Silva Lopes whose standards I have tried to reach.

Carlos Balsa and Carlos Santos who helped me in the review process.

Miguel Ferreira who grew with me in the wind energy area and who always tried to show me the practical engineering questions.

Christian Feigenwinter who showed me the way to the wavelet world.

João Viana Lopes that helped me in early steps of signal processing techniques and Lyx.

Albano Alves, José Rufino, José Exposto and Paulo Matos who patiently helped me in my problems with sofware.

Dionísio Afonso Gonçalves whose idea of me I am trying to achieve.

I also thank particularly the Bragança Polytechnic Institute, the School of Technology and Management and the Mechanical Technology Department who patiently supported my research. My special thanks to *João da Rocha e Silva*, *João Eduardo Pinto Castro Ribeiro*, *Manuel Luís Pires Clara*, colleagues who kept things working while I was away. I apologise to those who I have inevitably missed. This work has been funded under project PRODEP III 5.3/N/199.0/4/01.

À Lena, Tomás e Francisco.

Contents

List of Figures

List of Tables

List of symbols

Roman characters

a	Scalar quantity
c	Speed of sound
c_p	Specific heat at constant pressure
d	Transducer path length
e	Water vapor pressure
q	Specific humidity
r	Mixing ratio of water vapor
s	Sonic path separation distance
s_k	Skewness
t	Time
u	Longitudinal flow velocity
u_*	Friction velocity
v	Transversal flow velocity
x	Longitudinal displacement
w	Vertical flow velocity
Co	Cospectra
E	Energy spectrum
Ex	Exuberance
F	Vertical flux

G	Storage flux
H	Hyperbolic hole
H_s	Sensible heat flux
K	Distribution kurtosis
K_c	Velocity deviation from transducer shadow effect
K_{c_T}	Temperature deviation from transducer shadow effect
L	Eddy scale
LE	Latent heat flux
Og	Ogive function
P_0	Static pressure
R	Aurocorrelation function
R^2	Linear correlation coefficient
R_0	Gas constant
Re	Reynolds number
Ri	Richardson number
R_{net}	Net radiation
S	Power spectrum
T	Oscillation period
	Absolute temperature
T_s	Sonic temperature
T_v	Virtual temperature
U	Boundary-layer flow velocity
	Mean flow velocity
$\mathbf{V}$	Wind velocity vector
V_d	Along-path wind velocity component
V_n	Cross-path wind velocity component

Greek characters

Γ_d	Dry adiabatic lapse rate
Ψ	Absolute humidity
α	Tilt angle
β	Roll angle
ϕ	Azimuth of incoming flow
γ	Rotation angle
ϵ	Energy dissipation rate
ρ	Density
σ	Standard deviation
θ	Inclination of the flow
	Potential temperature
θ_v	Virtual potential temperature
η	Viscous dissipation scale
ω	Frequency
ψ	Mother wavelet
	Relative humidity
ν	Dynamic viscosity
τ	Time shift

Operators

$.\hat{.}.$	Fourier transform
$\overline{...}$	Time average
$\langle \ldots \rangle$	Conditional averaging
$\ldots'$	Fluctuating part
$\overline{a'a'}$	Variance of a'

$\overline{a'b'}$	Covariance of $a'b'$
$g(\omega)f^*(\omega)$	Convolution of $g(\omega)$ and $f(\omega)$

Abreviations

agl	Above ground level
ASTER	Atmosphere-Surface Turbulent Exchange Research
CPU	Central processing unit
DFT	Discrete Fourier Transform
DNS	Direct Numerical Simulation
DT	Block averaging and detrending
EPA	Environmental Protection Agency
ETHZ	Eidgnössische Technishe Hochschule Zürich
FFT	Fast Fourier Transform
LES	Large-Eddy Simulation
MCR	Institute of Meteorology, Climatology and Remote Sensing
MR	Mean removal
NCAR	National Center for Atmospheric Research
PAM	Portable Atmospheric Mesonet
PDF	Probability Density Function
RMF	Running mean filter
SGS	Sub-grid scaling
WA^{s}P	Wind Atlas Analysis and Application Program

Chapter 1

Introduction

1.1 Wind Energy

The wind energy in Europe

Wind power is present for more than 2000 years in western and eastern civilizations, and only in the last 200 years it was dethroned by energy provided mainly from chemical sources: coal, oil or nuclear. The oil chock in the 70's and the increase in environmental awareness fomented the search of alternative power supply sources.

Modern wind energy developments started in Denmark, where the suitable geographical conditions, social and political factors promoted the wind turbine technology to a success case. Danish flat terrain and moderate to strong winds promoted the research and industrialization of larger wind turbines and wind farms. The commercial wind turbine size increased in the last ten years astonishingly: 150% for the turbine diameter and 900% for the nominal power. Nowadays the wind turbines are the biggest mechanical devices in the world, with a rotor diameter over 100 m placed at 100 m height.

European Union political compromise for 2030 aim the contribution from renewable energy sources to be 36% of all energy need (European Union Directive 2001/77/CE), with large contribution from wind energy. In 2002, 2% of European electricity needs was from wind and European Wind Energy Association targets 2020 for wind power to achieve 12% of worlds electricity needs.

Besides the development of new and larger wind turbines (megawatt and multi-megawatt turbines), the wind farms sites were diversified and from the flat regions of Denmark, wind farms have spread to complex or mountainous terrains, as found in Portugal, Spain or Greece, and offshore wind farms, as in Denmark, Sweden or Holland.

The Portuguese case

The main incentive for Portugal to develop its renewable energy sources has been the target laid down in the European Unions Renewables Directive, which states that the proportion of renewable electricity should reach 39% in the Portuguese system by 2010 (Resolution of the Council of Ministries RCM 63/2003 from April 28). If large hydro schemes continue at their current average output, by 2010 large hydro will be responsible for 19.4% of the overall electricity demand, leaving an equal share of 19.6% for other renewable technologies (table 1.1). Predicted wind energy contribution will be 17% of nations energy need, corresponding to a wind farm installation rate of about 2 MW per day, according to *International Energy Agency*.

Table 1.1: Endogenous installed and planned capacity (evolution 2001 to 2010). By December 2003 the wind power installed in Portugal was 288.6 MW. Data from *International Energy Agency*.

Resources	2001 [MW]	2010 [MW]
Wind	101	3750
Small hydro	215	400
Biomass	10	150
Solid waste	66	130
Wave	0	50
Photovoltaic	1	150
Large hydro	4209	5000

Wind assessment studies made in Portugal since 1992 (Restivo and Petersen, 1993) show that contrary to Northern European countries, the resources are low along the coast line. Higher wind resources could be found in the Country's mountainous regions of the north and centre, due to acceleration of the Atlantic or Continental flow over the mountain ranges. The first Portuguese large wind farm was installed in 1996 (10.2 MW at Fonte da Mesa - Lamego) and by the end of 2000, 70 % of the 116 MW already in operation were sited in mountainous areas of north and centre of the Continent (Rodrigues, 2000).

Wind assessment studies follow the recommended methodology, which consists on the measurement for, at least, a year of wind velocity and direction by cup anemometer and wind vane placed at hub height (International Energy Agency, 1990). The mean wind field characterized by 10 min averages made at 0.5 to 0.33 Hz sampling frequency measurements is applied in linear-code simulation programs such as WA^{s}P, providing a spacial distribution of the possible wind conditions in the vicinity of the measuring mast (Troen and Petersen, 1989).

European Wind Energy Association recognizes that standard wind resource assessment

studies for complex terrain require different methodology than applied in flat terrain, both from measurement and wind flow prediction, and are listed as one of research and development objectives for wind industry (European Wind Energy Association, 2004). Wind turbine aerodynamic and structural performance associated with vibrations during operations due to variations in wind flow are also among fundamental research and development objectives for the industry. High turbulence levels and inclined flow due to orography are likely to diminish wind turbine performance and increase fatigue load in the structure, and must be among important problems to be addressed for wind turbine sitting over complex terrain such as in most of Portuguese locations.

1.2 Previous studies

The development of wind energy over mountainous terrain is still based in simplified assumptions on the evolution of the mean and turbulent flow used in early flat terrain studies, and seldom sonic anemometers are included in flow studies for wind energy purposes. Fragoulis et al. (1996) reports the use of sonics in research groups such as RISØ from Denmark, CIEMAT from Spain, CRES from Greece or NREL from United States, as one of the first steps to characterize the wind structure in complex terrain. Length scale analysis by Marti et al. (1999) or the quantification of the vertical components of the flow by Ribeiro (1998) are some of the examples on recent use of sonic anemometer in wind energy projects, although not used in the core of the assessment study, showing the sonic only as a complementary tool for a specific task. More complete use of sonics is presented by Kelley (1999) when using also the sonic temperature to be included in the measurement of the stratified flow field or by Kelley et al. (2000) to assess turbulence/rotor interactions.

The ability of measuring the vertical component of the wind flow was also explored in studies regarding cup anemometer performance (Papadopoulos et al., 2001). Pedersen (2004) defines the concerns on complex terrain inclined airflow by addressing both cup anemometer and turbine's power curve performance in inclined flow over complex terrain.

The rare use of sonic anemometers in the wind energy area is compensated by its long-time use in micrometeorologic field since Suomi (1957). Nowadays large field experiments, EBEX00, Map-Riviera, or Litfass (Oncley et al., 2000; Rotach et al., 2000; Beyrich et al., 2000) are possible with joint efforts of many institutions where equipments and methods are first confronted before the measurement campaign. In those studies, a sonic anemometer was a basic instrument for heat, momentum or scalar fluxes measurements from flat terrain to mountain slopes, from tropical forests or Arctic environment. Sonic field comparisons are documented for some of those projects, being a fundamental step to better know the instrument at hand.

However, most publications on sonic anemometer performance are from wind tunnel measurements to quantify the known transducer shadow effect, a velocity defect caused

by transducer array that distorts the measurements (Hanafusa et al., 1982; Coppin and Taylor, 1983; Wyngaard and Zhang, 1985). Early studies examined the flow distortion assuming axes independent of each other rather than the flow distortion around the whole probe assembly due to lack of a large low-wind tunnel and high speed acquisition data (Oncley, 1999).

To our knowledge, sonic calibration with the whole probe assembly was first studied by Baker et al. (1989), who tested 3 sonics at the *Environmental Protection Agency - EPA* wind tunnel under different flow inclinations. Soon after, manufacturers such Applied Technologies Inc. presented flow distortion studies for their products (Kaimal et al., 1990; Kaimal, 1990b,c) incorporating internal software corrections in the instrument.

There were attempts made to summarize the array distortion in a generic frame (Mortensen et al., 1995), although the most complete description of the problem may be found at Oncley (1999). There are as many publications on sonic calibrations as the models and brands commercially available, however there is no standard design calibration procedure for these instruments (Cuerva, 1999).

Vogt (1995) presented the more complete setup with systematic control of the rotation and inclination of the whole sonic assembly inside the wind tunnel test section. His work was followed independently by Heinemann et al. (1997) for a Solent 1012 Sonic Anemometer.

However, low Re characteristics of wind tunnel test section raise the question on sonic anemometer distortion under real atmospheric conditions. The separation bubble around each transducer diminishes for larger Re and array distortion tend to be smaller. We have to consider also that each sonic manufacturer presents different transducer array configuration thus measurements are affected differently.

Sonic comparisons in real atmosphere are reported by Oncley (1996), Christen et al. (2000) or Högström and Smedman (2004). However the comparisons were made under different flow conditions, with different instruments and experimental procedures. Oncley (1996) tested Applied Technologies Instruments (K-probe model), New University of Washington (NUW model), Campbell Scientific Inc. (CSI-3 model) and Gill Instruments (HS model) sonics both in wind tunnel and at a test site. In field measurements Oncley recurred to the flip-rotated technique to determine the differences in flow distortion when each unit (same model) was placed up-side down. The recovering time from wet to dry weather conditions on a test site was also investigated. On the other hand, Christen et al. (2000) used the array distortion and the application of software correction for Gill and Metek sonics from Vogt et al. (1997) and extended the comparison also to Campbell sonics for flat grass covered terrain. Finally, Högström and Smedman (2004) reports a Gill sonic wind tunnel and field calibration, the latter made in a coastal area. Another common feature of those studies is the terrain vegetation in all cases: low grass coverage over a flat terrain.

1.3 Thesis contribution

The contribution of this thesis may be divided in 4 parts: measurement techniques, instrument knowledge, site characterization and post-processing methodologies.

The contribution from measurement techniques are from the use of well known measurement procedures of eddy-covariance from micrometeorology applied to wind energy. Sonic anemometers are already widely used in micrometeorology and there is a need for information on turbulence and vertical components of the airflow over complex terrain for wind energy applications. The use of experimental techniques from a different field present an alternative path to wind energy standard procedures.

The instrument knowledge contribution relates in a strict sense to the characterization of a Metek (model USA1) sonic anemometer under controlled conditions. The characterization and identification of the strengths and weaknesses of a NUW, CSAT-3 Campbell and Gill HS sonic anemometers in a flow with large roughness and large temperature and humidity gradients are also among the contributions from instrumentation. In a broad sense, the use of a variety of instruments enabled the experimental technique to be mastered.

Site characterization contribution refers to the mean and turbulent flow characterization of two complex sites in Madeira Island. The coastal site of Caniçal and the Paul da Serra plateau were places where sonic measurements enable a more complete characterization of the turbulence field. However, to address such flows, alternative tools such as wavelet and quadrant analyses where applied and yielded a clearer picture of the turbulent field in those sites.

The post-processing methodologies based on ogive function, wavelet and quadrant analyses belong to a whole set of known tools also with applicability to the wind energy field. Complex terrain turbulence, the role of coherent events, and detection schemes are proposed with scalograms and autocorrelation scalograms.

A final contribution of this thesis is showing the need for systematic turbulence and vertical velocity components measurements in a complex terrain site. Cup anemometer measurements will still be required for long term characterization of the mean wind field and seasonal variability of the flow. However, a second step is proposed by including turbulence characterization as a standard procedure. Firstly, to identify flow features that may be pernicious to turbine operations and secondly to quantify the vertical component of the flow, which is known to affect cup anemometer measurements with consequences to wind turbine output, power curve performance and by adding extra yaw loads onto a wind turbine.

1.4 Flow over complex terrain

If the terrain is not horizontally homogeneous, when changes in surface roughness length occur or different scalar sources are present, a difficult and complex problem for flow analysis is posed. In micrometeorology, such a terrain is complex, and may represent a wide variety of surfaces: urban, mountains, tropical forests or sand dunes amongst others. From a wind energy perspective, a complex terrain is generally associated with complex orography: the objective is to avoid siting the turbine in places that may lead to lower productivity and higher fatigue loads. In the context of this work we may recall Kaimal and Finnigan (1994) definition for complex terrain flow, which is characterized by the change in the elevation of the terrain that forces large-scale changes in the pressure field, subjecting changes in the velocity and turbulence fields.

Measurements of the whole mean and turbulent field in real complex topography is virtually impossible. The number of instruments needed would be financially prohibitive, with no guarantee that the depth of the perturbed flow would be within the tower height. The most complete field experiment so far was the Askervein Hill experiment with the deployment of 50 towers in two lines parallel to the flow (Raithby et al., 1996). Wind tunnel modeling or computer simulations are the obvious choice for studying such flows.

Petersen et al. (1998) presented a review on wind power meteorology addressing basic concepts of boundary-layer and showing that the terrain inhomogeneities alter the spectra: energy is redistributed from longitudinal flow component to the vertical by rapid distortion. However, it has not been yet achieved a mathematical frame that translates the physical features of the flow by the normalization of the complex surface. Each terrain is a single case that need to be studied independently, although simplifications for two-dimensional ridges or axissimmetric hills helped to parametrize linear asymptotic models for the mean wind flow. Kaimal and Finnigan (1994) presents extensively the results based in such models, from which it is shown that the flow pattern over and around a mountain or hill is dominated by its shape, size, roughness and by the stability of the flow. A more complex analysis of the topographic effects and stratification can be consulted at Baines (1995).

Common features of complex terrain flows are the upwind deceleration, speed up, separation bubble and the wake region, where a full description could be found in Kaimal and Finnigan (1994). The authors emphasize the lack of knowledge in the near wake and separation bubble because the complexity of the flow spans tridimensionally, with statistical unsteadiness and large scales where the instantaneous velocity field never approaches the time-mean field. Reynolds decomposition of the flow into mean and turbulent components is compromised presenting a purely formal meaning (Kaimal and Finnigan, 1994).

Along large eddy structures induced by the orography, other type of flow structures are observed even in simple wall flows. These structures, *turbulent structures* or *quasi-coherent structures*, are regions of space or time where the flow field has a characteristic coherent flow pattern, which can occur at different positions and times, Pope (2000). Here we refer

Robinson (1991) definition of a coherent structure as a

> three-dimensional region of the flow over which at least one fundamental flow variable (velocity component, density, temperature, etc.) exhibits significant correlation with itself or with another variable over a range of space and/or time that is significant larger than the smallest local scales of the flow

Pope (2000) identifies several coherent structures mainly from flow visualization or Direct Numerical Simulation -DNS- results such as: low-speed *streaks*, *ejections* of low-speed fluid outward from the wall, *sweeps* of high speed fluid toward the wall, and *vortical structures* of several forms: hairpins, pockets, bulges, deep valleys, etc.

Several detection and identifications schemes can be applied depending on the time and space resolution of the data. A single point measurement excludes detection schemes based on vorticity that may be overcome by the use of several combined techniques that are addressed in Appendixes B and C.

1.5 Ultrasonic anemometer

The basic working principle of ultrasonic anemometry lies on the measurement of the transit time for a sound pulse to cross a known path length. If there is a wind component along the path, the transit time will be increased or decreased from the no-wind case depending on the direction of the component. The sound pulse is transmitted and received by a piezoelectric transducer placed in the end of an array that forms, in the generic case, a 3 component measurement volume (Oncley, 1989; Wyngaard, 1981; Schotanus et al., 1983; Shimizu et al., 1999; Baker et al., 1989) are some examples of the use of 3-dimensional term when characterizing a sonic anemometer measurement. When the measurement is made in 1 point, the information is related to the 3 components of that point in space, therefore 1 dimension and 3 components will be a more rigorous description.

Suomi (1957) is considered the first successful attempt to build an anemometer – thermometer instrument based on sound pulses, although according to Kaimal and Businger (1963) Carrier and Carlson (1944) were the first to describe a true air speed indicator for use on a blimp. The wind velocity was obtained by measuring the phase difference between the signals of two microphones located up and downwind from a continuous source of sound.

The phase difference principle was the basis for the presentation of a new sonic by Kaimal and Businger (1963), with two pairs of transducers operating simultaneously per path, each one dedicated either to transmit or receive (figure 1.1). The phase detection could be made independently of amplitude variations in the received signal, being a more stable and less noisy than a pulse system. The dilemma on which system would be more suitable lasted for almost 20 years until Hanafusa et al. (1980), Hanafusa et al. (1982) and

Coppin and Taylor (1983) presented two sonics based on sound pulses. It was found that changing the timing of the path measurement allowed the same information to be obtained using each transducer alternatively as a transmitter and a receiver, although being able to transmit on only one path at a time. This design enable to obtain twice the sampling rate of which available from earlier instruments and has been a standard ever since.

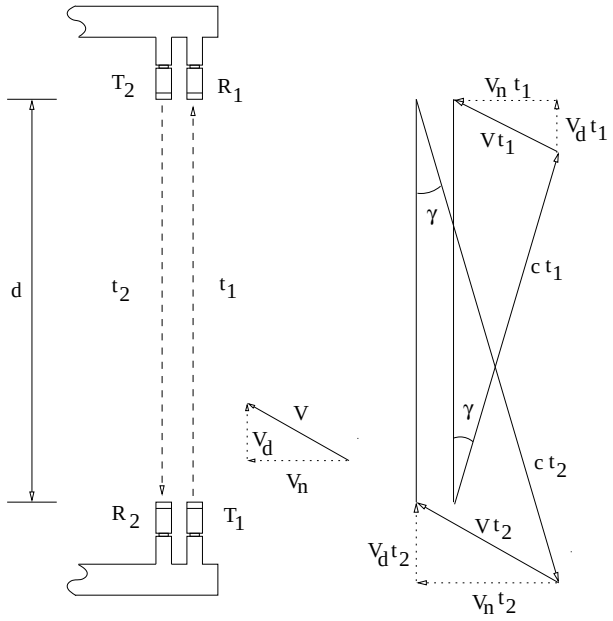

Figure 1.1: Sound-ray vectors from a single-axis anemometer showing the principle of operation. T and R represent respectively the transmitter and receiver. Adapted from Wyngaard (1981).

1.5.1 Velocity measurement

The basic working principles of a sonic anemometer are reviewed in Kaimal and Finnigan (1994), although, by historic reasons we will refer to the Wyngaard (1981) with the support of figure 1.1, where the only difference from contemporary instruments lies on the two pairs of transducers that are replaced by a single transmitter/receiver.

The wind velocity vector $\mathbf{V}$ has V_d and V_n velocity components, in parallel and transversal directions to the sound pulse. We assume that these velocities correspond to the mean flow field that crosses the air volume within the sonic array. The traveling time between two simultaneous sound pulses, one being transmitted by T_1 and being received by R_1, and other by T_2 to R_2 are, from figure 1.1:

$$t_1 = \frac{d}{c\cos\gamma + V_d} \tag{1.1}$$

$$t_2 = \frac{d}{c\cos\gamma - V_d} \tag{1.2}$$

where t_1 and t_2 are the traveling times between transmitter and receiver, and d is the path length, c is the sound speed in air, and $\gamma = \sin^{-1}(V_n/c)$. Thus, and recurring to expressions (1.1) and (1.2), the wind velocity may be measured by the reciprocals:

$$V_d = \frac{d}{2}\left(\frac{1}{t_1} - \frac{1}{t_2}\right) \tag{1.3}$$

Equation (1.3) gives an absolute calibration (Coppin and Taylor, 1983) which depends only on the path distance between transducers. For one-component sonic anemometer, the measurement will arrive from a single time measurement along the existing path. For two- or three-component sonic anemometers, the wind velocity is calculated by the trigonometric decomposition of the array. A complete description of a non-orthogonal sonic array can be found in Zhang et al. (1996).

The linear sound pulse model has not been questioned until Cuerva and Sanz-Andrés (2000) present a more complex model for measuring under non-steady, non-uniform atmospheric conditions. Their model show that the Mach number and time delay from sonic pulses distort the measurement in the normal operation range. In this case, the sound pulse travel is not linear but follows a wave propagation front that is drifted by the flow. The model shows that the path length is prone to influence the attenuation of the measurement, as well the time delay, specially for frequencies above 10 Hz. This model may be of interest the sonic anemometer designers for future implementation into commercial models. The pulse traveling time is not available for the users difficulting an independent confrontation of the proposed model.

1.5.2 Array geometry

Other fundamental difference on the evolution of sonic anemometer is the array geometry. Kaimal and Businger (1963) model presented an orthogonal geometry and the sonic should be mounted aligned up-wind with the flow streamlines. As the wind direction varies, the coordinate transformation would be required along with sonic tilt corrections. Orthogonal paths in the array turned then, unnecessary. New geometries have emerged with intersecting paths, sampling the same volume of air to avoid path separation problems or flow distortion. The non-orthogonal geometries aim the non-existence of paths in the horizontal plane. Those geometries evolved according to different manufacturer solutions. Nowadays, the UW-Sonic transducer array design has been the most common with 60° angles to the horizontal design (Zhang et al., 1996). (Kaijo Denki Company in Japan present arrays with 45°).

The transducer distance in early instruments also evolved: Kaimal and Businger (1963)

reports on different paths, from 103 to 50 cm for a one-component sonic anemometer, while Kaijo Denki Company presents nowadays an unit with a path length of 5 cm. The path-length sets the limit of the measurable eddy size. For sonic design considerations, two rules-of-thumb based in the same 20 to 1 ratio are invoked: the path length to transducer diameter ratio and the measurement height to path length (Oncley, 1999). Both design criteria are related to the expected use of the instrument. Thus, an instrument such as the Kaijo Denki should not be lower than 1 m above ground and the transducer diameter should not exceed 0.25 cm. The manufacturers are recurring to smaller path length to transducer ratios while Kaimal and Finnigan (1994) also assumes the acceptance of a higher degree of flow distortion and transducer shadowing as the price for compactness in the sampling volume and consequent improvement in frequency response.

The array geometry and path length are design factors that distort the flow. Distortion caused by the sonics has been studied for several years (e.g. Kaimal (1978), Wyngaard and Zhang (1985) or Kaimal et al. (1990)) and can be divided into two categories: transducer shadowing and array-induced distortion. Kaimal (1978) identified one contribution to sonic anemometer flow distortion as the underestimate of velocity caused by partial shadowing of the path by the transducers. He generalized in wind tunnel measurements for the normal and along path velocities, V_n and V_d, where the inclination of the flow is defined by $\theta \equiv \arctan|V_n|/|V_d| = 90^\circ - \gamma$ that:

$$\frac{(V_d)_m}{V_d} = \begin{cases} c + (1-c)\theta/\theta_d & 0 \leq \theta \leq \theta_d \\ 1 & \theta_d \leq \theta \leq 90^\circ \end{cases} \tag{1.4}$$

Kaimal (1978) found that the velocity attenuation (related to c) is a function of the path-length to transducer diameter ratio, ranging from 70 to 93% for ratios between 10:1 and 50:1. Wyngaard and Zhang (1985) modified expression (1.4) to

$$f(\theta) = c + 1(1-c)\sin\theta \tag{1.5}$$

for use in a theoretical discussion of transducer shadowing effects on turbulent statistics.

The array-induced distortion is also due to other parts on the measurement system, such as arms, struts and mounting boom. Tower and electronic boxes add up into factors to be considered, although a careful experimental setup mitigate their effects into the experimental uncertainty limits. The arms, struts, mounting booms and the path length to transducer diameter ratio depend mostly in the sonic design, requiring individual calibration either in wind tunnel or before field experiment.

Field calibration is a complementary test to surpass the fact that the wind tunnel turbulence levels are lower than in the boundary-layer. The separation of the flow around the transducer array may be different and the compensations for the transducer shadow effect established in wind tunnel may be excessive. A field calibration with two identical

instruments, placed closely but mounted differently, one in the correct position and other upside-down, provides the missing information on the transducer shadow effect. This is the so-called flipped and rotated test (Oncley, 1996), made by NCAR with NUW sonics.

1.5.3 Spectral response

Kaimal and Finnigan (1994) points out that the main limitation of the sonic anemometer to frequency response is the one imposed by the line averaging along the acoustic paths. The spatial separation of the individual path lengths is no longer a major concern, because the manufacturers have chosen arrays that sample the same volume of air, with the exception of Applied Technologies Inc. (from Longmond, Colorado) that still builds the orthogonal K-probe among other non-orthogonal sonics. Wyngaard (1981) indicates that streamwise wavenumber spectra become distorted at streamwise wavenumbers $k_1 \simeq 2\pi/\overline{u}$ of the order of d^{-1} while Kaimal and Finnigan (1994) generalizes based in another rule-of-thumb for calculating the onset of spectral distortion attributable to path length d, or separation distance s, as the larger of these two relations: $k_1 d$ or $(k_1 s) = 1$. However these corrections are necessary only in special conditions. Wamser et al. (1997) show that only corrections for spectral response of sonic anemometers due to spacial averaging of turbulent fluctuations along sonic path are needed for the vertical velocity variance when sonic is close to the ground (1 m and flat terrain). Also the theoretical model performance for complex atmospheric conditions by Cuerva and Sanz-Andrés (2000) shows that the attenuation value for the longitudinal spectrum at $k_1 d = 1$ decreases by 5%, which is an even smaller limit than Kaimal's.

According to Wyngaard (1981), the path-length is the 'distance constant' of the sonic anemometer, which corresponds to a magnitude gain of one in turbulence resolution when compared to cup anemometers.

1.5.4 Temperature measurements

Sonic anemometer is a shorter form of ultrasonic anemometer/thermometer and may lead to the oblivion of temperature measurements, which though secondary for the wind energy, are fundamental for heat flux measurements.

Recalling figure 1.1, and applying the trigonometric relations $V^2 = V_n^2 + V_d^2$ and $\sin(\gamma) = V_n/c$ into equations (1.1) and (1.2) will yield:

$$t_2 - t_1 = \frac{2dV_d}{c^2 - V^2} \tag{1.6}$$

$$t_2 + t_1 = \frac{2dc\cos(\gamma)}{c^2 - V^2} \tag{1.7}$$

The sound wave propagation c is determined by the fluid density and by the elastic properties of the medium (air):

$$c^2 = 403T_0(1 + 0.32e/p) \tag{1.8}$$

where e/p is the water vapor pressure by the atmospheric pressure, and T_0 is the absolute temperature. According to some authors the value 0.32 varies slightly. It is dependent on the specific heat capacities of dry and moist air at constant pressure, which both vary with temperature. The factor 403 is the product of the specific heat ratio by the gas constant, both for dry air. If we substitute e/p in equation (1.8) by the specific humidity, $q \approx 0.622e/p$, the equation becomes:

$$c^2 = 403T_0(1 + 0.51q) \tag{1.9}$$

Due to similarity between equation (1.9) and the virtual temperature $T_v = T_0(1+0.61q)$, defined as the temperature at which dry air has the same pressure, Kaimal and Gaynor (1991) named the *sonic temperature*, $T_s = T_0(1 + 0.51q) \approx T_v$. Thus, equation (1.9) can be written as:

$$c^2 = 403T_s \tag{1.10}$$

and by substituting c from equations (1.1) and (1.2), the sonic temperature is:

$$T_s = \frac{d^2}{1612}\left(\frac{1}{t_1} + \frac{1}{t_2}\right) + \frac{V_n^2}{403} \tag{1.11}$$

Kaimal and Finnigan (1994) argue that the sonic derived temperature T_s should be treated as the virtual temperature T_v and may be used directly in its place where the buoyancy from moisture should be included.

1.5.5 Concluding remarks

Wind energy assessment studies are based on cup anemometry, following internationally accepted practices (International Energy Agency, 1990; Pedersen et al., 1999). The standards evolved to accommodate new anemometers such as sonics, though mainly for turbulence measurements and not so much for measurement of the vertical component of the mean flow. Pedersen et al. (1999) refers as main advantage the dynamical response of the sonic anemometer, but repeats the concerns (Kaimal, 1978) on the disadvantages of the instrument for long-term use in wind energy: cost, lack of accuracy, sensitivity to precipitation and flow distortion from the transducer array. The technology evolved since those statements and the sonics for the past 10 years became a standard in flux measurements (Businger et al., 1990).

Cost The cost has been reduced, as any other electronic-based device. Nowadays even commercial 2-component sonic anemometer are available for leisure sailing boats. The purpose of the instrument has to be considered, i.e. research or engineering. Different manufacturers present models for both purposes, where the use for latter type must be weighted with the cost of 3 other instruments for wind turbine assessment studies: cup anemometer, wind vane, and thermometer.

Lack of accuracy As pointed out in Pedersen et al. (1999), the resolution and precision of the instrument does not mean absolute accuracy. Indeed the accuracy of the instrument can be questioned due to the array distortion, which can be measured and quantified for future compensation on the data set. Nowadays, some manufacturers like ATI, Young or Campbell provide flow distortion software, that can be (de)activated by the user.

Sensitivity to other than fair-weather conditions That limitation is seldom applied in boundary-layer research. The momentum flux is changed by the drag of the precipitating droplets and that can be easily verified in the time series. Another practical question is in the recovery time of the instrument, or how long does it take for the droplet on the transducer to dry out and to consider the measurements valid again. The problem lies on the size of the transducer. A rain drop tends to stay longer in smaller transducers, while larger ones dry faster. However, larger transducers tend to be affected earlier by the falling rain. For other weather conditions, Siebert and Teichman (2000) found that a sonic from Gill Instruments under cloudy conditions in mountain sites presented no change in the instrument performance. Finally, temperature operation limits of the piezoelectric sonic transducers are quite broad, being the lower limit -40 °C, avoiding the common freezing of the cup anemometer or wind vane during rigorous mountain weather.

Finally, the main reason for using sonic anemometers is their high resolution compared with other instruments.

1.6 Eddy correlation technique: procedure and limitations

1.6.1 Definition of the problem

When flux measurements are concerned, a standard procedure has not been reached yet (Massman, 2003). See for instance Biltoft (2003a) on the scalar versus the net (vector) momentum flux calculations from Stull (1984) and the questions by Mahrt et al. (2000) on the lost of the sign of $\overline{u'w'}$ and $\overline{u'v'}$ during the computation process.

Other questions on data processing techniques such as averaging and detrending, coordinate rotation, low and high frequencies corrections, flux corrections for cross contamination are some additional open questions (Finnigan, 1999; Massman, 2003). Long-term carbon fluxes for instance are being recalculated in order to include this new post-processing techniques, Finnigan et al. (2003).

Biltoft (2003a) defines the problem clearly to an experimentalist, and the following text is based on his notes, where a eddy covariance flux measurement from a stationary site poses two basic problems:

1. The turbulent transfer of heat (or momentum) flux, through one surface or level in the atmosphere, occurs as irregularly spaced events characterized by their duration, intensity, and spatial location. In contrast, the tower-mounted sonic obtains measurements at discrete intervals from a fixed location at some unknown distance downwind of the flux source. The objective is to come-up with a workable procedure that produces a time average that converges toward a flux space-time ensemble average. Through the ergodic hypothesis we assume that time, space, and ensemble averages are related (Garrat, 1994). Time and space averages can be related with varying degrees of success, depending on the capabilities of the instrument, site conditions, instrument exposure, data handling, and the scales of motions that occur during the measurement period.

2. The intermittent and irregular character of the events poses a problem in flux measurements. The averaging needed to approximate and ensemble average obscures the duration, intensity, and spatial location of individual flux events. There are three basic alternative approaches to eddy covariance flux measurement: block averaging and mean removal - MR; block averaging and detrending - DT; and running mean filtering - RMF. Each approach offers advantages and disadvantages. It is up to the experimentalist to consider the measurement objective and choose between a procedure that provides a good approximation of the average ensemble flux and a procedure that emphasizes the transient characteristics of individual localized flux events (Kaimal and Finnigan, 1994; Biltoft, 2003b).

1.6.2 Sampling and averaging

The choice of sampling and averaging times used to create a turbulence realization depends on the use to be made of the flux information and the amount of time that the experimenter is willing or able to invest in the data analysis. Each chosen realization is one of an ensemble of possible realizations: one measurement objective is the estimation of the flux ensemble. Because fluxes are intermittent in space and time, it would be ideal for the experimentalist to sample over the entire time of interest and carefully analyze each time series and its spectra prior to choosing averaging times. However, equipment, data storage,

time limitations, and other criteria make this impossible. The analyst is then left to make the best use of time-averaged turbulence based on the resources at hand which include the previously mentioned MR, DT, and RMF flux estimation techniques. Kaimal (1990a) provides some basics tests to check the validity of the field data, although limiting the averaging interval to 15-20 min averages of the time series. Some sampling and averaging considerations are discussed below:

Stationary and integral scale. Early flux sampling and averaging time estimates were based on the assumption of measurement over homogeneous site during stationary meteorological conditions. The boundary-layer model consists of a turbulent inertial sublayer with an identifiable spectral peak that defines an integral scale. Measurements in the real atmosphere deviate often from the homogeneous, stationary and ideal conditions where the spectrum shows no identifiable integral scale. In this situation each realization is not independent of the next because all are samples of some larger process (Kaimal and Finnigan, 1994). Foken and Wichura (1996) offer a simple stationarity test by comparing 30-minute averaged flux of quantity a with the average of six-5-minute averages obtained over the same sampling time. If

$$0.7 < \frac{\overline{w'a'}_{5min}}{\overline{w'a'}_{30min}} < 1.3 \tag{1.12}$$

the data set is considered sufficiently stationary for reasonable flux computation.

Scale separation Data sets usually consist of turbulent motions superimposed on slowly varying larger amplitude ones. Scale separation between the two is often sufficiently small that they are difficult to isolate. In this situation a systematic under-estimate of the flux occurs due to a failure to capture the largest flux-generating scales, and random errors occur as a consequence of selecting and inadequate record length, which must be balanced against overestimation due to the inclusion of larger scales motions. Some of these larger scale motions generate no flux, while other larger scale motions contribute to the overall flux as a consequence of localized convergence/divergence. The experimentalist must decide whether or not those motions contribute to the flux measurement. Therefore, how the flux data are to be used must be carefully considered in the design of a flux measurement program.

Defining mean and fluctuating quantities Flux calculation is based on the selection of appropriate averaging for defining a mean vertical velocity $\overline{w}$ and the means of the transported quantities, $\overline{u}$ or $\overline{T}$. For the vertical flux $\overline{F}$ of a generalized quantity a, the flux is represented as:

$$\overline{F} = \overline{(\overline{w} + w')(\overline{a} + a')} = \overline{w'a'} \tag{1.13}$$

Products of mean quantities $\overline{wa}$ and mixed products $\overline{w}\overline{a'}$, $\overline{w'}\overline{a}$ are identically zero if we assume that $\overline{w}$ and the averages of fluctuating quantities are zero. Unfortunately,

the turbulent atmosphere is often not that simple. In some cases $\overline{w}$ is non-zero, indicating the presence of unresolved flux or some inadequacy in the selected averaging time or method for defining the mean. Optimum averaging periods vary with the state of the atmosphere and the quantities to be measured. To ensure the inclusion of all flux-carrying wavelengths, Oncley (1989) used a cumulative integral of the cospectrum to determine the minimum required averaging times. Wyngaard (1973) shows that the averaging time for turbulence statistics is a function of stability. Once different stability conditions are encountered it is necessary to change the averaging time. Wyngaard (1973) also finds that the covariance of $\overline{u'w'}$ requires the longest averaging time. It seems reasonable to let the minimum time required to obtain the statistical convergence of the Reynolds stress, τ_{uw}, determine the averaging time for all the statistics. This time could be found by testing different averaging times for convergence of covariance, but it was found to be more efficient to examine the cospectrum since the covariance is the integral of the cospectrum over all frequencies given by the ogive function, equation (1.14).

$$Og_{u'w'} = \int_{\infty}^{f_0} Co_{u'w'}(f)df \tag{1.14}$$

Oncley (1989) showed averaging times ranging from 5.6 to 27.8 minutes from stable to unstable conditions for $\overline{u'w'}$, and 2.8 and 16.6 minutes for $\overline{w'T'}$.

Mean removal - MR Selecting sequential non-overlapping block averaging times and performing a mean removal on the u and T realizations is the simplest flux estimation method. The basic premise is that each selected realization is an independent sample of the flux ensemble and that the averages of these samples approximate the ensemble. Averaging times that are too long include the effect of meanders and trends that overestimate the flux. Because it is fairly quick and easy to do, simple mean removal can be performed over several averaging times within the measurement period. This allows one to search for an optimum averaging period.

Detrending - DT Detrending of u and T realizations prior to mean removal can overcome some of the limitations of the MR method, and a trend removal can be particularly useful for a temperature record responding monotonically to a diurnal heating/cooling cycle, Kaimal and Finnigan (1994). However most trends in meteorological data are non-linear and vary with time. When the fit is poor, or when DT is performed over inappropriate averaging times, the result can be far worse than no detrending; and detrending should be used only on data that fail a stationarity test, equation (1.12), and receive close inspection. Detrending has to be performed very carefully, because it offers no guarantee that the true spectrum can be retrieved. As Kaimal and Finnigan (1994) pointed, particular detrending method used often determines the shape of the detrended spectrum and the location of its maximum. Trend removal should be performed only if trends are physically expected or clearly apparent in the time series.

Running mean filtering - RMF With running mean filters, the fluctuating components are obtained as deviations from instantaneous mean from a low-pass filter of user selected length that moves through the data. This technique can include a variable time interval and averaging window that adapts to the physical properties of turbulence, Treviño and Andreas (2000), or the averaging window can be fixed length. The RMF technique offers great advantage when the measurement objective is to study the details of individual flux events. However, fluctuating averages do not necessarily vanish with RMF, violating Reynolds averaging principle (Kaimal and Finnigan, 1994; Bendat and Piersol, 2000). According to Biltoft (2003b), the adaptive RMF technique of Treviño and Andreas (2000) probably minimizes the errors from the violation of the Reynolds averaging principle, but has not been subjected yet to independent testing.

1.6.3 Axis rotation

In order to obtain vertical fluxes of momentum and scalars from sonic measurements, a real experimental setup cannot guarantee a perfect parallelism with the surface and perpendicularity to gravity. The tilt error in friction velocity u_* or in a scalar flux is of the order of 5% per degree of tilt in the vertical plane aligned with the mean wind direction. Consequently, it is often necessary to rotate the coordinates of three-component sonic wind data to correct for this tilt (Horst, 2001). Three methods are available: direct use of known (measured) angles, imposition of requirements on the means and stresses (classic or triple/double rotation method), and imposing/assuming that the sonic is in a parallel plane to the surface.

Theoretically, the mean vertical wind must equals zero for long period. Though being true for flat homogeneous surface, it is questionable for complex terrain. The double/triple rotation method and the planar fit method are the most common methods for coordinate rotations, though more publications are pruning to the last (Massman, 2003). Planar fit method however requires data in wide a range of wind directions: 90° or greater. More details may be found in Wilczak et al. (2001).

1.6.3.1 Double/triple rotation

The time series is averaged to produce a mean wind vector $\overline{V}$, where $(\overline{u_s}, \overline{v_s}, \overline{w_s})$ are the sonic components in orthogonal coordinates. The first step is rotating the system in order to $\overline{v_s} = 0$. The whole time series is rotated by an angle γ defined as:

$$\gamma = \arctan\left(\frac{\overline{v_s}}{\overline{u_s}}\right) \tag{1.15}$$

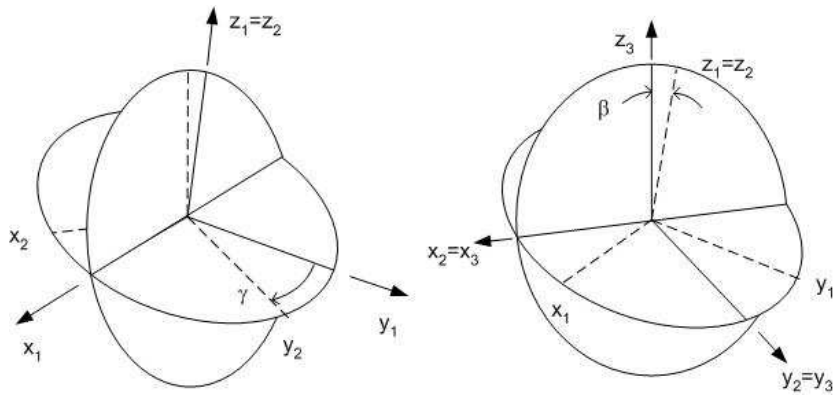

Figure 1.2: Coordinate rotation scheme of the flow. γ is the angle between S_1 and S_2 and β between S_2 and S_3.

Mathematically, the rotation of the mean wind vector $\overline{V}$ into the new reference frame S_2 (figure 1.2) will correspond to:

$$\overline{V}_{S_2} = \mathbf{B}\overline{V}_{S_1} \tag{1.16}$$

where the transformation matrix $\mathbf{B}$ is given by:

$$\mathbf{B} = \begin{bmatrix} \cos\gamma & -\sin\gamma & 0 \\ \sin\gamma & \cos\gamma & 0 \\ 0 & 0 & 1 \end{bmatrix} \tag{1.17}$$

A second rotation is needed to force $\overline{w_s} = 0$ where the mean velocity vector $\overline{V}$ is rotated by angle β finally into streamline coordinates. β is the angle defined as the mean vertical velocity component by the mean horizontal velocity:

$$\beta = \arctan\left(\frac{\overline{w_s}}{\sqrt{\overline{u_s}^2 + \overline{v_s}^2}}\right) \tag{1.18}$$

The rotation is achieved by applying again expression (1.16) where the matrix $\mathbf{B}$ is replaced by $\mathbf{C}$:

$$\mathbf{C} = \begin{bmatrix} \cos\beta & 0 & \sin\beta \\ 0 & 1 & 0 \\ -\sin\beta & 0 & \cos\beta \end{bmatrix} \tag{1.19}$$

Taking $\mathbf{A} = \mathbf{B} \times \mathbf{C}$, expression (1.16) is valid for scalar fluxes such as the heat flux $\overline{w'T'}$ where $\mathbf{A}$ replaces $\mathbf{B}$ and the mean wind vector is replaced by the covariances referenced in

the initial frame. The stress tensor obtained by 5 min averages may also be rotated, and since matrices **B** and **C** are orthogonal, so is matrix **A**, and the inverse of **A** is equal to its transpose, $\mathbf{A}^{-1} = \mathbf{A}^T$. The rotation of the tensor assumes:

$$\begin{bmatrix} \overline{u'u'} & \overline{u'v'} & \overline{u'w'} \\ \overline{v'u'} & \overline{v'v'} & \overline{v'w'} \\ \overline{w'u'} & \overline{w'v'} & \overline{w'w'} \end{bmatrix}_{S_3} = \mathbf{A} \begin{bmatrix} \overline{u'u'} & \overline{u'v'} & \overline{u'w'} \\ \overline{v'u'} & \overline{v'v'} & \overline{v'w'} \\ \overline{w'u'} & \overline{w'v'} & \overline{w'w'} \end{bmatrix}_{S_1} \mathbf{A}^T \tag{1.20}$$

An optional third rotation forcing the $\overline{v'w'}$ covariances to be null may be applied Aubinet et al. (2000), where the α is given by :

$$\alpha = \frac{1}{2} \arctan\left(\frac{\overline{v_s w_s}}{\overline{v_s^2} - \overline{w_s^2}} \right) \tag{1.21}$$

If the raw data is available, the best option is to rotate the data set prior to the statistics calculation. If not possible, Aubinet et al. (2000) recommends working with half-hour mean values. However, a major disadvantage to long-term studies is the possibility that $\overline{w} \neq 0$ during the flux-averaging periods. Massman and Lee (2002) summarizes the limitations of setting $\overline{w} = 0$ for every half an hour: it eliminates the mean flow component of the flux, thereby causing a systematic underestimation of the individual fluxes in the long-term balance; and filters the low frequency components of the turbulent flux.

1.6.4 Obtaining turbulent atmospheric spectrum

Due to changes in the boundary-layer stability or flow velocity, the extraction of the frequency information of the turbulent field requires the use of combined statistic and spectral techniques. We present here a list of topics that should be reviewed before embracing spectral analysis:

1. First, the series length or the measurement time must be defined, as for a short time the low-frequency information will be lost and longer times may carry low-frequency information associated with changes in flow conditions. Two approaches are possible: defining a time interval from which the spectra is going to be derived; or from the flow stationarity conditions, obtaining the time from which the spectra is to be derived.

   (a) The first is present throughout the literature and has an advantage of enabling a standard time for fluxes calculation and comparison (Kaimal and Finnigan, 1994). The averaging time, or the record length is optimized to fit 2^n samples for FFT algorithms. In this case there is no statistical stationarity. Time series detrending is needed leading to unresolved fluxes as discussed in subsection 1.6.2.

(b) The second is the determination of the time intervals by the ogive function, equation (1.14) (Oncley, 1989). No detrending is necessary, being required a simple mean removal. However, in long term flux measurements the window length may vary with the stability conditions.

2. Rotation of the coordinate system by one of the methods, as in subsection 1.6.3.

3. Eliminating the edge effects by a cosine tapper prior to the Fourier transform, Kaimal and Finnigan (1994).

4. Calculation of the FFT-spectrum.

5. Averaging the raw FFT-spectrum into logarithmic spaced frequency classes.

6. Normalization of the spectral density by the variance. If the cospectra is to be obtained, the normalization is by the covariance. For the frequency axis, the normalization is obtained for different wind velocities and measurement hight with the expression $f(z-z_0)/\overline{w}$, where z_0 is the measurement height and $\overline{w}$ is the mean vertical velocity.

7. Fitting the single spectra by a cubic spline.

8. Averaging the fitted curves into a set of M logarithmic spaced non-dimensional frequency classes considering the layer stability.

Finally, because the spectra of any quantity in the boundary-layer is represented in a log-log scale, fewer values are averaged in the low-frequency range, what causes the spectral to be jagged at the low-frequency range. Kaimal and Finnigan (1994) suggested the spectral splicing method to smooth spectra either in the low and high-frequency ends. The time series is divided into N non-overlapping blocks of equal length for the calculation of N single high-frequency part. To deal with the low frequency end, the series is resampled at a lower rate and the spectrum is computed. Both spectra are then averaged into logarithmic spaced frequency bands such that an overlapping region of bands at the transition from low to high-frequency spectra exists. This technique is illustrated in section A.3 of Appendix A.

The spectral analysis of atmospheric turbulent signals poses extra difficulties because of non-stationary time series. New tools have became available during the last years in addition to the traditional approaches such as FFT. These new tools include wavelet and also quadrant analysis. For the sake of comprehensiveness of the present study these methodologies are dealt in Appendixes B and C.

1.7 Thesis outline

This thesis is divided in 10 chapters, including the present Introduction and 4 Appendixes.

Chapter 2 compares the strengths and weakness of 4 sonic anemometers (3 manufactures) under a field calibration during EBEX00 experiment. The sonics operate under adverse conditions, large evapo-transpiration and above a canopy flow. All sonics used in EBEX00 had a non-orthogonal array with differences only in the path length.

In Chapter 3 we quantify the absolute flow distortion of a 5th non-orthogonal sonic anemometer (Metek model USA-1) and show that the flow pattern through and around the sonic array is complex, where accelerating and decelerating areas coexist within few degrees apart. Velocity and temperature corrections for the distortions are also discussed in this chapter.

The Metek (model USA-1) sonic anemometer could be used confidently in complex terrain measurements, and the first case is dealt in Chapter 4. It reports measurements results in a wind farm located in a coastal area of Madeira Island. Sonic and cup anemometers were compared and turbulent flow described. Due to flow complexity, Fourier, wavelet and quadrant analysis were used to fully characterize the turbulent field.

The second complex terrain case reports measurements results at the Paul da Serra plateau also in Madeira Island, at 1500 m altitude, Chapter 5. Here also a comparison between cup and sonic anemometer is presented. Besides turbulence characterization, this chapter also address the spacial divergence of the flow field over the plateau.

Chapter 6 summarizes the main conclusions and shows the proposals for future areas of investigation.

Fundamental and practical questions related to the methodologies used in the main core of the study are presented in the Appendixes. In appendix A we present a discussion on periodogram performance based on Fourier techniques while the basis for wavelet technique and comparison with Fourier spectra are dealt in Appendix B. Quadrant analysis method is presented in Appendix C and statistical questions related to combination of short and long term statistics, and bootstrap technique are in Appendix D.

Chapter 2

Sonic field comparison

Abstract

This chapter is concerned with the performance of sonic anemometers from 3 different manufacturers, NUW sonic from NCAR, model CSAT-3 from Campbell Scientific Inc., and model HS from Gill Solent Instruments during a field calibration that preceded the EBEX00 field experiment held in San Joaquin Valley, California. The site was a flat cotton field with canopy flow, light winds and with large evapotranspiration values. The sonics were located up to 9 m apart, but that did not influence the correlation of the 1st statistical moments that were about 99% for horizontal velocity and temperature. Comparisons were also for non-dependent and temperature dependent parameters, such as $\overline{u'u'}$, $\overline{u'w'}$, $\overline{w'w'}$ and $\overline{w'T'}$, with mean correlations of 99%; and u_* or $\overline{T'T'}$ with 93 and 92%, in agreement with comparisons for different coveraged terrain. A detailed analysis showed a temperature drift in the Gill HS sonic and by spectral methods we identified a systematic flux overestimation of the NUW sonic that could be attributed to aliasing. Strong thermal gradients and light winds forced the flow into laminar regime, breaking down the required spacial homogeneity with direct consequences in the 2nd moment comparisons and compromising eddy flux measurements once there is no spacial homogeneity. Campbell CSAT-3 sonic was the instrument that presented the best 2nd statistical moment performance, but differences between instruments are negligible for wind energy resource and turbulence studies.

2.1 Introduction

Sonic anemometers can be evaluated either under controlled wind tunnel conditions or in field experiments. The Reynolds number Re is generally lower in the well-controlled flow in the tunnel than in a fully turbulent atmospheric flow. Field calibration campaigns enable the measuring of the sonic response under real conditions, and spacial differences due to singularities in the terrain orography and roughness had to be accounted. By field calibration one can also evaluate the flux response of each instrument to changes in the weather conditions, temperature or humidity, which may lead to unexpected offset or instrument drifts.

A cotton field in California was selected due to wind stability, flatness of the terrain and the fact that it could simulate a forest environment, characterized by the close canopy of the cotton under workable conditions (the height of the cotton was below 1.5 m), and high temperature and evapo-transpiration values from the irrigation system in furrows and plant leaves. This site differs from previous sonic comparison in the land coverage, i.e. bare soil, low grass over a flat terrain, ocean or even forest, Christen et al. (2000), Wilson et al. (2002) Högström and Smedman (2004). Also the flow, during the night and part of the day was occasionally dampened by thermal effects leading to a laminar regime, and the stability proved to be a key issue to compare results.

A NUW, two CSAT-3 and a Gill HS sonics were compared with correlations up to 99% for velocity and temperature 1st moment linear regression, 99% for velocity spectra, 99% for momentum flux cospectra and 93% for heat flux cospectra for unstable conditions. Poorer results were obtained for stable statification. The comparison recurred to bootstrap technique to establish the uncertainty of the quantity we are estimating (Yo, 2003). This technique is based in resampling methods where the data is sampled with replacement to provide virtual distributions of the quantity under comparison (see section D.2 in Appendix D).

Chapter outline

An overview of the objectives and scope of a larger experiment that followed the sonic comparison, EBEX00, is presented in the next subsection (subsection 2.1.1). The experiment is described in section 2.2, with site, tower and instrument deployment description (subsection 2.2.1). Micrometeorological facility and instrument specifications are summarized in subsections 2.2.2 and 2.2.3. The results are presented and discussed in section 2.3 in four steps: the general features of the flow with the results from the profile tower (subsection 2.3.1); comparison of the parameters that were not and depended on temperature measurements (subsections 2.3.2 and 2.3.3); comparison of the spectral response of each instrument according to flow stability (subsection 2.3.4). Section 2.4 concludes this chapter.

2.1.1 EBEX00 overview

The primary objective of the Energy Balance Experiment - EBEX00 - was to find why micrometeorological measurements of the individual terms of the basic physical quantities (sensible H_s and latent heat flux LE, net radiation R_{net}, soil heat flux and storage G) often cannot achieve closure. It is quite common for experimental data sets to have $H_s + LE + G$ be only 70% of R_{net}, Gash and Dolman (2003). Apparently, the measurement systems, or perhaps the method itself, is unable to measure night-time respiration fluxes in low windspeed conditions. Secondly, there is a frequent failure to close the energy balance in daytime, when the energy measured leaving the surface as evaporation, and sensible and soil heat flux falls short of the available net radiation, Gash and Dolman (2003). As an example, compare the data of Araujo et al. (2002), who obtained 80% closure over tropical rainforest, with those by Finch and Harding (1998), who recorded better than 95% over grass. The error is significantly larger than the error expected for the measurements of any of the terms independently, Foken and Oncley (1995), listed both instrumentation and fundamental problems for causing this error partially discussed by Finnigan et al. (2003). EBEX00 addressed this problem by:

- Measuring all terms of the energy budget directly at comparable scales. In particular, by deploying enough sensors to create an average of each term over a relatively large area (1.6 km by 0.8 km), which should encompass several flux footprints. These included 9 tower sites and 32 heating arrays.

- Performing side-by-side comparison of instruments from different manufacturers.

- Comparing processing methods of different research groups using a reference data set. This included the filtering of the time series and flow distortion corrections of the eddy-correlation measurements.

Additionally, temperature and wind profiles were measured at 3 locations to provide information about site homogeneity (Oncley et al., 2000).

Several research groups participated in this project: National Center for Atmospheric Research - NCAR, University of Bayreuth, University of Basel, City University of Hong-Kong, University of Padova, or the Royal Dutch Meteorology Institute - KMNI were present with a team and equipment, while other Universities participated only individually. The logistics was guarantee by NCAR, providing several Portable Atmospheric Mesonet III - PAM III and Atmosphere-Surface Turbulent Exchange Research - ASTER - stations, the central facility for the sonic comparison.

2.2 Experiment description

2.2.1 Site description and deployment

The typical cloud-free skies and intensive agricultural activity at the San Joaquin Valley in California made it a suitable area for the deployment of EBEX00. The selected site was a flat, flood irrigated cotton field 10 km North of Kettleman City, in which the evapotranspiration reached maximum values of 400 Wm^{-2}. The terrain slope is 0.1°, and to allow flood irrigation the field has 22 m wide canals running North-South direction every 0.8 km with road beds along each side (Oncley et al., 2000).

Figure 2.1 shows the tower array and the mean wind direction. Most flux measurements where made 4 m above the canopy and thus the fetch in near-neutral conditions was expected to be 400 m (Horst and Weil, 1994). The tower layout minimizes the influence from both the canals and adjacent fields. The tower spacing of 200 m was chosen to have this footprint totally within the cotton field and to have overlapping footprints from adjacent towers to identify any sections of the field with significantly different fluxes. Even though a reasonably homogeneous area was selected, from *in situ* observations we found variations on the cotton height and density over the field.

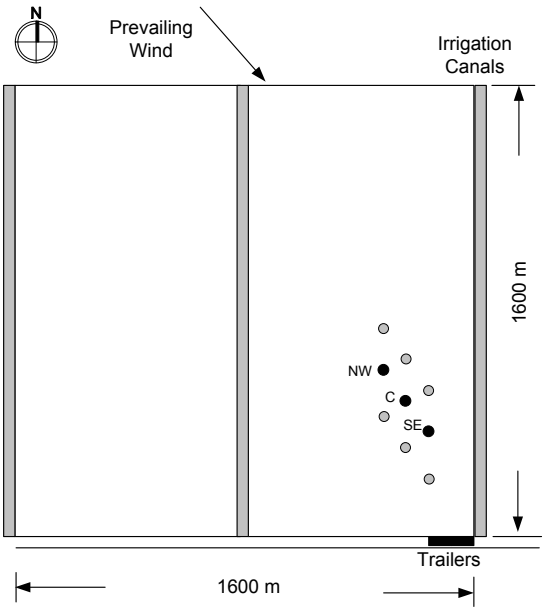

Figure 2.1: Tower site layout for EBEX00. All sites measured momentum, sensible, and latent heat flux at one or more heights, net and upwelling visible and infrared radiation, and soil temperature, moisture and heat flux. The NW, C, and SE sites also measured wind, temperature, and humidity profiles at 6 or more levels and downwelling visible and infrared radiation.

2.2.2 The micrometeorological facility

Atmosphere/Surface Turbulent Exchange Research - ASTER - is a portable micrometeorological facility for measurement of surface fluxes of momentum, sensible heat, water vapor or surface fluxes of trace chemical species (Businger et al., 1990). ASTER is made of several tower-mounted sensor arrays, each supported by an independent data acquisition system (the ASTER data acquisition module - ADAM), i.e. field computers that sample and format the measured data, which can be located up to a kilometer from the ASTER operations field base to which they are connected via fiber optic cable to an ethernet link (Businger et al., 1990). For EBEX00, ASTER configuration had two 10 m towers supporting sensor arrays with sensors for the following measurements: vertical profiles of wind, temperature, and humidity; radiation fluxes; and soil temperature, soil moisture, and soil heat fluxes. The ASTER sensors at EBEX00 was a mix of commercial instruments and NCAR's developments, table 2.1.

Mean temperature and humidity were measured with a hygrothermometer developed at NCAR and previously used with the NCAR Portable Automated Mesonet - PAM (Militzer et al., 1995). These hygrothermometers are integrated sensors which utilize a platinum resistance thermometer and solid state relative humidity sensor inside an aspirated radiation shield enclosure. Wind profiles were measured with commercial propeller-vane wind sensors which have been modified at NCAR to obtain a high resolution vane azimuth using an optical encoder. Measurement of the surface energy balance is achieved using up-looking and down-looking pairs of short and long-wave radiometers in tandem with soil heat flux plates and soil temperature sensors (Businger et al., 1990).

The serial and analog data input to the ADAM arrived asynchronously and was time tagged before buffered, ordered in time sequence, and transferred to the base station computer. The raw data and 5-min averages are available at NCAR's site along all the data from other experiments where NCAR has participated.

In spite of the great flexibility of ASTER/ADAM system, the number of instrument connection ports was limited, requiring independent logging systems for Kaijo-Denki unit from the KMNI and the CSAT 3 unit from Hong-Kong University, which suffered several power failures during the comparison. For the independent logging systems, the clock was synchronized to ADAM and the data transfered after the experiment. Unfortunately, only 30-min average data of KMNI already processed fluxes was transfered to NCAR. The lack of availability of CSAT 3 sonic from Hong-Kong University (40% availability) and the lack of raw data from the KMNI Kaijo-Denki sonic led these instruments to exclusion from this comparison. A Young RS unit from University of Bayreuth was also removed because of a software problem found and described in section 3.3.3.

Table 2.1: Sensors available with ASTER at EBEX00.

	Sensor and Manufacturer	Measured quantity	Rate [Hz]	Quantity
◦	3-D sonic Applied. Tech.	u, v, w, T_s	10	2
◦	3-D sonic U. of Washington.	u, v, w, T_s	20	2
◦	PT100 Atmosph. Instr. Research.	T	20	3
◦	UV Hygrometer Campbell Sci.	vapor density	20	2
◦	Prop. anemometer NCAR-R.M. Young	u and v	1	7
◦	Hygrothermometer NCAR-Vaisala	T and Rh	1	7
◦	Dew Point EG&G	Dew point	1	7
◦	Pressure sensor NCAR	Pressure	1	7
◦	Net Radiometer Micromet Sys.	Net radiation	1	1
◦	Prec. Spec. Pyranom. Eppley	Short-wave rad.	1	1
◦	Prec. Inf. red Pygeom. Eppley	Long-wave rad.	1	1
◦	Soil temp. sen. NCAR	T_{soil}	1	12
◦	Heat flux plate Micromet Sys.	Soil heat flux	1	1
◦	Surf. temp. sen. Everest	$T_{surf.}$	1	1
◦	Ultraviolet rad. Eppley	Ultra Violet rad.	1	1

2.2.3 Instruments description

The 7 sonics were deployed in 5 independent towers aligned perpendicular to the mean flow direction, at 4.7 m height, in a tower array with a 3 m separation, figure 2.2. Only 4 sonics were compared:

1. A Gill HS unit from University of Basel identified as GILL HS placed at tower #1.
2. A CSAT 3 Campbell Scientific unit from University of Basel identified as CSI CH placed at tower #1.
3. A CSAT 3 Campbell Scientific unit from University of Bayreuth identified as CSI D unit placed at tower #2.
4. NUW unit from NCAR placed at tower #4. Used as the reference sonic.

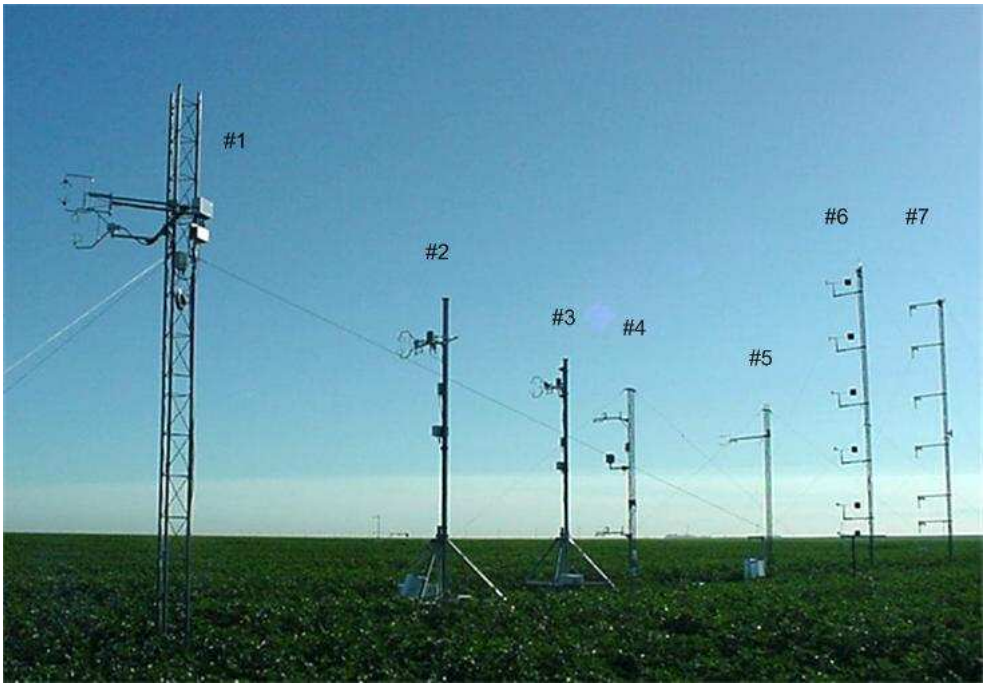

Figure 2.2: Sonic comparison array. From left to right: tower #1 GILL HS and CSI CH, #2 CSI D and RS Young (already removed), #3 CSI HK (not considered), #4 NUW, #5 Kaijo-Denki KMNI (not considered), #6 mean wind profile, #7 mean temperature and humidity profile. *Photo by Andreas Christian - U. Basel.*

All sonics presented in this comparison are non-orthogonal arrays and supported by a horizontal boom, table 2.2. The path-length varies between 20 cm for the NUW unit to 11.6 cm to the CSAT3 from Campbell Scientific. As mentioned in section 1.5, the non-orthogonal is the most common geometry and is based in the University of Washington

Table 2.2: NUW, CSAT3 and Gill HS sonics specifications according to manufacturers, App (2002), Cam (2004) and Gil (2004).

Sensor Spec.		NUW	Campbell CSAT	Gill HS
analog input		0	0	6
analog output		1	1	1
path-length	[mm]	200	116	153
int. samp. rate	[Hz]	200	60	100
out. rate	[Hz]	20	20	20
filtering	(point averag.)	10	3	5
accuracy	$u[\mathrm{ms}^{-1}]$	$\pm$ 0.03	$\pm$0.04	$\pm$0.01
	$T_s[^\circ\mathrm{C}]$	$\pm$ 0.10	-	-
	$c_{20^\circ C}[\mathrm{ms}^{-1}]$	-	$\pm$0.01	$\pm$ 0.01
resolution	$u[\mathrm{ms}^{-1}]$	0.01	0.001	0.001
	$T_s[^\circ\mathrm{C}]$	0.01	-	-
	$c_{20^\circ C}[\mathrm{ms}^{-1}]$	-	0.001	0.002

sonic model (Zhang et al., 1996) where the NUW unit (New UW) is an upgrade from early model, which inspired the development of the CSAT-3 and Gill HS models from Campbell and Gill Instruments. By visual inspection, the main external difference between these sonics is the 20 cm NUW path-length, compared with the 11.6 cm of the CSAT 3 and the 15 cm of the GILL HS (figure 2.3). This particular path-length distance of the NUW sonic is to benefit from the early flow distortion results of the UW model.

The measuring parameters are also comparable, with accuracy ranging from 4 to 1 cms^{-1} for CSAT and GILL HS models. The wind speed resolution ranges, according to manufacturers specification, from 1 cms^{-1} for the NUW to 0.1 cms^{-1} for the CSAT3 and GILL HS models (Cam, 2004; Gil, 2004).

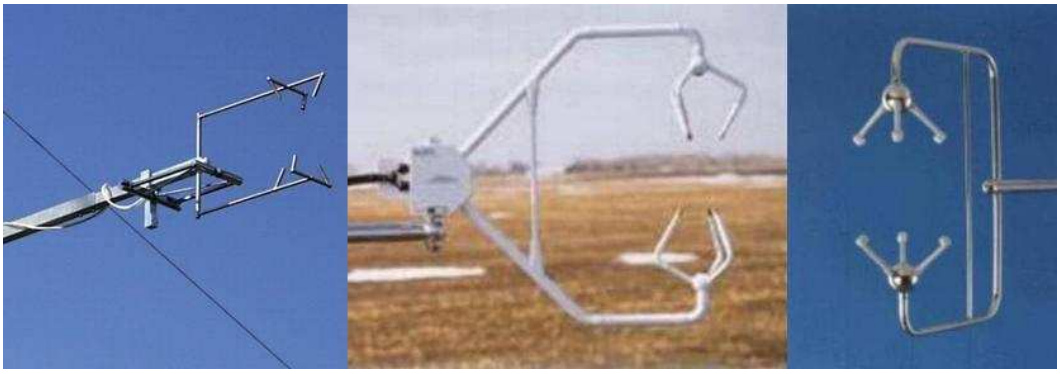

Figure 2.3: NUW, CSAT-3 and Gill HS sonic anemometers.

All models have programmable software via RS-232 port. The output rate of each sonic was programmable up to a maximum of 20 Hz. The sampling rate of each instrument corresponds to the internal microprocessor capabilities, varying from 60 to 200 Hz. The values measured at those rates are filtered differently, i.e. a 10 point average reduces to 20 Hz the 'instantaneous' values. The output of all sonics was set to 20 Hz.

Generally, all commercially available sonics have the electronics inside a box connected to the transducer array by a 2 m cable. The NUW sonic, that shares the same electronics and transducers as the ATI K-Probe, is simpler because the microprocessor is placed inside the array supporting boom. The electronic box is unnecessary and the overall installation is simpler.

The NUW sonic is not commercially available, but it was chosen to be the reference instrument because 4 other NUW units, and 5 K-probe ATI units where deployed throughout the EBEX00 field. The sonics and other fast response instruments had a data quality control flag that indicates when the instrument was properly operating. For the comparison we excluded all time intervals when at least one sonic presented such flag up.

2.3 Results and Analysis

2.3.1 General Circulation

The results from profile tower C (figure 2.1) were used to characterize the sonic comparison period. The predominant wind was from the North-West direction, figure 2.4. Table 2.3 summarizes the mean and standard deviation values of the wind velocity, dry and wet temperature, and water vapor pressure for 7 levels above ground level: 1.7, 2.7, 4,7, 5.7, 6.7, 8.7 and 10.7 m agl. The mean wind velocity difference from the lowest to the highest levels was 2.1 ms^{-1}, and the mean dry temperature and water vapor pressure over the tower was 2.1°C and 3 hPa. Thus, the sonic comparison was made under light wind and large temperature and evapotranspiration gradients as expected for such terrain and vegetation.

The wind velocity standard deviation is the only quantity that increases with height, figure 2.5, but the turbulence intensity decreases in the first two bottom levels, from 42 to 36%, with a constant value close to 31% for higher levels. The ratio of the fluctuations over the mean value of the rest of the quantities also decreases with height, with larger fluctuations at the first two lower levels, and almost constant values from 4.7 to 10.7 m high. We observe on figure 2.5 that turbulence intensity remains constant from 4.7 m to higher levels while dry temperature deviation decays with height. From the values in table 2.3 we may assume wet temperature ratio constant from 4.7 m to higher levels above ground. At 6.7 m high the water vapor pressure values are not consistent with the neighbour levels 5.7 and 8.7 m, and water vapor pressure at 6.7 m was removed from any further analysis.

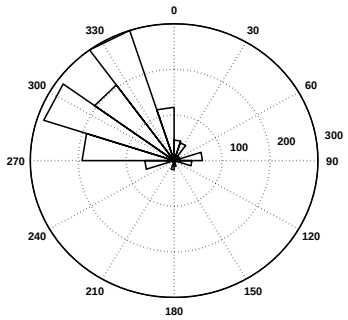

Figure 2.4: Wind rose during the comparison period.

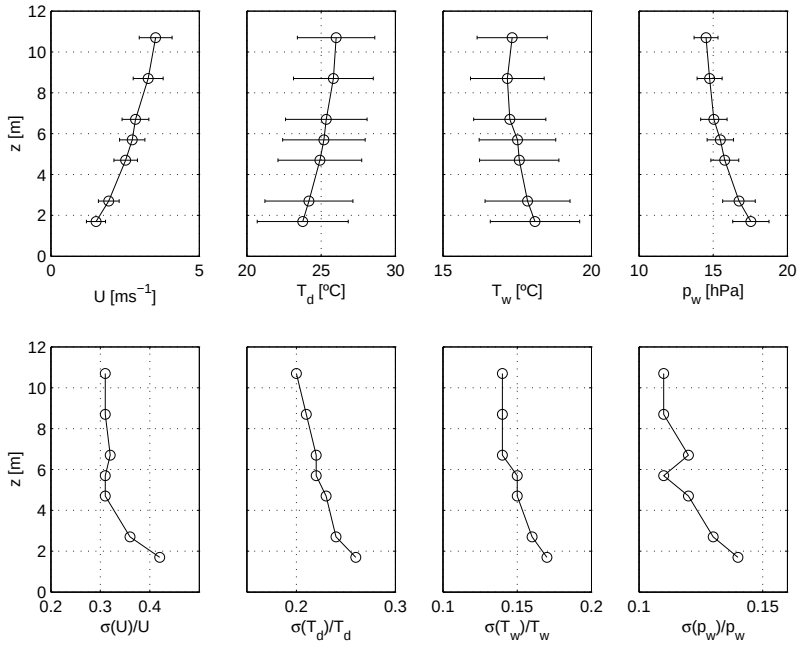

Figure 2.5: Mean Profile tower of the wind velocity, U, dry and wet temperature, T_d and T_w, and water vapor pressure, p_w according to the values of table 2.3.

After verification of all variables, velocity, wet and dry temperature, and water vapor pressure profile time evolution, a wet temperature overestimation at 8.7 m was also identified. Although the offset when compared to the next levels was minor, that was hardly physically justified, leading to the elimination also of this level. Also shown in figure 2.6 is the difficult visualization of stability transition. The soil heat is so intense that a temperature inversion is identified only in the two time instants in the profile tower, namely at 08:50 UTC where the plot shows an almost uniform temperature profile or the inversion, and at 11:47 UTC, where only the higher levels show larger temperature values than the lower levels. In this case, the wet temperature slope is negative in the 3 lower profile levels, changing to positive in the upper profile levels.

Table 2.3: Profile tower C statistics for the wind velocity (U), dry and wet temperature (T_d and T_w) and water vapor pressure (p_w).

		z [m]						
		1.7	2.7	4.7	5.7	6.7	8.7	10.7
U	[ms^{-1}]	1.52	1.95	2.52	2.74	2.85	3.28	3.53
T_d	[°C]	23.76	24.18	24.92	25.19	25.35	25.83	26.01
T_w	[°C]	18.10	17.85	17.57	17.51	17.25	17.17	17.33
p_w	[hPa]	17.54	16.74	15.78	15.48	15.05	14.76	14.52
σ_U	[ms^{-1}]	0.64	0.70	0.79	0.85	0.90	1.01	1.11
σ_{T_d}	[°C]	6.13	5.92	5.64	5.56	5.49	5.37	5.22
σ_{T_w}	[°C]	3.01	2.86	2.67	2.58	2.43	2.48	2.36
σ_{p_w}	[hPa]	2.45	2.20	1.88	1.78	1.78	1.69	1.61
σ_U/U	-	0.42	0.36	0.31	0.31	0.32	0.31	0.31
σ_{T_d}/T_d	-	0.26	0.24	0.23	0.22	0.22	0.21	0.20
σ_{T_w}/T_w	-	0.17	0.16	0.15	0.15	0.14	0.14	0.14
σ_{p_w}/p_w	-	0.14	0.13	0.12	0.11	0.12	0.11	0.11

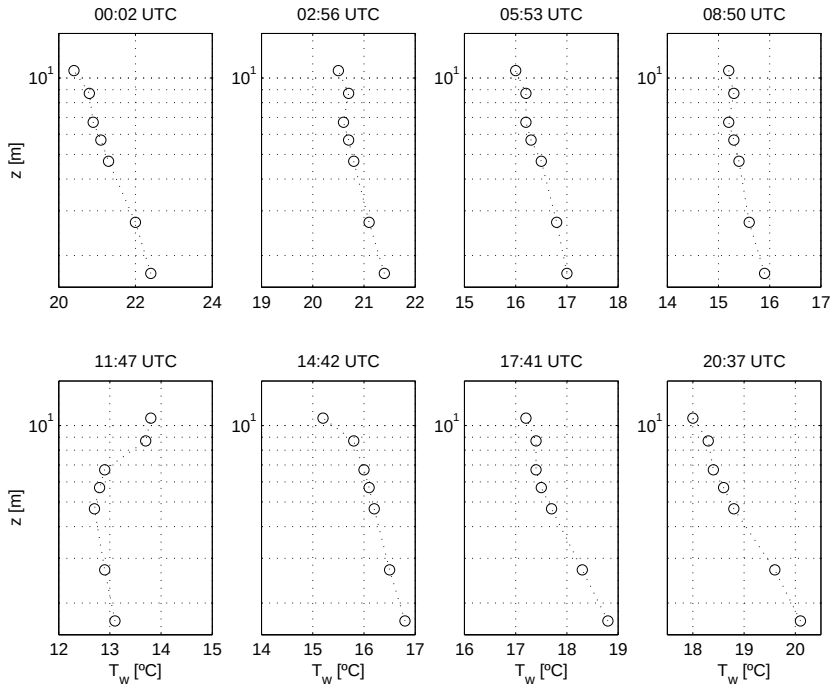

Figure 2.6: Twenty four hour wet temperature profile evolution for detection of a bad level at 8.7 m. Time axis refers to UTC time and the difference to local time is +7 h.

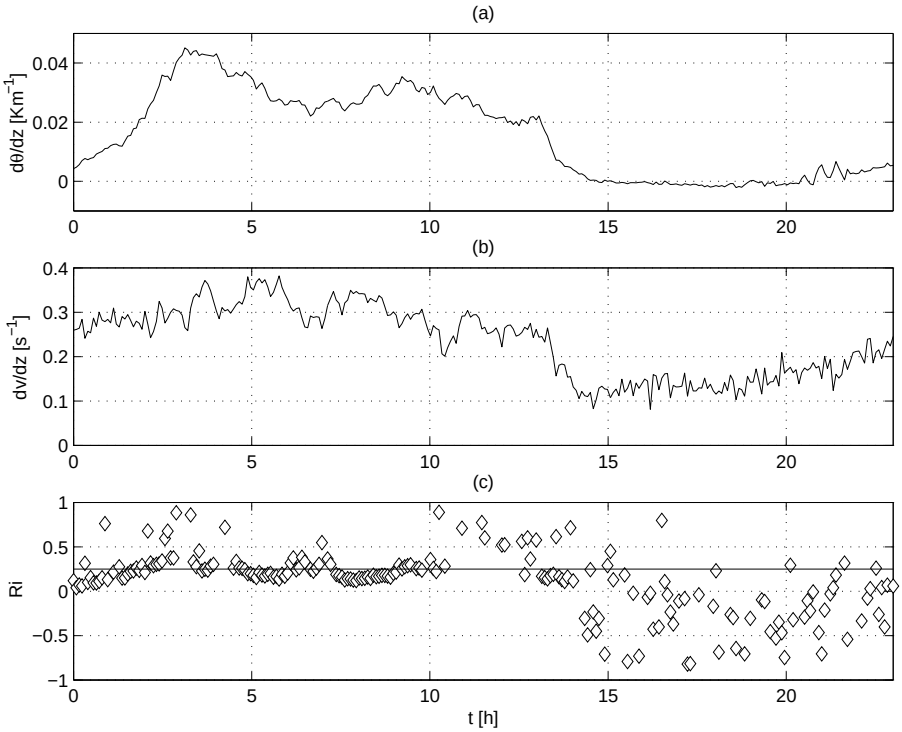

Figure 2.7: Twenty four hour evolution of $d\theta/dz$ (a), dv/dz (b) and Ri (c). The time axis refers to UTC time and the difference to local time is 7 h. Night-time corresponds to 3.5 to 13:30 h.

Figure 2.7a shows a 24 h evolution of the potential temperature gradient profile already corrected for the moisture and figure 2.7b shows the velocity gradient time evolution. Figure 2.7c also presents the time evolution of Richardson number,

$$Ri = \frac{(g/\overline{\theta_v})(\partial\overline{\theta_v}/\partial z)}{(\partial\overline{u}/\partial z)^2} \tag{2.1}$$

where g is the acceleration of gravity, θ_v is the virtual potential temperature defined as $\theta_v = \theta(1 + 0.61r)$ for $\theta = T(z) + \Gamma_d z$ where $\Gamma_d = 9.8$ K/km is the dry adiabatic lapse rate and r is the mixing ratio of water vapor. The virtual potential temperature θ_v includes thus the buoyant effects of water vapor and liquid water in air (Stull, 2000). Figure 2.7c abscissa refers to UTC time, from which the local time can be obtained by adding 7 h, thus night-time corresponds from 03:30 to 13:30 h.

We observe that the mixing process reduces and inverts (due to day-time heating) the potential temperature gradient throughout the day. When solar radiation decreases, the gradient recovers as the turbulent mixing process decreases. The velocity gradient is positive, figure 2.7b, with a reduction by the mixing process during day-time heating. As the heating decreases, the velocity gradient recovers until reaching nigh-time values.

Figure 2.7c shows a strong stratification starting at early afternoon into the whole night, where the critical value of $Ri_c = 0.25$ (represented at 2.7c with a continuous line) is often reached and surpassed. By sunset, the flow is stable and tends to laminar. During day-time, turbulent mixing is more effective due to the heating the ground, Ri becomes negative. The large scatter observed in figure 2.7c is likely to be from the low values of the velocity gradient during that period of time.

The Ri was also calculated for different layers and the evolution is similar to the one presented in figure 2.7 and for this reason we refrain from presenting. In the layer where the sonics were compared, 4.7 m agl, turbulence generated by a mixed process of mechanical and convective phenomena is limited only to 4 hours. During the rest of the period, turbulence is entire mechanical driven and generated by wind shear.

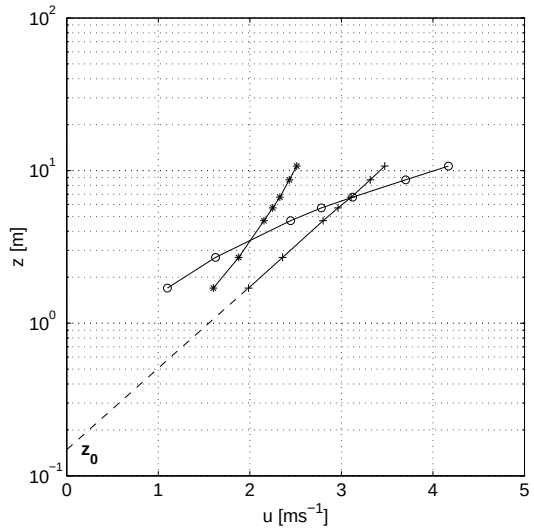

Figure 2.8: Wind velocity stability profiles and roughness length. Stable , ∘, unstable, ∗ and neutral stratification, +.

The velocity profile is depicted in figure 2.8. Stable stratification is represented by ∘. Unstable stratification, represented by ∗, is not so clearly defined due to the low wind velocity values at the site while the neutral stratification curve, +, shows a typical log-law boundary-layer velocity profile, where a $z_0 = 0.15$ m roughness length is obtained, corresponding to the mid-value from roughly open (cultivated areas with low crops and occasional obstacles) to rough (high crops) according to the Davenport-Wieringa roughness-length classification (Stull, 2000).

Figure 2.9a shows the velocity spectra for unstable and stable stratification (thicker line). These curves are identical to those from developed turbulence over flat terrain. The characteristic length for unstable is 560 and 171 m for stable stratification. Both curves collapse onto the -5/3 exponential decay of the inertial subrange (dotted line). We observe that the high frequency contribution to the energy spectrum is minimal, and that from a

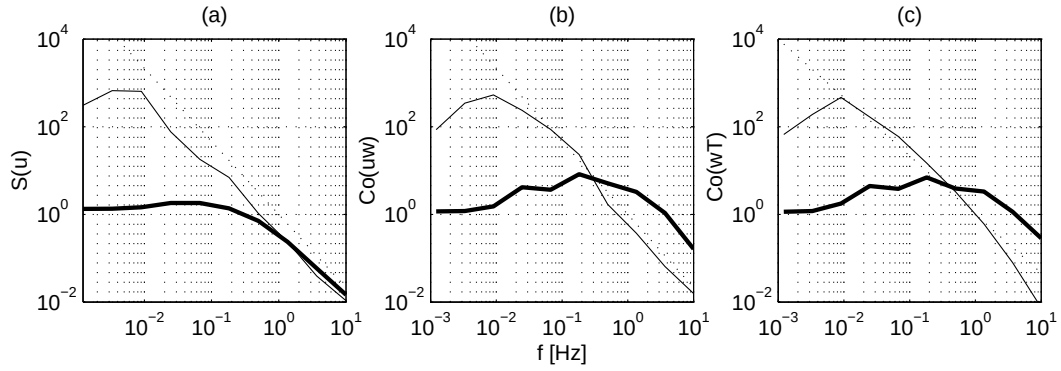

Figure 2.9: Velocity spectra $S(V)$ (a), momentum flux cospectra $Co(uw)$ (b) and heat flux cospectra $Co(wT)$ (c) for unstable and stable stratification - thicker line. The $f^{-5/3}$ inertial decay for (a) and (b) and $f^{-4/3}$ for (c) are plotted for reference.

sonic operating at 20 Hz almost all energy associated to the turbulent energy cascade is resolved. The cospectra of the momentum flux and heat flux, figure 2.9b and 2.9c, present the normal shape for such conditions but indicate that for stable conditions there is still some energy at the high-frequency end that is not captured. The extended range in wT, with $f^{-4/3}$ decay implies that the smaller eddies transport heat more effectively than momentum, pointing to the need for higher frequency response in surface layer measurements of heat flux compared to momentum flux (Kaimal and Finnigan, 1994).

2.3.2 Results of comparisons of parameters not containing temperature

In spite of careful installation in the field, all sonics had to be rotated due to different azimuth and inclination into the same streamline referential. The rotation and tilt angles γ and β, obtained from the same common data set for all sonics are presented in table 2.4. There was a knowledge of the flow direction prior to the field campaign, from which the sonic could be oriented in order to minimize the rotation.

Table 2.4: Sonic rotation and and tilt angles, γ and β.

Sonic	γ °	β °
NUW	37.45	-3.00
CSI CH	-3.72	-1.04
CSI D	39.50	1.46
GILL HS	-0.04	-0.66

Velocity direct comparison are summarized in table 2.5 for increasing larger averaging intervals based in equation (D.1). There is a close agreement for the wind velocity values for 5-min intervals, that improves for longer averaging intervals. The regression slope is 0.99 for CSI CH and GILL HS sonics and the velocity offset is lower than 6 and 2 cm s^{-1} respectively. For the CSI D sonic the slope is slightly lower, 0.97, and the offset 5 cm s^{-1}. The mean correlation is 98% for the CSAT-3 models (CSI CH and CSI D units) and is 1% lower for the GILL HS model. By increasing the averaging interval to 30-min, the slope closes to the unity with a reduction on the offset and an increase in the correlation to 99% for all instruments. The R^2 correlation value agree with the results of 99.5% from Högström and Smedman (2004) for a SOLENT 1210R3 sonic anemometer from Gill Instruments for 30-min averages and the increase in the statistics estimators is only 0.2% for doubling the averaging time from 30 to 60-min.

Table 2.5: Sonic linear regression results $y = a + bx$ and correlation coefficient R^2: flow velocity for 5, 30 and 60-min averages, V_{t-5min} to $V_{t-60min}$.

quantity-time interval	Type	a	b	R^2
V_{t-5min}	CSI CH	0.061	0.986	0.977
	CSI D	0.054	0.968	0.976
	GILL HS	0.020	0.988	0.974
$V_{t-30min}$	CSI CH	0.013	1.010	0.995
	CSI D	0.031	0.979	0.991
	GILL HS	-0.035	1.015	0.993
$V_{t-60min}$	CSI CH	0.001	1.015	0.997
	CSI D	0.024	0.983	0.993
	GILL HS	-0.051	1.022	0.995

Classical uncertainty analysis for a field comparison is not suitable because each measurement include unstationarities that will contaminate the uncertainty calculation. Uncertainty with a 95% confidence is given by:

$$U_{95} = 2.1\sqrt{\sigma_{B_i}^2 + \sigma_i^2} \tag{2.2}$$

where σ_{B_i} and σ_i are respectively the instrument accuracy and σ_i the measurement standard deviation. Thus, the 95% uncertainty associated with the velocity measurements for 5-min interval will be respectivelly for the NUW, CSAT (CSI CH and CSI D), and GILL HS sonics respectively 1.34, 1.35, 1.33 and 1.36 ms^{-1}. Such large values give no additional information on instruments agreement. Figure 2.10 shows the 5-min velocity comparison along with the probability distribution of the correlation coefficient obtained by bootstraping the original data series. We observe that the mean value of the $PDF(R^2)$ coincides with the same value presented in table 2.5, although additional information is obtained from the shape of the

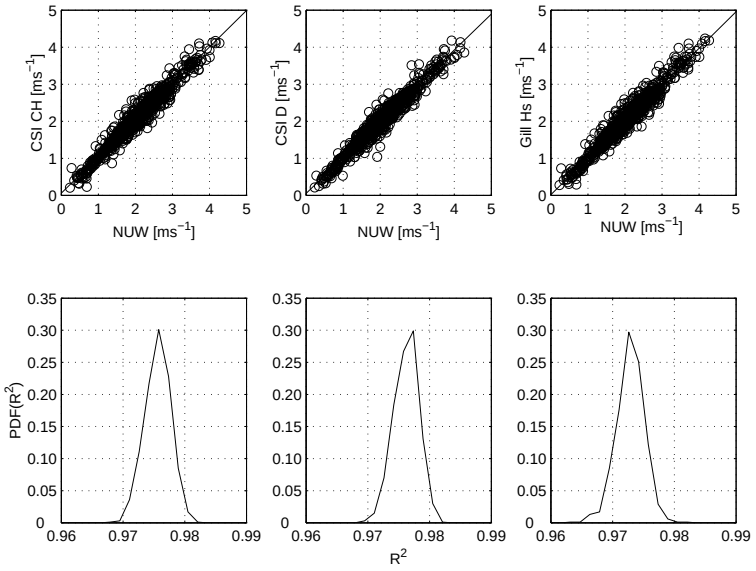

Figure 2.10: Total velocity comparison for 5 min intervals and probability distribution of the correlation coefficient.

distribution, binded in the upper and lower limits to 1%. The $PDF(R^2)$ show that there is a linear correlation between two data sets, and the correlation coefficient is represented by a narrow distribution binded in a 1% limit, confirming the linear fit of the data by providing an uncertainty value inferior to 1%. Needless to mention that for larger time intervals, 30 and 60-min, as the correlation coefficient tends to the unity the correlation distribution narrowes.

We also conclude from the results that spacial displacement between instruments is irrelevant for this comparison. Note that CSI CH and Gill HS are located 9 m from the NUW and CSI D is 6 m apart. The differences detected in the mean velocity field offset are inferior to the instrument accuracy. The best results are obtained for the CSAT-3 models (CSI CH and CSI D) where the offset, in the worst case, is 0.01 ms^{-1} inferior to the instrument accuracy. Gill HS offset is the only instrument where the offset is higher than the accuracy, 0.035 ms^{-1} for a $\pm$0.01 ms^{-1} accuracy.

Vertical velocity $\overline{w}$ was also compared but no correlation was found from the comparisons of NUW sonic against C-SAT models (CSI CH and CSI D) and Gill HS. A correlation of 68.4% (slope of 0.774 and a neglegible offset) for 5-min averaging intervals was found at CSI CH and Gill HS sonics which is not improved for longer averaging intervals. Note that these instruments were in the same mast, figure 2.2, while the CSI D was 3 m away from CSI CH and NUW was 6 m away. We conclude that vertical velocity field in such terrain is not comparable even for instruments located few centimeters apart, CSI CH and Gill HS case. This result may be the ensemble of several features, such as the low vertical velocity values, $\overline{z} = 0.044$ ms^{-1} and $\sigma_z = -0.691$ ms^{-1} for the whole period, or experimental

features, such as the closeness of the tower or the different geometry of each instrument to mention only a few.

Table 2.6: Vertical velocity variance $\overline{w'w'}$ and friction velocity u_* linear regression $y = a+bx$ and correlation coefficient R^2 for increasing averaging intervals.

t	model	$\overline{w'w'}$			u_*		
		a	b	R^2	a	b	R^2
5-min	CSI CH	0.001	0.924	0.937	0.033	0.857	0.839
	CSI D	0.001	0.950	0.928	0.026	0.471	0.717
	GILL HS	0.001	0.848	0.936	0.036	0.860	0.818
30-min	CSI CH	0.001	0.938	0.985	0.017	0.963	0.912
	CSI D	0.000	0.974	0.986	0.009	0.580	0.876
	GILL HS	0.001	0.854	0.986	0.017	0.983	0.898
60-min	CSI CH	0.000	0.940	0.990	0.014	0.984	0.927
	CSI D	0.000	0.972	0.991	0.004	0.608	0.910
	GILL HS	0.001	0.856	0.990	0.014	1.006	0.915
120-min	CSI CH	-	-	-	0.013	0.988	0.938
	CSI D	-	-	-	0.003	0.619	0.933
	GILL HS	-	-	-	0.013	1.010	0.930

The vertical velocity variance comparison excluded all undeveloped turbulence values that did not comply with the exclusion criteria of $\overline{w'w'}^{1/2}/\overline{u} > 1.0$. Larger than 5-min averages were calculated with expression (D.9). For 30-min averaging interval we reach correlations of 98.6%, improving to 99.1% when adding an extra hour to the averaging interval (table 2.6). Against CSAT-3 models and Gill HS, NUW overestimates $\overline{w'w'}$ by 6, 3 and 15%. The mean correlation of $\overline{w'w'}$ is closer to the 97% presented by Högström and Smedman (2004) or Christen et al. (2000) and is presented in figure 2.11 with the bootstraped distribuition of the correlation coefficient, binded in all 3 cases to an interval inferior to 1%. Again spacial distribution of the sonics did not compromise the comparison, with correlation of 98.6% for all sonics, even for those 9 m apart. This lead us to the conclusion that there was not an instrument or tower related problem that justify the poorer results of the vertical velocity 1st statistical moment comparison. We may assume the results as a consequence of the low mean vertical velocity field where the fluctuations are in the same order of magnitude.

Friction velocity u_* was also compared after eliminating all undeveloped turbulence values and we observe in table 2.6 that the final offset is close to 0.01 ms^{-1} for the CSI CH and GILL HS sonics, whereas for CSI D unit the offset may be considered null. The slopes for CSI CH and GILL HS sonics are close to the unit, but for the CSI D there is a 62% difference from the reference sonic. The R^2 increases with the averaging time as expected,

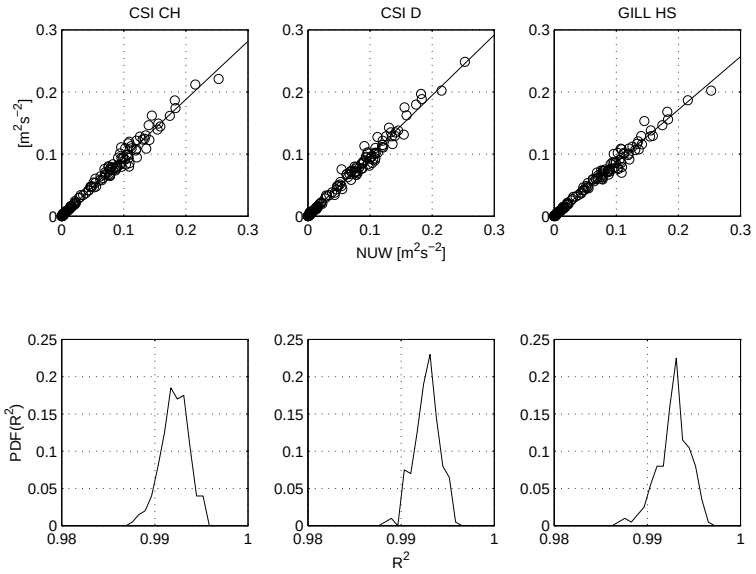

Figure 2.11: Vertical velocity variance $\overline{w'w'}$ comparison results.

and reaches 93% after 120-min average, as in Christen et al. (2000) comparison. The CSI D convergence is slower, reaching the same magnitude of the correlation coefficient of the other sonics just after one hour. The best results are found for CSI CH and GILL HS units (9 m apart from NUW) with a deviation of 3.7 and 1.7%. These values are one order of magnitude smaller than the ones found by Högström and Smedman (2004), 12% for a R3, 17% for a R2 Gill Solent sonics for 30-min averages. The worst comparison was from NUW against CSI D, 42% for the same time interval. We found no explanation for this slope difference.

Figure 2.12 shows the comparison plots for 5 and 120-min averages. We observe that in spite of filtering characteristics of the averaging process there are still large scatter for $u_* > 0.2$, which accounts for the poorer regression values when compared to the total velocity ones, 99.9%.

2.3.3 Results of comparisons of parameters containing temperature

Comparison of sonic measurements of temperature from NUW sonic against CSI CH, CSI D and Gill HS sonics are presented in table 2.7 for 5-min averages. Again, NUW and CSAT sonics show a close agreement for the first statistical moment, $R^2 = 0.999$. However, we observe that the two CSAT 3 units (CSI CH and CSI D) have a temperature offset of -0.58°C among each other while the Gill HS model presents an offset of +0.48°C to the NUW, and an almost 15% larger slope. By the correlation result for the GILL HS, 99.5%, we could be tempted to consider it a good agreement. However, figure 2.13 shows a drift

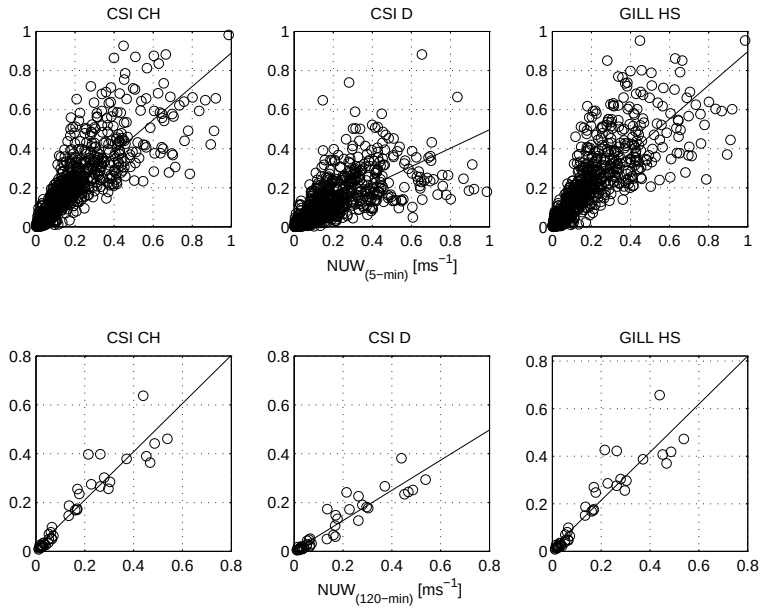

Figure 2.12: Friction velocity u_* comparison results. The top line corresponds to 5-min results and the bottom line to 120-min results.

on the results depending on the enviromnent temperature. The best fit is obtained by a logarithmic regression where the correlation coefficient reaches a value of $R^2 = 0.999$, identical to that found in case of velocity measurements. The correlation distribution is 0.1% lower and 0.001% wider than the NUW-CSAT 3 comparison.

Table 2.7: Sonic linear regression results $y = a + bx$ and correlation coefficient R^2 of the sonic temperature, T_s, for 5-min averages. For Gill HS sonic a logarithmic regression, $y = a + b\ln(x)$ improves R^2 0.4%.

quantity	Type	a	b	R^2
T_s	CSI CH	-0.616	0.997	0.999
	CSI D	-0.030	1.015	0.999
	GILL HS	0.478	1.144	0.995
		-74.587	$32.272\ln(T_{nuw})$	0.999

Table 2.8 presents the results for the temperature variance $\overline{T'T'}$ and heat flux $\overline{w'T'}$ comparison. These comparisons are generally presented only for 30-min intervals, easily verified from the mean R^2 improvement from 78 to 92% from 5 to 30-min averaging intervals. Temperature variance results are similar, showing an almost perfect agreement of NUW against Gill HS and a 3.6 and 4.8% underestimation of the CSAT-3 units. We observe in figure 2.14 that the correlation coefficient distribution is different for all units,

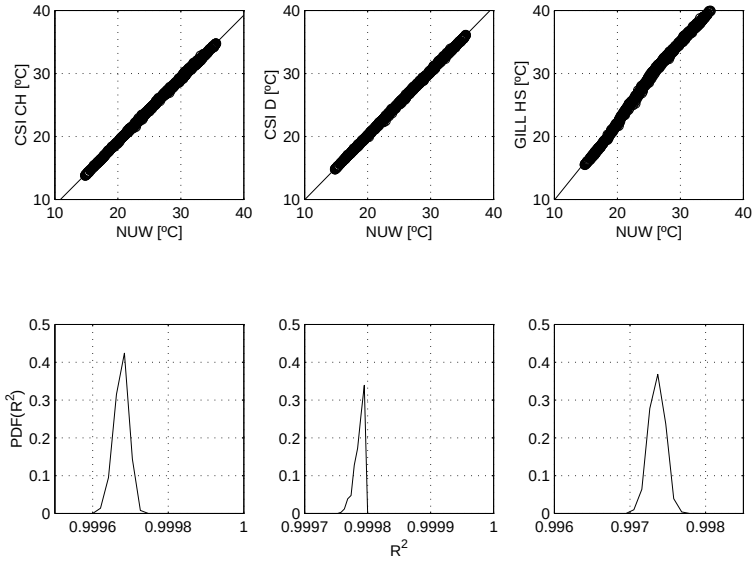

Figure 2.13: Sonic temperature comparison for 5 min intervals and probability distribution of the correlation coefficient. Note the temperature drift of the Gill HS model for temperatures above 20°C.

Table 2.8: Sonic linear regression results $y = a + bx$ and correlation coefficient R^2 for temperature variance, $\overline{T'T'}$, and heat flux covariance, $\overline{w'T'}$.

t	model	$\overline{T'T'}$			$\overline{w'T'}$		
min		[°C^2]			[ms^{-1}°C]		
		a	b	R^2	a	b	R^2
5-min	CSI CH	0.012	0.876	0.771	0.000	0.863	0.903
	CSI D	0.010	0.894	0.839	0.001	0.875	0.910
	GILL HS	0.017	0.914	0.735	0.000	0.851	0.893
30-min	CSI CH	0.004	0.964	0.917	0.000	0.894	0.983
	CSI D	0.005	0.952	0.951	0.001	0.912	0.980
	GILL HS	0.010	1.001	0.882	0.000	0.875	0.981
60-min	CSI CH	0.003	0.979	0.946	0.000	0.895	0.988
	CSI D	0.003	0.969	0.972	0.001	0.918	0.988
	GILL HS	0.009	1.016	0.910	0.000	0.880	0.985
120-min	CSI CH	0.004	0.971	0.956	-	-	-
	CSI D	0.002	0.982	0.984	-	-	-
	GILL HS	0.009	1.019	0.913	-	-	-

being CSI D the one with an R^2 distribution half narrower than the other units. We also observe in table 2.8 that the temperature drift of the Gill HS sonic is probably responsible

for the larger scatter and the 5% correlation values inferior to the average of the other instruments. The mean correlation is 3% inferior to the results presented by Högström and Smedman (2004) on ocean and agricultural sites at 10 m agl, stronger winds (around 10 ms^{-1}), and excluding daytime periods with strongly dominating latent heat fluxes and nightime periods with relatively large negative sensible heat fluxes.

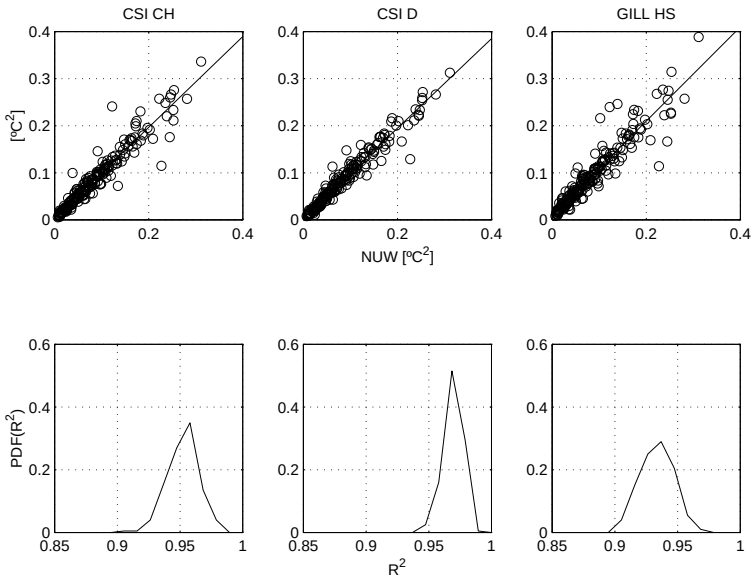

Figure 2.14: Temperature variance $\overline{T'T'}$ comparison for 30-min averaging intervals.

The heat flux $\overline{w'T'}$ comparison show that NUW sonic overestimates in 11.3% the heat flux against all other sonics for a 30-min averaging interval, table 2.8, although the correlation rounds 98%, a 3% improvement when compared to results from Högström and Smedman (2004) and meeting the best results from Christen et al. (2000). We observe in figure 2.15 that the R^2 distribution for all 3 comparisons is narrow, being limited inferiorly and superiorly to 0.5% limit.

The comparison results of the parameters containing temperatures, summarized by tables 2.7 and 2.8 indicate that the 1st statistical moment of the temperature measurements agree quite well, $R^2 = 0.999$, in the shortest averaging interval, 5-min. We also verify that Gill HS sonic is penalized by the temperature drift, presenting the worse correlation, $R^2 = 0.995$. Temperature variance appears to be somehow linked to the instrument separation, note in table 2.8 that the best correlation is from the closest instruments, $R^2 = 0.951$ for CSI D while the data dispersion increases for the instruments 9 m apart. Such results are 3% worse than Högström and Smedman (2004) results for sonics located in the same mast. From the analysis we also verify that NUW sonic systematically overestimates the temperature variance and heat flux, being the last an overestimation in the order of 10%.

Contrary to $\overline{T'T'}$, $\overline{w'T'}$ seems independent from instrument separation, $R^2 = 0.98$ for the standard 30-min averaging intervals. The linear fit of the data, the reduced data

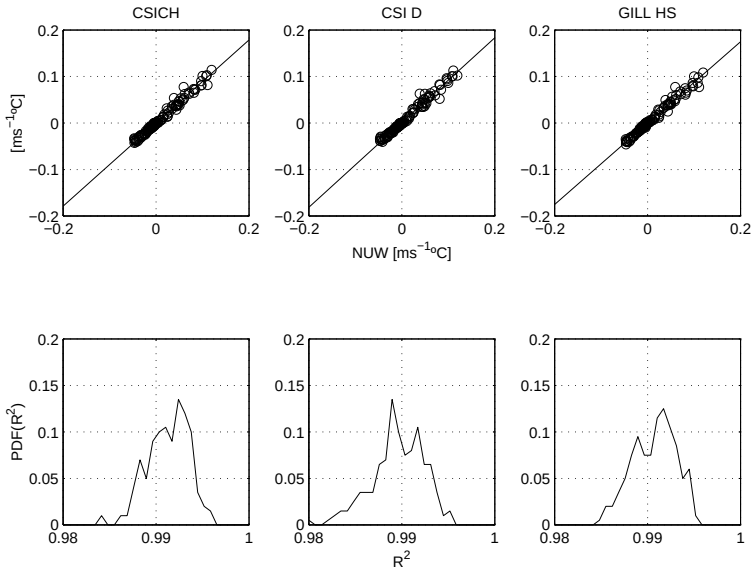

Figure 2.15: Sonic heat flux comparison for 30-min averaging intervals and probability distribution of the correlation coefficient.

dispersion given by the correlation coefficient of the heat flux, the low uncertainty values given by the $PDF(R^2)$ at figure 2.15, and the 3% better results than Högström and Smedman (2004) comparison, and meeting the best results from Christen et al. (2000), show no indication that flow passing through NUW is different from other instruments. NUW overestimation is most likely instrumental and will be discused in the next subsection.

2.3.4 Spectral Comparison

The spectral performance analysis of the sonics was based in 2 sets of data of 3-hours duration that differed in stability, with Ri equal to -0.036 for light unstable and +0.076 for stable stratification. Table 2.9 shows the statistics of the flow for these two sets which were characterized by low velocity and large turbulence intensity, 28% and 13% respectivelly. The ogive function of the momentum and heat fluxes was also produced in order to verify if the 3-hour data set was long enough for comparison, figure 2.16. As expected, we observe that different convergence times were obtained: while the momentum flux converged after 5 s for unstable stratification, 10 times longer intervals were required in case of stable; for the heat flux, the convergence time was 100 s to unstable and 500 s for stable stability, confirming the poor correlation results of 5-min intervals in table 2.8.

The spectral comparison was performed recurring to the FFT extraction of the same number of points in each data series thus targeting only an energy comparison of the velocity, momentum and heat fluxes. Figure 2.17a to 2.17f show the spectra comparison for unstable and stable stratification where each axis represent the logarithmic of the

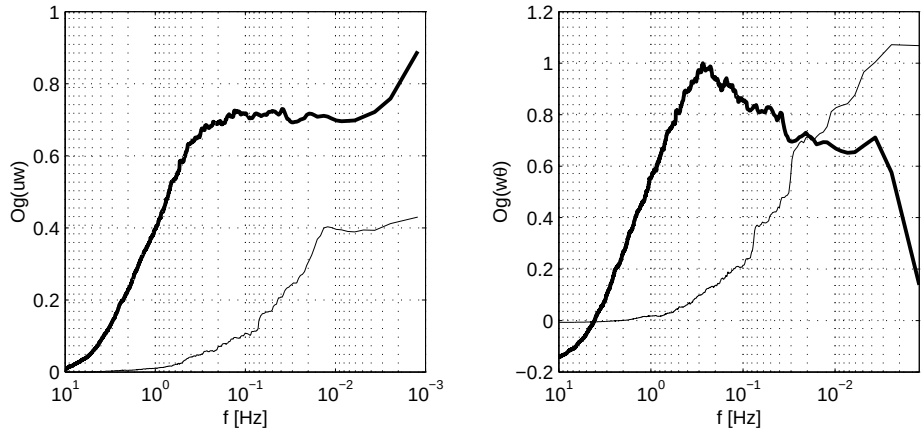

Figure 2.16: Ogive of the momentum and heat flux. Thicker line for unstable stratification.

Table 2.9: Statistics of the unstable and stable stratification data sets of the spectral comparison.

	$\overline{V}$ [ms^{-1}]	it	$\sigma(V)$ [ms^{-1}]	$sk(V)$	$k(V)$	$\overline{Ri}$	$\sigma(Ri)$
Unst.	1.8143	0.28	0.5060	0.1700	2.5876	-0.036	0.026
Stab.	2.0942	0.13	0.2699	0.4622	3.3516	0.076	0.064

power. From the exponential decay of the inertial range we observe that higher energy is contained at lower frequencies decreasing exponentially as the frequency increases. All sonics show identical power spectra however the number of points at the high frequency end is much higher than the low frequency one, thus the resolution of the comparison is biased toward the high frequency. To avoid that, we recur to the spectral splicing and smoothing procedures discussed in subsection 1.6.4 to provide an equal spectral power resolution along the frequency axis.

Velocity, momentum and heat flux spectral comparisons are presented in table 2.10. By considering the offset residual for each case, inferior to 1% with the exception of CSI CH sonic for unstable stratification, we will focus the analysis of the results solely in the slope and correlation coefficients. The velocity spectra results (table 2.10) shows that there is only one case, NUW against CSI CH, where the slope is close to the same value, 13 to 11% overestimation from unstable and stable stratification. For unstable stratification and comparing against CSI D and Gill HS, we note that NUW sonic underestimates the spectral energy respectivelly 18 and 71% while overestimating 15 and 23% for stable stratification. The correlation coefficient change is not so large, a 3.9% decay for CSI CH and 1.8% for CSI D from ustable to stable stratification, while Gill HS reduction is residual, 0.1%.

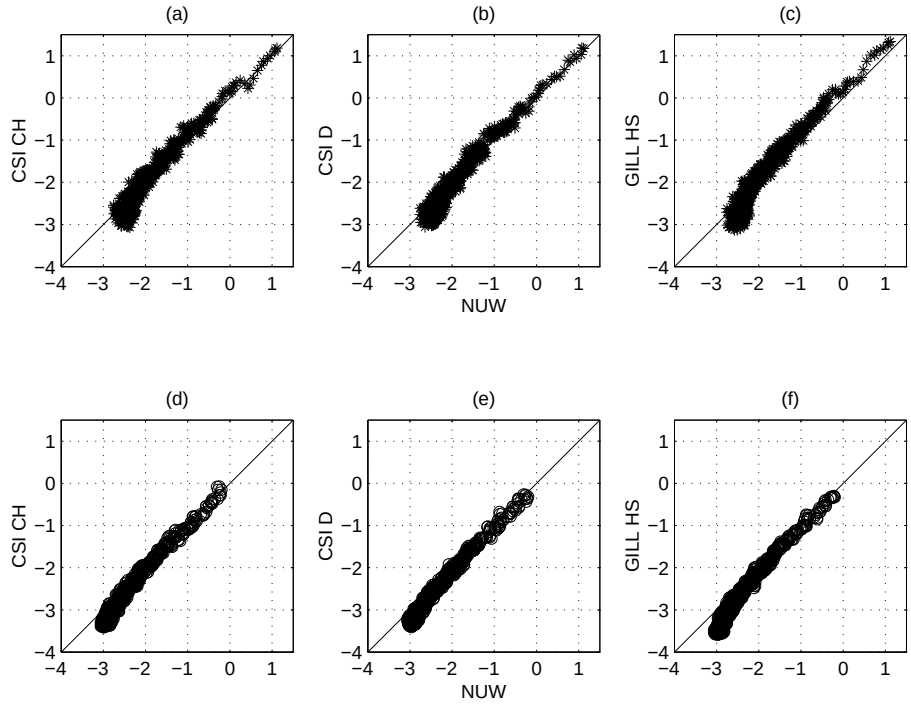

Figure 2.17: Logarithmic velocity power spectral density comparison without the spectral slicing and smoothing procedure for unstable $*$ and stable stratification $\circ$. The unit line is plotted for reference.

Table 2.10: Spectra and cospectra comparison for the velocity, momentum and heat flux for unstable and stable stratification.

quantity	Type	Unst.			Stable		
		a_u	b_u	R_u^2	a_s	b_s	R_s^2
$S(v)$	CSI CH	-0.017	1.129	0.998	-0.013	1.112	0.959
	CSI D	0.029	1.182	0.989	0.004	0.816	0.971
	GILL HS	0.088	1.712	0.997	0.003	0.845	0.996
$Co(\overline{u'w'})$	CSI CH	0.017	0.723	0.994	0.000	0.773	0.988
	CSI D	-0.028	0.750	0.970	0.001	0.997	0.993
	GILL HS	0.026	1.156	0.995	0.000	0.925	0.995
$Co(\overline{w'T'})$	CSI CH	0.067	0.503	0.893	-0.001	0.781	0.846
	CSI D	0.043	0.645	0.949	0.001	0.807	0.912
	GILL HS	0.035	0.099	0.940	0.001	0.209	0.688

The odd results from the velocity spectra comparison are better justified by the observation of figure 2.18a to 2.18f. It is clear in the figure that instruments disagreement

are in the low-energy end of the spectra (high-frequency end), where the energy decay of NUW sonic does not follow the same rate as the other sonics, a clear aliasing problem. However, on the 3 higher decades of the velocity power spectral density comparison for either stability conditions there is a proper linear fit. By removing the aliased values from the comparison there is an increase in the correlation coefficient of 1.3 and 0.5% for CSI CH and CSI D respectively for unstable stratification.

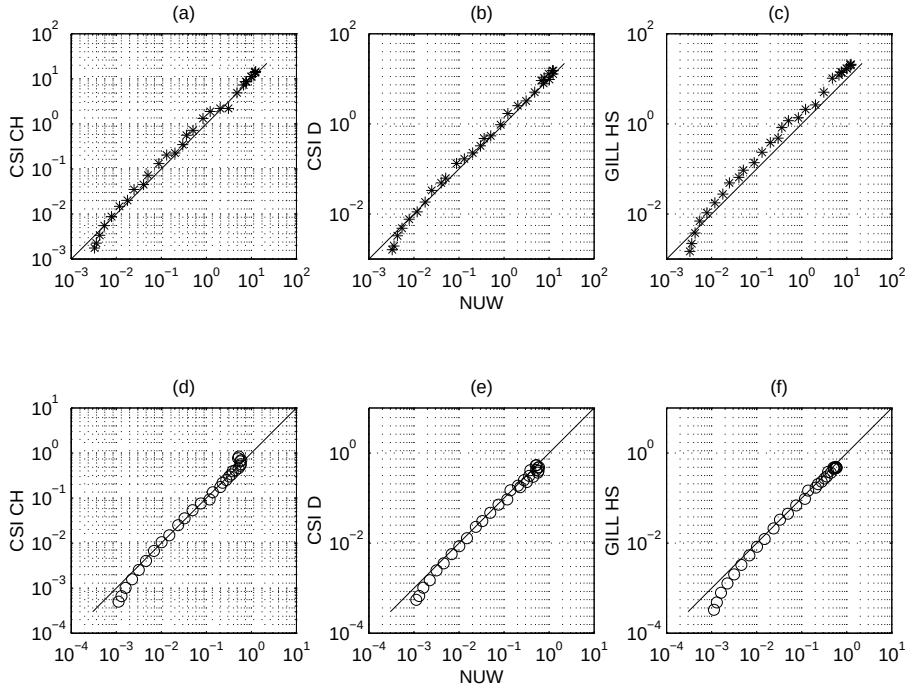

Figure 2.18: Velocity power spectral density for unstable $*$ and stable stratification $\circ$. The unit line is plotted for reference.

The momentum $\overline{u'w'}$ spectral comparison is also presented in table 2.10. The offset rounds 2% for unstable case and vanishes for stable stratification. Here we observe the same difference in sonic response as in the velocity spectra case, with different slope values according to stratification. For instance, against CSI CH, NUW sonic overestimates the momentum cospectra by 25% under unstable conditions while presenting a 0.7% underestimation for stable stratification. The correlation coefficient reaches 99% for all sonics independently of stratification where the exception is CSI D under unstable stratification, $R^2 = 97\%$. To justify the better results for the stable stratification we present the $\overline{u'w'}$ cospectra comparison in figure 2.19, where we clearly observe the better fit of all sonics for stable stratification when compared to the more scattered values of the unstable stratification case. Note that the flow of the stable case was steadier than unstable stratification one: the mean velocity was 13% higher and turbulent intensity 54% lower, which may account for the better comparison obtained for the momentum flux.

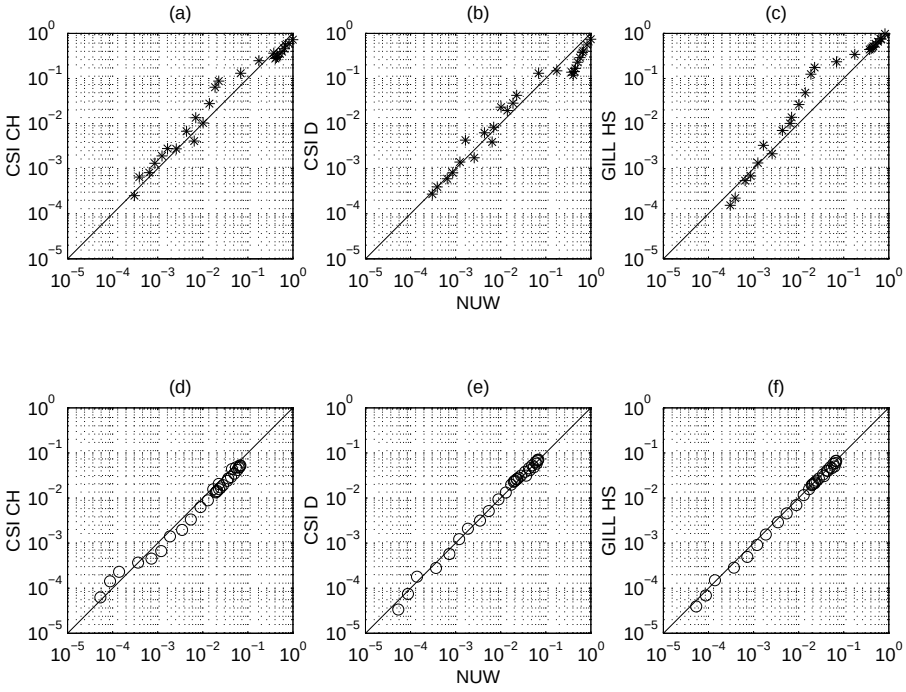

Figure 2.19: Momentum $\overline{u'w'}$ comparison of the spectra for unstable $*$ and stable $\circ$ stratification. The 1:1 line is plotted for reference.

The heat flux comparison results, table 2.10, are the poorer of all spectra comparison, presenting better results for unstable stratification. Again, as verified in table 2.8, NUW sonic overestimates the heat flux when compared to the other sonics. The instrument comparison is better for unstable stratification, with lower overestimation values from the NUW sonic, although with larger data scatter, figure 2.20a to 2.20f. Disregarding the stable stratification results, the correlation range from 89% for the CSI CH to 95% for the CSI D sonic, table 2.10. These results may be explained by the better mixing mechanism of the unstable atmosphere.

The comparison with statistical methods presented in the previous subsections presented better estimates than the ones obtained with spectral methods. There is a clear reason for that, the data set corresponds to 5 days of comparison while the data set for the spectral method corresponded only to 3-hours of measurements. The main advantage of this spectral comparison lied in the identification of the NUW aliasing feature, which explain the overestimation of parameters such as $\overline{w'w'}$, u_*, $\overline{T'T'}$ or $\overline{w'T'}$. This feature is wiped away by the 5-min statistics but clearly identified for instance in figures 2.18 or 2.20.

We also verified from the spectral comparison that for such light winds the better estimates are achieved for steadier conditions, in our case lower turbulence intensity values at the stable stratification case. The exception laid in the heat flux comparison where the mixing of the flow of the unstable case still better the comparison estimates.

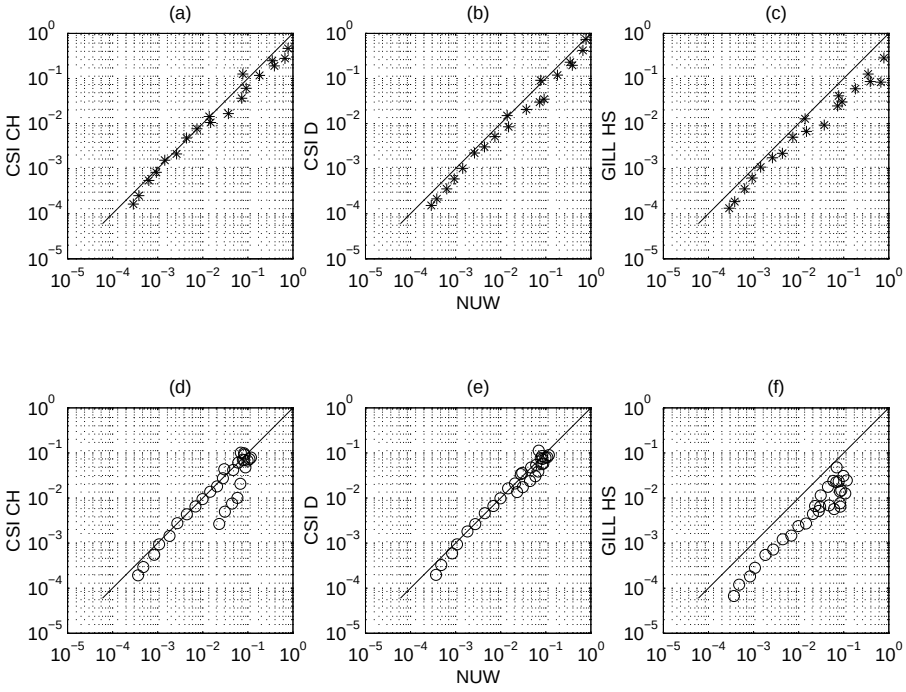

Figure 2.20: Heat flux $\overline{w'T'}$ comparison of the spectra for unstable $*$ and stable $\circ$ stratification. The 1:1 line is plotted for reference.

Table 2.11: Slope and correlation coefficients, b and R^2 obtained from statistical and spectral methods for $\overline{w'T'}$. The subscripts $_{stat}$ for parameters obtained with statistical methods and $_u$ and $_s$ respectively for the spectral comparison for unstable and stable stratification. $\Delta\epsilon = (stat - spec)/stat$ is the difference between the statistical and spectral indicators.

		b_{stat}	b_u	b_s	R^2_{stat}	R^2_u	R^2_s
$Co(\overline{w'T'})$	CSI CH	0.895	0.503	0.781	0.998	0.893	0.846
	CSI D	0.918	0.645	0.807	0.998	0.949	0.912
	GILL HS	0.880	0.099	0.209	0.985	0.940	0.688
$\Delta\epsilon$	CSI CH	-	0.438	0.127	-	0.105	0.152
	CSI D	-	0.297	0.121	-	0.049	0.086
	GILL HS	-	0.888	0.763	-	0.046	0.302

Table 2.11 compares the slope and correlation coefficients obtained with statistical and spectral methods. Note that the longer data series in the statistical comparison is responsible for closer instrument agreement. Taking the statistical method as the reference, and defining $\Delta\epsilon$ as the non dimensional difference between the two methods, we observe contradictory information. The correlation coefficient closes to the reference value for

unstable stratification, only a 5% difference for CSI D and Gill HS. This means that the data dispersion under stable stratification is larger, there is as less effective mixing of the flow that lead larger differences for instruments placed 6 and 9 m apart. On the other hand, we obtain better $\Delta\epsilon$ for the slope under stable stratification, that may be justified by the stronger and steadier flow, approaching to the mean wind field of the overall analysis. What is worth pointing is the R^2 improvement for CSI D and Gill HS was just 5% for the whole series of 5 days against 3-hour data under unstable stratification.

Table 2.12: Slope and correlation coefficient with the respective standard deviation obtained from the bootstrapped samples for the spectral comparison according to flow stability.

quantity	Type	Unstable				Stable			
		b	σ_b	R^2	σ_{R^2}	b	σ_b	R^2	σ_{R^2}
$S(v)$	CSI CH	1.129	0.020	0.998	0.005	1.112	0.089	0.959	0.016
	CSI D	1.182	0.060	0.989	0.003	0.816	0.047	0.971	0.008
	GILL HS	1.712	0.022	0.997	0.001	0.845	0.014	0.996	0.002
$Co(\overline{u'w'})$	CSI CH	0.723	0.010	0.994	0.054	0.773	0.019	0.988	0.005
	CSI D	0.750	0.032	0.970	0.022	0.997	0.016	0.993	0.003
	GILL HS	1.156	0.008	0.995	0.027	0.925	0.018	0.995	0.002
$Co(\overline{w'T'})$	CSI CH	0.503	0.070	0.893	0.070	0.781	0.069	0.846	0.045
	CSI D	0.645	0.037	0.949	0.037	0.807	0.071	0.912	0.040
	GILL HS	0.099	0.009	0.940	0.009	0.209	0.043	0.688	0.078

The spectral results presented in this section are incomplete without an indication of the experimental uncertainty associated with the comparison. Table 2.12 recovers the comparison information of table 2.10 adding the information of the standard deviation of the PDF's of b and R^2 according to stability. We have observed that the better agreement for the velocity spectra was under unstable conditions, and that is also true in σ_b and σ_{R^2}, where the mean values of all instrument are respectively 3% and 0.3%. Momentum flux, due to stronger and steadier conditions of stable stratification case yield mean σ_b and σ_{R^2} respectively of 2% and 0.3%, while heat flux yield a mean instrument σ_b and σ_{R^2} of 4%.

2.4 Conclusions

EBEX00 site was characterized by light winds and large temperature gradients, with a stable stratification during night and great part of the day, where the temperature gradients tend to damp the turbulent mixing mechanism often forcing the flow into laminar regime. From the top of the vegetation until the sonic height, 4.7 m, the flow was affected by the roughness of the terrain, 15 cm, half-way between roughly open and rough (Stull, 2000).

Assuming a 30-min average as the reference, all sonics agreed quite well in 1st moment estimation, with correlations of 98.6% for horizontal velocity and 99.9% for temperature measurements independently of the spacial separation, up to 9 m, over large roughness terrain, light winds and large latent and sensible heat gradients. The temperature measurements converged faster, and 5-min averages were enough to establish an almost perfect linear fit for the comparison most likely because temperature turbulent scales are smaller. Also as temperature measurements are concerned, we found that the Gill HS unit presented a temperature drift that may compromise all temperature related measurements, namely the 2nd order ones for longer periods.

The horizontal velocity showed an almost perfect agreement between instruments as opposed to the vertical component of the velocity field, with no correlation between instruments. That is justified by the fact that the flow may be considered horizontally bidimensional and the mean vertical velocity is one order of magnitude smaller than the fluctuations along z-axis, 0.04 against 0.70 ms^{-1}.

The ogive function (figure 2.16) showed that a 5-min average did not include all features of the flow and longer averages intervals had to be considered, specially when comparing higher statistical moments. Here, some discrepancies between instruments arose although the average value of the correlations between all 4 sonics were comparable to the results from Högström and Smedman (2004) or Christen et al. (2000). The mean correlation of $\overline{w'w'}$, u_* and $\overline{w'T'}$ were respectively 98.6%, 93.3% and 98.1%, being the results independent of the spacial separations of the instruments. The only parameter that presented worse mean correlation result, penalized by Gill HS temperature drift was $\overline{T'T'}$, with $R^2 = 91.6\%$ and dependent on the instrument distance.

Another look at second moment statistics was given by the spectral analysis. We may consider the spectral comparison presented as a 2nd moment comparison for 2 data sets of 3-hours that differed in stability. Additional parameters were compared, namely $\overline{u'u'}$ and $\overline{u'w'}$ and the mean correlation was respectively 99.4 and 99.2%. The correlation of the momentum flux differed according to flow conditions, where the 99.2% mean correlation decayed 0.6% when there was less energy in the flow.

Stability plays an important role in the mixing of the flow. What seems to be an homogeneous flow may not be so under such light wind conditions and strong thermal gradients. That is clear in the case of the heat flux calculated under stable and unstable stratifica-

tion. The mean correlation coefficient for unstable stratification was 92.7% decaying to 81.5% for the stable stratification, inducing large instruments discrepancies for night-time respiration fluxes in low windspeed conditions.

Other important source of discrepancies in flux measurements are instrument related originating strong divergences in 2nd statistical moment comparison. The reference sonic NUW is a case of systematic overestimation of the momentum and heat fluxes due to aliasing identified in the spectral comparison. Note that NUW sonic overestimates the sensible heat flux, $H = \rho c_p \overline{w'T'}$, by 12% against CSAT-3 models or the Gill HS unit. On the other hand, Gill HS temperature drift will be the source of error for long term flux measurements.

The global appreciation of the sonics point out the high accuracy and precision (repeatability) of the 1st statistical moments. The analysis of the 2nd statistical moment indicates best overall performance of the Campbell Instruments CSAT-3 sonic. However, differences between instruments may be considered negligible for wind energy resource and turbulence studies.

Chapter 3

Sonic calibration

Abstract

The transducer shadow effect of a Metek (model USA-1) sonic anemometer was mapped in a large wind tunnel with 0.4 to 0.2% turbulent intensity for velocities ranging from 4.2 to 16.1 ms^{-1}. The measurements were performed imposing a constant rotation along the whole instrument azimuth range, 0 to 360°, with an inclination angle ranging ±25° with the plane of the flow. The transducer shadow effect led in certain conditions to a velocity defect of at most 12% from the true velocity. We also verified that the transducer array accelerated the flow even for no inclination, yielding measurements that overestimate the true velocity up to 5%. The effects of the array geometry in measured spectra decreased with an increase in flow velocity and were negligible. Corrections for the sonic measurements reduced the mean deviations from the true velocity to 0.1% for 4.2 and 8.7 ms^{-1} and 0.0% for 12.0 and 16.1 ms^{-1}. Sonic temperature measurements against a Vaisala TRH sensor (model HMP 35A-CS107) were compared but no correction was recommended because deviations from the reference instrument were negligible: 0.1% for 4.2 and 8.7 ms^{-1} and 0.4% for 12.0 and 16.1 ms^{-1}. The knowledge enable its use with confidence in turbulence measurements made in complex terrain.

3.1 Introduction

This chapter describes the calibration of a Metek (model USA-1) and a RM Young (model 81000) sonic anemometers, made with the Meteorology, Climatology and Remote Sensing Laboratory - MCR - team in April 2001 according to the procedure developed by Vogt (1995) at the Institute of Fluid Dynamics at the Swiss Federal School of Technology, ETHZ. These instruments were included in a calibration campaign of 10 Metek (model USA-1), a RM Young (model 81000) and a Gill (HS model) to evaluate the performance and map the transducer shadow effect of each instrument. We concentrated solely upon the description of Metek unit S-N 199701001 and Young 81000 S-N 344 . The results of 4 other Metek units are used only to aid the characterization of the wind tunnel flow.

Chapter outline

Wind tunnel setup and instruments are described in section 3.2. Each sonic calibration program comprised measurement at 4 wind tunnel velocities, and rotation along the vertical axis at 11 different inclination angles. Section 3.3 presents the results and analysis for the calibration divided as follows: Wind tunnel test section and reference instrument determination (subsection 3.3.1). Mapping the transducer shadow effect and temperature transducer shadow effect (subsections 3.3.2.1 and 3.3.2.2) and presenting strategies to overcome such limitations once deviations in velocity measurements reached up to 12% of the true velocity and deviations for temperature measurements were found to be within a 0.3% range. Determination of a software error on the transformation matrix from Young 81000 sonic non-orthogonal coordinates to flow orthogonal coordinates (subsection 3.3.3). The conclusions of this chapter are presented in section 3.4.

3.2 Experimental techniques

The ETHZ wind tunnel presents a test section of $3.9 \times 1.1 \times 1.6$ m preceded by a 9:1 contraction where the maximum admissible wind velocity is 42 ms^{-1}. The tunnel is equipped with a barometer and a mercury column thermometer scaling from 600 to 825 mmHg and -10 to 54°C respective. The velocity in the tunnel was measured by a Pitot tube and Meteolabor rotor anemometer, model ONZ. The Pitot tube was connected to a Betz manometer scaled from 0 to 300 mmH_2O; the rotor anemometer resolution was 0.097 ms^{-1}, precision 0.1 ms^{-1}, accuracy 3% and a distance constant 2 m. Relative humidity and temperature were made with a Vaisala TRH sensor, model HMP 35A-CS107, with $\pm 1\%$ accuracy, figure 3.1.

The wind tunnel velocity measured by the Pitot was given by (3.1), where K is the Pitot shape factor, Δh_{Betz} is the height given by the Betz manometer and ρ_{air} is the corrected air

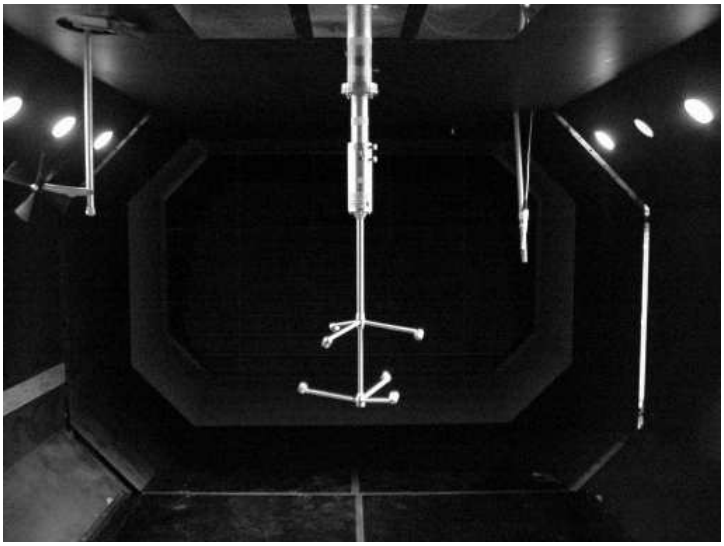

Figure 3.1: Downstream view of ETHZ wind tunnel test section. Metek model USA-1, Meteolabor ONZ rotor anemometer and TRH Vaisala model HMP 35A-CS107 (center, left and right respectively).

density according to equation (3.2) for atmospheric pressure P_{atm} and absolute humidity Ψ.

$$V_{Pitot} = \sqrt{\frac{K\Delta h_{Betz}}{\rho_{air}}} \tag{3.1}$$

$$\rho_{air} = \frac{P_{atm} - 0.378\Psi}{2.87T_{dry\,air}} \tag{3.2}$$

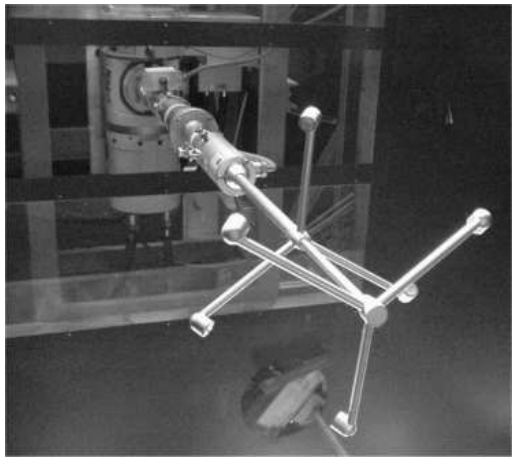

Figure 3.2: METEK (model USA-1) sonic anemometer coupled to the CNC-NIKKEN milling head.

The anemometers were installed in a shaft in the wind tunnel section in an up-side down position. The shaft was connected to a two dimensional CNC-NIKKEN milling machine head, hear forth CNC-NIKKEN (figure 3.2) with computer controlled rotation and inclination. The anemometer was suspended with the north pointing to the flow and the vertical alignment was measured by a Kell-Strom digital inclinometer, model AeroAngle II Pro 3600. The point of origin of the movement was defined once the leveling was guaranteed.

Different wind tunnel velocities were used: 4, 8, 12 and 16 ms^{-1} for the METEK sonic (model USA-1) dedicated to wind energy studies and thus requiring larger range of velocities; and 2, 4, 6 and 8 ms^{-1} for sonics dedicated to micrometeorological studies where the sonic is generally installed at heights lower than 10 m or within plant canopy. The measurements were made in the middle of the wind tunnel test section with Re ranging from 3.8×10^6 to 3.0×10^7 for the 199701001 unit.

Table 3.1: Velocity and atmospheric conditions prior to each run: V_{rotor}, V_{Pitot} and V_{sonic}, T_{air}, T_{sonic}, P_{atm}, relative humidity ψ, vapor pressure P_{vap} and air density ρ_{air}. The unit serial number and measurement date are identified in the first column.

METEK unit	V_{rotor} [ms^{-1}]	V_{Pitot} [ms^{-1}]	V_{sonic} [ms^{-1}]	T_{air} [°C]	T_{sonic} [°C]	P_{atm} [hPa]	ψ [%]	P_{vap} [hPa]	ρ_{air} [kgm^{-3}]
	4.214	4.118	4.217	24.01	23.96	966.62	23.65	7.072	1.130
199701001	8.661	8.617	8.661	24.01	23.92	966.35	23.44	7.009	1.130
(26.04.01)	12.038	11.946	12.012	24.15	23.92	966.22	22.58	6.810	1.129
	16.115	15.931	16.069	24.43	23.94	966.08	21.18	6.494	1.128
	2.284	2.362	2.297	23.76	24.42	959.15	29.96	8.827	1.122
200104017	4.367	4.170	4.370	23.75	24.48	961.95	30.02	8.838	1.125
(25.04.01)	6.590	6.520	6.603	23.78	24.50	964.08	30.03	8.854	1.127
	8.621	8.336	8.615	23.85	24.54	963.15	30.02	8.894	1.126
	2.175	1.869	2.203	23.57	24.04	956.49	25.52	7.432	1.120
200104011	4.170	4.137	4.146	23.52	24.08	956.49	26.42	7.668	1.120
(25.04.01)	6.405	6.408	6.351	23.58	24.12	956.49	27.40	7.985	1.120
	8.400	8.362	8.331	23.66	24.19	956.35	29.15	8.537	1.119
	2.382	2.433	2.398	23.22	23.11	958.08	23.34	6.655	1.123
200104018	4.174	4.376	4.175	23.21	23.14	958.08	23.39	6.666	1.123
(24.04.01)	6.447	6.189	6.451	23.24	23.19	958.08	23.47	6.701	1.123
	8.450	8.189	8.424	23.32	23.25	958.08	23.71	6.803	1.123
	2.366	2.358	2.400	23.97	24.20	963.68	29.77	8.883	1.126
199912002	4.368	4.167	4.366	23.96	24.21	963.95	29.45	8.781	1.127
(25.04.01)	6.435	6.416	6.431	23.78	24.01	966.62	25.42	7.496	1.131
	8.582	8.463	8.565	23.86	24.01	966.62	24.61	7.295	1.131

The velocity measurements by the rotor anemometer, Pitot tube and sonic anemometer for each run are presented in table 3.1, which includes also air and sonic temperature, relative humidity, and the calculated vapor pressure and air density for each run. In spite of temperature increase between runs, temperature and relative humidity may be considered constant for each step of the calibration, see subsubsection 3.3.2.2.

The CNC-NIKKEN allowed a 50° variation of the inclination, thus once the support was aligned with the vertical, we could vary the sonic with a ±25° inclination, being negative when the instrument was pruned downstream while measuring ascending (positive) vertical components. A 0.2 RPM rotation was then introduced to the instrument for each individual inclination, with complete sequential counter and clock-wise rotations, corresponding respectively to wind rotating from 0 to 360°, and 360 to 0° successively. The CNC-NIKKEN sweep program (table 3.2) corresponds to 11 independent rotations for each angle. Sonic data, CNC-NIKKEN trajectory, rotor and T/RH sensors where logged

Table 3.2: CNC-NIKKEN sweep program. Each step of the sweep lasted 5-min

Step	Inclination - ϕ[°]	Rotation - θ
01	-25.0	C-CW
02	-17.5	CW
03	-10.0	C-CW
04	-5.0	CW
05	-2.5	C-CW
06	0.0	CW
07	2.5	C-CW
08	5.0	CW
09	7.5	C-CW
10	17.5	CW
11	25.0	C-CW

into a computer and monitored with LabView, with all inputs synchronized by the same clock and the experiment was controlled visually on screen by periodic observations of the test section.

The data output was similar to the one presented in figures 3.3a to 3.3f, where sonic u, v and w velocities with sonic temperature T_s are presented in figures 3.3a and 3.3b. Flow conditions such as air temperature T, relative humidity ψ and rotor velocity V_{rotor} are captured in figures 3.3c and 3.3d. The CNC-NIKKEN trajectory is controlled in figure 3.3f by a 4000 mV flag activated when each step of the sweep program of table 3.2 was on. The flag was deactivated to 0 mV when the CNC-NIKKEN milling head was positioning the sonic into next inclination. The overall time consumed for mapping one sonic at 4 flow velocities was over 4 hours.

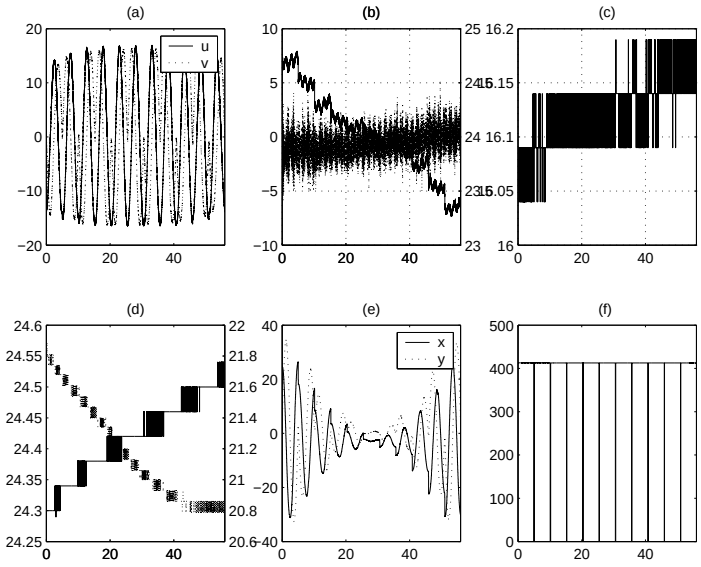

Figure 3.3: Data output of sonic calibration: (a) longitudinal u and transversal v sonic velocity in ms^{-1}. (b) vertical sonic velocity w in ms^{-1} - continuous line and left y-axis; sonic temperature T_s in °C - dotted line and right y-axis. (c) rotor velocity V_{rotor} in ms^{-1}. (d) Test section temperature T in °C - continuous line and left y-axis; relative humidity ψ in % - dotted line and right y-axis. (e) x and y CNC-NIKKEN trajectory [mm]. (f) 4000mv flag to warn program step jump as from table 3.2. The abcissa of (a) to (f) represent time in minutes.

All sonics were programmed for the highest sampling frequency, 20 Hz for the METEK USA-1, with no filtering or internal software correction. Before installing the sonic into the wind tunnel, the self calibrating test was performed according to the manufacturers instructions. This is a feature of some sonics (Young 81000 model was the only unit where this option was not available) that allows the calibration of the instrument after transportation. A slight change in the path-length due to transportation or bad handling may cause measurement errors. The protocol consists in measuring the path distance between transducers and then introducing the sonic array into a zero wind velocity chamber with known temperature and humidity, which may be a simple and closed box with nothing but air at rest inside. The values are then introduced into the sonic software that recalculates the sound pulse travel for the new undisturbed flow conditions.

Table 3.3 compares new and old calibration values for 5 Metek sonics. Although there are less than 0.2 mm differences from the old to the new calibration of the 199701001 unit P_1 and P_3 paths, there is a 2.6 mm difference for P_2, which will lead to an underestimation of 1.38% on the velocity measurement for that particulaly path.

Table 3.4 complements the information on the Metek (model USA-1) sonic anemometer specifications.

Table 3.3: Path length measurements before sonic self-calibration. The values in italic refer to the old calibration measurements.

Metek Ser. No.	P_1 [1/10 mm]	P_2 [1/10 mm]	P_3 [1/10 mm]	T[°C]
97 01001	1879	1910	1873	23.1
	1880	*1884*	*1871*	-
99 12002	1736	1766	1742	24.2
	1722	*1760*	*1738*	-
2001 04011	1736	1729	1733	23.6
	1731	*1729*	*1733*	-
2001 04017	1737	1734	1740	23.3
	1735	*1733*	*1736*	-
2001 04018	1736	1738	1738	23.1
	1736	*1734*	*1734*	-

Table 3.4: Specifications of Metek (model USA) sonic anemometer.

Quantity	Measuring range	Resolution
Wind velocity	0 - 60 ms^{-1}	$\pm$0.01 ms^{-1}
Wind components	-60 - 60 ms^{-1}	$\pm$0.01 ms^{-1}
Wind direction	0 - 360°	$\pm$0.40°
Temperature	-30 - 50° C	$\pm$0.01° C

3.3 Results and analysis

3.3.1 Reference instruments

The first step on the analysis was to determine which instrument would be used as reference: the Pitot tube or the ONZ rotor anemometer. Both instruments agreed quite well, the correlation was 0.9993 and the slope was 1.014. However, figure 3.4 showed a minor disagreement at low velocity, and because there was no information on the resolution of the wind tunnel's barometer, thermometer, and Betz manometer, there was no way to quantify the uncertainty of the velocity measurements by the Pitot tube, and therefore we choose the ONZ rotor anemometer as the reference instrument.

Two main reasons for choosing the ONZ rotor anemometer as a reference instrument against the Pitot tube were the better agreement of the rotor with the 1:1 slope for lower velocities and the rotor specifications which enabled uncertainty quantification. The flow velocity measured by the Pitot, though with acceptable results when confronted to the

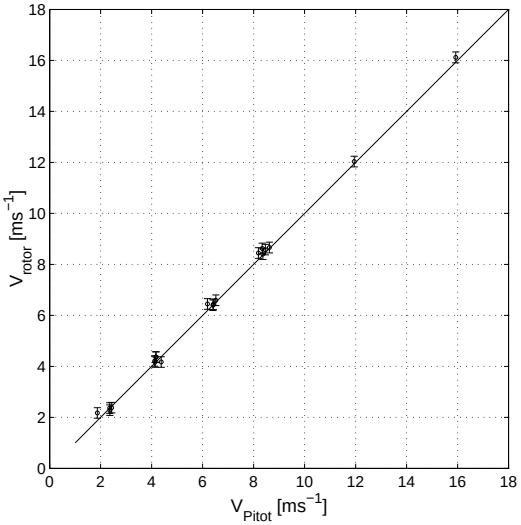

Figure 3.4: Pitot tube and ONZ mean flow measurements for the wind tunnel section. The 1:1 line is plotted for reference. The limit bars are for a 95% experimental uncertanty of the ONZ rotor anemometer.

rotor's, is indirectly made, thus carrying intrinsically several error sources: thermometer, barometer and Betz manometer. Also there was no prior information upon any calibration program of those two instruments, pruning our choice to the rotor anemometer as the reference instrument. Nevertheless, the correlation coefficient of rotor-Pitot comparison, $R^2 = 0.999$, indicated that no major measurement error was undertaken by using such instruments.

Figure 3.5 shows the plots for the 5 sonics for a null inclination and the Pitot tube. The 4 measurements in each graphic correspond to the mean value of each run. The correlation between each sonic against rotor is 1.00, although we should bear in mind that only 4 points are being correlated and 3 degrees of freedom are not enough to advocate a perfect correlation. That was not the original intention due to wind tunnel time limitation, although the consistency of correlation results for all sonics from the same manufacturer increase the confidence in a linear relation. The slope for each sonic anemometer is within 2% of the 1:1 ratio: sonics 1997001, 2001104017, 2001104011, 2001104018, 199912002 and Pitot slopes are respectively 0.990, 1.024, 1.024, 1.018, 1.023 and 1.014.

The uncertainty of the measurements presented by the error bar figures 3.4 and 3.5 were obtained according to equation (2.2) for a 95% confidence interval.

Figure 3.6 present the 95% uncertainty evolution calculated for different velocities. The ONZ rotor anemometer mean uncertainty was 1.2% varying from 2.7% to 0.5% as the velocity inside the test section increased. That is an expected feature once the systematic bias is constant while the measurements standard deviation decreases as the flow gets steadier. The mean uncertainty of the sonics is larger, varying from 3% for the 1997001

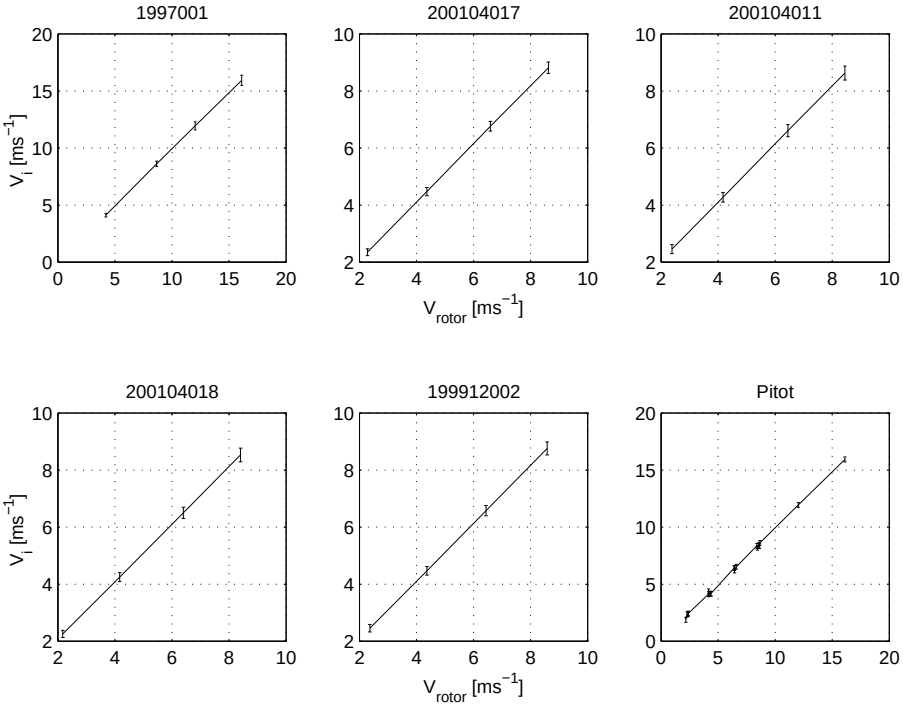

Figure 3.5: Mean flow results of 5 METEK units and the Pitot tube. All ONZ against sonic R^2 are equal to 1.00 while the R^2 from the Pitot tube is 0.9993. The slope are respectively 0.990, 1.024, 1.024, 1.018, 1.023, 1.014.

and 20010417 units to 4% for the rest of the units.

There could be 2 reasons for the larger uncertainty values of the sonics: the higher sampling rate of the sonics may capture larger fluctuations compared to the rotor anemometer; in spite of having a null inclination, there is still some flow distortion as a sonic rotates during the measurement. Figure 3.6 shows the uncertainty values already filtered at the same sampling rate of the rotor anemometer, 0.5 Hz, so we can exclude a sampling related problem.

The larger uncertainty values from the sonics are possible also due to the distortion field created by the transducer array or separation from sonic and rotor anemometer inside the test section. To avoid interference between the sonic rotating movement and the rotor anemometer, both instruments were placed almost 75 cm apart; the rotor was installed closer to the wall of the test section measuring lower turbulence levels.

No formal information on the homogeneity of the turbulence field inside the test section, or any other particularity was pointed out by local responsible upon that issue and therefore we have to assume an uniformed turbulence field. However, we have recurred to the measurements from the sonics under the previously stated conditions, 4 velocity measurements and null inclination, to determine the turbulence levels inside the test section

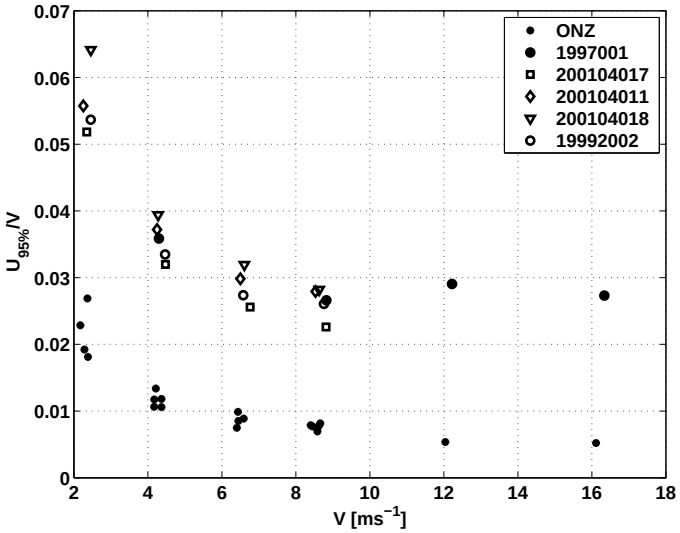

Figure 3.6: Sonics and rotor anemometer 95% uncertainty evolution with wind velocity.

and the results are similar to the ones depicted in figure 3.6 and will not be presented here.

The curve shows larger turbulent intensity values for lower velocities that decrease as mean flow velocity increases. The mean turbulent intensity is 0.4%, ranging from 0.9% for the lower velocities, 2 ms^{-1}, decreasing to 0.2% for 16 ms^{-1}. The results from the ONZ rotor anemometer agree with the sonics, 0.4% to 0.2% from lower to higher velocities.

Figure 3.7 shows the autocorrelation function of the Metek USA-1 9701001 sonic run according to the rotation θ induced by the CNC-NIKKEN device for a 0° inclination. From the autocorrelation we observe that there is, for all velocities, a phase correlation induced by the transducer array, reproducing approximately the 60° shift of the array configuration. This phase shift acts in the turbulent measurements as a low-frequency input in the turbulence spectrum, contaminating the energy spectrum.

Besides the low-frequency contamination of the spectrum, the power spectral density of the flow is not well characterized by the sonic, figure 3.8. This may occur because the sonic is rotating and the measurements are not independent on the azimuth of the instrument. Also the 20 cm of the transducer path-length filtering characteristics decreases the resolution for the low turbulence conditions at the wind tunnel. Here we observe that the peak, located at 0.2 Hz corresponds to the CNC-NIKKEN frequency rotation. This peak is present for all velocities, though clearer for the lower velocity case. For frequencies higher than 0.5 Hz, the energy spectrum decreases to a constant value, showing that the sonic is unable to resolve the lower scales inside the tunnel, assuming white-noise feature.

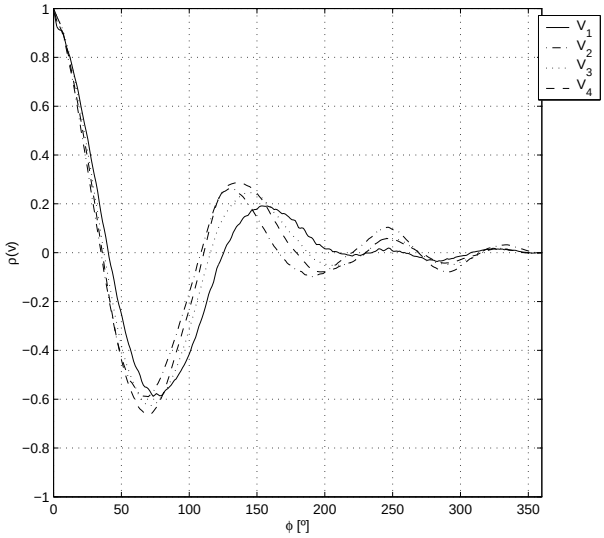

Figure 3.7: Autocorrelation function of the velocity measurements as the sonic rotates with angle ϕ, for V_1 to V_4 (4 to 16ms^{-1}) and a null inclination angle.

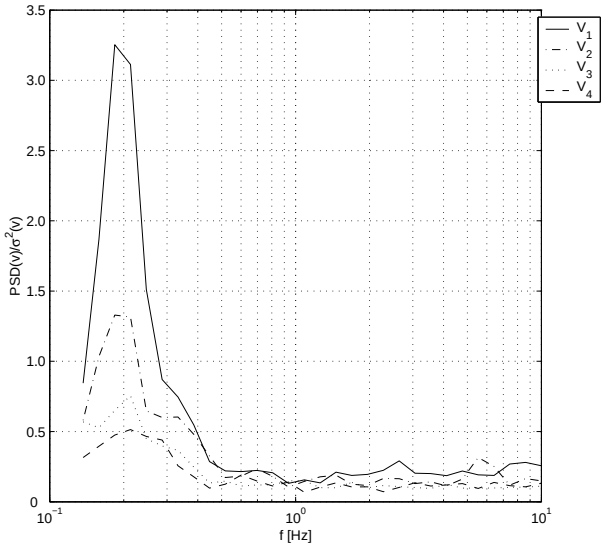

Figure 3.8: Velocity power spectral density for V_1 to V_4, 4 to 16ms^{-1} and 0° inclination.

3.3.2 Transducer shadow effect

3.3.2.1 Velocity

During one rotation, the inclination θ of the instrument was constant and we analysed the deviation with K_c defined as

$$K_c = \left(\frac{V_i - V_{i\,rotor}}{V_{i\,rotor}} \right) \times 100 \tag{3.3}$$

where V_i is the measured velocity and $V_{i\,rotor}$ is the ONZ measured velocity both at the same run i. Figure 3.9 shows K_c evolution with rotation ϕ of the sonic for a given angle θ. This figure shows the instantaneous measurements with a large dispersion of points, a normal and expected consequence of the sampling rate, 20 Hz. The line presents the filtered values by a gaussian window over each 200 points (10 s), presenting a more clear evolution of the curve. A more complete description of this technique may be consulted at section A.2.

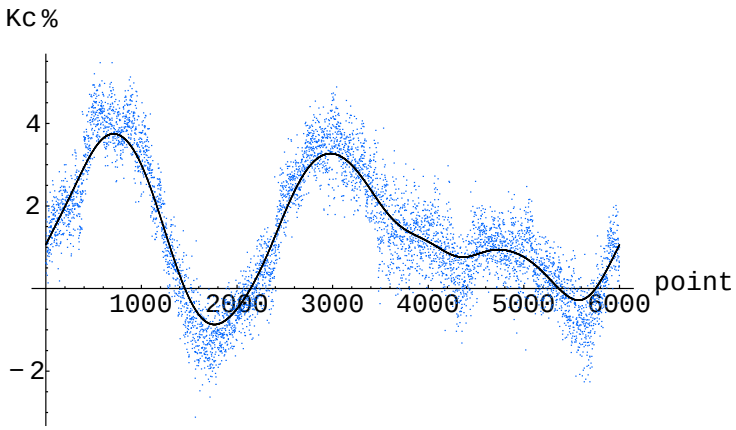

Figure 3.9: K_c evolution with sonic rotation ϕ for a given inclination angle θ. Dots for 20 Hz values and line for filtered results obtained by a FFT gaussian window.

The procedure used in figure 3.9 was extended for all 11 inclination angles based in the filtered curves for each inclination. We finally build a surface representing the deviation caused by the transducer array distortion for the 4 velocities, figure 3.10, were we observe a symmetry between all velocities for the valleys and peaks, figure 3.11. The symmetry is bounded to the physical structure of the instrument, transducer array and support, and is repeated each 120° either for positive and negative inclinations. The phase shift between negative and positive inclinations is 60°, corresponding to the angle between up and low transducers, which may lead to a partial data correction according to equation (1.4). This will lead to the exclusion of relevant information due to one particular aspect to be further discussed.

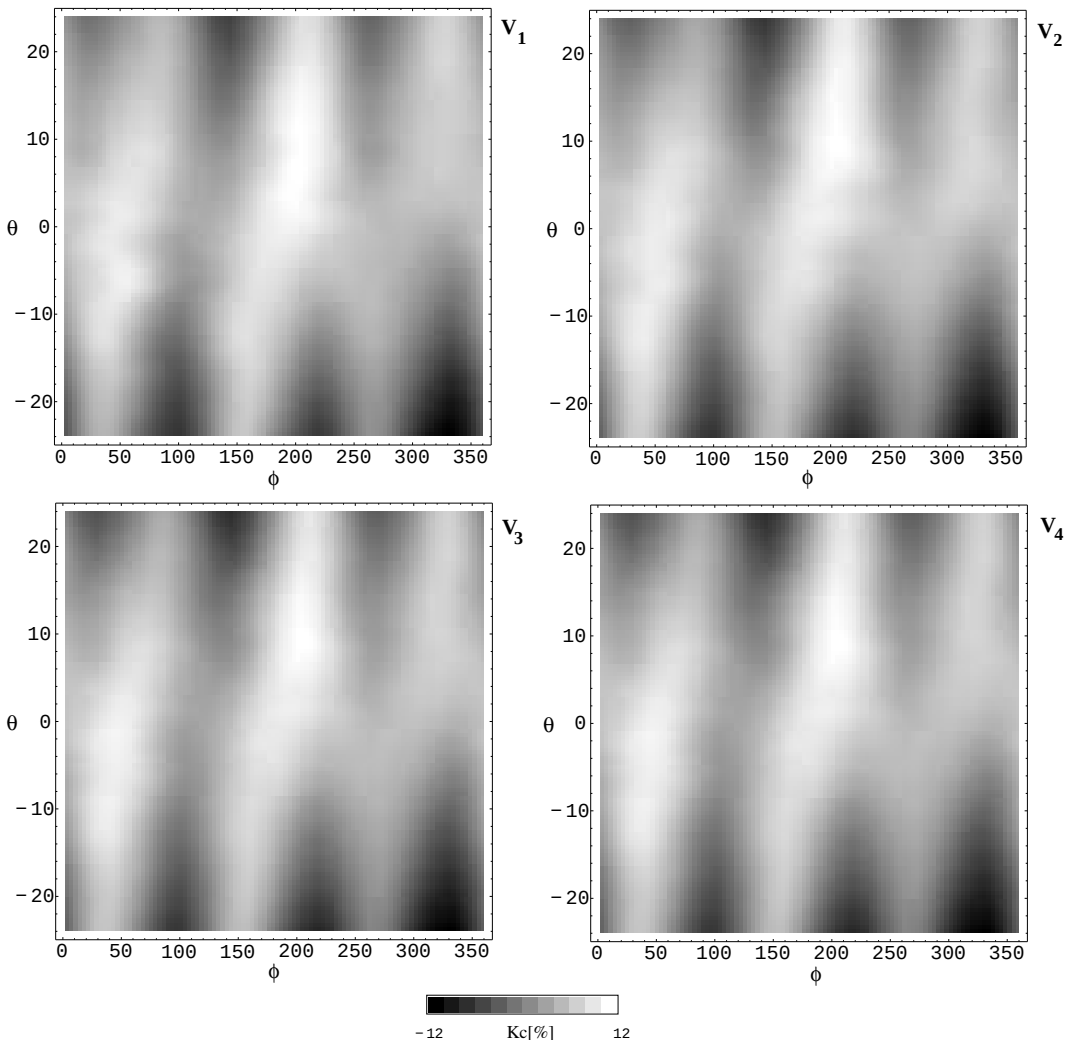

Figure 3.10: K_c surface distortion map for V_1 to V_4 according to sonic rotation ϕ and inclination angle θ.

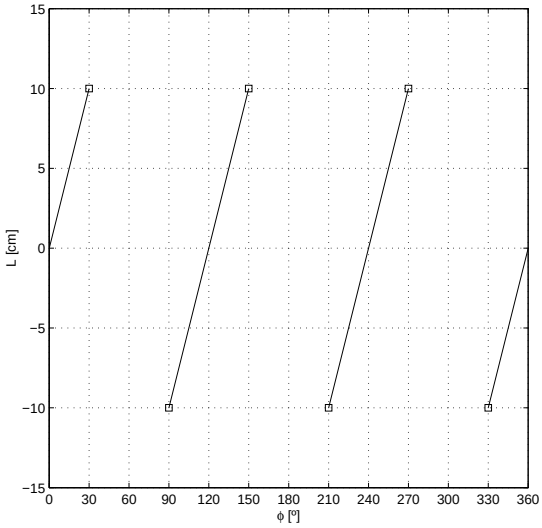

Figure 3.11: Planar representation of the transducer array arrangement for azimuth ϕ and path-length L. The continuous line stands for the acoustic travel direction.

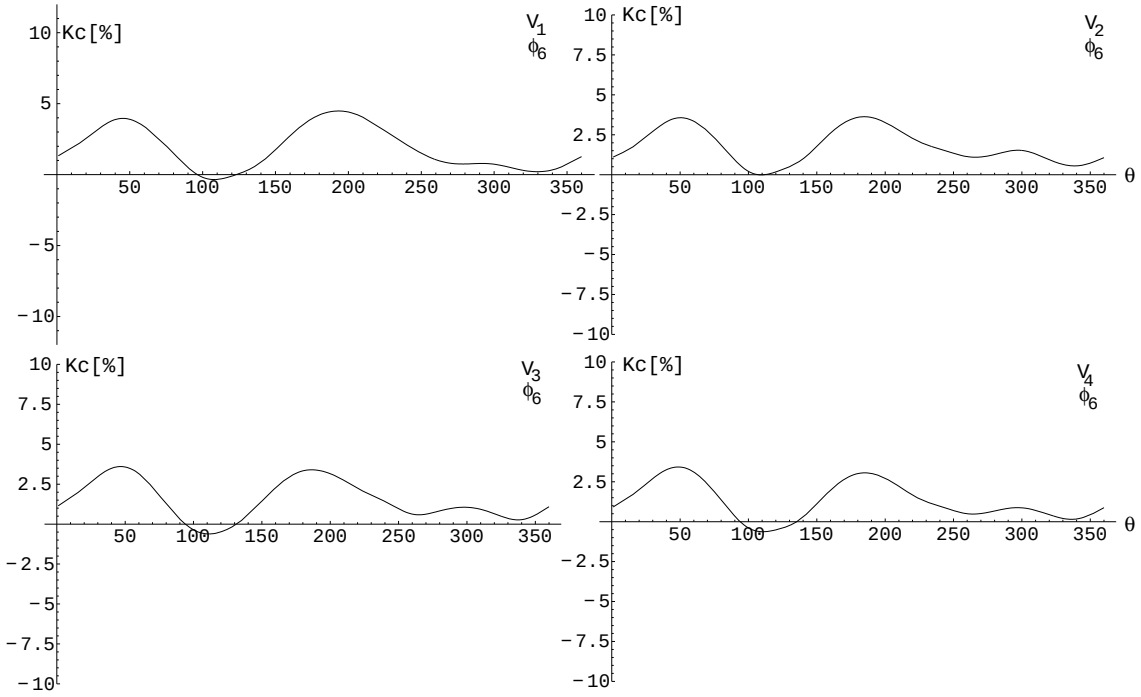

Figure 3.12: K_c at $\theta_6 = 0°$ for V_1 to V_4.

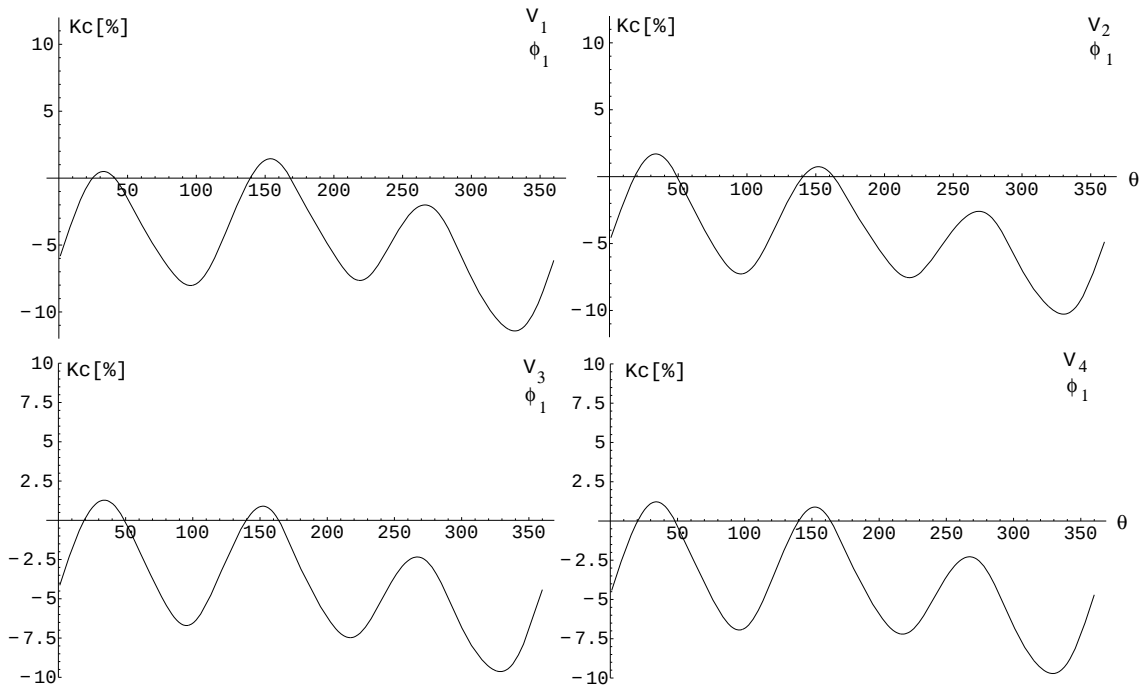

Figure 3.13: K_c at $\theta_1 = -25°$ for V_1 to V_4.

Figure 3.10 shows that the distortions for the 4 velocities are similar differing only by scale. For a null inclination angle, $\theta_6 = 0$, the deviation varies between 4.50 and -0.25% for V_1 and from 3.0% to -1.0% for V_4. The reduction of K_c between both extremes is 0.75%. Figure 3.12 shows a cross section at constant $\theta = 0°$ K_c evolution for V_1 to V_4, where we verify that for a null inclination the sonic overestimates the velocity excepting for a ϕ interval between $[100, 140°]$. The curves at figure 3.12 are very similar, with no shape and minor scale differences, being the maximum K_c difference between V_1 and V_4 just -1.0%.

As for the extreme inclination cases, $\theta_1 = -25°$ and $\theta_{11} = +25°$, figures 3.13 and 3.14, K_c fluctuations are larger. For negative inclination angles, figure 3.13, K_c oscillates from positive to negative values, although the latter is more frequent along the sonic rotation. There is no major influence of the velocity; it is less than 1% for V_1 to V_4. For extreme positive inclination, K_c also oscillates from positive to negative values with a phase shift when compared to a negative inclination.

Finally, we compare the differences between K_c for all velocities, $K_c^{V_4} - K_c^{V_3}$, $K_c^{V_3} - K_c^{V_2}$, $K_c^{V_2} - K_c^{V_1}$ and $K_c^{V_4} - K_c^{V_1}$, figure 3.15, where we verify that the maps are almost the same and the deviation difference is at most 1.6% for the low velocity case, $K_c^{V_2} - K_c^{V_1}$, while is 1.1% for $K_c^{V_4} - K_c^{V_3}$ and $K_c^{V_3} - K_c^{V_2}$. The difference between extreme cases, $K_c^{V_4} - K_c^{V_1}$, hardly reaches $\pm 2\%$ for inclination larger than 20°.

Each K_c velocity map presented accelerating and decelerating areas, ranging from +5 to -12%. The large accelerating areas, 5%, are restricted to inclinations close to +10° with

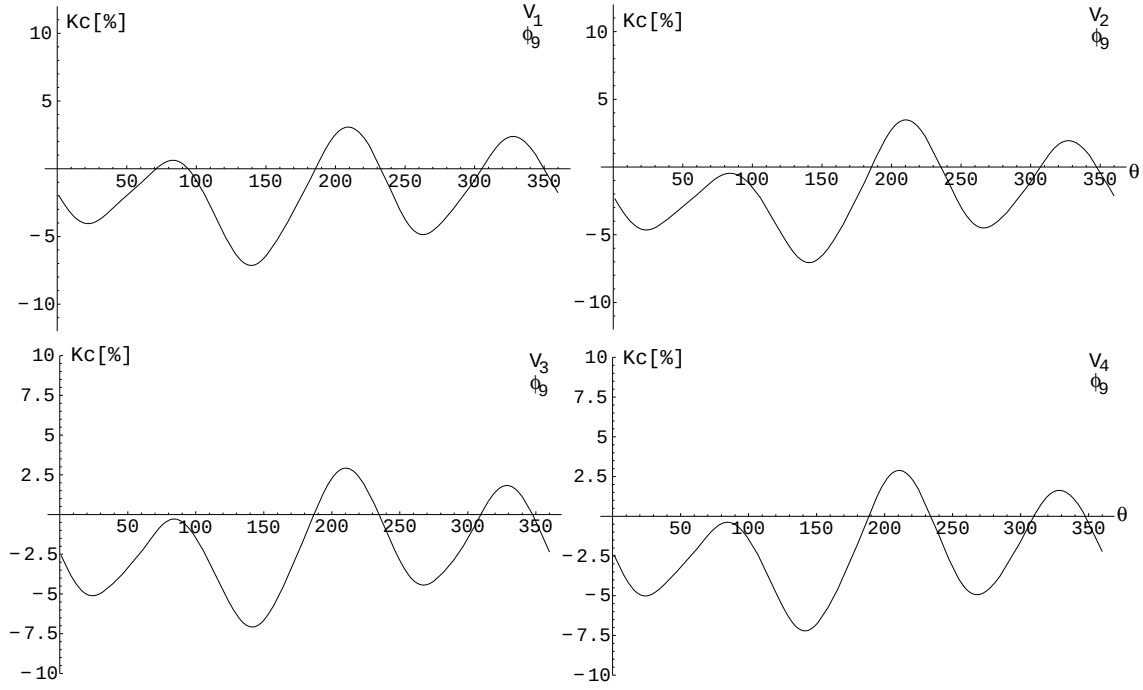

Figure 3.14: K_c at $\theta_{11} = +25°$ for V_1 to V_4.

azimuth of 200°, whereas minor acceleration areas are aligned with the acoustic path of the transducers. Crossing the information from figure 3.10 with the planification of the transducer array geometry presented in figure 3.11 we verify that the acoustic path from top-bottom transducers presents, for every inclination, a velocity defect.

The velocity deviation closes to zero only when the sonic is vertically aligned. For larger inclination angles, larger are the deviations within the acoustic path direction and vicinity. But even for a large inclination, for instance $\theta = -25°$, the larger distortions occurred when a sonic path is up-stream aligned with the flow. With a 30° rotation, the deviation drops to zero, starting positive for more 30°. For large inclinations, what the distortion maps indicates is that the upstream transducer is blocking the flow. As the sonic rotates, the acoustic path gets misaligned with the flow, thus accelerating between acoustic paths. This effect is present for every inclination, being weaker for lower inclinations, also with a lower blockage effect.

The 60° transducer array shift is observable at the velocity distortion map, figure 3.10, at the velocity autocorrelation function, figure 3.7, at the power spectral density of the velocity, figure 3.8. Velocity is affected to a maximum of 12% for extreme inclinations, but the sonic responds similarly to different wind conditions: $K_c^{V_4} - K_c^{V_1}$ is bounded within a -2 and +2% range where a single correction matrix build upon the mean of the 4 K_c maps will sufice (Vogt, 1995).

The transducer shadow effect is a know phenomenon associated with the flow bloc-

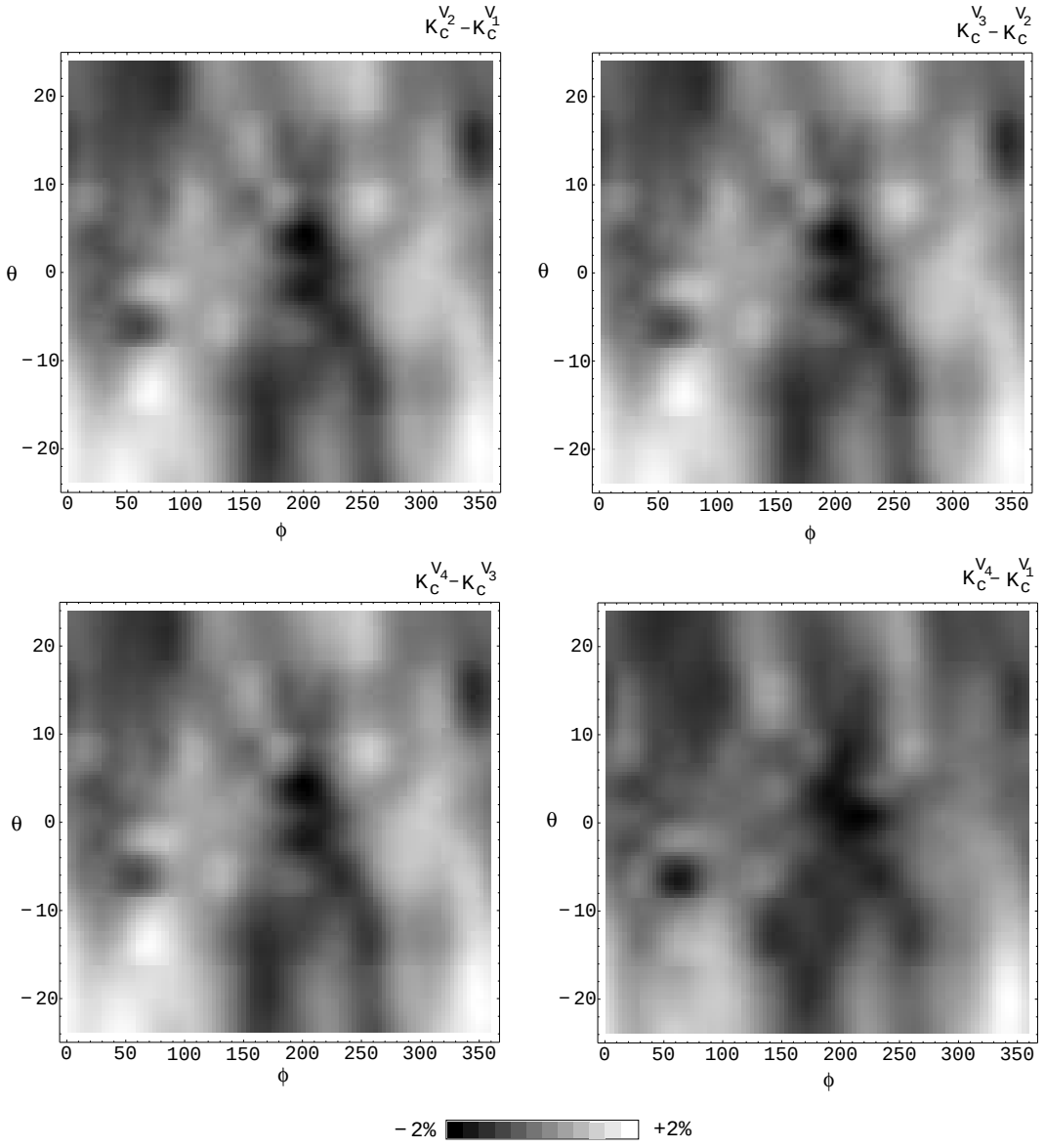

Figure 3.15: $K_c^{V_2} - K_c^{V_1}$, $K_c^{V_3} - K_c^{V_2}$, $K_c^{V_4} - K_c^{V_3}$ and $K_c^{V_4} - K_c^{V_1}$.

kage by the transducers leading to a velocity defect of the true velocity as mentioned in subsection 1.5.2. However, an important difference has to be pointed out since sonic anemometer literature refers only to a velocity attenuation instead of velocity excess as in Hanafusa et al. (1980), Coppin and Taylor (1983), Wyngaard and Zhang (1985), Kaimal et al. (1990), or in a reference book by Kaimal and Finnigan (1994). For instance, we encounter areas where the velocity is overestimated by 5% for a null inclination and 200° azimuth (figure 3.12). In fact, the incoming flow is accelerated by the whole assembley, transducer array and suporting arms, and that is also relevant for measurement correction.

The correction of the measured values is performed according to equation (3.4), where the measured components are multiplied by the correction matrix and then added to the offset component of the velocity at a given azimuth. A table for each azimuth dependent coefficient was constructed with 90 intervals of 4 degrees each, table 3.5.

$$\begin{Bmatrix} u_c \\ v_c \\ w_c \end{Bmatrix} = \begin{bmatrix} a^{\phi}_{uu} & a^{\phi}_{uv} & a^{\phi}_{uw} \\ a^{\phi}_{vu} & a^{\phi}_{vv} & a^{\phi}_{vw} \\ a^{\phi}_{wu} & a^{\phi}_{wv} & a^{\phi}_{ww} \end{bmatrix} \times \begin{Bmatrix} u_m \\ v_m \\ w_m \end{Bmatrix} + \begin{Bmatrix} u^{\phi}_{off} \\ v^{\phi}_{off} \\ w^{\phi}_{off} \end{Bmatrix} \tag{3.4}$$

Table 3.5: Correction table and coefficients for 4° intervals of the azimuth ϕ according to equation (3.4).

ϕ	[0, 4°[	[4, 8°[	...	[148, 152°[	...	[352, 356°[	[356, 360°[
a^{ϕ}_{uu}	0.984	0.989	...	0.958	...	0.979	0.982
a^{ϕ}_{uv}	-0.037	-0.057		-0.030		-0.067	-0.076
a^{ϕ}_{uw}	-0.129	-0.114		-0.004		-0.157	-0.147
a^{ϕ}_{vu}	-0.026	-0.021		-0.001		-0.020	-0.020
a^{ϕ}_{vv}	1.134	1.049		1.022		1.054	1.024
a^{ϕ}_{vw}	0.147	0.149		-0.004		0.163	0.147
a^{ϕ}_{wu}	-0.021	-0.020		-0.064		-0.018	-0.018
a^{ϕ}_{wv}	0.116	0.090		-0.048		0.078	0.098
a^{ϕ}_{ww}	1.047	1.033		1.015		1.049	1.051
u^{ϕ}_{off}	0.025	0.005		0.045		0.043	0.027
v^{ϕ}_{off}	-0.042	-0.056		0.000		-0.046	-0.065
w^{ϕ}_{off}	-0.001	-0.010	...	-0.003	...	-0.030	-0.014

We analyse again the sonic velocity based in the corrected u_c, v_c and w_c components for V_4 (figure 3.16) and the offset drops to ±2% of the reference velocity. From θ ranging from ±5°, the sonic is underestimating the flow at most by 2%, and for θ ranging from 5 to 20° the sonic is overestimating the flow by the same amount. For large inclinations, the

correction is again negative but the distortion from the transducers are excluded from the measurements. The same type of picture is obtained for the other velocities, V_1, V_2 and V_3, and we refrain from presenting them.

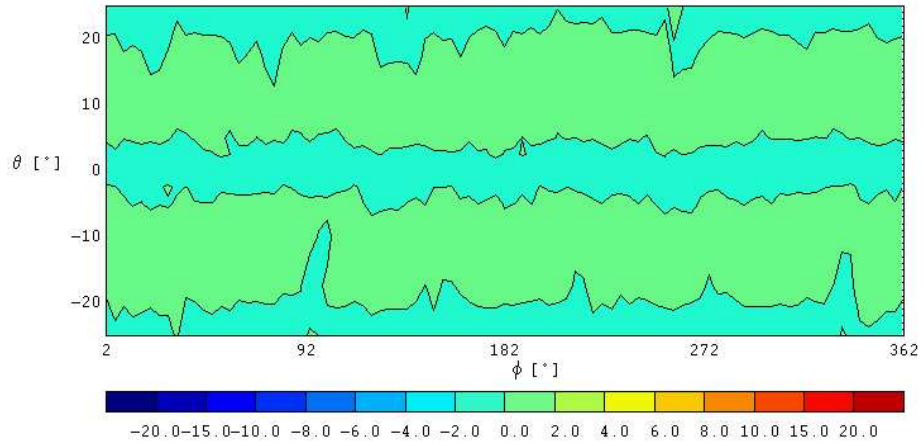

Figure 3.16: $V_{sonic} - V_{rotor}$ [%] after aplying the correction matrix for V_4.

Table 3.6 summarizes the mean, maximum and minimum offset of $V_{sonic} - V_{rotor}$ after correction. The 95% experimental uncertainty obtained from figure 3.6 is recalled and we conclude that the corrected measurements are in a smaller interval, where the absolute maximum is 2.7% for a 3.6% uncertainty. Considering just the distortion analysis, we verify that the correction for V_1 is the less effective with areas where the velocity defect is 2.7% and the overestimation is 1.6%. However the mean deviation drops to -0.1%. The same mean velocity differences are achieved for V_2 while for V_3 and V_4 the mean difference is null and the extreme values range between -1.7 to 1.1%. Assuming that for wind energy purposes velocities below 4 ms^{-1} are close to the cut-in limit of the wind turbines, or the energy conversion is residual, sonic measurements hardly will be biased after the transducer shadow effect corrections.

Another important feature is the amount of corrections to be done. Low velocities require larger corrections, an expected feature once the boundary-layer around the transducers decreases as Re increases, what leads us to another problem: how much should the sonic measurements be corrected under real atmospheric conditions? Turbulence levels inside a wind tunnel test section are lower than under atmospheric conditions. The separation bubble around each transducer tends to diminish as Reynolds increases and thus under real atmospheric conditions smaller corrections may be required. This question will most likely be answered when the flip and rotating tests are performed under real atmospheric conditions, as mentioned in section 1.2. Based on the lack of foundation on the use of a dumping factor in the correction matrix for this unit, we maintain the existing correction matrix because it eliminates the footprint of the transducers from the velocity measurement.

Table 3.6: Limits and mean results of $V_{sonic} - V_{rotor}$ [%] after applying the correction matrix into the sonic measurements.

	Max [%]	Min [%]	$Mean$ [%]	$U_{95\%}$ [%]
V_1	1.5	-2.7	-0.1	3.6
V_2	1.6	-0.7	0.1	2.7
V_3	1.1	-1.7	0.0	2.9
V_4	1.1	-1.7	0.0	2.8

3.3.2.2 Sonic Temperature

Last section analysis was repeated for the sonic temperature measurements now including the flow heating due to friction during each run. Table 3.7 shows that variations of temperature and relative humidity depend on the velocity of the flow. For the V_1 run, the test section cools down 0.24°C over the whole measurement, while the flow heats by the same amount for V_4. However, we can assume that for each inclination the mean temperature and relative humidity conditions are constant because such 0.24°C variations occur in a group of 11 different inclinations. The temperature and humidity increment for each step, $\Delta T(s_{V_i})$ and $\Delta\psi(s_{V_i})$, are thus 11 times smaller than the overall temperature variation.

Table 3.7: Temperature and humidity evolution at the test section.

	$\Delta T(V_i)$ [°C]	$\Delta T(s_{V_i})$ [°C]	$\Delta\psi(V_i)$ [%]	$\Delta\psi(s_{V_i})$ [%]
V_1	-0.240	-0.022	0.070	0.006
V_2	0.040	0.004	-0.350	-0.032
V_3	0.120	0.011	-1.020	-0.093
V_4	0.240	0.022	-0.950	-0.086
$\overline{x}$	0.040	0.004	-0.563	-0.051

However, the flow conditions have to be considered in spite of the low dependency of the speed of propagation of the sound on the air humidity, see subsection 1.5.4. We recall also that the sonic temperature may be taken as the virtual temperature, i.e. the dry air temperature under the same pressure conditions, and the deviation of the measured acoustic virtual temperature against the real air temperature is linear dependent from the absolute humidity content of the air, equation (1.8), requiring temperature corrections before comparison of results by equation (3.5).

$$T_v = T_{ref}(1 + 0.61q) \tag{3.5}$$

where T_v is the virtual temperature, to be compared with sonic temperature T_s. Temperature measured by the Vaisala TRH probe is assumed T_{ref} and $q = e/p$ is the water vapor pressure by the atmospheric pressure, table 3.1.

Table 3.8: Temperature comparison for null inclination. Corrected temperature from the Vaisala TRH (model HMP 35A-CS107) sensor, T_{ref}, sonic temperature T_s, instruments offset $T_{ref} - T_s$, sonic temperature standard deviation $\sigma(T_s)$, sonic temperature deviation from the reference value, $\Delta\epsilon(T) = (T_s - T_{ref})/T_s$ and 95% uncertainty of T_s.

	T_{ref} [°C]	T_s [°C]	$T_{ref} - T_s$ [°C]	$\sigma(T_s)$ [°C]	$\Delta\epsilon(T)$ [%]	$U_{95\%}$ [°C]
V_1	26.15	23.96	2.20	0.04	-0.73	0.07
V_2	26.18	23.91	2.27	0.05	-0.76	0.10
V_3	26.27	23.91	2.36	0.06	-0.79	0.12
V_4	26.42	23.93	2.49	0.07	-0.83	0.15
$\overline{x}$	26.26	23.93	2.33	0.06	-0.78	0.11
$\sigma(x)$	0.12	0.02	0.13	0.01	0.04	0.03

The 4 runs in the test section were made under different velocities varying from 4 to 16 ms^{-1}. For accurate temperature measurements the velocity in the tunnel should maintain while different temperatures were imposed to the flow. That was not possible therefore temperature comparison for wider limits than the presented in table 3.1 are not possible. Alternatively we present in table 3.8 the comparison for the reference instrument temperature, T_{ref}, against the sonic temperature T_s. The values are already corrected for moisture and correspond to the null inclination case. Table 3.8 presents also the offset $T_{ref} - T_s$, standard deviation of the sonic temperature $\sigma(T_s)$, deviation from the true temperature value defined as $\Delta\epsilon(T) = (T_{ref} - T_s)/T_{ref} \times 100$ and the 95% experimental uncertainty $U_{95\%}$ of the sonic temperature.

The mean offset is 2.33°C but a linear correlation with velocity provide an offset of 2.08°C to a slope adjustment of 0.025 with $R^2 = 0.973$. This means that the instrument offset increase by 0.025°C for a velocity increment of 1 ms^{-1}. It is a temperature measurement contamination by the velocity field but that can be neglected for almost all engineering purposes. That is true also for standard deviation where the slope is 0.026°C/ms^{-1} with $R^2 = 0.997$, or $\Delta\epsilon$ slope that equals to 0.8%/ms^{-1} with $R^2 = 0.991$, or uncertainty slope of 0.007°/ms^{-1} with $R^2 = 0.999$. The increase of 0.3°C observed in T_{ref} is not accompanied by T_s that mantains an almost constant value, and we observe that such increase is hardly followed by a $\Delta\epsilon$ increase. That is because $\Delta\epsilon$ is referenced for absolute temperature so the deviation is reduced to -0.8%.

Defining Kc_T the same way as the velocity K_c in equation (3.3), and with the Vaisala

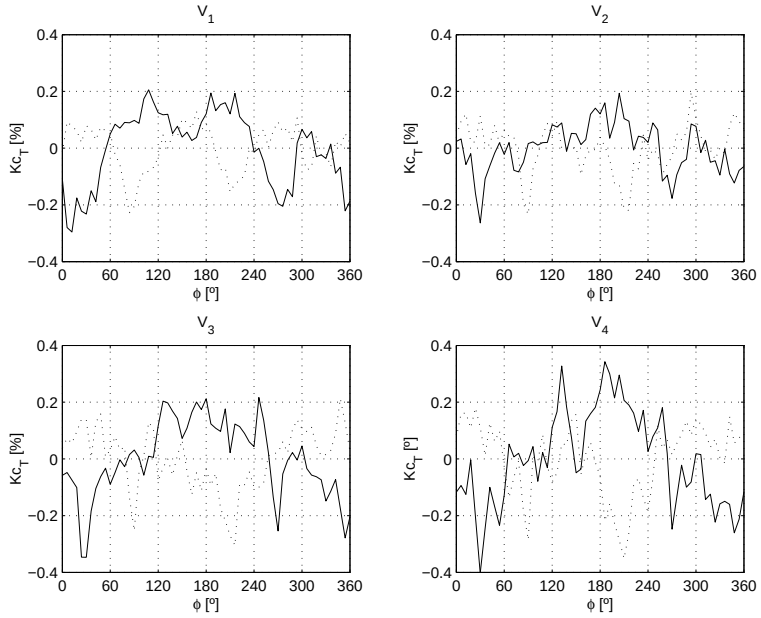

Figure 3.17: Kc_T for inclination $\theta_1 = -25°$ and $\theta_{11} = +25°$, continuous and dotted lines respectively.

TRH (model HMP 35A-CS107) as the reference instrument, we verify from figure 3.17 that Kc_T evolves similarly for each inclination. For instance, for θ_1 the temperature deviation is negative from 240 to 60° and positive from 60 to 240°, and for the first two velocities the curve is smoother, although the maximum Kc_T for V_1 and V_2 is 0.1% lower than for V_3 and V_4. Nevertheless, the overall Kc_T values are small, and less than 0.4% for V_3 and V_4.

By the analysis of the sonic temperature autocorrelation function at inclinations of -25 and +25° for 4 velocities we verify that there is a periodic behavior of the sonic temperature at V_1 (figure 3.18), where the larger oscillations are associated with positive inclination (descending wind). The oscillation is linked again to the geometric array configuration, with a 60° shift from top and bottom transducers. This effect propagates, for the +25° case, also to V_2, now with a 30° shift, the next harmonic of the first oscillation. As for the negative inclination (ascending wind) at V_2, this periodic effect disappears. For higher velocities and negative inclination there is no oscillation. For +25°, the autocorrelation coefficient suggests that still some oscillation is present at V_4 for a 60° shift, although not as clear as the V_1 and V_2 cases.

For the null inclination case, figure 3.19, the indication of an oscillation at V_1 is not totally clear, where the figure suggests the presence of an 30° oscillation superimposed by high frequency noise. Compared to figure 3.18, the autocorrelation coefficients are 50% smaller. The same features are found at V_3, in this case without the noise what leads to the conclusion that, at V_3, a 30° oscillation may be present as a consequence of a 2nd harmonic of the array configuration. Finnaly, for V_2 and V_4 cases, the autocorrelation coefficients do

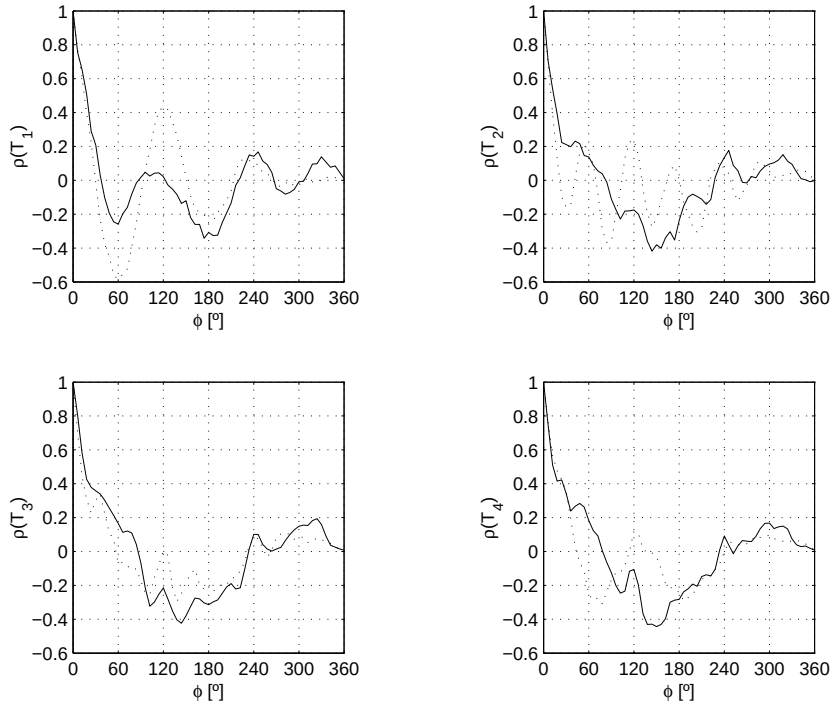

Figure 3.18: Sonic temperature T_s autocorrelation for inclinations $\theta_1 = -25°$ (continuous lines) and $\theta_{11} = +25°$ (dotted lines). Left top to bottom right refers to flow velocity from V_1 to V_4.

not seem to suggest any oscillating behaviour of the sonic temperature measurements.

The power spectral density $PSD(T_s)$ of the sonic temperature highlights the temperature measurements results. The sonic rotation is clear at 0.2 Hz peak and decreases as the velocity increases, disappearing for V_4, figures 3.20a to 3.20d. An higher frequency harmonic close to 2.1 Hz is also present for V_1 and V_2, and is almost negligible at V_3 and V_4. There is an important peak at 8.1 Hz present at all velocities, which may be associated with the transducer array once it approximates to 3×2.7 Hz. Here the 2 Hz natural harmonic of the 0.2 Hz rotation frequency is not so well captured once the upper and lower transducers are not vertically aligned when the sonic path is upstream. Besides these peaks, for other frequencies the spectra resembles the normal white-noise spectra. The singularity detected at 8.1 Hz in the temperature power spectra (figure 3.20) is also linked to the transducer array design that should be accounted in the field measurements. Contrary to the velocity transducer shadow effect, no correction due to transducer shadow effect are required for temperature corrections because in spite of the detection of periodicity on the signal, Kc_T rounds 0.3%. This periodicity smooths down with increasing Re due to better mixing of the flow. On the other hand, the data dispersion increases with the flow velocity affecting the accuracy of the instrument and increasing the experimental uncertainty in 0.8°C from V_1 to V_4. Sonic temperature offset of 2.08° was determined and

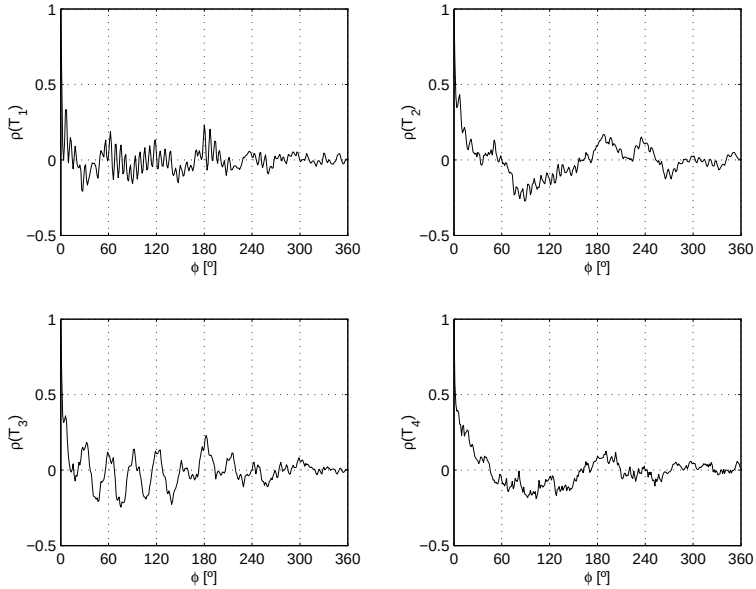

Figure 3.19: Sonic temperature T_s autocorrelation for null inclination $\theta_6 = 0°$ and velocity to V_1 to V_4 (top left to bottom right).

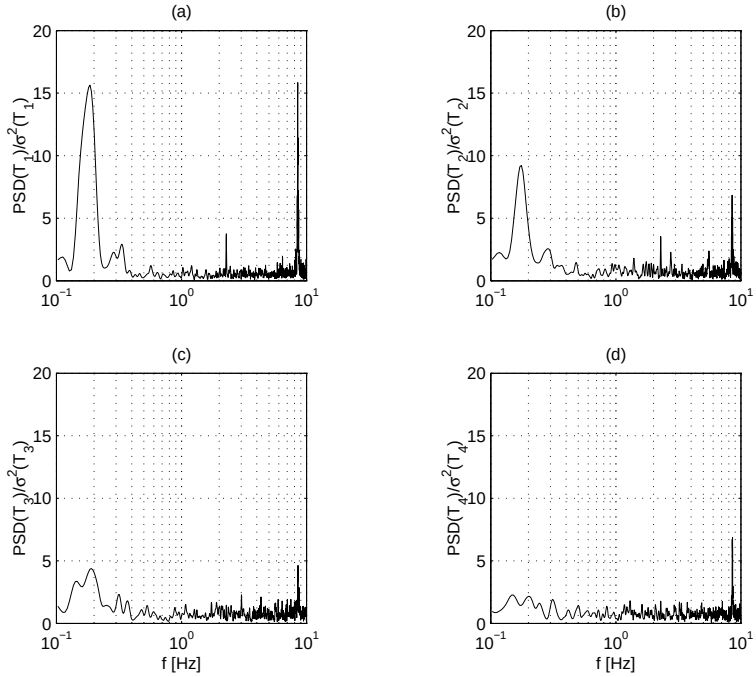

Figure 3.20: Sonic temperature power spectral density. (a) to (d) correspond to V_1 to V_4 respectively. The inclination is null ($\theta = 0°$).

is also velocity dependent, $0.025°\mathrm{Cm}^{-1}\mathrm{s}$, but that may be neglected for general purposes. We thus assume that the transducer shadow effect in temperature measurements for this instrument are limited and independent of velocity, contrary to the accuracy that decreases due to velocity contamination.

3.3.3 Young 344 case

The experimental procedure was repeated for the Young 344 sonic with good results at a first glance. The velocity measurements agree with the wind tunnel velocity as depicted in figure 3.21. The distribution from V_{young}/V_{rotor} closes to a gaussian distribution, where the 1st to 4th statistical moments are respectively 1.003, 0.0100, 0.156 and 3.030.

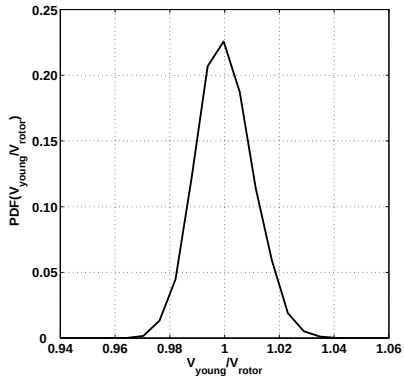

Figure 3.21: Young 344 relative velocity V_{young}/V_{rotor}. 1st to 4th moments are 1.003, 0.010, 0.156 and 3.030.

In spite of these early indicators, during the experiment monitorization we observed from the real time logging system that the vertical component of the instrument w was inconsistent for large inclinations, $\theta \geq 5°$. Figures 3.22a to 3.22d presents the relative longitudinal u_{young}/V_{rotor}, transversal v_{young}/V_{rotor}, vertical velocity w_{young}/V_{rotor}, and the relative temperature T^s_{young}/T_{tunnel} measurements for a complete rotation with $\theta = +17.5°$. In figures 3.22a and 3.22b the results present the expected sinusoidal evolution as the sonic rotates along the CNC-NIKKEN axis. However, the vertical component, figure 3.22c, that should maintain near constant value independently of the flow direction, presented an intermittent sign change during the rotation. The temperature, figure 3.22d, did not show any unexpected feature besides the normal T_s/T offset (not corrected for moisture).

When comparing the flow velocity measurement, we take the modulus of each sonic component, wiping out any unexpected sign change, and justifying the close results of the velocity PDF from figure 3.21. When the inclination is small $\theta \approx 0°$, the sine of the flow component closes to null, and the signal switch may be mistaken with turbulence. As the inclination increases, so the vertical component of the flow and the error becomes more

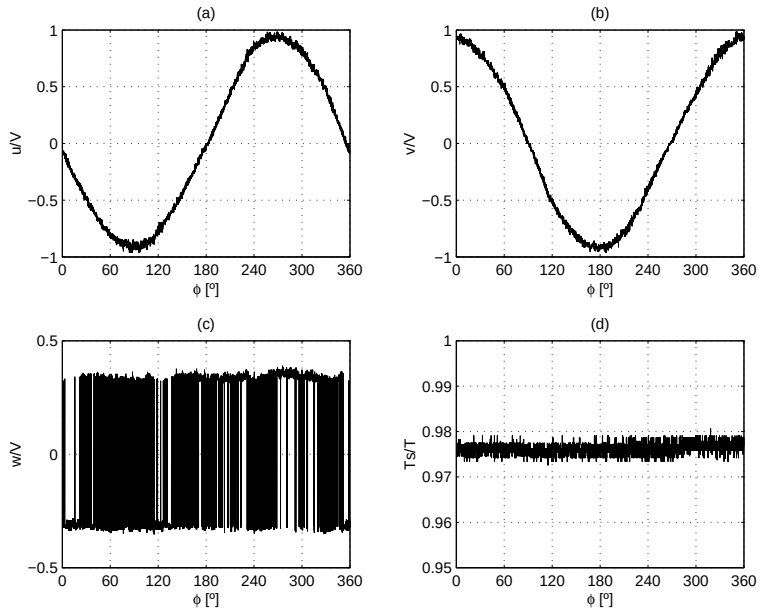

Figure 3.22: (a) Young 344 sonic relative longitudinal velocity, u_{young}/V_{rotor}, (b) relative transversal velocity, v_{young}/V_{rotor}, (c) relative vertical velocity, w_{young}/V_{rotor}, and (d) relative temperature, T_s^{young}/T^{tunnel} during a complete rotation for $\theta = +17.5°$

evident. We may exclude a hardware problem once the modulus of the vertical component is correct, which leads to a software error.

The Young 344 sonic presented a non-orthogonal transducer array. Therefore a transformation matrix existed, managed internally by the manufacturer software to convert the measurement to an orthogonal reference frame. This transformation matrix had a glitch in a sine sign what led to the odd evolution at figure 3.22c. This problem was reported to the manufacturer (Ribeiro, 2001) who agreed with the diagnosis and corrected the glitch. However, the tests from this unit were aborted and there was no more information on this instrument.

3.4 Conclusions

A Metek sonic anemometer (model USA 1) was calibrated in a large wind tunnel and the transducer shadow effect mapped for 4.2, 8.7, 12.0 and 16.1 ms^{-1}. For each velocity, the measurements comprised of a a sonic complete rotation along the azimuth and inclination θ ranging from -25 to 25°. We identified:

1. Flow acceleration and deceleration areas that were bounded by the acoustic path from each pair of transducers associated with the array blockage of the flow. The velocity defect for $\theta = \pm 25°$ closed to 12%. The sonic array also presented acceleration regions between the transducers that originated measurement differences up to 5% for $\theta = \pm 25°$. As the sonic inclination decreased, $\theta \approx 0°$, these differences were reduced to values around 2%.

2. Wind velocity distortion maps for 4 different velocities differed less that 2%. A single correction based in equation (3.4) could correct the measurements to a mean velocity difference from -0.1 to +0.1% for 4.2 and 8.7 ms^{-1}. For velocities above 8.7 ms^{-1} the mean difference after correction was null.

3. The effects of the array geometry in the power spectral density were smoothed down as the flow velocity increased. This effect was associated with the reduction of the boundary-layer around the transducers as Re increased.

4. The transducer shadow effect affected the sonic temperature measurement within a $\pm 0.3\%$ range, thus the temperature measurements were not corrected.

5. In the temperature measurements the power spectral density showed the influence of the geometry array in a higher harmonic (8.1 Hz) requiring caution in spectral analysis of parameters that are temperature dependent.

We also concluded that the correlation of the mean velocity measured by the sonic against the Meteolabor (model ONZ) rotor anemometer was $R^2 = 1$. On the other hand, temperature measurements presented an offset of 2.08°C with velocity dependence of $0.025°C/ms^{-1}$, which can be neglected.

The knowledge of the Metek (model USA-1) sonic anemometer enable its use with confidence in turbulence measurements made in complex terrain as described in the next 2 chapters.

Chapter 4

Complex terrain - Case I

Abstract

Sonic and cup anemometer measurements were made on the nacelle of a wind turbine located in a coastal area of Madeira Island to investigate possible causes for turbine performance below expected. The wind flow proved to be very complex with large unsteadiness. By conditioning the analysis to the data that presented acceleration values below 2 ms^{-2} we obtained a 45-min data subset, though being non-stationary, it was the steadier obtained from the whole data series. Wavelet and spectral analysis revealed the existence of periodic events with an oscillation period from 2 to 3-min. From the acceleration criteria a 3 hr data subset that presented strong transient characteristics was also analysed with the same tools. The same events were detected from wavelet analysis although superimposed by larger scale events.

To increase statistical significance of the results, ogive function was applied and defined a time block of 40-min for the analysis of the whole series. From PDF intermittency methods we detected 3 types of flow: Type A, a steadier one (9.4% of the measurements) with no reverse flow; Type B, a moderate to strong flow (84.3% of the measurements) where up to 15% of the flow is reversed; and Type C, the most complex flow, where the reverse flow surpassed 15%. Flow visualization, spectral, wavelet and quadrant analyses were applied for each flow type unveiling different features. It was also found that flow unsteadiness was from gusts, sweeps and ejections. Sweeps and gusts dominated Type B flow and ejections Type C. The events changed in scale when mean advection conditions were altered and were the cause of large vertical velocity components (-18.75 and +22.29 ms^{-1}). Consequences for measurements were relevant: mean sonic corrections for sonic velocity measurements were 3.23% and comparison of sonic against cup anemometer showed a 2.3% overestimation from the latter due to large flow inclination and unsteadiness of the flow. It was also revealed that

events with period of 2.9-min coexisted persistently with coherent structures. Comparison with simulation results by Palma et al. (2002) with VENTOS® software confirmed that those events were eddies in the vicinity of the turbine, and the difference from measured against simulated oscillation period was 14%.

4.1 Introduction

We report sonic and cup anemometer measurements made at São Lourenço wind farm (Caniçal), in Madeira Island, in a region close to a cliff at 100 m altitude in a peninsula, exposed to incoming flow from the ocean.

Low productivity, abnormal vibration and fatigue in certain machine organs lead to the investigation of the flow at the site. The following questions were addressed:

1. Quantification of sonic anemometer measurements corrections by equation (3.4).
2. Description of mean and turbulent wind fields with sonic instantaneous values and with 10-min averages considering the stationarity of the wind field (International Energy Agency, 1990; Pedersen et al., 1999).
3. Comparison of sonic against cup anemometer measurements.

The complexity of the flow has consequences to sonic and cup anemometer measurements. Sonic transducer shadow effect originate a mean velocity correction of 3.23% and due to large turbulence intensity and gust factors cup anemometer deviates from sonic measurements by 2.3%. However, the major set-back refers to the statistical unsteadiness of the data, impairing traditional statistical and spectral analysis based on FFT algorithms for the detection of isolated events.

The flow unstationarity lead to the adoption of two different methodologies for identification of a smaller data set that could be analysed by conventional methods. Data sub-sets were selected by visual inspection and by acceleration criteria. Visual inspection proved to be unfruitful but using the acceleration criteria we obtain a 45-min data set with steadier wind that was analysed by spectral and wavelet methods.

Based on the ogive function for the identification of stationary data sets a time interval of 40-min, i.e. to 2.3 times the integral time scale of the flow was also identified. A second type of flow analysis was based on 32×40-min time intervals with techniques such PDF intermittency, flow visualization, spectral, wavelet and quadrant analysis to increase the statistical significance of the results.

Three types of flow were identified and independently analysed: an almost steady flow corresponding to 9.4% of the measurements, a moderate to strong wind, corresponding

to the more frequent type of flow at the site, 84.3%, where up to 15% of the flow is reversed, and the most complex flow, where the reverse flow surpasses 15%. These flow types were analysed with wavelet and quadrant analyses techniques showing the existence of larger events, sweeps, ejections and gusts, that coexisted either simultaneously or not with periodic eddies in the vicinity of the measuring point.

The results from the measurements were compared with independent flow simulations made by Palma et al. (2002) with VENTOS® software, that also showed the existence of two large eddies in the wind turbine area created by a nearby mountain range. Measurement comparison against simulation was possible for the steadier type of flow with a close agreement on the oscillation periods identified in the simulation, 2.9 measured against 2.5-min event.

However, measurements indicated that the flow was more complex than predicted by the simulations due to unstationarities of the flow field. Measurements showed a dynamic reshape and periodicity changes of the events due to changes on the energy input of the flow. The wind farm was removed from the site after the identification of these flow phenomena.

Chapter outline

Site and experiment descriptions are in section 4.2. The results from transducer shadow effect corrections are also in this section. Results and analysis are in section 4.3. This section is divided in 8 subsections: the first two show the mean and turbulent flow at the site and the comparison of cup against sonic anemometer (subsections 4.3.1 and 4.3.2). The application of acceleration criteria and ogive function are in subsection 4.3.3 and the analysis of the detected data sets is in subsection 4.3.4. The analysis here is extended to 2 data sets and to the whole series: a stationary and an highly unstationary subsets, named Period A and B, where flow visualization, spectral and wavelet analyses are applied; and the identification of 3 types of flow from the whole series based in PDF intermittency. The 3 types of flow spectral, wavelet, and quadrant analyses are in subsections 4.3.5 to 4.3.6. The results and analysis is concluded with the comparison of measurement against simulation results from Palma et al. (2002) with VENTOS® software in subsection 4.3.8. A final summary of the conclusions is in section 4.4.

4.2 Experiment description

4.2.1 Site description

Madeira Island is located in the Atlantic Ocean approximately 500 km west of the African coast. The Island is 50 km long–east-west–and 25 km wide–north-south. Caniçal wind farm was located in the east end of the Island, in an isthmus of a narrow peninsula known as São Lourenço Cape. That strip of land is approximately 6 km long by 1000 m wide, narrowing gradually to the cape (figure 4.1). The altitude of the wind farm site varies from 100 to 160 m. The north slope of the terrain is limited by vertical escarpments that drop to the sea from 100 m height. The South slope is smoother with man made platforms of 400 m wide by 200 m long inside the wind farm terrain. The turbines were located close to the escarpments in an attempt to benefit from northerly wind, figure 4.2.

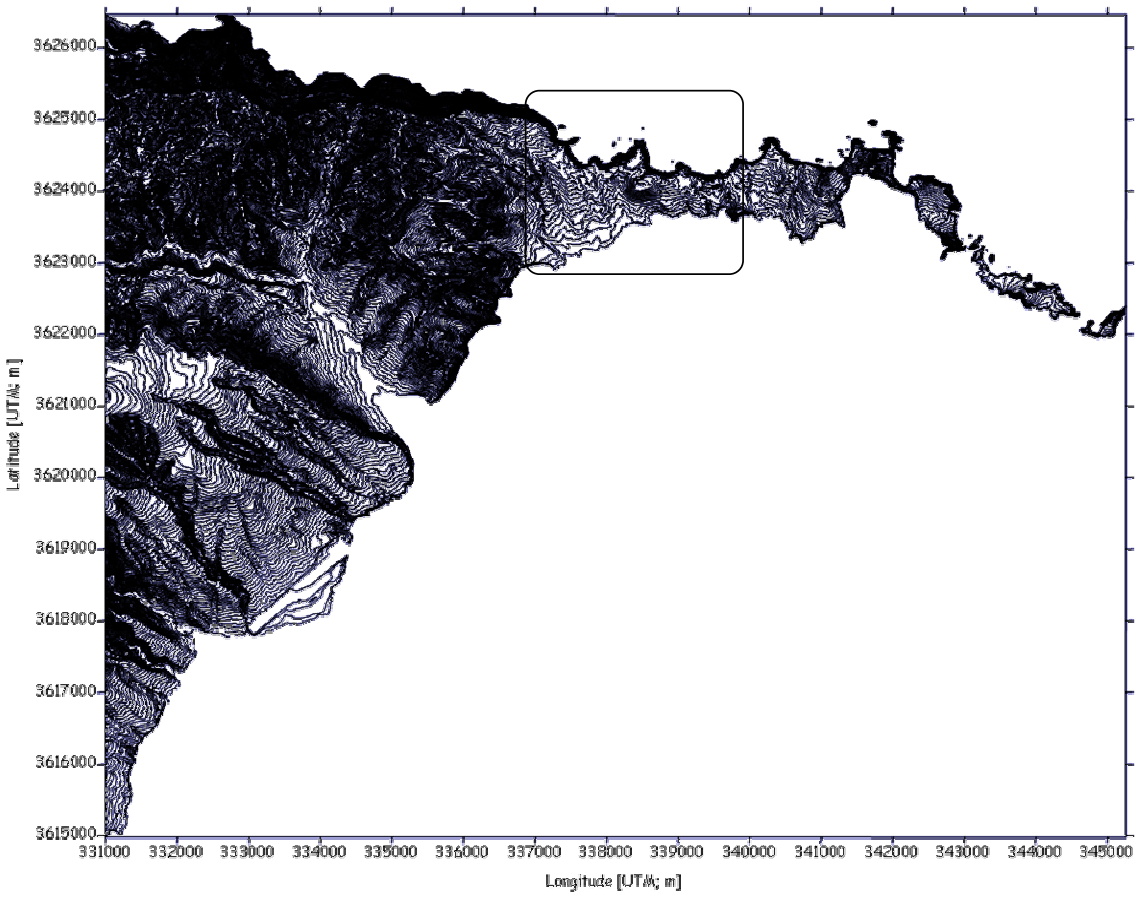

Figure 4.1: São Lourenço cape and the location of the wind farm.

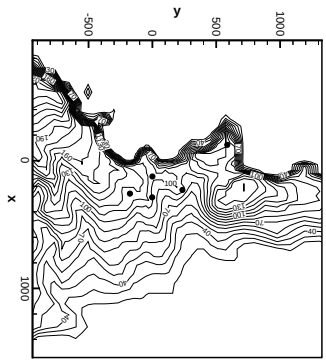

Figure 4.2: Caniçal wind farm. The sonic was installed in the southest turbine (400;0) in $x - y$ coordinates. North direction points with negative x-axis.

The long term data from the airport of Santa Catarina, located 8 km from the site, shows an average wind velocity of 5.6 ms^{-1} at 10 m a.g.l. from the north quadrant for 80% of the time. The moderate to strong winds in that area presented an opportunity for wind conversion systems. A 3 MW wind farm, with 5 turbines of 600 kW nominal power, was installed; however after 3 months of operation, the degradation of some turbine parts due to vibrations and low productivity called for a more detailed analysis than that available at the time when the decision to build the wind park was made.

4.2.2 Experimental apparatus and procedure

The measurement setup comprised an ultrasonic anemometer (Metek model USA-1) and a cup anemometer (NRG model 40). The sonic anemometer described in chapter 3 was installed and leveled in a 2 m boom at the top of the nacelle of the southest turbine (figure 4.2) and the cup anemometer was placed at the end of an arm perpendicular to the main boom one meter below the sonic anemometer to avoid interference between instruments, see figure 4.3. Both instruments were connected to different logging devices: the sonic to a laptop computer and the cup anemometer to a data logger (NRG model 91000 Plus). For lower interference between the turbine and the measurement equipment, the turbine nacelle was downstream aligned with the wind, with the blades in a 'Y' position.

The data collected at a sampling rate of 20 Hz covered the period from 12:35 of 2001 October 10th to 11:35 of October 11th. The total data for the analysis was roughly 22 hours due to interruptions in the sequence for periodic visits for checking instrument and measurement status.

Figure 4.3: Experimental setup. The sonic anemometer METEK model USA-1 was mounted on the top of the main boom, and the NRG model 40 cup anemometer mounted below. The wind vane and anemometer from the wind turbine control system (not used in the experiment) can also be see in the bottom right of the picture.

4.2.3 Corrected against uncorrected sonic measurements

As discussed in chapter 3 the sonic anemometer measurements have to be corrected due to transducer shadow effect and overestimation of measurement due to flow acceleration through the transducer array. The corrections are proposed following equation (3.4). The comparison of the corrected values against measured showed that the corrections will lead to minimum differences in total velocity (figure 4.4a) but larger deviations for the vertical component of the flow (figure 4.4b).

Corrected against uncorrected velocity differences are 2.7% while for vertical velocity they are 6.4%, and in both cases velocity is reduced. This means that measured velocity is overestimated, contrary to the general perception of transducer shadowing as pointed out in section 3.3.2.

The dispersion is also larger for vertical velocity and correlation worse than for total velocity case, $R^2 = 0.913$ against $R^2 = 0.999$ (figure 4.4). The larger dispersion of vertical velocity corrections are most likely due, as we will see in next section, to large vertical

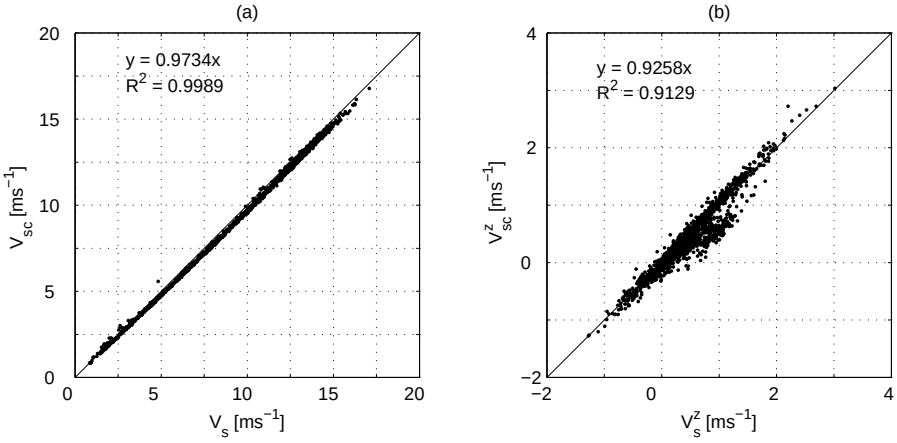

Figure 4.4: Velocity comparison for the measured V_s velocity and corrected sonic velocity V_{sc} (a). Vertical velocity comparison for the measured and corrected sonic velocity (b).

components. The corrections are thus larger and so the differences between the values of measured and corrected.

4.3 Results and analysis

4.3.1 Mean and instantaneous wind fields

The wind was mainly from North quadrant, 77% of the data is in a 30° interval around the North direction, whereas the remaining 23% is scattered in other directions, figure 4.5. The mean horizontal wind was 10.33 ms^{-1} with an ascending mean vertical component of 0.49 ms^{-1}, table 4.1. The whole series presents large values for the standard deviation of the horizontal components, where the series hardly complies with Willis and Deardorff (1976) equation on Taylor's frozen turbulence hypothesis, where $\sigma(V)/\overline{V} = 0.49$. The mean fluctuations on the vertical plane are also large: the mean standard deviation is 2.38 ms^{-1}.

The most striking results, however came from the vertical velocity, with ascending and descending components respectively of 22.29 and 18.75 ms^{-1}. The probability density function of the wind velocity field (figure 4.6a) shows a bi-modal distribution with the main peak for a 13.5 ms^{-1} and a secondary peak close to 7.0 ms^{-1}. The distribution shows that winds over 5 ms^{-1} are predominant, over 87% of the occurrences. A diferent feature is captured by the PDF of the vertical component (figure 4.6b) with a single mode, though with large tail values. The vertical PDF also alerts to the fact that 32% of the measured flow surpasses 20% of the mean horizontal velocity, twice the maximum of the traditional 10% vertical velocity normally considered in wind turbine design.

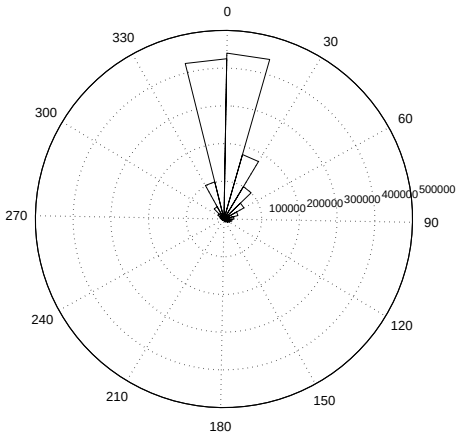

Figure 4.5: Wind rose for Caniçal.

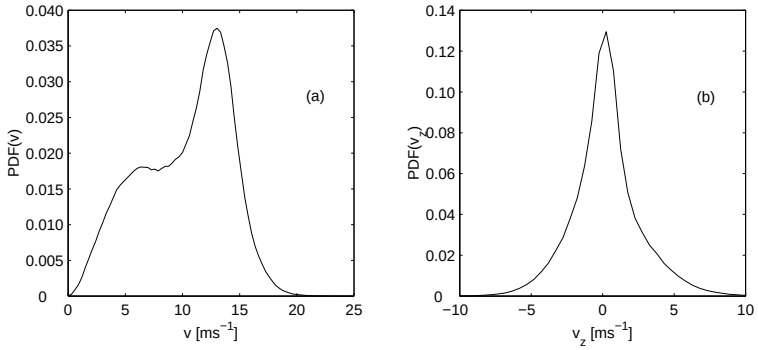

Figure 4.6: PDFs of the horizontal (a) and the vertical wind velocity (b).

Table 4.1: Statistics of the time series from October 10th, 12:35 to 11th, 11:35. 10-min statistics of turbulence intensity it, gust factor G, and turbulent kinetic energy TKE in m^2s^{-2}.

	$\overline{V}$ [ms^{-1}]	$\sigma(V)$ [ms^{-1}]	$sk(V)$	$k(V)$	min [ms^{-1}]	max [ms^{-1}]
$\overline{v}$	10.33	3.94	-0.34	2.22	0.03	29.87
$\overline{v_h}$	9.89	4.29	-0.37	2.10	0.00	28.54
$\overline{v_z}$	0.49	2.38	0.28	4.65	-18.75	22.29
it	0.34	-	-	-	0.10	0.54
G	2.12	-	-	-	1.27	3.78
TKE	16.64	-	-	-	2.40	30.40

Turbulence indicators

Turbulence intensity, $it = \sigma(V)/\overline{V}$, and gust factor, a parameter associated to the acceleration of the flow, defined as $G = max(V)/\overline{V}$, are calculated for 10-60 min averaging intervals and are standard turbulence and gust characterization parameters (Petersen et al., 1998; Burton et al., 2001). These values were calculated for 10-min averaging intervals and are also in table 4.1. Mean turbulence intensity is 0.34, i.e. over 3 times larger than the 0.10 observed in ordinary wind turbine sites. The minimum turbulence intensity was equal to 0.10 while the maximum was 0.54. Mean gust factor G is also large: 2.12. Again, the minimum value observed is close to the expected in values in less complex terrain, while a maximum value of 3.78 shows that the flow during the measurement period was characterized by strong gust conditions. Table 4.1 concludes with turbulent kinetic energy statistics, with mean of 16.64 m^2s^{-2} and standard deviation of 7.43 m^2s^{-2}.

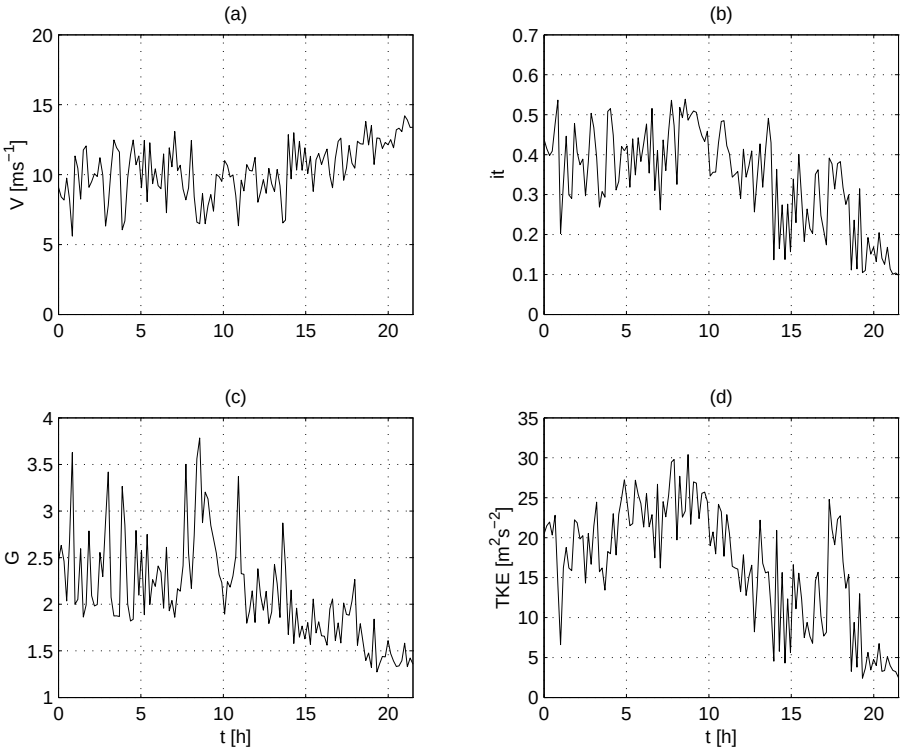

Figure 4.7: Velocity, turbulence intensity, gust factor and turbulent kinetic energy for 10-min periods for the time series from October 10th, 12:35 to 11th, 11:35.

The time series of 10-min averages of velocity, turbulent intensity, gust factor and turbulent kinetic energy are in figure 4.7. Resuming again to turbulent kinetic energy, we verify that the series often surpasses 20 m^2s^{-2} in the first 10 hours with maximum of 30.40 m^2s^{-2}. Turbulence intensity and gust factor (figures 4.7b and 4.7c) were also larger in the first 10 hours of measurement and decreased as the wind flow velocity increased for

more steady conditions: it and G often surpassed 0.50 and 3.5 respectively in the first 10 hours decreasing to values of less than 0.30 and 2.0 for winds over 10 ms^{-1}, figure 4.7a.

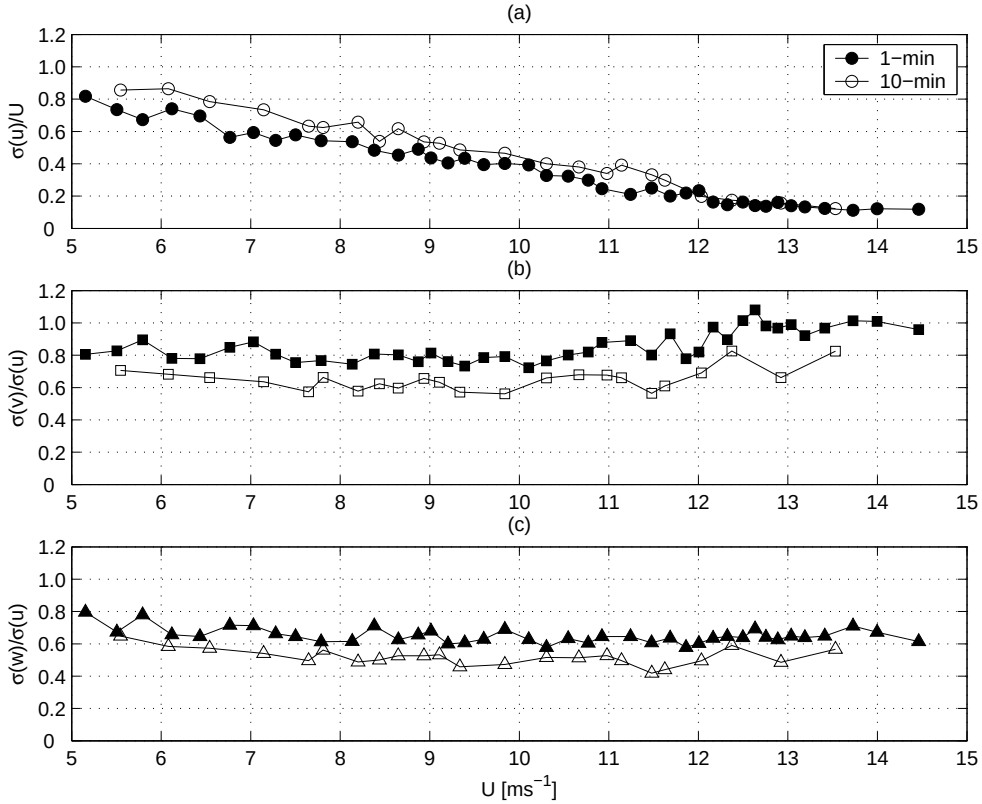

Figure 4.8: Average longitudinal turbulent intensity and turbulent ratios, $\sigma(v)/\sigma(u)$ and $\sigma(w)/\sigma(u)$ for 10 and 1-min intervals (color filled).

We compare the turbulent ratios by velocity class (figure 4.8) after rotating the data set into streamline coordinates. Such rotation was performed according to the procedure in subsection 1.6.3.1 to 1 and 10-min averaging intervals. As expected, longitudinal turbulent intensity decays as wind velocity increases (figure 4.8a), but present large turbulence values: only for velocity above 12 ms^{-1} that longitudinal turbulence is less than 0.20 and 1 and 10-min statistics converge.

The anisotropy of turbulence at the site is confirmed by the turbulent ratios of transversal and vertical components, $\sigma(v)/\sigma(u)$ and $\sigma(w)/\sigma(u)$, at figures 4.8b and 4.8c. Comparing against international standards IEC (1999) we verify that $\sigma(v)/\sigma(u)$ and $\sigma(w)/\sigma(u)$ 10-min averages are not far from flat terrain values, 0.8 and 0.5, being slightly larger for 1-min averages. Relative turbulent ratios are close also to results from other complex sites (Papadopoulos et al., 2001), but because longitudinal turbulence intensity is very large, so are the absolute transversal and vertical turbulence intensities once $it_u = 0.8it_v$ or $it_u = 0.5it_w$.

The velocity spectrum was calculated for the whole period according to the procedure in subsection 1.6.4. From figure 4.9a we verify that the events with larger energy contents are over 50-min periods. The same spectrum is presented in figure 4.9b in a linear scale

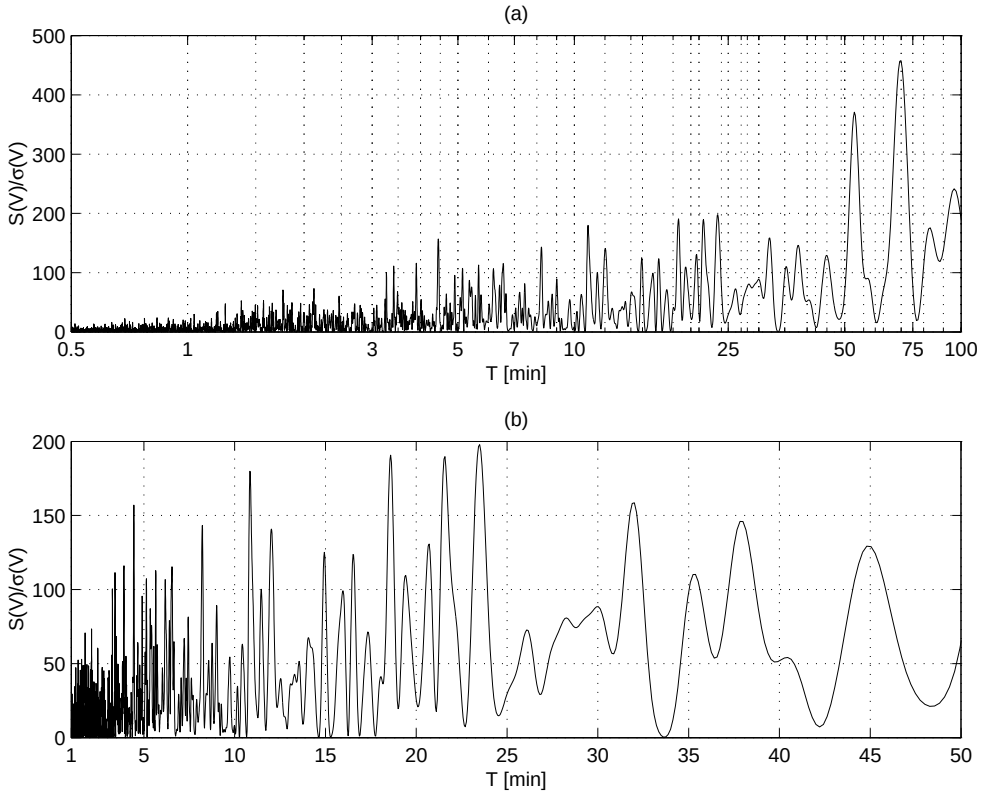

Figure 4.9: Normalized spectrum of velocity at Caniçal (a). Enhancement of the normalized velocity spectrum in a linear scale from 1 to 50-min period (b).

bounded to an interval from 1 to 50-min period. The analysis of the spectrum is difficult because several events present the same energy content in a large range of scales. Note for instance that from periods inferior to 32-min we encounter also events with oscillation periods ranging of 24, 22, 17, 11 and 4-min that have more energy. Closing our analysis into events inferior to 10-min, we observe several peaks that almost match the energy content of the previous peaks.

The presence of several energy peaks in the spectrum at figure 4.9b are a consequence of the unstationarity of the series. There is no clear energy-gap thus a trend removal will not suffice (subsection 1.6.2), for instance, one hour of data will be affected by the scales already identified. The challenge here is obtaining a large set enough that will provide clear spectral information, or accepting the unstationarity and working with different analysis tools. This problem is addressed in section 4.3.3.

4.3.2 Sonic against cup anemometer comparison

The METEK (model USA-1) sonic results were compared with the 10-min average time series produced by the cup anemometer, figure 4.10a. The cup anemometer systematically overestimates the mean wind velocity compared against the sonic. The comparison in figure 4.10b shows that both instruments are correlated: $y = 0.88x + 1.36$ with $R^2 = 0.856$, i.e. with an offset of 1.36 ms^{-1} and a 12% slope difference between instruments. The reasons for such difference was investigated. By comparing instruments divergence, $\Delta\epsilon =$

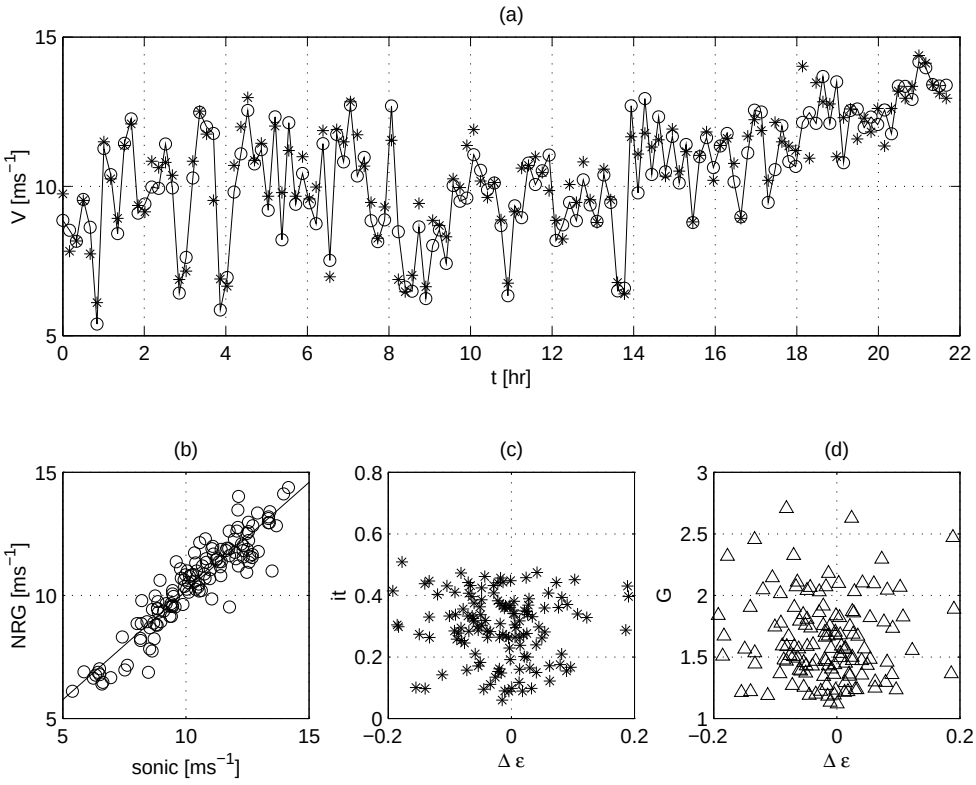

Figure 4.10: Time series of sonic $\circ$ against cup $*$ (a). Sonic against cup anemometer (b). Instruments divergence $\Delta\epsilon$ against turbulent intensity it (c). Instruments divergence $\Delta\epsilon$ against gust factor G (d).

$(V_{sonic} - V_{NRG})/V_{sonic}$, with turbulent intensity and gust factor we found no correlation, figures 4.10c and 4.10d. In fact, $\Delta\epsilon$ includes several sources of error that we may classify as experimental or flow related: experimental sources may be found in the calibration curve of the NRG cup anemometer, once there was no independent calibration besides the one presented by the manufacturer. We may also note that two independent logging devices stored data, without clock synchronization.

Flow related issues are however more likely to be the reason for such discrepancies. Note for instance in figure 4.10a that for velocity decrease the cup anemometer measurement,

in the majority of cases, is larger than the sonic measurement, and for velocity increase cup anemometer often overestimates the sonic measurement. Wyngaard (1981) showed that cup anemometers respond faster to wind speed increases ($u > 0$) than wind speed decreases causing the anemometer to overspeed.

Another flow related issue is the cup anemometer sensitivity to vertical component of the flow. Papadopoulos et al. (2001) showed that for complex terrain the deviation of cup anemometer measurement from reference value varies from 4 to -4% depending on manufacturer for flow inclinations from -10 to 12° (NRG cup anemometer was not referenced). Also Kristensen et al. (2003) shows that in homogeneous and neutrally stratified flow all cup anemometer bias will be of 1% however pointing out that for very complex terrain with strong gusty winds the mean bias tends to be larger.

The mean flow inclination at Caniçal was 4.8°, thus within the reference values from Papadopoulos et al. (2001). Table 4.2 compares the results for two periods separating the sonic velocity into horizontal and vertical components where we observe that cup anemometer overestimates the velocity in just 2.3%, but the horizontal component in 9.4%. The vertical component of the flow for that period is 0.47 ms^{-1}, corresponding to 5.5% of the velocity of the mean flow and to an inclination angle of 3.0°, being coherent with Papadopoulos et al. (2001) results. For steadier wind, the overestimation drops to 0.9% for total velocity while for the horizontal components instruments difference is of 3.5%.

Table 4.2: Sonic and cup anemometer comparison for 2 distinct periods. Total velocity measured by the METEK (model USA-1) sonic anemometer, v, horizontal and vertical plane velocity obtained from the sonic anemometer, v_h and v_z, and mean velocity measured by the NRG (model - 40) cup anemometer v_c for 2 different periods: the 1st related to 10 hr data while the 2nd corresponds to the 12 hr of the more steady flow.

		$\overline{V}$ [ms^{-1}]	$\overline{\sigma(V)}$ [ms^{-1}]	$\overline{it}$	$\overline{G}$
	v	9.71	3.97	0.42	2.43
Sonic	v_h	9.08	4.28	0.49	2.56
	v_z	0.47	2.81	-	-
Cup	v_c	9.93	3.49	0.36	1.82
	v	10.79	2.97	0.29	1.85
Sonic	v_h	10.50	3.20	0.33	1.90
	v_z	0.48	1.85	-	-
Cup	v_c	10.88	2.65	0.25	1.48

The presence of large vertical components also affect turbulence intensity estimates, 0.36 against 0.42 of the sonic (table 4.2), but these differences decrease for a period where the flow is steadier, 0.25 against 0.29. In spite of a clear indication, we have to consider that also overspeeding influences also turbulence intensity estimates. Kristensen (2000) confirms that the asymmetric response of the cup anemometers to increase and decrease in wind speed does not influence the determination of variance or even higher order moments.

However, his results were obtained in flat terrain and assuming isotropic turbulence within Taylor's *Frozen Turbulence Hypothesis*. Yahaya and Frangi (2003) presents results for urban boundary-layer, for a light 3 to 6 ms^{-1} wind with 0.40 turbulence intensity, obtaining mean velocity differences of 6% and variance differences of 15% after spectral correction.

Sampling issues Here we have to consider another source of difference related to different sampling rates of each instrument. Sonic anemometer receives more information by sampling faster, 20 against 0.50 Hz of NRG cup anemometer, thus explaining the large differences in gust factor estimates. For steadier flow, cup anemometer gust factor estimates are closer to sonic.

What would be the differences in estimators if the sonic measure with the same sampling rate as the cup anemometer? We tested two alternatives: cup anemometer with distance constant of 2 to 3 m, corresponding to 0.50 and 0.33 Hz sampling rate. The data series was divided in 40-min blocks, and filtered with and anti-aliasing lowpass FIR filter to simulate cup anemometer measurements (table 4.3). The mean deviation of the longitudinal component is close to 0.1% while the lateral component 0.0% independently of the sampling rate. As the statistical moments increase, the number of points loss by the lower sampling rates are not compensated by the increase in the sample size and therefore the deviation increases. However, the absolute differences of statistical moments for each case (table 4.3) are small indicating that the loss of information did not compromise the statistics.

Table 4.3: Statistics of the simulation for wind vane and cup anemometer measurements at 0.50 Hz and 0.33Hz, $c1$ and $c2$. The reference value is the sonic measurement for each 40-min block and is given by u_s. u and v mean and standard deviation, $min(x)$ and $max(x)$ are in ms^{-1}. The error is calculated according to the following expression, $\epsilon = (u_{ci} - u_s)/u_s \times 100$, whose units are in %.

x	$\overline{x}$	$\sigma(x)$	$sk(x)$	$k(x)$	$min(x)$	$max(x)$
u_s	8.97	5.15	-0.59	2.40	-12.42	26.31
u_{c1}	8.96	5.00	-0.58	2.34	-8.67	20.76
u_{c2}	8.96	4.95	-0.58	2.33	-8.65	20.01
ϵ_{u2-u1}	-0.11	-2.91	-1.69	-2.50	-30.19	-21.10
ϵ_{u3-u1}	-0.11	-3.92	-0.82	-2.64	-30.36	-23.92
v_s	-0.01	2.99	-0.29	3.89	-20.27	17.99
v_{c1}	-0.01	2.67	-0.27	3.67	-11.83	11.84
v_{c2}	-0.01	2.55	-0.24	3.58	-11.49	12.28
ϵ_{v2-v1}	0.00	-10.70	-6.90	-5.66	-41.64	-34.19
ϵ_{v3-v1}	0.00	-14.72	-17.24	-7.97	-43.32	-31.74

Disregarding vertical velocity component, similar results to the presented in this chapter may be obtained by measuring the flow with cup anemometers with a different logging scheme, for instance by keeping all 0.5 Hz data instead of 10-min averages.

4.3.3 Ways to extract stationary data sets

In order to extract more information from the data, statistical convergence tests were performed to establish a mean time where the series maintain its mean and variance constant. Such mean time was not encountered for data subsets ranging from 10 to 100 min. We obtain 150% error for the variance for a 10-min time interval and the mean error converges to values lower than 10% for 100-min time interval while variance mantains 100% error for periods larger than 200-min. The flow is unsteady and that fact inhibts sectioning the data blindly into 10, 30 or 60 equally spaced time intervals without any further consideration on what is being lost during the process.

We present two alternative approaches to overcome this problem: detecting a time series that approaches stationarity by the acceleration criteria or determining the time required by the ogive function to converge. Both paths are explored in the following subsections.

4.3.3.1 Acceleration criteria

In a turbulent flow, for the flow velocity to be constant the acceleration must be null within a specified time interval. The acceleration of the flow was calculated based in 3 time intervals, 600, 60 and 1 s conditioned to an acceleration limited from 1 to 2 ms^{-2}. Table 4.4 shows the fraction of the time series that comply with the criteria, for instance, 63.7% of the whole series acceleration is lower than 1 ms^{-2} for a Δt of 1 s. For a Δt of 60 s only 33.1% of the data presents acceleration inferior to 1 ms^{-2} but this condition was not hold for periods longer than 7 minutes. The relaxation of the criteria to the modulus of 1.5 ms^{-2} allowed one period of 31 minutes, and for 2 ms^{-2} the time interval increased to 45 min.

Table 4.4: Fraction of that data series f^a that comply with the acceleration criteria for different Δt's.

a $[\mathrm{ms}^{-2}]$	$f^a_{\Delta t_{600s}}$	$f^a_{\Delta t_{60s}}$	$f^a_{\Delta t_{1s}}$
$\leq \lvert 1.0 \rvert$	0.117	0.331	0.637
$\leq \lvert 1.5 \rvert$	0.582	0.561	0.706
$\leq \lvert 2.0 \rvert$	0.727	0.352	0.815

We selected the time interval from 20.7 to 21.5 hr, named period A, which acceleration was inferior to 2 ms^{-2}. Figure 4.11 shows temporal evolution of the flow velocity for 1-min average and the acceleration in the same interval.

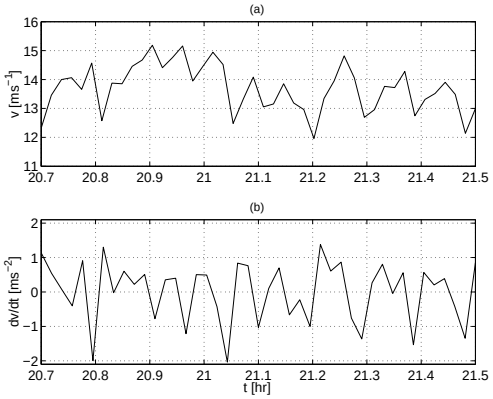

Figure 4.11: (a) Wind velocity over the selected period A – 1-min average, from 20.7 to 21.5 hr. (b) Acceleration of the flow based on the 1 minute average.

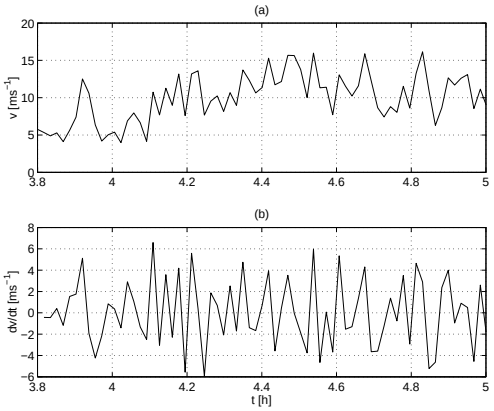

Figure 4.12: One minute average of the wind velocity field and the acceleration of the flow corresponding to period B.

From the acceleration criteria another data set was selected, now looking for a unsteady set with high turbulence. The criteria was selecting data where the acceleration of the flow exceeded 2 ms^{-2}. Figure 4.12 present the time series and the acceleration of the wind velocity field of Period B. The time was from 3.8 to 5.5 hours, corresponding to 108 minutes of data. Again, the criteria had to be relaxed in order to obtain such long number of continuous points. From the wind velocity field picture, it is possible to observe the existence of abrupt changes in the wind velocity modulus, increasing from 5 to 16 ms^{-1} in few minutes, for instance close to hour 4. Those abrupt changes are confirmed by the flow acceleration picture, presenting often values that exceeded 6 ms^{-2}.

The acceleration criteria lead us to two data sets: one as close to stationarity as one could obtain from such data set, named Period A, and another named period B, with large velocity changes due to turbulence.

4.3.3.2 Ogive function

From the acceleration criteria we obtained a 45-min data set (Period A), but that may not be long enough to include statistically significant amount of events we are trying to investigate. We recur thus to the ogive function to establish a a standard time interval enabling an evaluation of the whole data set. The series was rotated into mean streamline coordinates and the mean removed from u, v and w in order to bring the low-frequency end to zero. The uw cospectum and respective ogive (figure 4.13a and 4.13b) shows the existence of several energy peaks of the same magnitude for events with periods from 3.0 to 11-min. Lower energy peaks are present also associated with 20 and 50-min events while the larger peaks are from 50 and 70-min events. From the analysis of figure 4.13b we verify that the ogive converges only after 300-min, but focusing into the time interval from 10 to 100 min, figure 4.13c, we observe that for 40-min time interval the ogive is constant. This is a suitable interval because it is long enough to include a statistical significant amount of events from 2 to 10-min period but is short enough to exclude all mesoscale events.

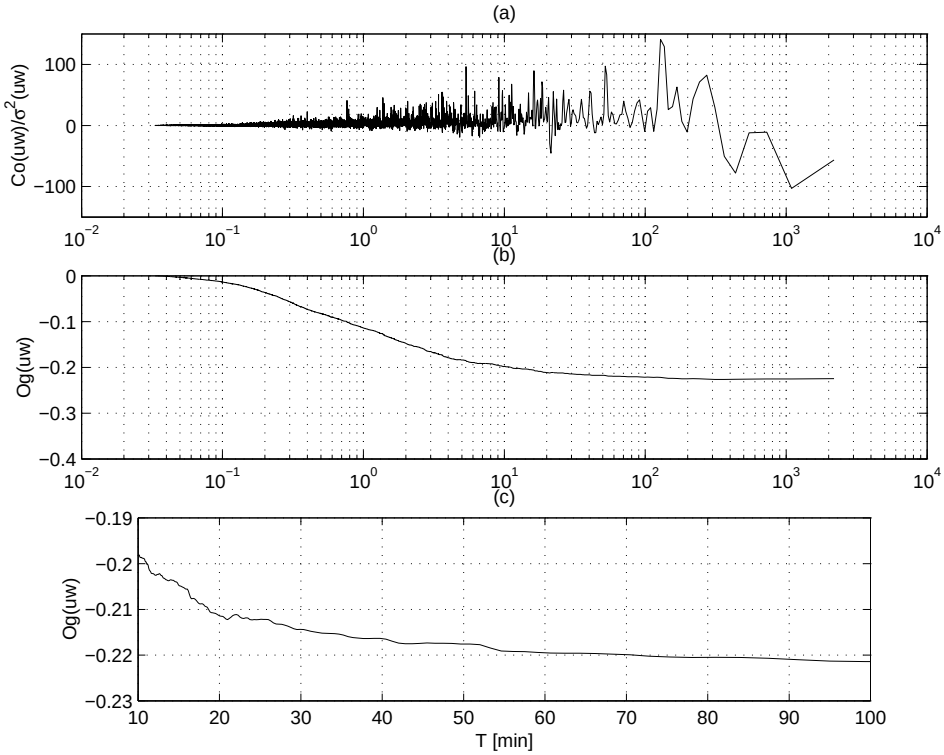

Figure 4.13: Momentum flux cospectra (a), ogive of the momentum flux (b) and ogive function in a linear scale for the interval between 10 to 100-min (c).

After defining the 40-min as the reference time interval, the data was rotated into streamline coordinates along an independent set of rotation angles for each time interval. The convergence of each set was verified by the convergence of the integral time-scale of the

total velocity V and streamline velocity u for each interval. We build from the convergence value of each set an integral time-scale distribution, table 4.5, where we verify that both V and u converge in average from 17.6 min and 15.1 min respectively.

Table 4.5: Integral time-scale distribution for the 32×40-min intervals of V and u.

τ	$\overline{\tau}$	$\sigma(\tau)$	$sk(\tau)$	$k(\tau)$	$min(\tau)$	$max(\tau)$
	[min]	[min]	-	-	[min]	[min]
V	17.56	1.14	0.27	2.30	15.44	19.77
u	15.12	2.89	-0.69	3.78	7.23	19.72

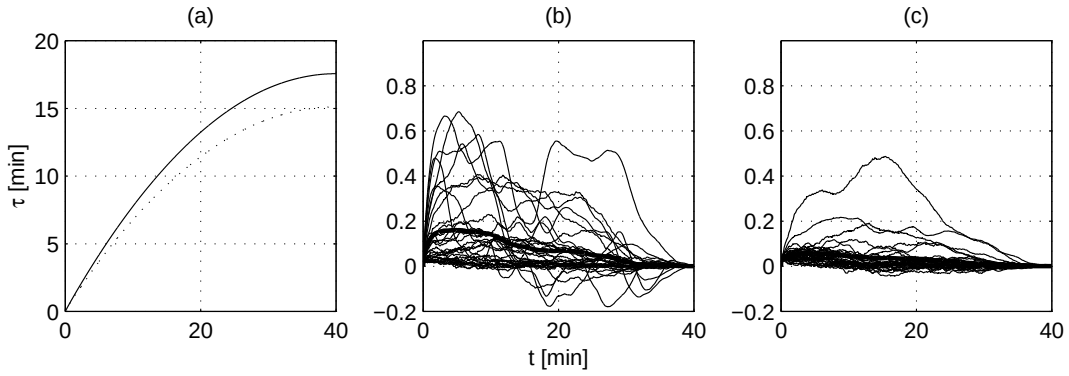

Figure 4.14: (a) Mean integral time-scale convergence for V and u (dotted line) of the 32×40-min time intervals. (b) v integral time-scale convergence for the 32×40-min intervals where the mean is represented by the thicker line. (c) w integral time-scale convergence for the 32×40-min intervals where the mean is represented by the thicker line.

Figure 4.14a presents the convergence of the mean integral time-scale for V and u where convergence is clear, 17.56 and 15.12-min (table 4.5). The statistics show that the scatter between each integral time-scale is reduced to a standard deviation on the convergence inferior to 3-min. For the cross and vertical velocity the results are not so clear thus justifying the presentation of all 32 integral time-scale results for v and w. In this cases the autocorrelation shows variations with opposite phase forcing the convergence to zero, resulting then a null integral time-scale. However, as the flow was rotated into streamline coordinates, the integral time-scale of v and w are expected to be inferior to the integral time-scale of u.

With this method we separate the whole data set into 40-min blocks to be analysed instead of a single data-set such as Period A or B in previous subsection.

4.3.4 Types of flows

4.3.4.1 Quasi stationary flow - Period A

The PDF of the wind velocity field and the vertical component for Period A (figures 4.15a and 4.15b) differ from figure 4.6, related to the whole series. The average wind field velocity was 13.69 ms^{-1} and the standard deviation of 1.47 ms^{-1} is 2.7 times smaller than the whole series value. The 3rd moment of -1.02 shows the increase of the unbalance to the left (-0.34 for the whole series). The kurtosis reaches nearly 6, showing a distribution almost 3 times narrower than the one relative to the whole series.

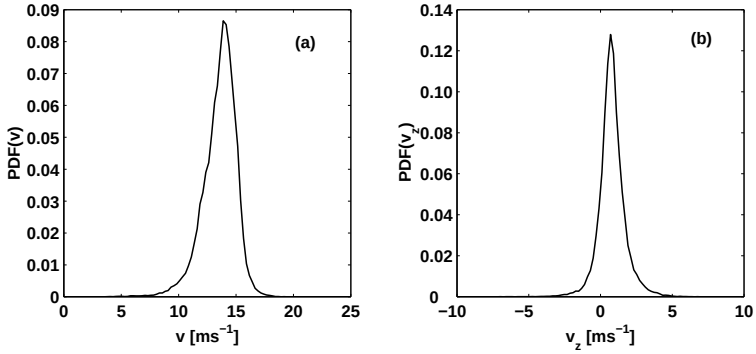

Figure 4.15: (a) PDF for period A from 20.7 to 21.5 hr of the wind velocity field. (b) PDF of the vertical component of velocity.

The same applies to the horizontal component of the wind field, where the differences compared to the velocity field statistics are almost null, table 4.6. The mean value differs 0.07 ms^{-1} and the standard deviation 0.03 ms^{-1}, which corresponds to a flow field where the vertical component is less influent and tends to a Gaussian distribution. The mean and standard deviations of the vertical component present almost the same value and the distribution may be considered symmetric: skewness is almost null. The shape of the distribution is sharper than the one related to the whole period, 7.42 to 4.65.

Table 4.6: Wind velocity statistics for period A, from 20.7 to 21.5 hr.

	$\overline{V}$ [ms^{-1}]	$\sigma(V)$ [ms^{-1}]	$sk(V)$	$k(V)$	min [ms^{-1}]	max [ms^{-1}]
$\overline{v}$	13.69	1.47	-1.02	5.97	2.15	22.49
$\overline{v_h}$	13.62	1.50	-1.11	6.30	1.97	22.48
$\overline{v_z}$	0.90	0.94	0.06	7.42	-6.85	7.39

Wavelet decomposition The wavelet analysis was performed on previously detrented data. A Morlet mother wavelet was used to decompose each scale according to subsection B. The degree of similarity between one scaled wavelet and the oscillation in the signal can be represented by a 2-D scalogram, where the x-axis corresponds to the time-wise evolution of the series, and the y-axis corresponds to the frequency or, in our case, the period of oscillation, figure 4.16. The scalogram shows the similarity of events in a non-dimensional

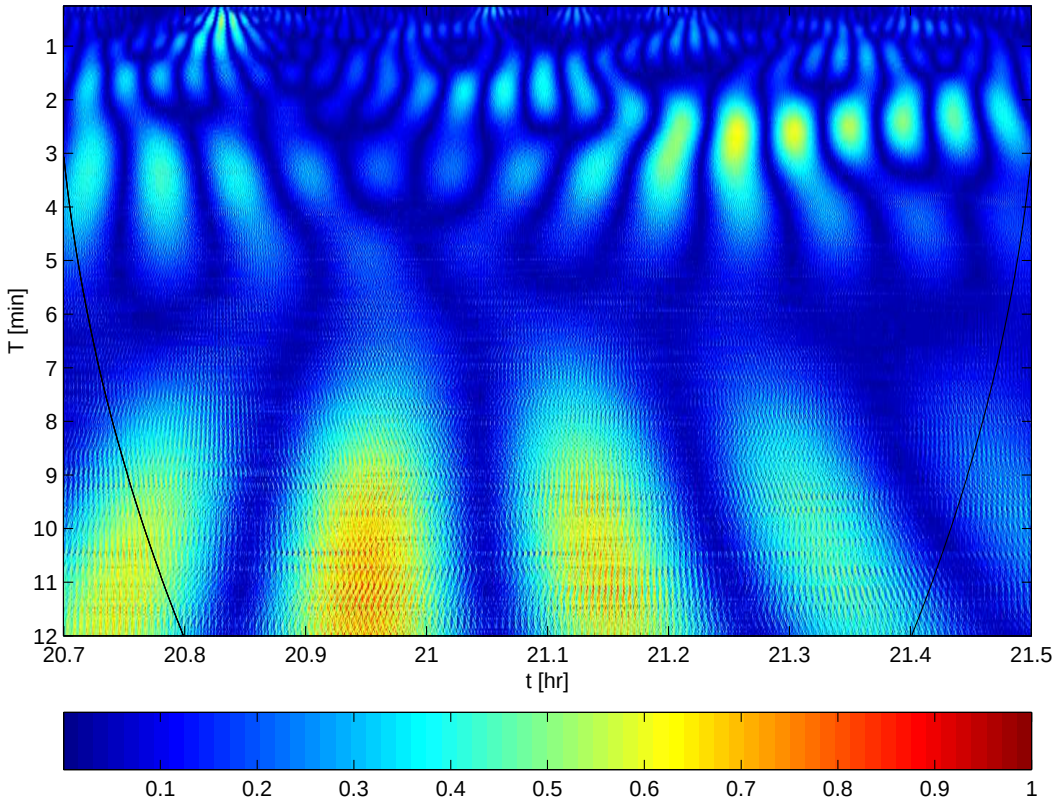

Figure 4.16: Period A scalogram. Wavelet similarity coefficients are depicted in a linear scale from 0 to 1.

scale between 0 and 1, where 0 means no similarity of an oscillation, and 1 means maximum similarity of an oscillation, both related to a particular time instant. The black line limits the cone of influence on the analysis related to the beginning and end of the data series and the information outside those limits should be neglected.

In figure 4.16, the lighter areas in the time interval, from 21.2 to 21.5 hr, represent the existence of a 2.5 minute oscillation in the data. In the same time interval, there is simultaneously a faster oscillation related to smaller scales, between 1 to 2 minutes. In the same time interval, the smaller scales separate into 2 different scale events: one close to 1.5 minutes and a larger one of 2.5 minutes. Considering the whole scalogram we observe continuously the existence of 1 to 2 minutes events. The events are present alone, in the time interval of 21.0 to 21.2 hr, or superimposed by larger scales, 11-min, such as in the

time intervals, 4 minutes events, from 20.8 to 21.2 hr.

The wavelet and Fourier spectra have approximately the same results (figure 4.17a and 4.17b). The wavelet peak is clearly related to 5.3 minutes period events. Two small bumps on the energy spectrum are related to lower energy frequencies associated with events with 1.3 minutes and 50 seconds. The Fourier spectrum peaks in energy decreasing order are 4.1 minutes, 50 s, 2 minutes and 7.8 minutes. The differences are explained on the theoretical fundamentals of each approach. The wavelet spectra corresponds to an average projection on the frequency plane of the square of all coefficients depicted in figure 4.16. The result is a smother curve, in opposition to the spikier one presented in figure 4.17b, where frequencies peaks around 2×10^{-2} Hz are identified as distinct events. The wavelet peak represents the average of all local maxima on the time-frequency plane, whereas in the case of the Fourier spectra, a peak means how many times a particular frequency appear in the series. In case of a time series with two frequencies close to each other but associated to different

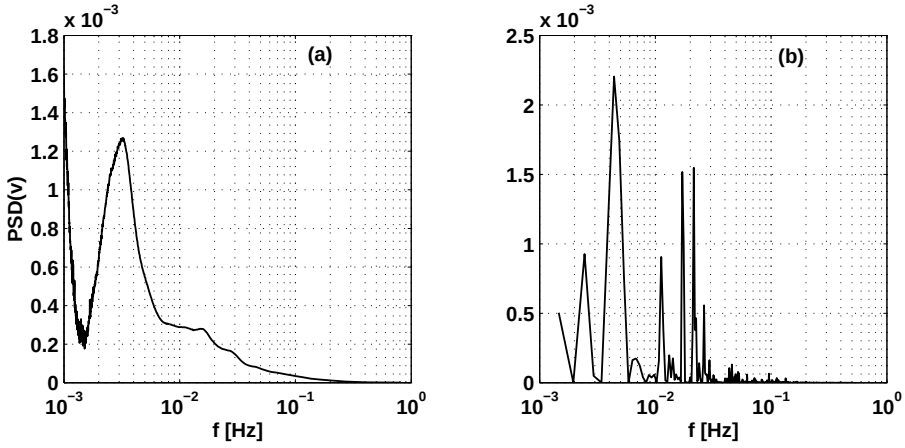

Figure 4.17: Wavelet (a) and Fourier (b) power density spectrum of period A.

time instants, the wavelet spectra peak will be an weighted average with the square of similarity coefficients. The same series analysed via Fourier will show as independent ones, weighted by the number of times each particular frequency appear in the series. For the detected peaks in the scalogram 4.16 and figure 4.17, it is possible to obtain the following information: the series shows 3 types of periodic events, a larger one, related to 5.3 minute periodic oscillation, and two shorter events, related to 1.5 to 2 minutes oscillation; a final oscillation mode is associated to events inferior to 1 minute.

Note that the series is not statistically stationary and the Fourier transform would be biased, see section A.2. By wavelet analysis, events with similar dimensions are not assumed as different entities, but as scale variations of the same event. Our understanding, explained by the scalogram in figure 4.16, is that the same event, or events scaled differently due to changes in the mesoscale wind conditions, are present.

4.3.4.2 Non stationary flow - Period B

Period B velocity distribution resemble the whole series and therefore we restrain from presenting the respective PDF. The statistics for Period B are in table 4.7 and comparing to Period A, this series is less steadier with dispersion values 3 times larger.

Table 4.7: Wind velocity statistics for period B, from 3.8 to 5.5 hr.

	$\overline{V}$ [ms^{-1}]	$\sigma(V)$ [ms^{-1}]	$sk(V)$	$k(V)$	min [ms^{-1}]	max [ms^{-1}]
$\overline{v}$	9.85	4.50	0.07	1.98	0.11	29.87
$\overline{v_h}$	9.25	4.85	0.08	1.88	0.00	23.58
$\overline{v_z}$	0.55	2.82	0.23	4.00	-18.75	22.29

Wavelet decomposition The scalogram, in figure 4.18, show 3 types of events. The shorter ones are related to oscillations with a period slightly less than 2 minutes, throughout the series, although with some scale variations. A larger type of event around 4 minutes, shifting to 3 minutes from hour 5 on. The largest events in the scalogram are in the interval of 4.5 to 5 hours, presenting dimensions of approximately 8 minutes.

We show again the comparison of wavelet and Fourier spectra, figure 4.19. Wavelet spectrum show 3 well defined peaks, corresponding to the maxima detected in the scalogram. Fourier spectrum presents energy peaks at the same location as the wavelet spectrum but with inferior resolution due to leakage.

Period A and B both show the existence of events approximately around 2-min period superimposed by larger scales (figures 4.16 and 4.18). The difference between scalograms basically resides in scales larger than 2-min.

4.3.4.3 Analysis by 40-min time blocks

The individual PDF of each 40-min time block for the rotated data is show the presence of three types of distributions: a narrow one centred close to 13 ms^{-1}, a second and wider distribution where the centre is in the interval from 4 to 5 ms^{-1}, and a third one, with a peak close 0 ms^{-1}. An interesting feature is that for the second and third types of distribution, part of the flow is reversed, i.e. u is negative. By the analysis of the mean PDF of u, we verify that 8.1% of the data corresponds to reverse flow and 20.2% of the mean flow ranges from 0 to 5 ms^{-1}, the minimun cut-in velocity for the wind turbine. From the whole time series roughly only 72% of the flow would have minimum conditions for turbine operations. The reverse flow criteria was used to identify and classify 3 types of flow (statistics are in table 4.8 while the mean PDF of the velocity components are at figure 4.20):

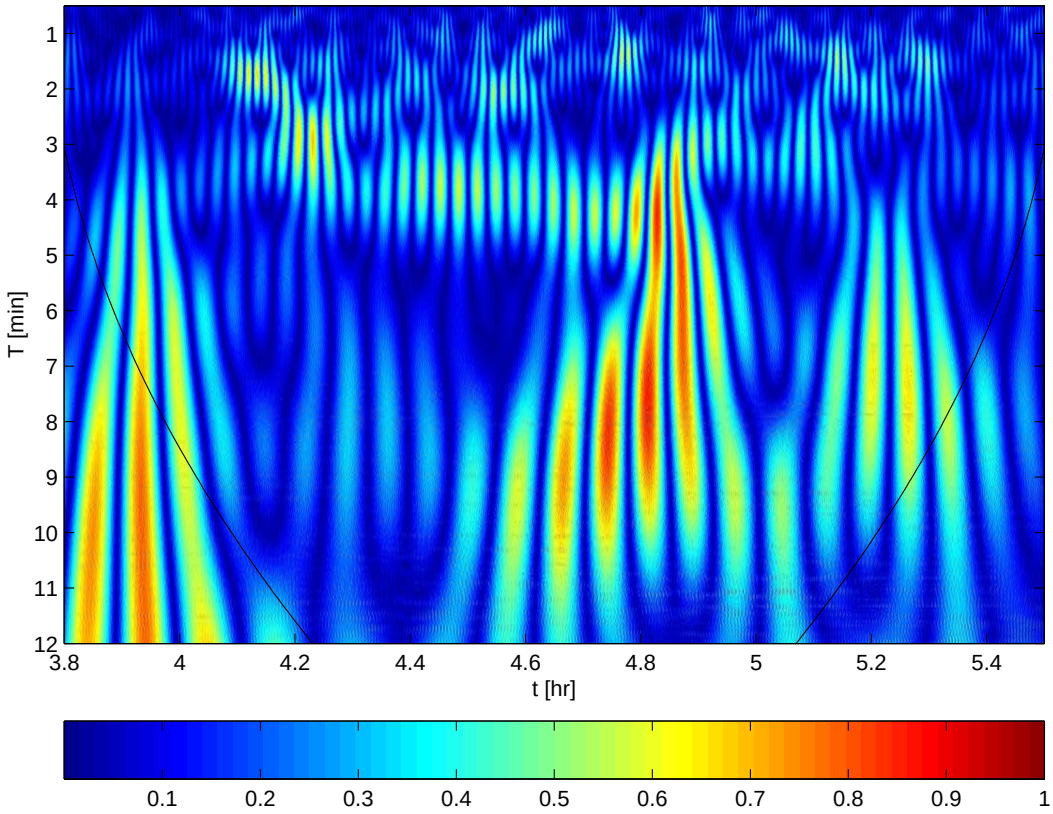

Figure 4.18: Scalogram of period B.

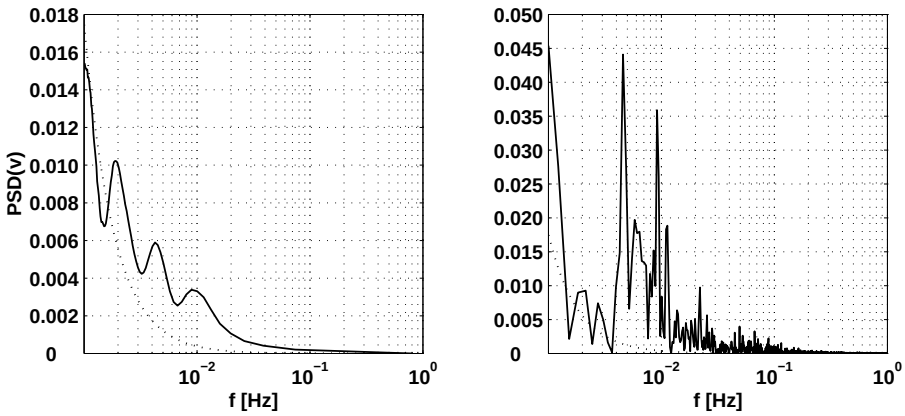

Figure 4.19: Wavelet and Fourier power spectral densities for period B. The dashed line represent the turbulent inertial range of $f^{-\frac{5}{3}}$.

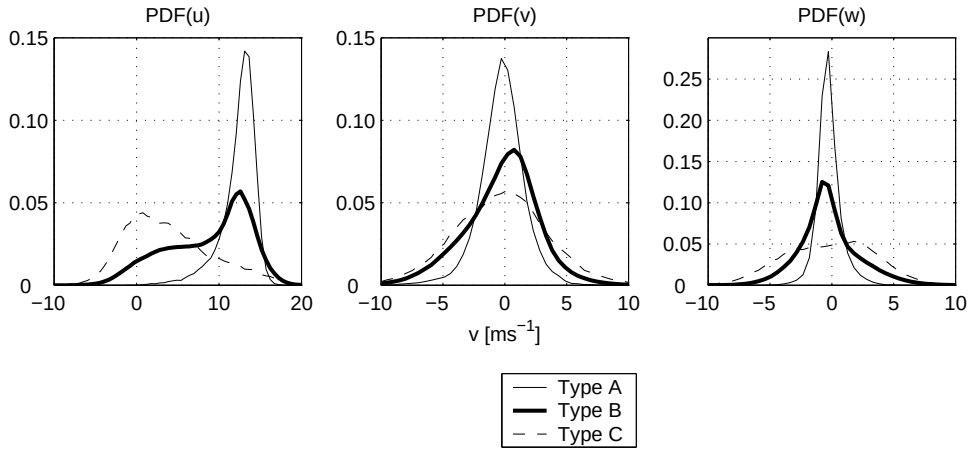

Figure 4.20: Longitudinal u, transversal v and vertical w velocity component PDF of flow types A to C. Statistical moments are presented at table 4.8.

Type A Moderate to strong and steady flow present only in 9.4% of the data series where the reverse flow is negligible, corresponding to 0.1% of the flow. The mean turbulence intensity is 14.3% with a 3.6% standard deviation. The gust factor was 1.42 and the difference between the total velocity and streamwise velocity was only 1.6%, which corresponds to a 'normal' flow for wind turbine operations. Stream, cross and vertical wind speed distributions are almost symmetrical, while cross and vertical component distribution are narrower with a kurtosis of 5.2 and 7.1 respectively.

Type B Moderate to strong wind corresponding to the more frequent type of flow at the site, 84.3%, and where the reverse flow reaches up to 15% of the data. Turbulence intensity increases to 35.3% with standard deviation of 10.3% and the gust factor increases to 2.12. The difference between total and streamwise velocity increases to 12.9%. Streamwise component presents a wide distribution, where the peak almost coincides with Type A peak but presents a large tail to the left from 9 to 2 ms^{-1}. Cross and stream wise distributions mantain the symmetry but the kurtosis decrease to 3.7 and 4.4 respectivelly.

Type C The more complex type of flow identified corresponding to 6.3% of the time series and where the reverse flow surpasses the 15% limit. The wind velocity is moderate with a 44.5% difference among the mean and streamwise component due to the reverse flow, present in 53% of the series. Turbulence intensity and gust factor rise up respectivelly to 52% and 3.3. Streamwise distribution is pruned to the left

Table 4.8: Statistics of the 3 identified types of flow. The PDF of each velocity component is presented in figure 4.20.

Flow Type	x	$\overline{x}$ [ms^{-1}]	$\sigma(x)$ [ms^{-1}]	$sk(x)$ -	$k(x)$ -	$min(x)$ [ms^{-1}]	$max(x)$ [ms^{-1}]
	u	12.61	2.17	-1.63	6.89	-0.72	21.84
A	v	0.01	1.85	-0.40	5.21	-14.56	9.50
	w	0.01	1.00	0.56	7.15	-8.15	9.18
	u	8.92	5.07	-0.53	2.38	-12.42	26.31
B	v	0.00	3.02	-0.33	3.74	-20.27	17.99
	w	0.01	2.46	0.44	4.36	-18.75	21.66
	u	4.17	5.26	0.57	2.88	-12.31	24.51
C	v	-0.06	3.80	0.05	3.21	-16.66	16.08
	w	0.03	3.63	-0.09	2.65	-14.90	17.45
A	V	12.81	1.99	-1.41	6.03	1.56	22.53
B	V	10.24	3.95	-0.29	2.22	0.03	29.08
C	V	7.51	4.03	0.87	3.39	0.19	26.28

with the peak closing to 0 ms^{-1}. Cross and vertical velocity distributions are almost identical, with no major differences in the statistical moments.

All 3 types of flow can be better visualized in figures 4.21 to 4.23, where a 40-min sample of each type is represented in the uv, uw and vw plane. Each arrow is scaled to the modulus of the mean velocity for a 30 s average, and points according to the sign and modulus of each component. The uv plane represents the top view, uw the lateral view and vw the front view of the flow approaching the turbine; vw may also be interpreted as the plane of the rotor. The figures are accompanied by the cospectra normalized by the covariance of each series to identify the common frequencies in each plane.

In figure 4.21 we observe that the Type A flow in the uv plane oscillates clock and counter counter-clock wise. The periods of oscillation are verified in the respective cospectra and correspond to periods of 4 and 2.8 min. The uv cospectra also indicates the existence of periodicity larger than 10 min in than plane. Oscillations in uw plane are lower in amplitude and with periodicity larger than 10 min. Focusing on higher frequencies, we observe the presence of 4.5, 2.8 and 3.2 min events for larger scales, accompanied by 35 and 46 s periodic events on a higher frequency range. The vw plane presents the view of the rotor plane where the velocity components change amplitude when rotating predominantly in the clockwise direction. Three different periods in the minute range are present in this series, 10.3, 5.1 and 2.1 min events. In spite of being the more constant flow in the series, this particular sample show the existence of periodicity in all 3 velocity components. Because we are observing a moderate to strong mean wind field, only a clock-wise rotation of the flow in the vw plane is visually verified.

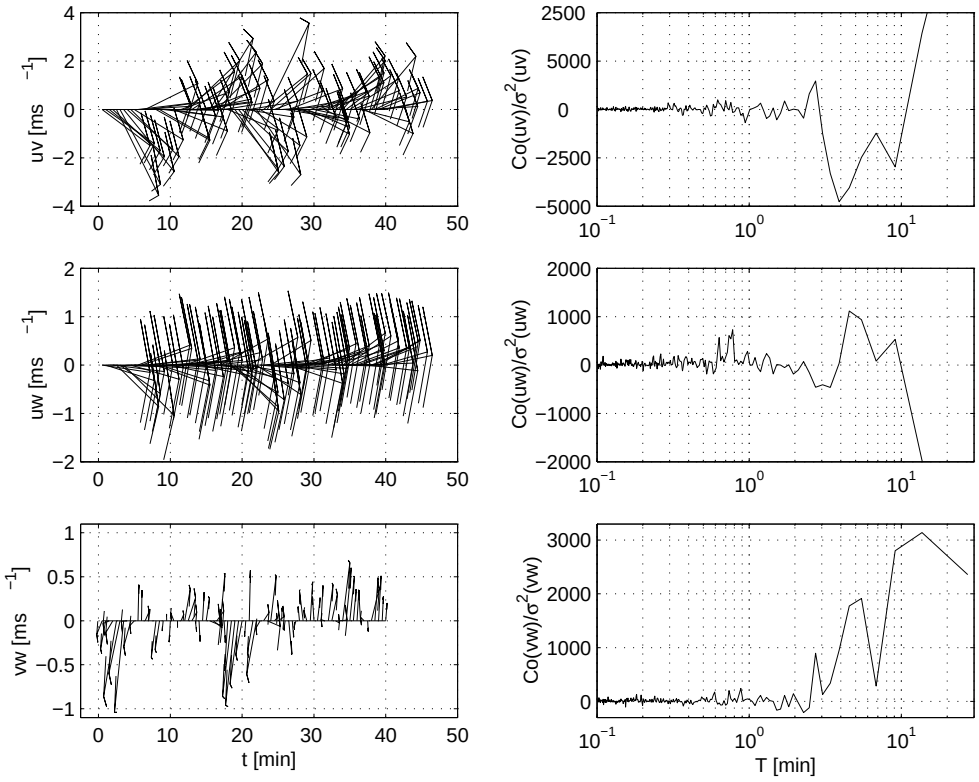

Figure 4.21: Type A flow visualization. Each arrow corresponds to a 30 s mean on the uv, uw and vw plane.

Figure 4.22 refers to the visualization of a sample of Type B flow, the more frequent flow type. All planes present larger oscillating features with amplitude changes, and at minute 6 we observe at uv plane the flow reversing (the arrow points down and slightly to the left and in the next 30 s points up slightly to the right). The oscillating periods are shorter than the Type A flow, 42 s and 1.2 min are most energetic peaks of the cospectra. At the uw plane, several oscillating events close to each other are present: 42, 48, 63 s and 1.7, 2.9, 4 and 7-min. The cospectra information is blurred by these frequencies, from which we do not know if they correspond to the same event that are being scaled as the mean flow velocity changes or different events that coexist independently in the frequency domain. From uw plane of figure 4.22 we observe that the flow is successively pointing toward the wall during several minutes then to point in the opposite direction (a feature not evident in Type A flow). The clear clock-wise rotation of the flow in the previous flow type is not particularly evident in the vw plane of flow Type B. As we observe from the cospectra of vw, the oscillations in this plane are at an higher frequency than for Type A, ranging from 12 to 42 s with successive phase changes and the 30 s resolution of each arrow are not able to resolve such frequencies.

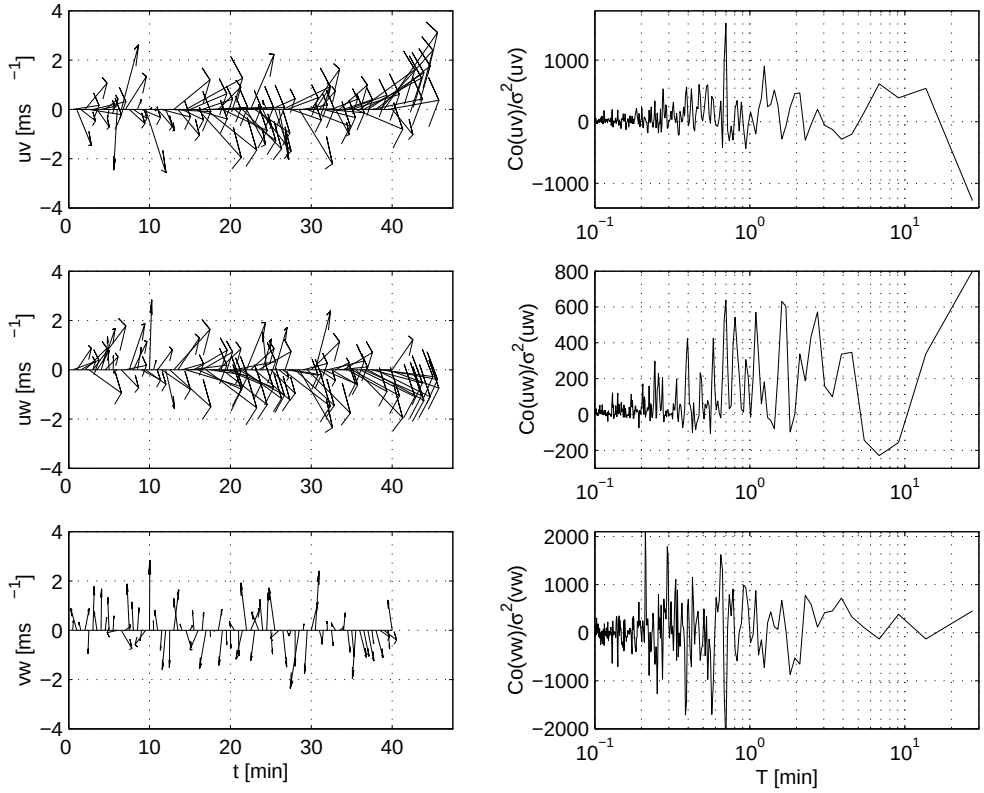

Figure 4.22: Type B flow visualization and periodicity. Each arrow corresponds to a 30 s mean on the uv, uw and vw plane accompanied by the cospectra of each series.

Figure 4.23 presents a sample of Type C flow, where the reverse flow may be visualized at uv or uw planes at the time interval from minute 3 to 7, or 12 to 15, or 23 to 29. The cospetrum of uv shows the presence, as expected, of several frequencies with the same energy from a large band, although it is possible to highlight 1.5 and 5.4 min as periods where the signal is more energetic. The uw cospectrum is less clear where the energy is contained, by decreasing order, at oscillations from 18 s, 5.1 min, 24 s, 2.5 and 1.0 min. Finally, the vw plane of figure 4.23 differs only in scale from the Type B flow. In this case, and as in the previous one, the visualization is inconclusive because the 30 s averages of each arrow do not capture the 24 or 48 s oscillations that exist in this plane. The lateral view of the flow, uw plane, at Type B and C show what appears to be a high-speed portion of the flow incoming to the wall being diverged up with lower velocity. This feature is discussed in the quadrant analysis at subsection 4.3.7.

We conclude this subsection by the analysis with the reverse flow criteria on the flow subsets selected by the acceleration criteria, Period A and B from subsubsections 4.3.4.1 and 4.3.4.2. The analysis of the PDF of the longitudinal velocity (not shown here) indicated no reverse flow for Period A thus it may be classified as Type A while Period B showed a reverse flow of 13%, corresponding to a flow Type B.

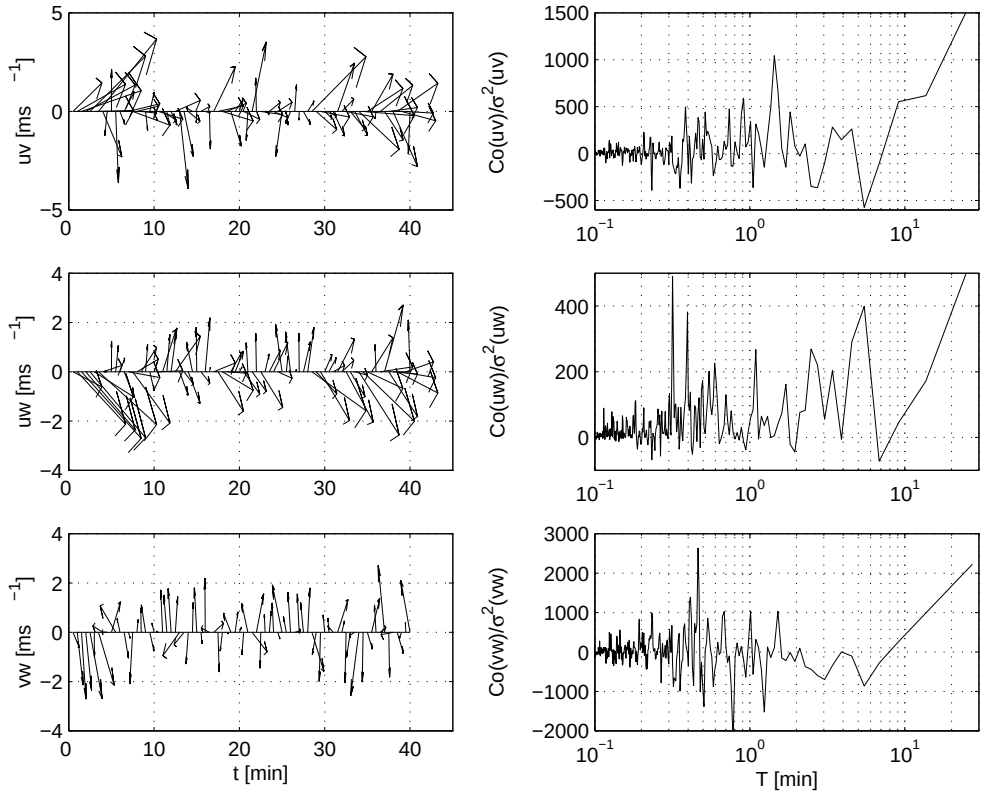

Figure 4.23: Type C flow visualization and periodicity. Each arrow corresponds to a 30 s mean on the uv, uw and vw plane.

4.3.5 Spectral analysis

Figures 4.21 to 4.23 were accompanied with the cospectra of the components of the plane under visualization. Type A flow top view at figure 4.21 showed the existence of an in rotor plane oscillation with periods of 4 and 2.8 min. As the flow becomes more complex (Type B and C) other peaks arise on higher frequencies: 42 s and 1.2-min oscillation periods for Type B and 1.5 to 5.4-min for Type C. Also lateral and rotor plane cospectra present several period peaks ranging from 18 s to 7-min showing the coexistence of different scale events. However, such information is incomplete because there is no indication whether the events occur simultaneously or at independent instants in the time series. Note also that all series under analysis were not statistical stationary, limiting the information that can be extracted from the Fourier spectral decomposition. The FFT algorithm is limited for such cases, requiring a more powerful tool such as the wavelet transform. Exploring however the potentialities of the Fourier spectrum, we build mean cospectra for the whole series.

The mean (co)spectra were based upon 32 data sets normalized by each (co)variance and smoothed according to the procedure at subsection 1.6.4. The $S(u)$, $S(v)$ and $S(w)$

spectra, in figure 4.24, show the usual exponential decay at the inertial subrange with no special features associated to any singularity. At the low-frequency end of the spectra the low-frequency transition to the inertial decay is poorly defined, probably because of the gusty behavior of the flow that forces constant changes in the energy input. The mean

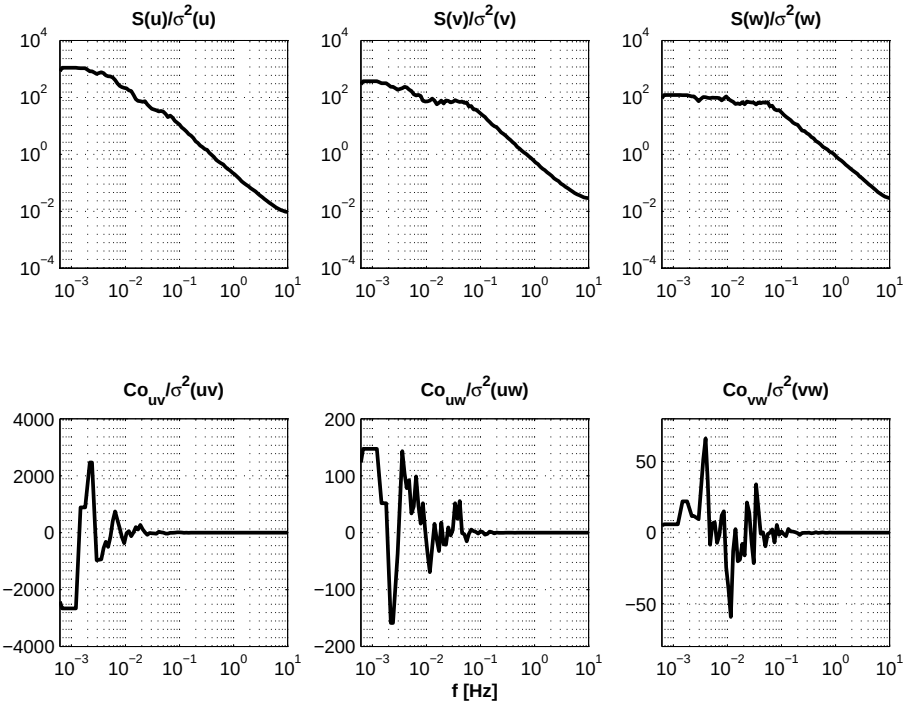

Figure 4.24: Mean spectra and cospectra of the time series for 32×40-min time intervals.

cospectra of uv, uw, and vw (figure 4.24) show predominant frequencies, some of them common in all cospectra. The information about the peak frequencies is presented at table 4.9 in frequency and time domain. The table organizes the cospectra peaks by an energy descending order. The values between brackets are the fraction of energy of each peak normalized by the larger peak: *e*.g. $Co(vw)$ present 4.2, 1.5 and 0.5-min oscillating events, where 1.5-min events have 90% and 0.5-min events have half of the energy of the 4.2-min events.

Grouping mean cospectra by size events we conclude that it differs from cospectra information in figures 4.21 to 4.23, related only to 40-min samples of each flow type, only in the period interval from 2 to 10-min events. For instance, large events such as 13.8-min are common in all cospectra, along with events inferior to 2.6-min. In such cases, events like 0.9, 0.7 or 0.5-min period may be understood as scale fluctuations of the same type of event due to changes in the mean flow velocity. The same scale shift affects larger events thus peaks related to 5.6 or 4.7-min events may represent the same physical phenomenon, to be discussed in subsection 4.3.6.

Table 4.9: Subtable A - Cospectra peak frequencies $Pf_{Co(uv)} \times 10^{-3}$ [Hz] in energy descending order from the cospectra at figure 4.24. Subtable B - Period, in [min], associated with the frequency peaks of A and the energy fraction of each peak assuming 100% for the most energetic peak.

A	1st	2nd	3rd	4th	5th	6th
$Pf_{Co(uv)}$	1.2	2.4	2.9	6.4	9.4	18.8
$Pf_{Co(uw)}$	2.4	1.2	3.5	6.4	11.5	41.8
$Pf_{Co(vw)}$	3.9	11.4	34.0	1.2	23.1	30.8
B						
$Pt_{Co(uv)}$	13.8 (100)	6.9 (93)	5.6 (37)	2.6 (28)	1.8 (14)	0.9 (10)
$Pt_{Co(uw)}$	6.9 (100)	13.7 (93)	4.7 (90)	2.6 (62)	1.5 (44)	0.4 (35)
$Pt_{Co(vw)}$	4.2 (100)	1.5 (90)	0.5 (51)	13.8 (33)	0.7 (32)	0.6 (32)

4.3.6 Wavelet analysis

At the moment we know from turbulence intensity values that the flow is anisotropic (section 4.3.1), and that from flow visualization and spectral analysis (subsections 4.3.4.3 and 4.3.5) we also know that events with scales from 30 s to 13-min are present in our series. Wavelet analysis allow, due to time depending characteristics, observe better how such scales are related, and if they are independent events or if they correspond to a reshaping process of the same type of event. We have applied wavelet analysis to the longitudinal, transversal and vertical components of the velocity vector for flow Type A to C (figures 4.21 to 4.23) based in a Morlet mother wavelet.

Type A scalogram (figure 4.25) shows that there are no relevant events in longitudinal and transversal velocity components inferior to 6-min period. In fact the scalogram do not exclude the existence of such events, but that if they exist, their energy is much lower. Type A flow is the steadier, and that is depicted in the scalogram. However, transversal component match the same energy contents of the longitudinal one for 6-min period event as seen in longitudinal and transversal wavelet spectra. It is also relevant the information of transversal component scalogram on the simultaneous presence of 8 and 16-min events during part of the series. These events are independent of 6-min period ones once they appear at different time instants. The first 6-min event detected was in the longitudinal component appearing in transversal component with a temporal delay over 5 min, and a 30-min delay in vertical component. Only two events were detected simultaneously in different velocity components: the 16 and 3-min events on the transversal and vertical velocity components.

Type B scalogram (figure 4.26) shows a more complex flow, where events inferior to 1-min in transversal and vertical components match the energy of larger scales. The energy contents of longitudinal component is almost 6 times larger as the other components. Note

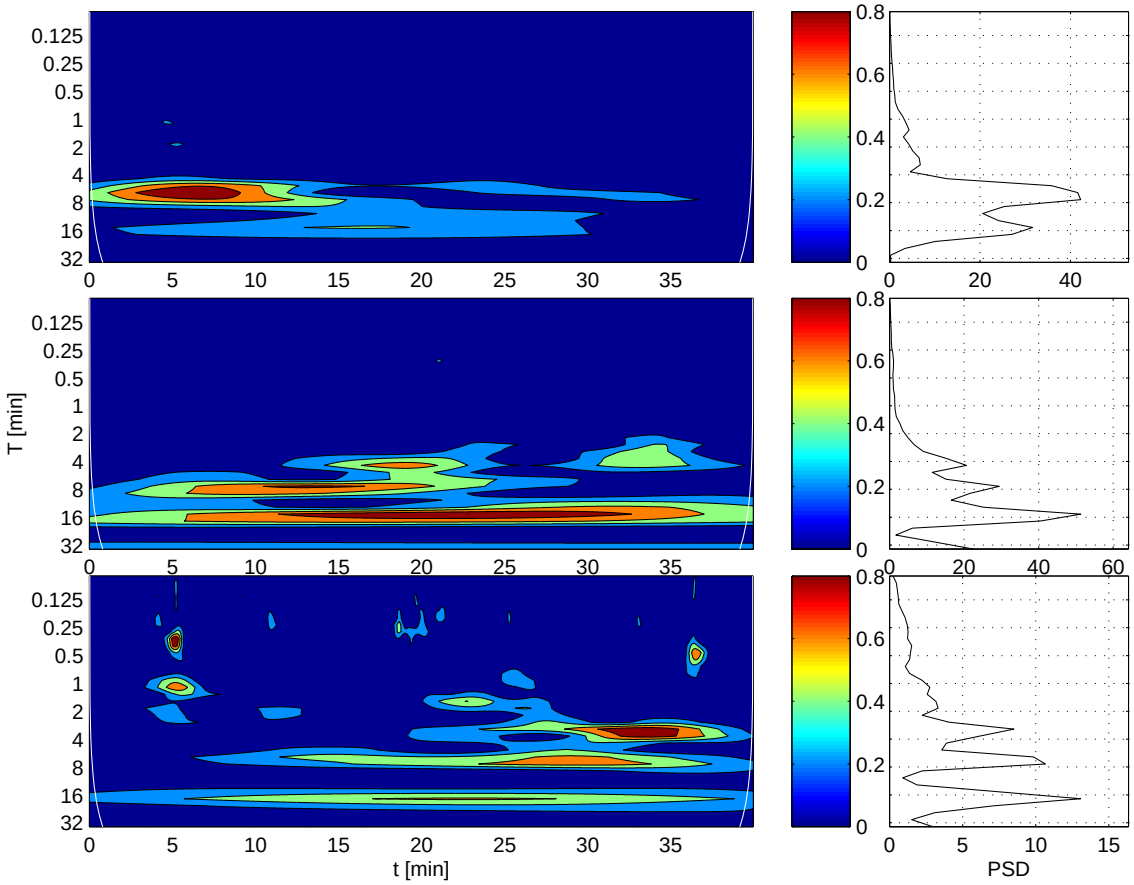

Figure 4.25: Type A flow scalogram and wavelet spectra of the longitudinal, transversal, and vertical velocity components.

an event of 3-min period that last over 30 min and matches the same energy contents of a large 16-min event during the same time. Again, we observe in different velocity components events that occur during the same time, such as the 8-min event in longitudinal and transversal planes, or the 16-min event in the longitudinal and vertical planes. Note also the small scale events, inferior to 1-min, are common in transversal and vertical planes, indicating a link between these components for such scales. Such link was confirmed by mean cospectra results at table 4.9 in previous subsection. Note also that in the longitudinal plane that the 3-min event maximum changes from 3 to 4-min scale as a consequence of a reshaping process.

The scalogram of Type C flow (figure 4.27) shows in the longitudinal component an event with 5-min period for almost the whole series, being the most energetic in the spectrum. This event is intermittent once it was detected also in the vertical component in the beginning and end of the time series. Transversal and vertical components present the same energy as Type B flow, but in transversal component there is a predominance of events of scale inferior to 1-min. The scalogram shows that this flow type is the one where

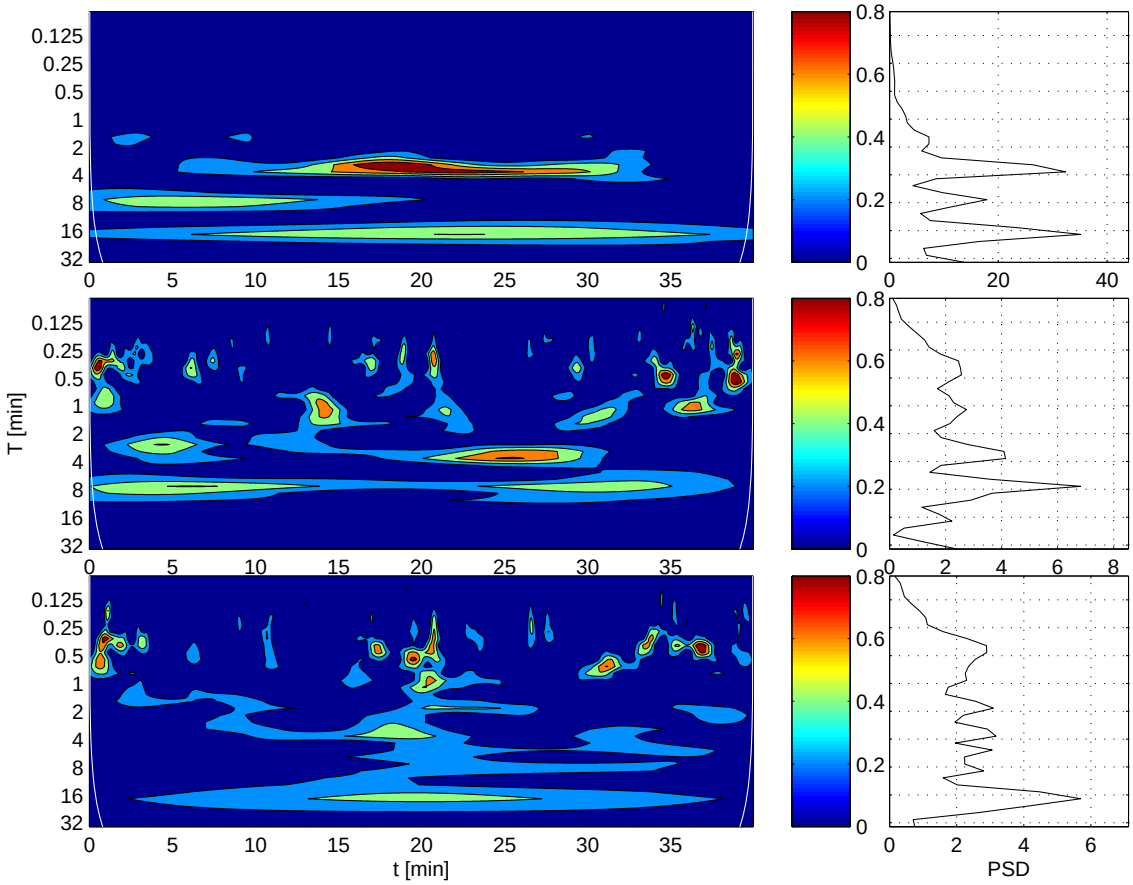

Figure 4.26: Type B flow scalogram and wavelet spectra of the longitudinal, transversal, and vertical velocity components.

the simultaneity between events is the lowest.

All scalograms share in common in the longitudinal plane a large energy content event with scale from 3 to 6-min with a duration longer than 15 minutes that reshapes with time. For instance a 3-min event become in the end of the series a 4-min event. Although being the same phenomenon, the unsteadiness of the series changes the energy input forcing the event to reshape and assume a different periodicity. This mechanism explains all the different peaks obtained from spectral analysis that point toward events with oscillating periods of 2, 3 or 4-min, which are most likely to be the same event rescaled due to transient feature of the flow. However, they coexist with other events with different scales that match the energy contents of this 4-min event. That is also true in the lateral and vertical wind components where smaller scales are as energetic as the larger than 10-min scales.

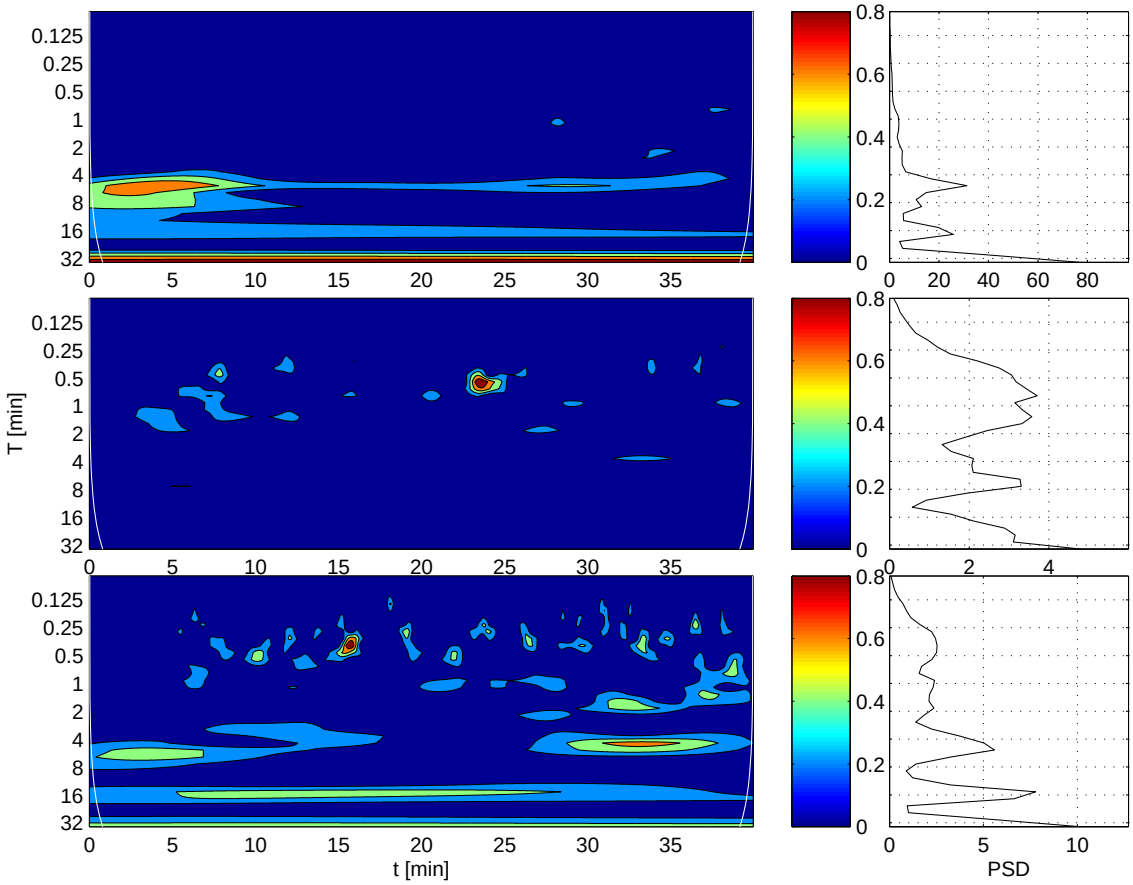

Figure 4.27: Type C flow scalogram and wavelet spectra of the longitudinal, transversal, and vertical velocity components.

4.3.6.1 Scalogram autocorrelation

Figures 4.25 to 4.27 hardly provide means for a pattern recognition of the repeatability of the set of scales identified in each scalogram. We recur then to autocorrelation of the scalogram (a detailed description is presented in Appendix section B.4 with an example of application) to identify the repeatability of the set frequencies from figures 4.25 to 4.27. The procedure handles the scalogram as any other time-dependent signal, with a temporal displacement τ of the scalogram, with the advantage of revealing events that where hidden by the normalization of the wavelet coefficients in each scalogram.

All autocorrelation scalograms show similar features where each event scale is correlated almost to a maximum time displacement τ. For each autocorrelation there is a gap at certain scales where the autocorrelation is almost null, clearly dividing the type of event by family size. Figure 4.30 shows this feature very clearly. The gap divides events smaller than 0.8-min and larger than 0.8-min. A second family of events with large autocorrelation for Type C longitudinal velocity are binded from 0.8 to 6.0-min events.

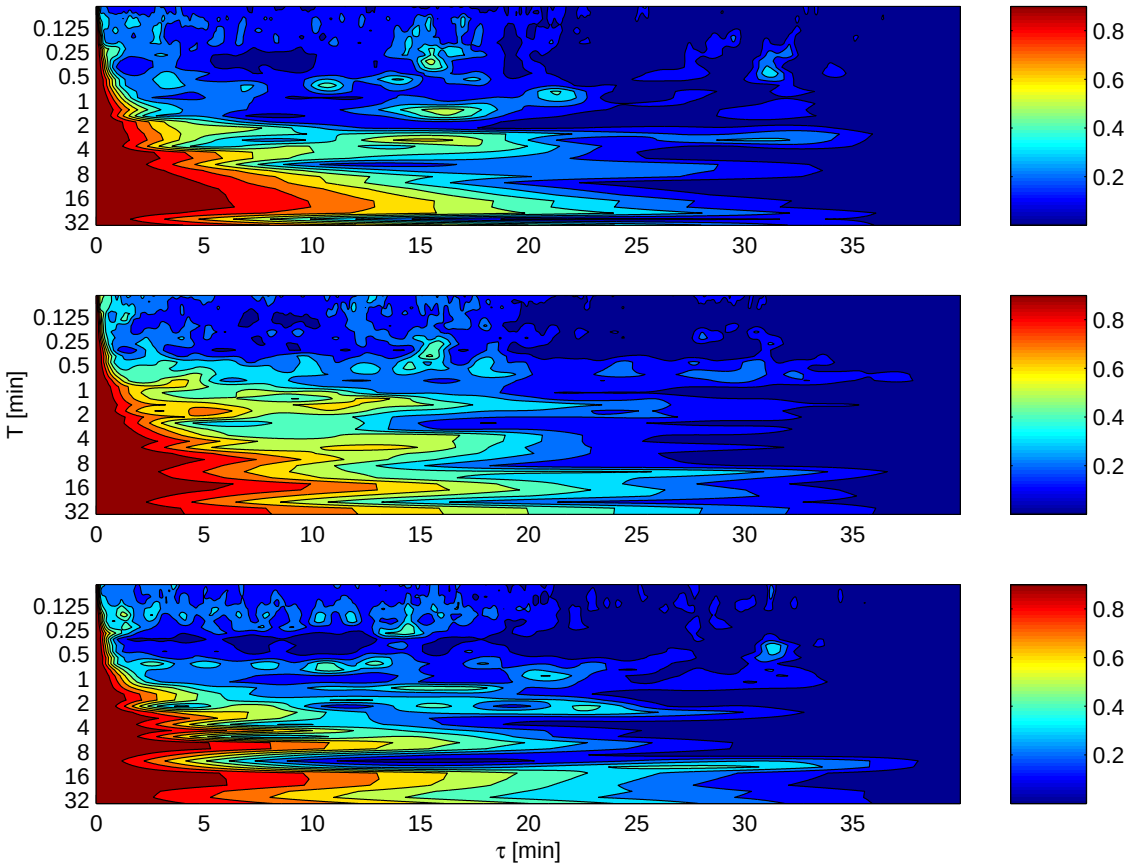

Figure 4.28: Type A autocorrelation scalogram of the longitudinal, transversal, and vertical velocity components.

Nevertheless, figures 4.28 to 4.30 are of difficult reading. Instead of discussing the scale correlation for 3 velocity components, we address this problem by quantifying the scale where the energy gap is located in each scalogram. The gap is at 0.8-min scale in the case of longitudinal component of Type C flow (figure 4.30). The same is true for transversal velocity but presenting an additional gap around 3-min and vertical velocity with gaps at 1.5 and 8-min scale. Table 4.10 summarizes the detected gaps in event autocorrelation for all flow types and velocity components.

These gaps divide the events in family size that may be resumed as small size events, limited by 1 to 3-min gap in autocorrelation, middle size events that vary from 1 or 3-min to 6 to 8-min events and large size events. That is true for Type A flow and Type C. In Type B flow the gap is not so clear.

The superposition of events with different scales turns the interpretation of the information from measurements difficult. However, table 4.10 helps in the identification of the scales and how they are linked. We also recall that the same event may change size, from 4 to 6-min scale if the energy input of the flow is changing. What is being observed in the

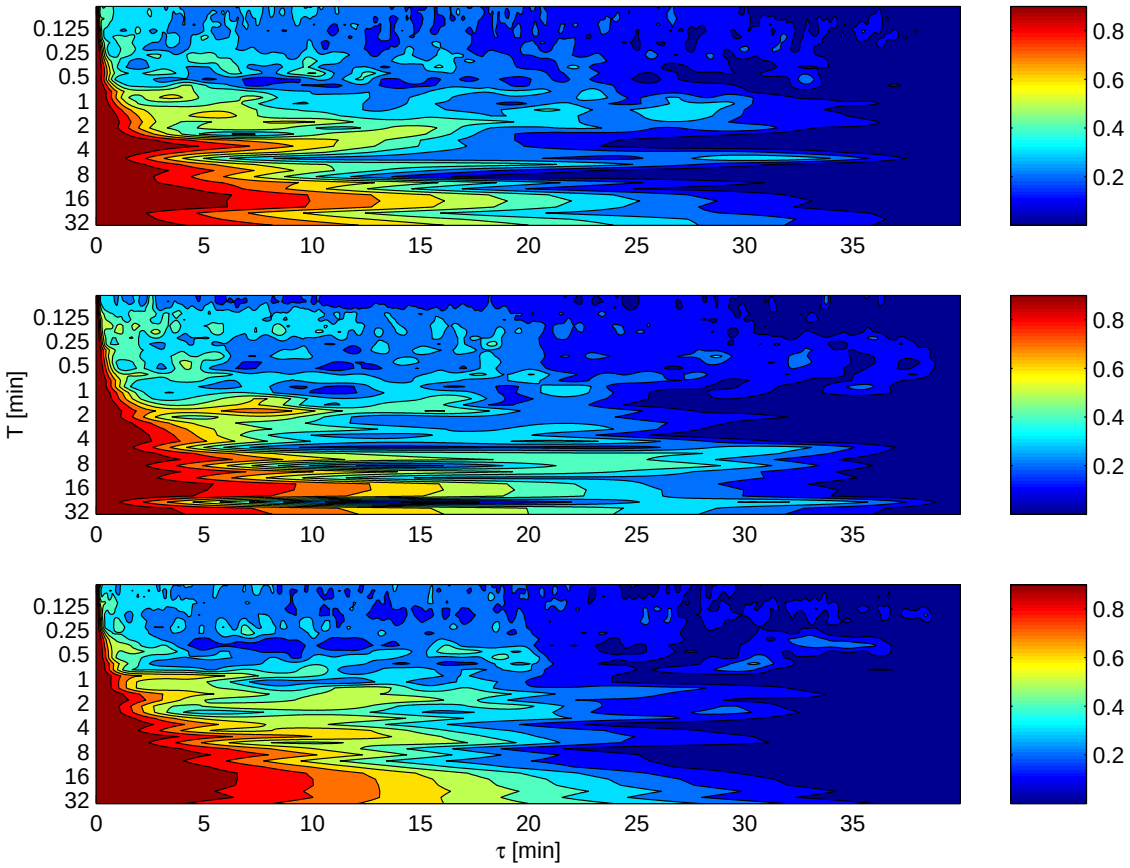

Figure 4.29: Type B autocorrelation scalogram of the longitudinal, transversal, and vertical velocity components.

Table 4.10: Summary of the detected scales that correspond to a gap in the autocorrelation scalogram from figures 4.28 to 4.30.

Scalogram autocorrelation	Velocity component	Event gap [min]	
Type A	u	1.5	8.0
Figure	v	3.0	8.0
4.28	w	3.0	8.0
Type B	u	-	8.0
Figure	v	-	6.0
4.29	w	-	-
Type B	u	0.8	6.0
Figure	v	0.8	3.0
4.30	w	1.5	8.0

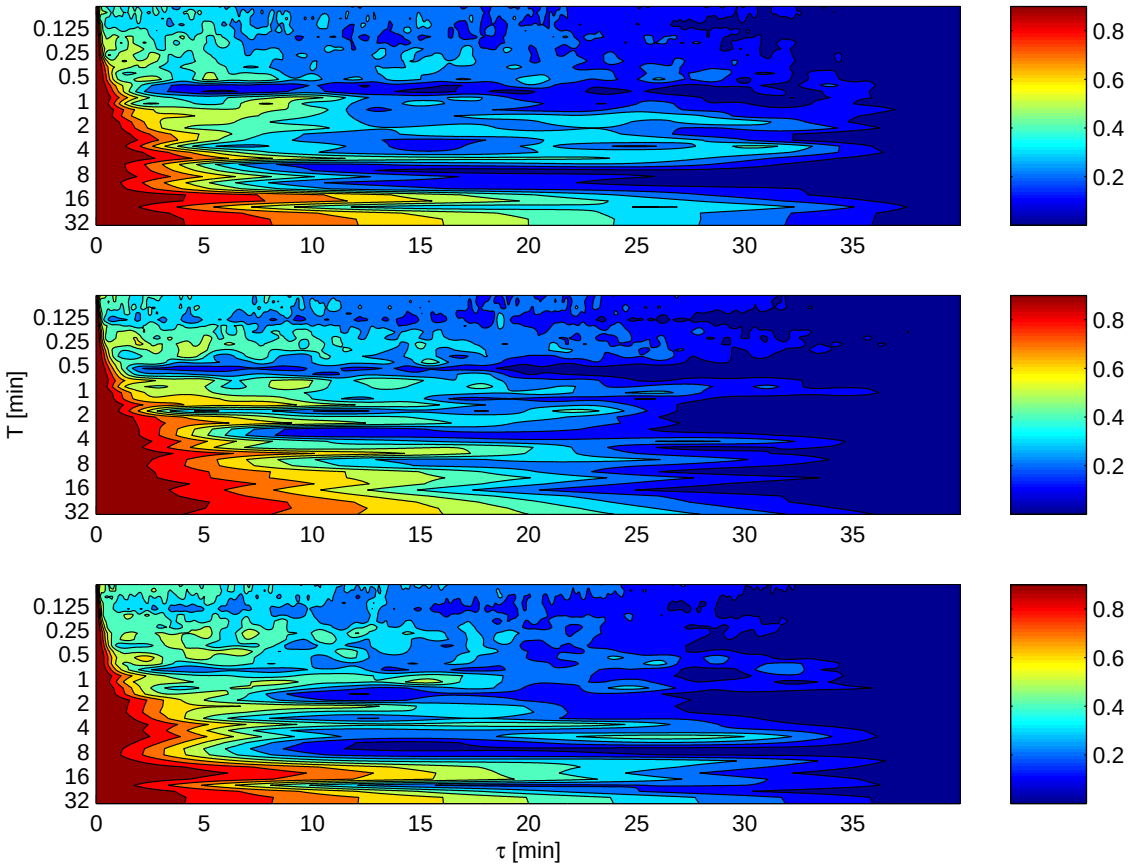

Figure 4.30: Type C autocorrelation scalogram of the longitudinal, transversal, and vertical velocity components.

scalograms in figures 4.25 to 4.27 is a transient phenomena where event size is readjusting for new flow conditions. Nevertheless, and by the summary information from table 4.10, we conclude that at least in flow Type A and C three types of events are present, separated by an uncorrelated scale that originates a gap in the autocorrelation scalogram at scales from 0.8 to 3-min and 6.0 to 8.0-min. The identification on what type of event is being detected is our goal in next two subsections.

4.3.7 Quadrant analysis

Pope (2000) refers quadrant analysis for studies on coherent structures at the near-wall regions of the boundary layer $y/\delta < 0.01$, where the observed structures are confined close to the wall, y and δ are respectively the instrument and free-flow distances from the wall. Shiau and Chen (2002) presents a quadrant analysis near ground with measurements from sonic anemometer, while Feigenwinter (1999) presents results for urban and Wesson et al. (2003) over forest boundary-layer. A common characteristic from Caniçal site study and

Shiau and Chen (2002) is the fact that both were made in coastal regions, however with great differences. The maximum mean wind velocity was 9.30 ms^{-1} and turbulent intensity and turbulence ratios where slightly inferior to flat terrain. Caniçal study was made over a site with higher complexity where the upstream separation of the flow has to be considered. We propose the extrapolation of quadrant analysis from application range, near-wall flow, to a flow separation area. The main goal is to identify common features and differences from the flow Types A to C.

Pope (2000) presents the quadrant analysis in a boundary-layer flow where the lateral velocity is null and the fluctuations of u' and w' are associated with coherent structures in the vertical plane. In atmospheric flows the coordinate rotation allows setting $\overline{v}$ and $\overline{w}$ to zero. Some residual lateral momentum flux still persists but the overall turbulent flux is dominated by the longitudinal component $\overline{u'w'}$.

Table 4.11: Quadrant analysis according to flow type. The subscribe $_s$ is for the samples identified in the previous subsection 4.3.4. The covariances are in m^2s^{-1}.

Flow Type	$\overline{uw}$	$\overline{vw}$	$\overline{uw}/\overline{vw}$	$1/Ex$	γ
A_s	-0.307	0.538	-0.571	2.024	1.937
B_s	-3.828	0.502	-7.634	4.274	1.132
C_s	-11.807	0.035	-333.333	10.870	0.750
A	-0.501	0.458	-1.094	2.169	2.549
B	-4.111	0.678	-6.061	3.413	1.851
C	-11.121	-0.522	21.277	9.259	0.731

Table 4.11 summarizes the results for the quadrant analysis applied to three type of samples and also to the whole series according to the flow type. Type A flow is not suited for quadrant analysis because $\overline{vw}$ is almost twice larger than $\overline{uw}$, Pope (2000). Longitudinal and lateral covariance ratio for Type B and C are 7.6 and 333.3 times for the samples, 6.0 and 21.3 times for the totality of the two sets. Thus 90.6% of the whole data series may be analysed by quadrant analysis.

The table also presents the inverse of the Exuberance to facilitate the evaluation of the results. However, prior to the identification of the type of structure, we have to alert that the terms *ejection* and *sweep* are associated with phenomena within the inner-layer. Nevertheless, *ejection* is a low-speed fluid outward from the wall and *sweep* a high-speed toward the wall, and we will maintain this terminology. The same is true for *gust*, as a fluid acceleration or deceleration in a certain time interval.

For Type B sample we verify that the ratio of organized over non-organized turbulence, given by the inverse of the Exuberance, indicates that organized turbulence, ejections, sweeps and gusts are over 4 times larger than inward or outward non-organized turbulence (figure 4.31). This value increases to 10.8 for the flow sample of Type C. For simplicity, we will refer just sweeps instead of sweeps and gusts because both are related to quadrant 4

and we ignore any identification procedure beyond the intermittency factor to identify the events. With the intermittency factor γ, that measures the ratio between ejections and

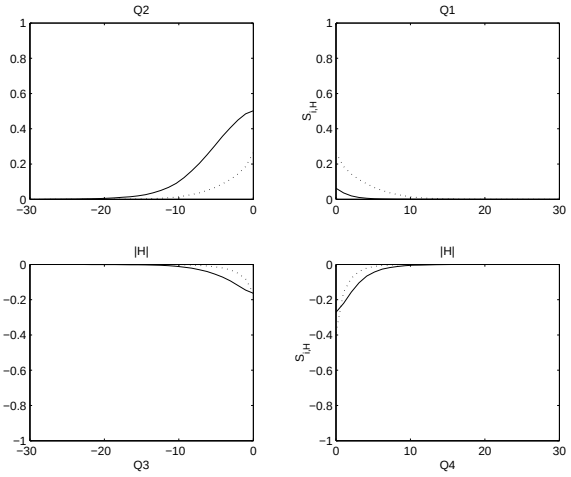

Figure 4.31: Type B flow flux and time of the longitudinal turbulent flux for all 4 quadrants. Continuous line for flux and dashed for time flux contribution.

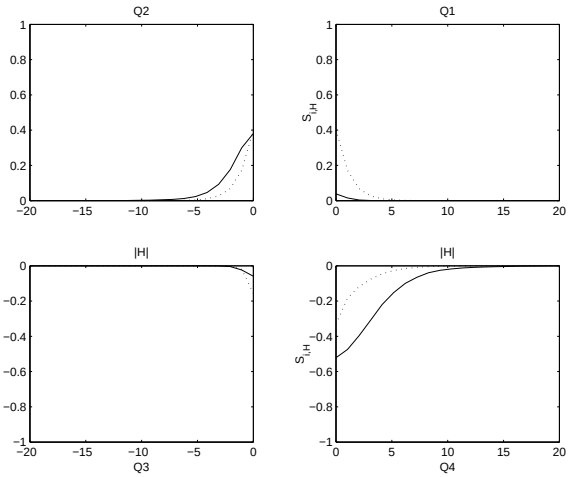

Figure 4.32: Type C flow flux and time of the longitudinal turbulent flux for all 4 quadrants. Continuous line for flux and dashed for time flux contribution.

sweeps, we verify that Type B and C differ in the balance between events (figures 4.31 and 4.32). For Type B sample γ is 1.3 while Type C is 0.8. In the first, there is a predominance of the ejections over the sweeps, while the second is the opposite. This pattern is enhanced when extending the analysis for the whole Type B and C series, ejections are 1.9 times the sweeps in Type B while sweeps are 1.4 times the ejections for Type C.

The cumulative stress and time fractions for flow Type B were also analysed (figure 4.33). Almost 80% of time the turbulent flux is predominantly from quadrant 2 and 4

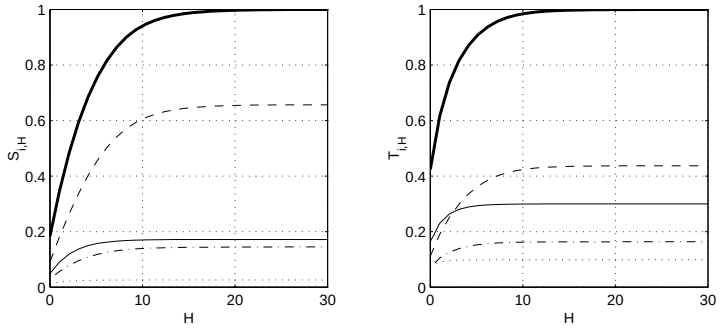

Figure 4.33: Type B flow cumulative flux and time of the longitudinal turbulent flux for all 4 quadrants. Thicker line for the overall contribution, dotted for quadrant 1, hashed for quadrant 2, dot line for quadrant 3 and continuous for quadrant 4.

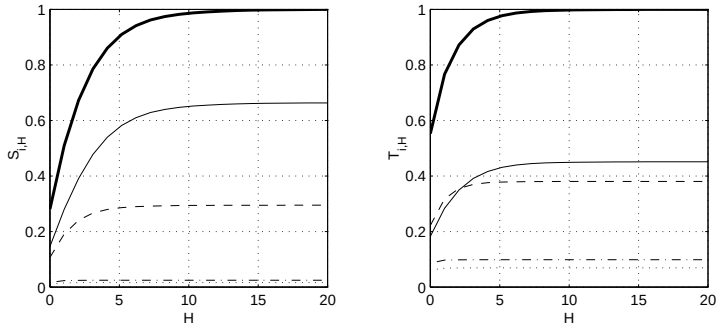

Figure 4.34: Type C flow cumulative flux and time of the longitudinal turbulent flux for all 4 quadrants. Thicker line for the overall contribution, dotted for quadrant 1, hashed for quadrant 2, dot line for quadrant 3 and continuous for quadrant 4.

(hashed and continuous lines), corresponding to turbulence inferior to $2H$. Each quadrant contributes differently for the turbulent flux, quadrants 2 and 4 are equally balanced while quadrant 1 is 5% inferior to Q-3. Alternativelly, the cumulative stress fraction indicates that only 50% of the stress is inferior to $2.5 \times H$, and the small scale turbulence is equally balanced in the 3rd and 4th quadrants. For $2.5 \times H$, the quadrant 1 stress contribution had already converged to 2% of the overall turbulent flux. For a hole size of $5 \times H$, we observe that 75% of the stress corresponds to 90% of the time, where the difference between quadrants 2 and 4 is 5%. However there is a clear distintion from 2.5 to $5 \times H$ on the stress contribution from the 2nd and 4th quadrants, 2nd quadrant stress is 3 times larger, indicating the predominancy of ejections over sweeps for that size interval. Larger structures, over $5H$, are present only in 10% of the series but correspond to 25% of the longitudinal stress, and are due solely to ejections from the wall. Turbulent transport by ejections is clear dominant in the large-scale domain for Type B flow.

As we verify in table 4.11, Type C flow is different because the sweeps are more frequent than the ejections (figure 4.32) and the scale of the events also differ. From the stress and

time fraction cumulative display (figure 4.34) we verify that almost 80% of the stress is bounded to size hole inferior to $2.5 \times H$, corresponding to more than 90% of the time, equally divided into the 2nd and 4th quadrants. For this small scale interval, the stress contribution of the 4th quadrant is almost twice the 2nd quadrant. For 90% of the time, the events are inferior to $5 \times H$ and correspond to 90% of the turbulent stress. Larger than $5 \times H$ scales correspond only to 3% of the time and 10% of flux. This large scale stress is predominantly from the 4th quadrant corresponding to sweeps or gusts in a smaller scale than the Type B flow.

4.3.8 Comparison against simulation results

The objective of this subsection is to compare the measurements results with simulation from VENTOS® software (Palma et al., 2002). Two problems have difficulted a direct comparison of results: having a stationary series from measurements; and controlling the velocity at a given point inside the simulation domain to match mean measurement conditions.

The comparison was for flow Type A for 2 reasons: the mean wind velocity differs only 0.5 ms^{-1} and the series was steadier as we may visualize in the last hours of figure 4.7a to 4.7c, where turbulence intensity and gust factor were at their minimum values. The simulation results for an 11 ms^{-1} northerly wind in the boundary of the mesh yield a 13.39 ms^{-1} at the measuring point (table 4.12). The velocity components from simulation have a narrower distribution than measurements: standard deviation of longitudinal component is 10 times smaller than the measured, transversal and vertical are 3 and 5 times smaller.

Table 4.12: 1st to 4th statistical moments of Type A flow velocity components and from the simulations at the same point from October 10th, 12:35 to 11th, 11:35, 2001. All velocity quantities are in ms^{-1}.

		$\overline{x}$	σ	sk	k	min	max
Measurement	u	12.61	2.17	-1.63	6.88	-0.72	21.84
	v	0.02	1.85	-0.40	5.21	-14.56	9.50
	w	0.01	1.00	0.56	7.15	-8.15	9.18
Simulation	u	13.39	0.21	-0.56	1.67	12.99	13.63
	v	0.26	0.62	-0.20	1.58	-0.72	1.09
	w	-0.17	0.22	0.55	1.80	-0.42	0.24

The simulations show in the vicinity of the turbine an eddy in the uv plane (Palma et al., 2002) with a period of oscillation of 2.45 for 1st harmonic, 1.21 min for the 2nd and 35 s for the 3rd (figure 4.35). The 1st harmonic dominates over the signal corresponding to 91% of the energy of the signal while the 2nd corresponds to 7.2 and the third to a residual

1.8%. The cospectra of the simulation components share the same frequency therefore we refrain from showing this result.

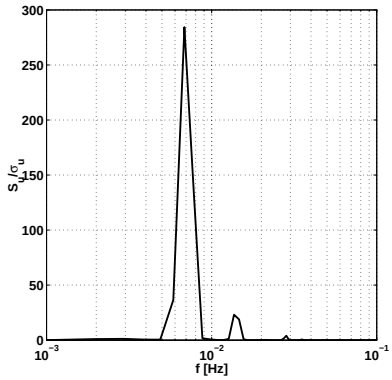

Figure 4.35: Normalized spectrum at turbine 2 site.

Figure 4.36 shows the normalized spectrum of u for Type A flow with the main harmonics of the simulation referenced. We observe that it differs from the spectrum at figure 4.35 in two aspects: a low-frequency event and the exponential decay are present. The mean oscillation period of this event is 6-min, confirmed by the wavelet spectra at figure 4.25, and the exponential energy decay is observable from the spectrum slope. Focusing in the events predicted by the simulation, we observe that the differences are small: the second peak in figure 4.36 correspond to events with 2.9-min oscillation period for a simulation prediction of 2.5-min event, a 24 s difference. This difference is reduced to less than 10 s for the 2nd harmonic, 1.4 to 1.2-min respectively. Other feature observable in figure 4.36 is the larger energy contents of the 2nd harmonic, for the simulation results it correspond to 7% of the 1st harmonic while from measurements it was 4 times larger.

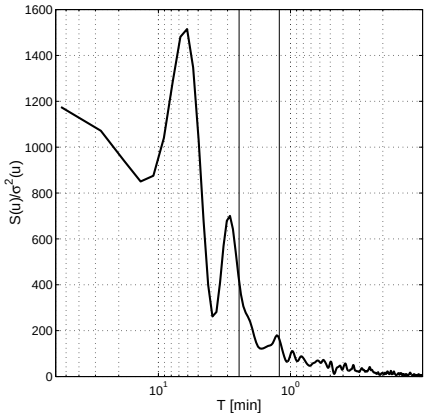

Figure 4.36: $S(u)/\sigma^2(u)$ of Type I flow. The vertical continuous lines reference the first two harmonics of the simulation.

The first conclusions of this comparison is the approximation of the simulation predic-

tion on the existence of periodic events in the range of 2.5 and 1.2-min oscillation period. However, larger scale events, 6-min oscillation period, were not captured by the simulation. We know also from the wavelet scalograms results at subsection 4.3.6 that the scale of the events changes with time once the series is nonstationary, and that different scale events coexist either simultaneously or not. Another indicator of this periodicity is observable from the first cospectra presented for the identification on the types of flows, figures 4.21 to 4.23.

Repeating the cospectra analysis to the Type A flow, 3×40-min blocks as in subsection 4.3.5, and excluding all large scale events, we build a mean $\overline{uv}$, $\overline{uw}$ and $\overline{vw}$ cospectra upon each individual cospectra normalized by the covariances for the frequency range at interest. Some of the most energetic peaks at mean $Co(uv)$, $Co(uw)$, and $Co(vw)$ (figure 4.37) agree with frequencies from simulation, namely in uv and vw planes.

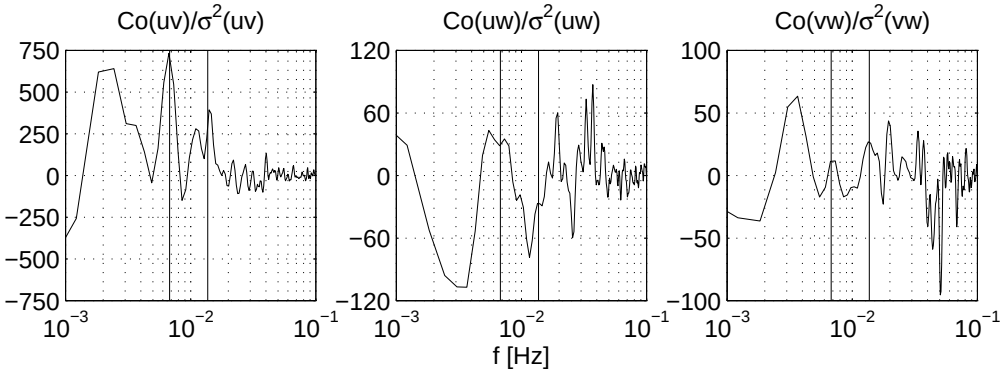

Figure 4.37: Mean uv, uw, and vw cospectra of the time series for 32×40-min time intervals. The vertical lines reference the 1st and 2nd harmonics of the frequency detected by the simulation.

The frequency peaks at figure 4.37 are organized in table 4.13 by energy decreasing order. The values between brackets are the fraction of energy of each peak normalized by the larger peak. By the energy rank we observe that the frequency of the eddies detected by the simulation are followed by larger eddies in the uv and uw plane, corresponding to 14 and 6.9-min events. The larger events in the vw plane correspond to 4.2 min events. The simulation results close remarkably to the 4th peak in the uv and uw planes, with 28 and 62% of the energy content. In the vw plane, the measured cospectra approaches the 2nd harmonic of the simulation, 1.5 against 1.2-min events, corresponding to the 2nd more energetic peak, 90%. Other interesting feature refers to the 3rd harmonic of the simulation, 35 s period events. Though corresponding in simulation to only 2% of the energy, the presence of half minute events was detected at $Co(uw)$ and $Co(vw)$ with over 30% of the spectral energy.

Table 4.13: Cospectra peak frequencies $\times 10^{-3}$ [Hz] in energy descending order of the peaks at figure 4.24. The value between brackets is the relative energy fraction of each peak.

		$Pf_{Co(uv)}$		$Pf_{Co(uw)}$		$Pf_{Co(vw)}$	
Measurement	1st	1.2	(100)	2.4	(100)	4.0	(100)
	2nd	2.4	(93)	1.2	(93)	11.5	(90)
	3rd	2.9	(37)	3.6	(90)	34.0	(51)
	4th	6.4	(28)	6.4	(62)	1.2	(33)
	5th	9.5	(14)	11.5	(44)	23.1	(32)
	6th	18.9	(10)	41.9	(35)	30.9	(32)
Simulation	1st h.	6.8	(100)	6.8	(100)	6.8	(100)
	2nd h.	13.7	(8)	13.7	(8)	13.7	(8)
	3rd h.	28.3	(2)	28.3	(2)	28.3	(2)

4.4 Conclusions

Northerly wind flow at Caniçal wind farm was complex with periodic events and coherent structures, incompatible with wind turbine operations. Because the measuring point was within the path of those events, the series presented large unstationarities requiring alternative methodologies based in acceleration criteria and ogive function for data analysis. The flow at the site presented the following characteristics:

1. The existence of eddies in the vicinity of the measuring point with a period of 2.9-min. This conclusion was confirmed from PDF intermittency, spectral and wavelet analysis. Such results were in agreement with simulation results presented by Palma et al. (2002) with VENTOS® software which yielded a 2.5-min oscillation period for these eddies.

2. Vertical components of the flow should be accounted for because 32% of the measured flow presented vertical components that exceeded 20% of the mean flow. These components were most likely associated with *sweeps*, *gusts* and *ejections* that coexisted with the eddies.

3. The wind flow was classified into 3 types of flow:

   Type A The steadier flow (comparable with simulation) with events of 1.4, 2.9 and 6-min.

   Type B The most frequent flow type, with similar periodicity as flow Type A. The differences were in the presence of events larger than $5 \times H$ that were responsible for 25% of the turbulent flux transport and corresponded to ejections from the wall.

Type C The simulation peaks were again present but there was an energy gap between 6 and 16-min events. Turbulent transport was made by scales inferior to $5 \times H$, 90% corresponding to sweeps or gusts.

4. The mean difference from cup to sonic anemometer was 2.3% as consequence of cup anemometer overspeeding and sensitivity to severe vertical components of the flow and was in agreement with cup anemometer flow inclination sensitivity from Papadopoulos et al. (2001).

Standard wind resource assessment methodology based in 10-min averages was not able to capture all the features and meanders of the flow at Caniçal wind farm because of inferior resolution. However, higher resolution measurements with cup anemometer and wind vane would make possible the detection of the events at the site, nevertheless with loss on wind vertical component. Detailed information of horizontal turbulent field may led to abandon such terrains before turbine siting.

Chapter 5

Complex terrain - Case II

Abstract

Sonic and cup anemometer (Metek model USA-1 and NRG model 40) measurements were made at 40 m agl to characterize the wind flow over Paúl da Serra plateau, Madeira Island, located at 1500 m altitude. The vertical component of the wind field proved to be reduced in spite of the tower location, close to a cliff with high slopes. Mean velocity measured by the sonic was 1% lower against cup anemometer while turbulence intensity was 11% higher. Spectral analysis confirmed statistical analysis on the turbulent characteristics of the flow as close to flat terrain (it=8%). Turbulence ratios $\sigma(v)/\sigma(u)$ and $\sigma(w)/\sigma(u)$ were 91 and 60% and the flow could be treated as stationary over 30-min averaging periods, validating cup anemometer results. No event that compromised cup anemometer measurements was identified. Spatial divergency of the flow over the plateau was also characterized recurring to cup anemometers measurements for 3 other stations located between 2 and 4 km apart. One station presented a 115 to 72° shift in wind direction depending on the incoming flow, most likely due to effects induced by the terrain. Mean velocity correlations proved to be higher for southwest flow for all stations than northeast flow, R^2 =89.6%. However, only in one station turbulence intensity and gust factor could be correlated for northeast wind to the station where sonic measurements took place. Turbulent intensity at all 4 stations was within wind turbine design values.

5.1 Introduction

This chapter reports sonic measurements made at a plateau at 1500 m altitude in Madeira island, to complement information from 4 measuring stations operating with cup anemometers. These stations were placed in locations to cover a representative area for future implementation of wind farms.

Due to the complexity of the terrain, steep slopes, cliffs that drop abruptly to the sea, the wind assessment study included sonic measurements made in one of the towers that is located close a cliff.

The measurements addressed the following questions:

1. Wind vertical velocity at hub height, 40 m agl.
2. Wind turbulence intensity.
3. Comparison of velocity, turbulence intensity and gust factor from sonic against cup anemometer.
4. Relating velocity and turbulence intensity to other stations in the field.
5. Identification of any special feature in the flow that would be pernicious to wind turbine performance.

The final objective was with pinpointed measurements with sonic anemometer to unveil and complement information obtained by cup anemometers following the recommended practices for wind turbine assessment studies (Pedersen et al., 1999). Sonic anemometer enables the measurement of vertical velocity, that is expected to be large on the edge of a plateau and, due to the higher resolution of the instrument, detects any special feature in turbulence.

The sonic measurements were made side-by-side with a cup anemometer and comparison of mean and turbulent intensity for that period are of interest because the short time when both instruments operated simultaneously would provide the necessary information for extrapolation with long term data from cup anemometer.

A total of 4 measuring stations were installed in the Paul da Serra for over a year and information on spacial divergence of the mean flow and turbulent indicators will aid in flow characterization over the plateau.

Chapter outline

This chapter is divided in 4 sections: introduction, experiment description, results and analysis, and conclusions. In the experiment description (section 5.2) we describe the

terrain and tower display, followed by the report on methodology and instrumentation used in the field. The sonic corrections due to transducer shadow effect and comparison with the cup anemometer at the same tower are at subsections 5.2.3 and 5.3.2. The result and analysis section deals first with the mean and turbulent wind field measured by the sonic anemometer, extending the analysis to series stationarity and spectral characterization of the turbulent flow in subsections 5.3.1 to 5.3.1.2. This section ends with the analysis of the divergence of the flow over the plateau from information of 4 measuring towers, subsection 5.3.3. The conclusions are presented in section 5.4.

Acknowledgment We would like to thank Empresa Electricidade da Madeira (Madeira Electrical Utility), Instituto Nacional de Engenharia Mecânica e Gestão Industrial – INEGI, and specially Prof. Álvaro Henrique Rodrigues for yielding the long-term data from stations PORT 210 to 213.

5.2 Experiment description

5.2.1 Site description

The local under analysis is a plateau at 1500 m altitude located on the western half of Madeira Island, named Paul da Serra. This plateau is roughly 24 km^2; to northeast and northwest the plateau is limited by cliffs that drop to sea level in just 2 km while to southwest and west the slope is slightly gentler (figure 5.1). About 10 km east, there is the highest peak in the Island, at 1820 m altitude. Figure 5.2 shows the map of the site and the location of 4 measuring stations: Port 210 to 213 (table 5.1).

Station Port 213 is located at 1554 m hight and is in the northern part of the plateau overseeing the northern coast of the Island. Port 212 and 210 are almost aligned southeast of Port 213: Port 210 is at an higher elevation, 1571 m, while Port 212 is in a more central area of the plateau, at 1463 m. Station Port 211 is the southern station of the triangle formed by the whole measuring set, located in lowest area of the plateau at 1412 m overseeing the southwest coast of the Island.

Measurements are being made with the stations equipped with cup anemometers at 20 a 40 m agl since February 2001, but we will reference only measurements made from August 2002 because it is the date that all stations were audited and new equipment installed, namely GSM communication devices that enable remote download of data and clock synchronization for stations Port 210 and 213.

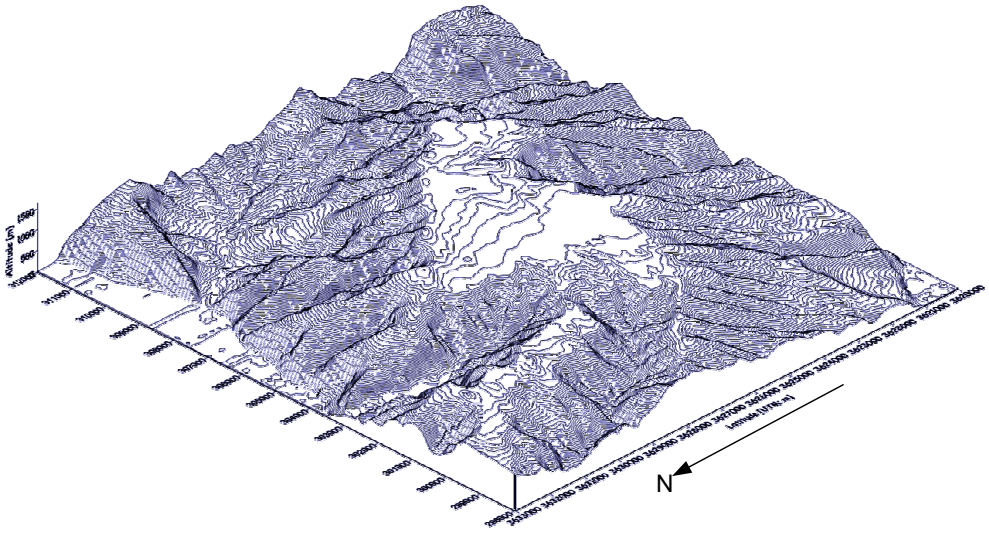

Figure 5.1: Paul da Serra elevation map. The location of measuring stations are presented in figure 5.2 and table 5.1.

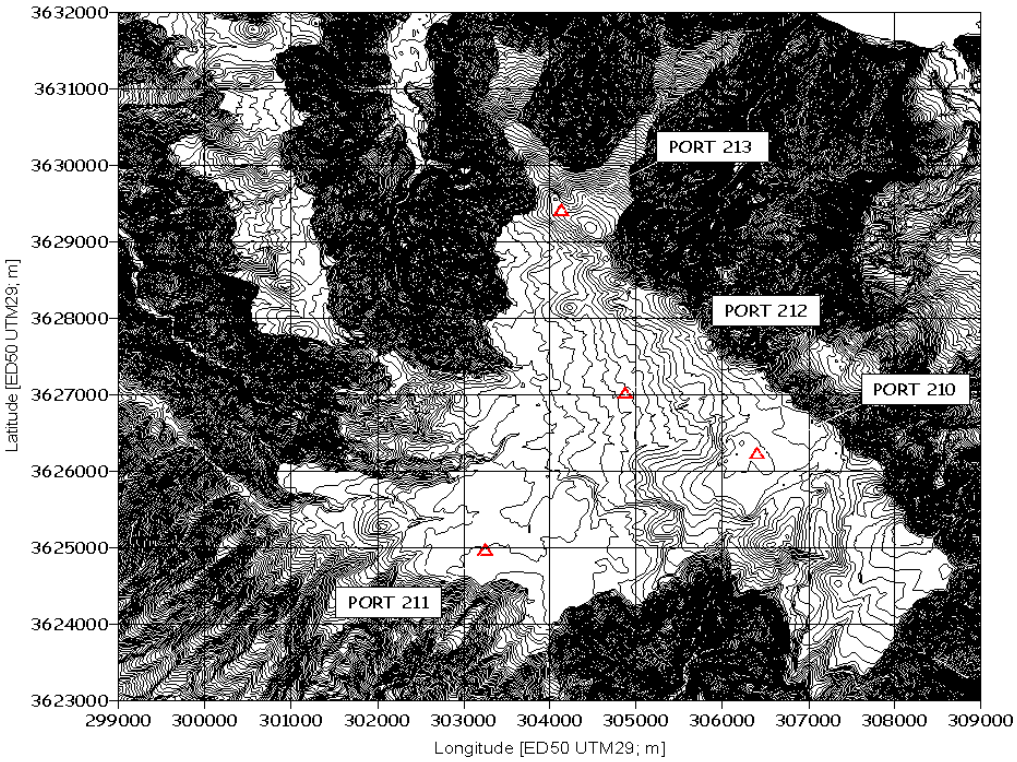

Figure 5.2: Paul da Serra plateau and location of the measuring stations.

5.2.2 Equipment set-up and measurement schedule

The sonic anemometer Metek (model USA-1) was installed in the top of the measuring station Port 213. To avoid tower interference it was placed upstream in a 2 m horizontal

Table 5.1: Measuring stations at Paul da Serra.

Station	UTM coordinate	UTM coordinate	altitude [m]
Port 210	306400	3626217	1571
Port 211	303246	3624954	1412
Port 212	304871	3627004	1463
Port 213	304129	3629840	1554

boom up oriented to geographical north. A NRG (model 40) was already installed at the same height, 40 m agl, and a second one at 20 m.

Power and data connection cables descend to tower base, being connected to the data-logger and power supply source. Because the site was remote, without any external power supply, the sonic was used in a remote mode. Two data storage options were used: collecting the data into a laptop computer thus without memory limitations; collecting the data into a 4 Mb PC-MCIA card from the sonic data-logger. The first configuration was used during the day with supervision, and by night the computer was disconnected and the data was stored in the PC-MCIA card for unmanned operations. In this second case the storage interval had to be increased from 1/20 s to 2 s averaging due to memory limitations. The NRG cup anemometer operated and stored data independently to a NRG-91000 Plus data-logger.

The measurements started in July 30 to 31 of 2002 and produced two data sets identified as Daily and Nightly periods differing only in averaging time of measured quantities, table 5.2. Data post-processing confirmed the quality of each data set with no value being neglected.

Table 5.2: Schedule and measurements parameters at Paul da Serra – station Port 213.

Date	Start time [hh:min]	End time [hh:min]	Sampling Rate [Hz]	Averaging time [s]
07/30	13:01	19:33	20	0
07/30 to 31	19:56	08:50	20	2

5.2.3 Sonic corrections

The distortion caused by the transducer array was corrected as in subsection 4.2.3 according to equation (3.4). The results are presented in figure 5.3 for 1-min averages for clarity. The corrections lead to a mean reduction of 2.5% in total velocity. That may be considered a large correction but the measurements were made for a particular wind direction thus the mean bias was not compensated by flow approaching from other directions were correction would be opposite thus reducing the mean offset.

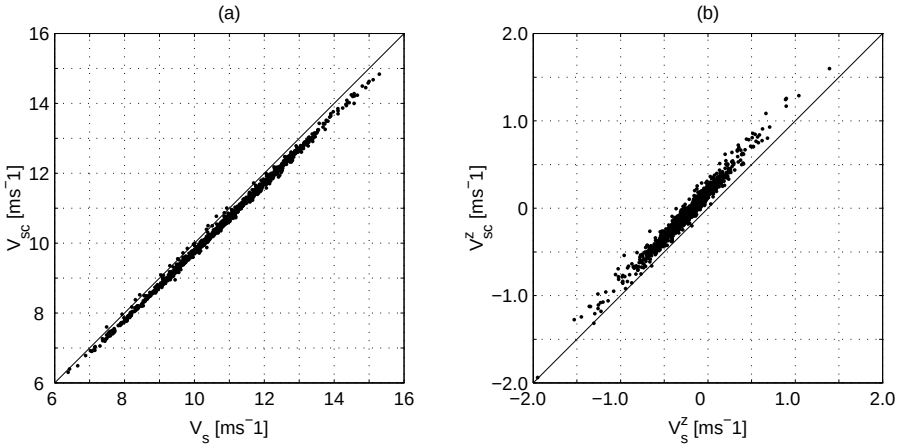

Figure 5.3: Velocity comparison for the measured V_s velocity and corrected sonic velocity V_{sc} (a). Vertical velocity V_s^z comparison for the measured and corrected sonic velocity V_{sc}^z (b).

Vertical velocity corrections present an underestimation of 17.3% from measurements to corrected value. Altough deviation is large, the absolute corrections are not due to low vertical velocity and mean correction for the vertical component is inferior to 0.2 ms^{-1}.

5.3 Results and analysis

5.3.1 Mean and turbulent wind field

During the measurements the wind was from the north quadrant bounded to a 30° interval (figure 5.4). The statistics of velocity (total, horizontal plane and vertical component), turbulent intensity, gust factor and turbulent kinetic energy are presented in table 5.3. Figures 5.5a to 5.5d show temporal evolution of velocity, turbulent intensity, gust factor and turbulent kinetic energy.

The mean wind velocity was slightly higher than the Caniçal flow at Chapter 4, 10.85 against 10.33 ms^{-1}. In spite of gradual increase during measurement, from 8 to 13 ms^{-1} at figure 5.5a, total and horizontal velocity fluctuations are inferior to Caniçal flow. Velocity standard deviation is 2.5 times inferior than previous complex terrain case, table 5.3.

The vertical velocity is ascending with a mean value of 0.24 ms^{-1}, half of the mean value of Caniçal flow and the standard deviation is 4.3 times smaller, table 5.3. Also the maximum and minimum values measured are bounded to a restrict interval from approximately 4 ms^{-1}, ascending or descending. These are remarkably low values for a tower located upstream and few meters from a steep slope as we verify from figure 5.2.

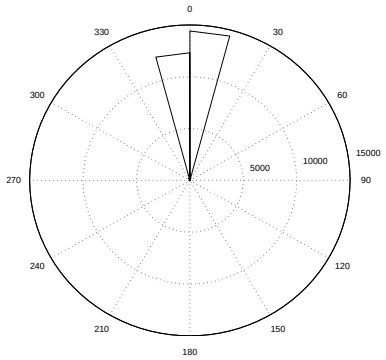

Figure 5.4: Wind rose at Port 213 during sonic measurements.

Table 5.3: 1st to 4th statistical moments of the flow velocity $\overline{v}$, horizontal velocity $\overline{v_h}$ and vertical velocity $\overline{v_z}$ in ms^{-1}. Turbulence intensity, it, gust factor G, and turbulent kinetic energy TKE in $\mathrm{m}^2\mathrm{s}^{-2}$ are calculated for 10-min averaging periods. The time series is depicted in figure 5.5.

	$\overline{V}$ [ms^{-1}]	$\sigma(V)$ [ms^{-1}]	$sk(V)$	$k(V)$	min [ms^{-1}]	max [ms^{-1}]
$\overline{v}$	10.85	1.64	-0.11	2.88	4.07	17.75
$\overline{v_h}$	10.83	1.65	-0.12	2.88	4.07	17.75
$\overline{v_z}$	0.24	0.55	0.13	7.83	-3.95	4.34
it_{10min}	0.08	0.03	0.69	2.85	0.02	0.16
G_{10min}	1.15	0.07	1.52	6.46	1.05	1.46
TKE_{10min}	0.40	0.37	1.78	6.12	0.03	1.70

Mean turbulent intensity is also low, 8 against 34% of Caniçal flow, surpassing 15% few times during measurement, figure 5.5b. It is also interesting to observe that the flow is not perturbed, at this height, by the upstream cliff few meters away.

Gust factor and turbulent kinetic energy are depicted respectively in figures 5.5c and 5.5d. Again, both parameters are lower than the ones recorded at Caniçal. Mean gust factor is almost half of the mean value while turbulent kinetic energy is 40 times lower. Note that from the 13th hour gust factor and turbulent kinetic energy increase and become spikier, however these maximum values are inferior to the minimum recorded at Caniçal flow, confirming the steadiness of the flow at station Port 213.

The probability density function of the mean wind and vertical velocity are presented in figures 5.6a and 5.6b. Both distributions are single mode, slightly asymetric, and for the case of PDF(V), approaching a gaussian distribution ($k = 2.88$). The vertical velocity PDF is narrower ($k = 7.83$) where 39.7% of the records correspond to descending while 60.3% to ascending wind.

Longitudinal turbulence intensity, $\sigma(u)/u$, and turbulent ratios are presented by velo-

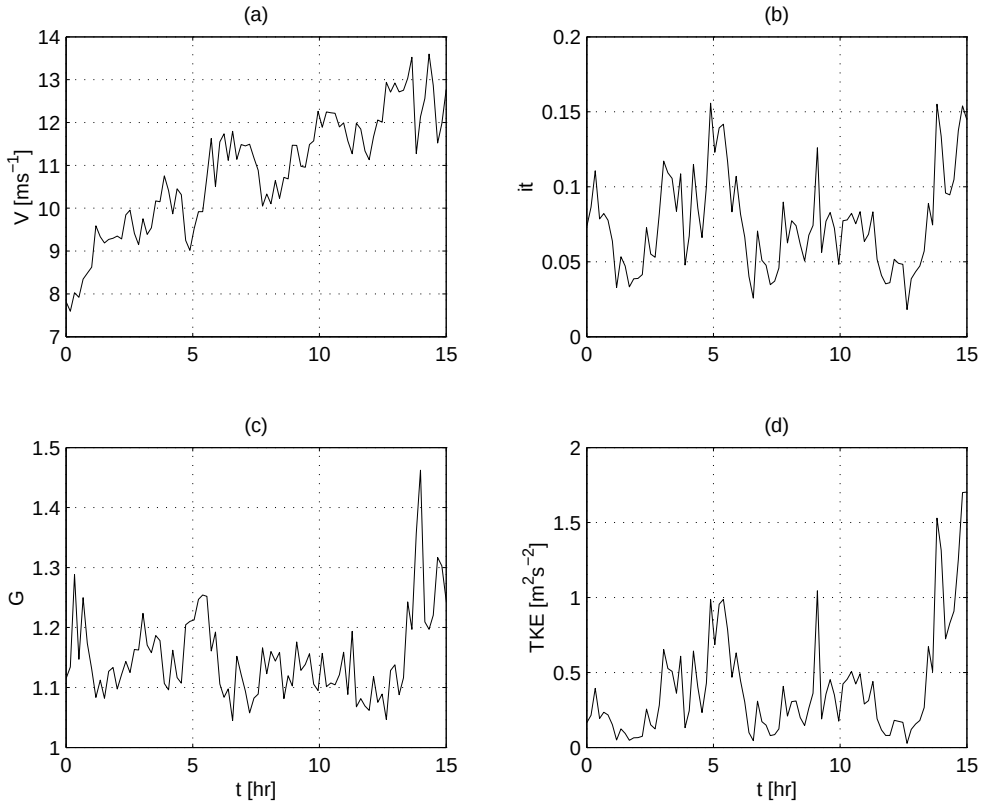

Figure 5.5: Velocity, turbulence intensity, gust factor and turbulent kinetic energy for 10-min periods at Port 213 during sonic measurements.

city bins in figure 5.7 for 1 and 10-min averaging intervals. Mean longitudinal turbulence intensity for 10-min is scatter but bound from 5 to 10%. The mean value equals total velocity turbulent intensity, 8%, with 3% standard deviation. For 1-min intervals, turbulence intensity decays to a constant value of 5% and standard deviation reduces to 1%.

Turbulence ratios $\sigma(v)/\sigma(u)$ and $\sigma(w)/\sigma(u)$ differ from Caniçal flow. Both turbulence ratios maintain a constant trend independently of wind speed at 1 and 10-min averages, while in Caniçal flow turbulent ratios increase with speed for 1-min and decrease for 10-min. In this case $\sigma(v)/\sigma(u)$ maintain a constant trend around the mean value of 91% and for velocities above 10 ms^{-1} the mean ratio increase 1%, 10% above the reference value for flat terrain, Papadopoulos et al. (2001). For 10-min averaging interval $\sigma(w)/\sigma(u)$ mantains a constant feature with a mean value of 60% (50% for flat terrain). On the other hand, 1-min statistics of $\sigma(w)/\sigma(u)$ present a slight decrease for larger velocities and a mean value of 82%. However, caution is recommended in this analysis because it does not cover a large range of velocity intervals because the flow is steadier than Caniçal and sonic measurements were unable to cover a wider range of velocities.

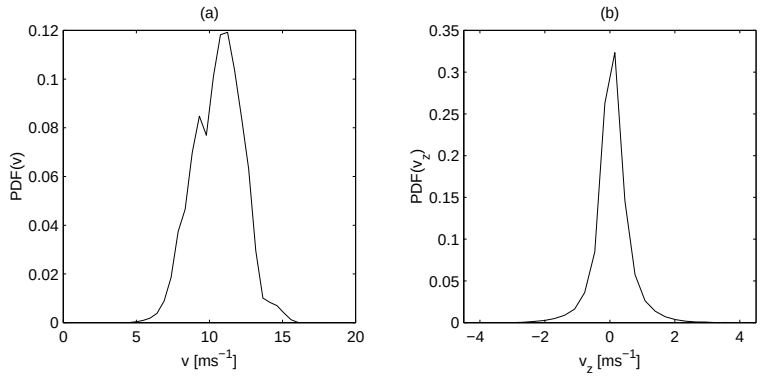

Figure 5.6: PDFs of the horizontal (a) and the vertical wind velocity (b).

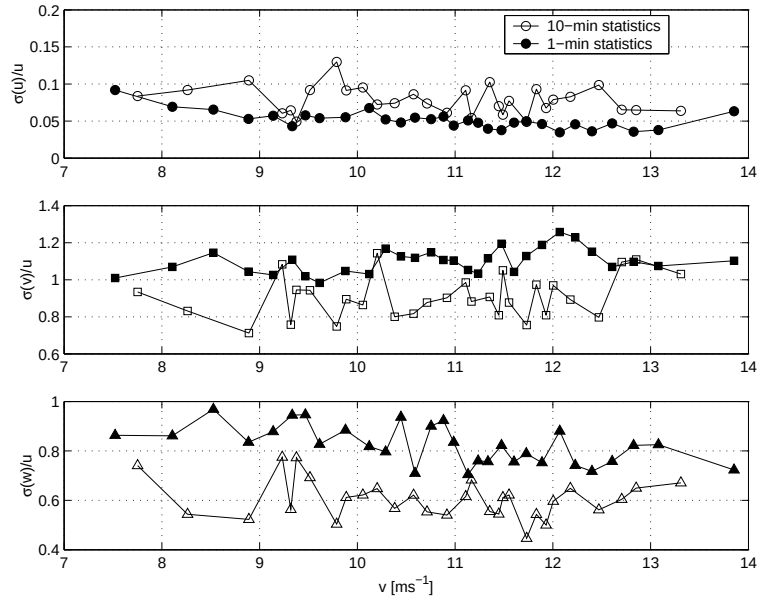

Figure 5.7: Average longitudinal turbulent intensity and turbulent ratios, $\sigma(v)/\sigma(u)$ and $\sigma(w)/\sigma(u)$ for 10 and 1-min intervals (color filled).

5.3.1.1 Stationarity of the series

The methodology recurring to the ogive function was repeated for Paul da Serra flow to establish time interval from which we may consider the series stationary. Therefore cospectra of momentum flux were calculated for the whole series after detrending and rotating into streamline coordinates, figure 5.8a.

The ogive function, equation (1.14), is shown in a semi-logarithmic scale in figure 5.8b and in a linear scale from 10 to 100 m in figure 5.8c. The convergence of the function is slow, but negligible contribution to the covariance at time intervals over 30-min are encountered,

figure 5.8c. We may conclude that the series may be treated as a stationary one for time intervals over 30-min. However, to confirm that statement a test was performed to the whole data set by comparison of covariances of all components, equation (1.12).

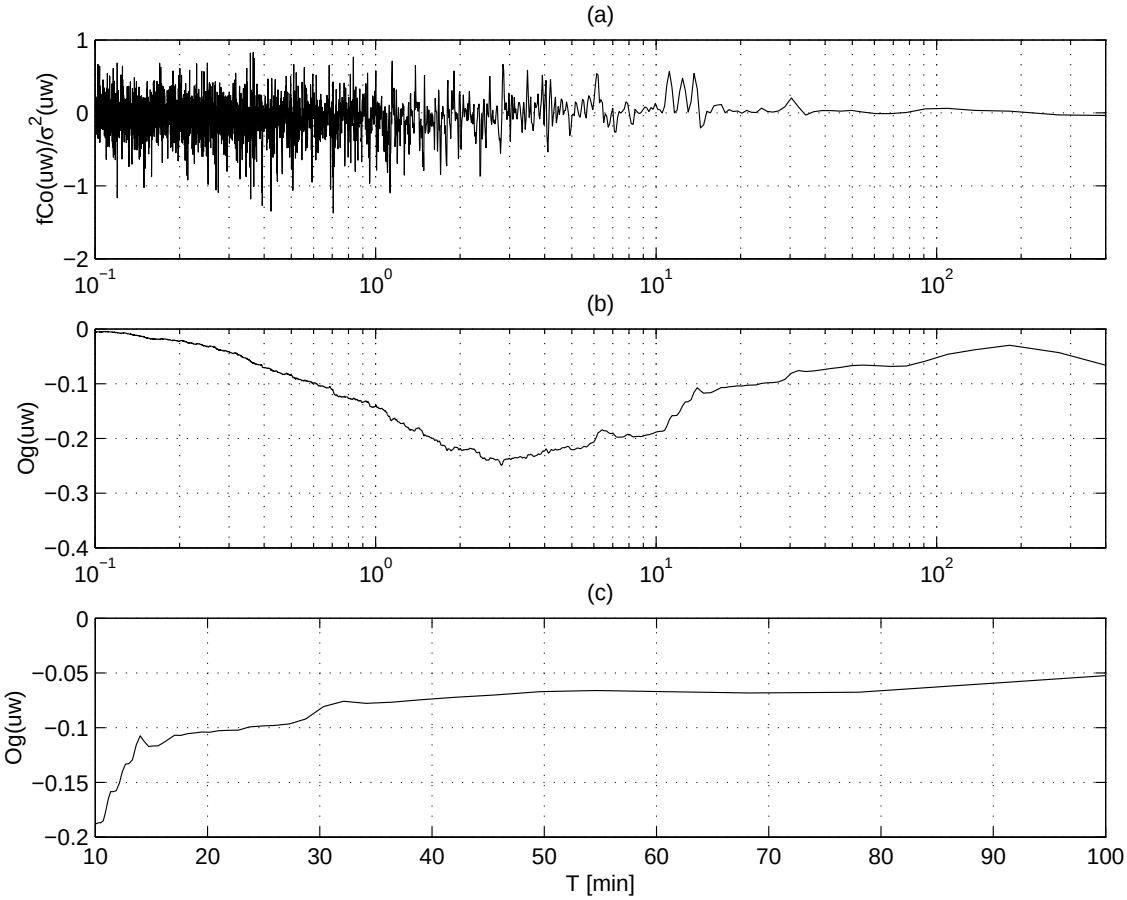

Figure 5.8: Momentum flux cospectra (a), ogive of the momentum flux (b).

The data set was divided into time blocks of certain length, corresponding to a time interval, for instance 10-min. Then, by comparing the mean covariances of longitudinal, transversal and vertical velocity components with the same data-set divided differently, we verify the existence of minor differences for time averaging larger than 30-min, table 5.4. Note that mean covariances differ less than 0.1 m^2s^{-2} for the same data-set of 10-min by 90 time blocks against 60-min by 15 blocks. For time intervals over 30-min also variances differ below 0.1 m^2s^{-2}. Therefore, and because the cup anemometer stored all 10-min averages it would include all large scale changes of the flow, with a measuring configuration that was suitable for this flow.

Table 5.4: Covariances for different averaging intervals. The size of the series remains the same once equals Time interval × time block. The differences from mean quantities are calculated for the reference quantity at 60-min.

Time interval $[min]$	Time block $[quantity]$	$\overline{u'u'}$	$\overline{v'v'}$	$\overline{w'w'}$ $[m^2s^{-2}]$	$\overline{u'v'}$	$\overline{u'w'}$	$\overline{v'w'}$
10	×90	0.84	0.68	0.29	-0.38	-0.03	0.05
20	45	0.95	0.76	0.32	-0.41	-0.05	0.06
30	30	1.01	0.82	0.34	-0.43	-0.05	0.07
50	18	1.07	0.85	0.35	-0.44	-0.06	0.08
60	15	1.10	0.88	0.36	-0.45	-0.06	0.08
differences	$x_{10} - x_{60}$	-0.26	-0.20	-0.07	0.07	0.03	-0.03
	$x_{20} - x_{60}$	-0.15	-0.12	-0.04	0.04	0.01	-0.02
	$x_{30} - x_{60}$	-0.09	-0.06	-0.02	0.02	0.01	-0.01
	$x_{50} - x_{60}$	-0.03	-0.03	-0.01	0.01	0.00	0.00

5.3.1.2 Spectra and cospectra

The next step of the analysis assumed the whole data set rotated into streamline coordinates. No detrending was necessary for transversal and vertical components of velocity because the mean offset of each component was zeroed by the rotation. Longitudinal component required a linear detrending due to the wind velocity increase during measurement. We will explore here spectra and cospectra obtained with the whole series and mean spectra of the velocity components based in time blocks where the series could be considered stationary.

Longitudinal velocity spectrum does not differ from a flat terrain spectrum except by a large energy peak with 11-min period, figure 5.9a. There are also present in the spectra peaks that detach from the traditional curve of the inertial subrange, $f^{-5/3}$, with periods of 2.5 and 4.0-min but with less than half of the energy of the main 11-min peak.

Cospectra that include the longitudinal velocity contribution, $Co(uv)$ and $Co(uw)$, are also affected by this 11-min event, being the latter the one with more energy in the overall cospectra comparison, figures 5.9d and 5.9e.

There is no indication in transversal and vertical velocity spectra in figures 5.9b and 5.9c of any singularity of 11-min period. In the case of the transversal velocity spectra we encounter however a slight indication of 2.5 and 4.0-min periods, and by the secondary events of 2.5 and 4.0-min present at $Co(uv)$ we may infer that these events are u and v related.

The cospectra at figures 5.9a to 5.9f show that, apart from one singularity with period of 11-min, associated to longitudinal velocity, and by two events with period of 2.5 and

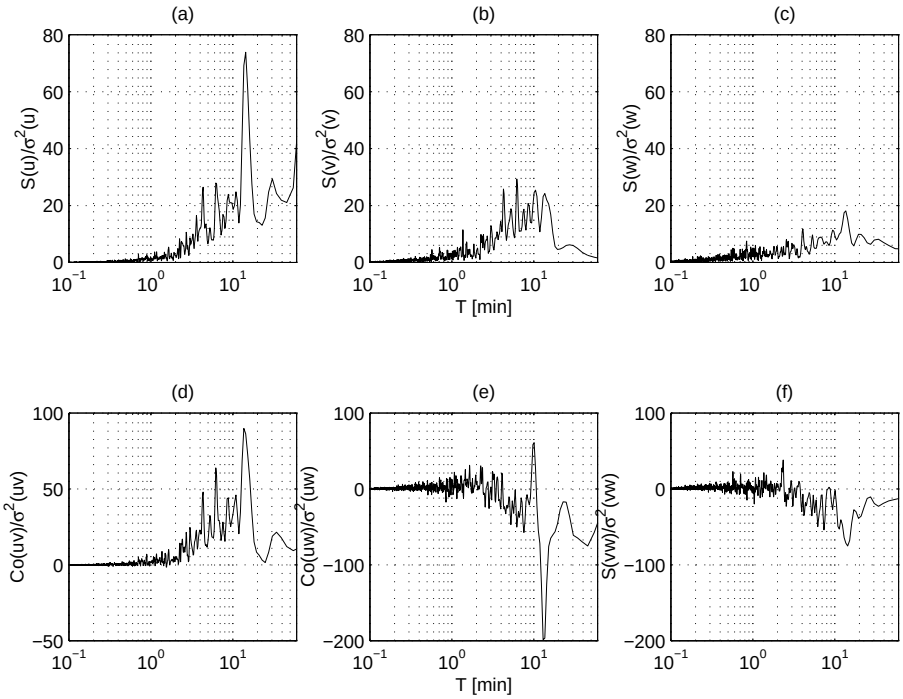

Figure 5.9: Spectra of longitudinal, transversal and vertical wind components normalized by variance, $S(u)$, $S(v)$ and $S(w)$, figures (a) to (c). Figures (d) to (e) represent $Co(uv)$, $Co(uw)$ and $Co(vw)$ normalized by the covariances.

4.0-min, associated to horizontal velocity, the spectral energy distribution of the flow at Paul da Serra may be assumed equivalent to flat terrain.

The events detected in figures 5.9a, 5.9b, 5.9d and 5.9e for the overall spectra were singularities associated with velocity increase during the measurement period. That is so because a mean spectra obtained from 15 data sets of one hour length do no present any recurrent singularity and show an evolution similar to the inertial sub-range for the $S(u)$ as depicted in figure 5.10. Note that for 10-min period no singularity is present. The only feature from the presented spectra is the deviation from the $f^{-5/3}$ slope for periods inferior to 1-min.

5.3.2 Comparison with cup anemometer

Sonic measurements were made with different recording parameters due to storage capability, table 5.2: one data set with instantaneous values recorded at 20 Hz during daylight (Daily period); one data set with records at 0.5 Hz, which match the sampling rate of the cup anemometer (Nightly period).

We compared for both periods the mean velocity, turbulent intensity and gust factor,

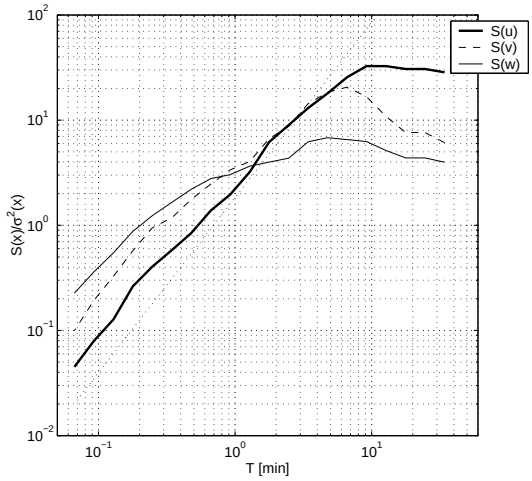

Figure 5.10: Mean spectra of longitudinal, transversal and vertical wind components normalized by variance for 15 blocks of one hour data series. The inertial subrange decay is represented with a doted line for reference.

Table 5.5: Sonic against NRG cup anemometer linear regression results $y = a + bx$ and correlation coefficient R^2 for Daily, Daily filtered, Nightly and Aggregate periods. Each quantity compared, mean velocity V, turbulent intensity it, and gust factor G are referenced for 10-min averaging intervals.

quantity	Series	size (points)	a	b	R^2
V	Daily	14	0.22	0.97	0.993
	Daily filtered	14	0.54	0.94	0.983
	Nightly	76	0.61	0.93	0.986
	Aggregate	90	0.61	0.93	0.992
it	Daily	14	0.01	0.80	0.707
	Daily filtered	14	0.00	0.93	0.840
	Nightly	76	0.00	0.94	0.950
	Aggregate	90	0.00	0.94	0.942
G	Daily	14	0.59	0.46	0.498
	Daily filtered	14	0.22	0.81	0.616
	Nightly	76	-0.01	1.01	0.912
	Aggregate	90	0.02	0.99	0.876

measured simultaneously by the sonic and cup anemometer for 10-min intervals, table 5.5. Velocity comparison showed minor differences of R^2 for both periods, 99.3% for Daily and Nightly period presented a correlation slightly inferior, 98.6%. This period also presented the largest deviation from the 1:1 slope, 7% against 3% for Daily period. One common

feature is the overestimation of cup anemometer when compared to the sonic. This subject is addressed further in this subsection.

Different results were obtained by the comparison of turbulent intensity and gust factor, where Daily period results are poorer, table 5.5. The correlation coefficient R^2 of turbulent intensity is 70.7% for the first period and 95.0% for the second. And the differences from the comparison are worse for the gust factor: correlation inferior to 50% for the Daily period and 91.2% for the Nightly period.

The source of those discrepancies was investigated by reducing the data set into a common frame because both periods were not equally measured. The reduction of Daily period was achieved by applying an anti-aliasing lowpass FIR filter to the same sampling rate of the Nightly period. A modified, or filtered Daily series was obtained and statistical estimators improved, table 5.5. The correlation coefficient for turbulent intensity increased 14% and gust factor, 12%. An additional advatage is obtained from resampling Daily series because it may be aggregated into Nightly series. The population for the comparison is thus larger and statistical estimates are enhanced.

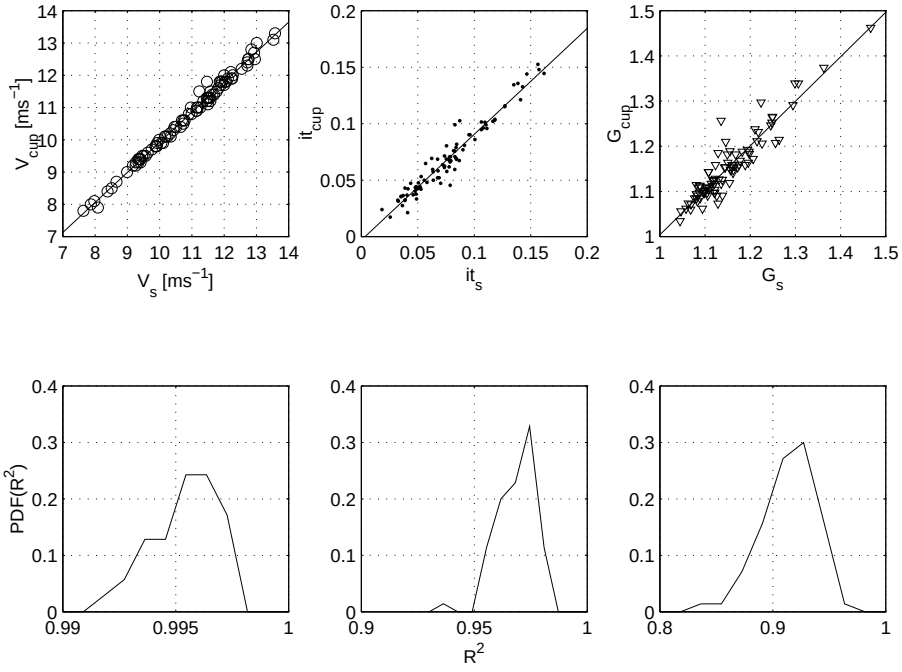

Figure 5.11: Sonic and cup anemometer velocity, turbulent intensity and gust factor linear regression in Port 213, Paul da Serra, July 30 and 31, 2002. The bootstrap correlation coefficient $PDF(R^2)$ is presented in the bottom line.

The comparison made for the aggregated series is depicted in figure 5.11 where we may assume the linear relationship between all estimators obtained from the sonic and cup anemometer. The mean velocity field is linearly correlated with a slope of 0.93, offset

of 0.61 ms^{-1} and a correlation of 99.2%. Because the vertical velocity presented small fluctuations, there was no difference in the statistical estimators if either horizontal or total velocity were used and for this reason we refrain from presenting such results. In this case, vertical velocity is not responsible for the overestimated value from the cup against the sonic anemometer.

Turbulence and gust factor obtained by either instruments are not different apart from residual offset, table 5.5 or figure 5.11. The larger difference is the underestimation of turbulent intensity by the cup anemometer about 6% while for gust factor it is 1%.

The deviation of the velocity, turbulent intensity and gust factor of the sonic against cup anemometer measurements was also investigated. The deviation for velocity was defined as

$$\Delta\epsilon(V) = \frac{(V_{sonic} - V_{cup})}{V_{sonic}} \tag{5.1}$$

and equally defined for turbulent intensity and gust factor. Table 5.6 summarizes the statistics of the 3 deviations. The mean deviation for velocity is 1% and null for gust factor. Also standard deviation of these two quantities is reduced, 1 and 2% respectively. The results for turbulent intensity are larger, 11% underestimation with 12% standard deviation. Also turbulent intensity presents wider limits than velocity and gust factor deviations, varying from a 48% underestimation to a 31% overestimation.

Table 5.6 also shows the deviation values for the velocity component in the horizontal plane where we may assume that 1st and 2nd statistical moments remain unchanged. Vertical velocity contribution in this case is irrelevant.

Table 5.6: 1st to 4th statistical moments of velocity, turbulent intensity and gust factor deviation for the NRG cup anemometer against the sonic anemometer for total and horizontal velocity (subscribes t and h).

	$\overline{\Delta\epsilon}$	$\sigma(\Delta\epsilon)$	$sk(\Delta\epsilon)$	$k(\Delta\epsilon)$	$min(\Delta\epsilon)$	$max(\Delta\epsilon)$
V_t	-0.01	0.01	0.69	3.55	-0.04	0.03
V_h	0.01	0.01	0.75	3.51	-0.04	0.03
it_t	-0.11	0.12	0.24	4.91	-0.48	0.31
it_h	-0.12	0.13	0.03	5.38	-0.58	0.31
G_t	0.00	0.02	1.15	7.13	-0.05	0.11
G_h	0.00	0.02	0.27	3.44	-0.05	0.06

We present in figure 5.12 the velocity temporal evolution of the 10-min velocity measurements from the sonic and cup anemometers. The deviations of the velocity, turbulent intensity and gust factor are also presented. We observe from the velocity and gust factor

deviation that both stay bounded within a 5% interval for almost the totality of the series. Turbulent intensity deviation evolution is more scattered but there is no evidence to associate such scatter with a particular velocity class or flow event.

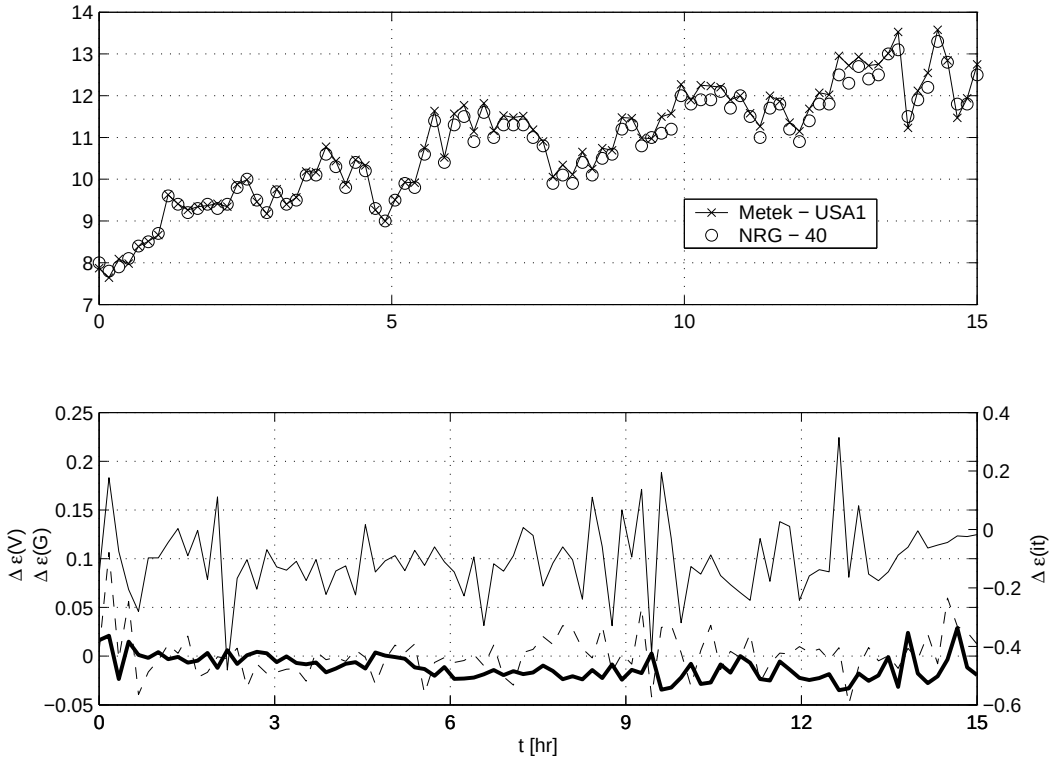

Figure 5.12: Sonic and cup anemometer velocity and velocity, turbulent intensity and gust factor deviations time evolution. Velocity and gust factor are on the left y-axis (thick and dashed lines) and turbulent intensity are in the right y-axis (thin continuous line).

The comparison from sonic against cup anemometer showed that both instruments are linearly related, although with differences that could not be attributed to any flow event. Wyngaard (1981) showed that cup anemometer respond faster to wind speed increases ($u > 0$) than wind speed decreases causing the anemometer to overspeed. As turbulence presents low levels, this effect is less evident than in Caniçal flow.

There is also no information on the u-bias, v-bias and w-bias of the cup anemometer, known to be the major contributors for mean wind speed measurement error, Papadopoulos et al. (2001), and we may add that both instruments were calibrated in different facilities.

Turbulent intensity measured by the sonic is slightly higher than the one obtained by cup anemometer, 6%, in spite of reducing Daily period to the same averaging interval as Nightly period. The differences are likely associated to the fact that sonic anemometer incorporates more information about the flow due to higher sampling rate. More turbulent scales are included, and we observed from the velocity spectra at figure 5.10 an excess of

energy for period inferior to 1-min. That effect was partialy compensated by the lowpass filter. However, for wind energy purposes this 6% underestimation will lead to a correction of mean turbulent intensity for station Port 213 from 8.0 to 8.5%, which is irrelevant.

Discrepancies in gust factor comparisons are also reduced, 1%, and are related to the higher sampling rate from sonic that capture different maxima than the cup anemometer.

5.3.3 Spacial divergence of the flow

The information from 4 measuring stations at the site enabled a more complete long-term analysis of the flow at Paul da Serra plateau; the analysis comprised one-month of simultaneous measurements for all stations: Port 210 to 213 (figure 5.2). There is no measurement from sonic anemometer, but the results presented in previous subsections may be extrapolated to present a more complete picture of the turbulent field over the plateau. We opted to select a month (February 2003) when the flow resembled the wind conditions during sonic measurements, with sightly low mean velocity but with larger turbulence intensity and gust factor, table 5.7.

Table 5.7: Stations statistics for February 2003

Station	v [ms^{-1}]	$\sigma(v)$ [ms^{-1}]	it	G
Port 213	9.51	5.33	0.139	1.69
Port 212	8.30	4.49	0.157	1.66
Port 210	8.31	3.91	0.141	1.66
Port 211	7.49	3.89	0.180	1.64

The wind rose for the month of February 2003 is presented in figure 5.13. The wind direction was mostly from northeast direction at stations Port 210, 212 and 213 but northwest for station Port 211. In fact there is a difference in wind direction of 93° from Port 213 and 211. This raises the question of data quality for that station.

5.3.3.1 Northeast quadrant flow

By its geographical location, Port 213 is the upstream station for north quadrant winds and the reason for a different wind direction at Port 211 was investigated by conditioning the analysis to those samples when the wind was between 0 and 90°(northerly to easterly winds), at Port 213. Figure 5.14 shows that for northeast winds at all stations in the north side of the plateau (Port 213, 212 and 210) are associated with northwest winds in Port 211, i.e. a difference of 115°.

Mean velocity, standard deviation, turbulent intensity and gust factors are compared for all 4 stations for north quadrant flow, table 5.8. Mean velocity of Port 213 remains close to

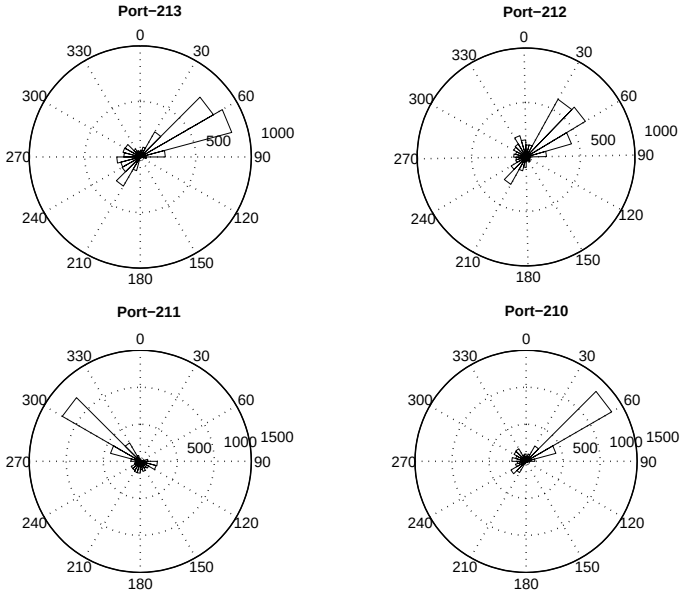

Figure 5.13: Wind direction at Paul da Serra during February 2003 at stations Port 210 to 213.

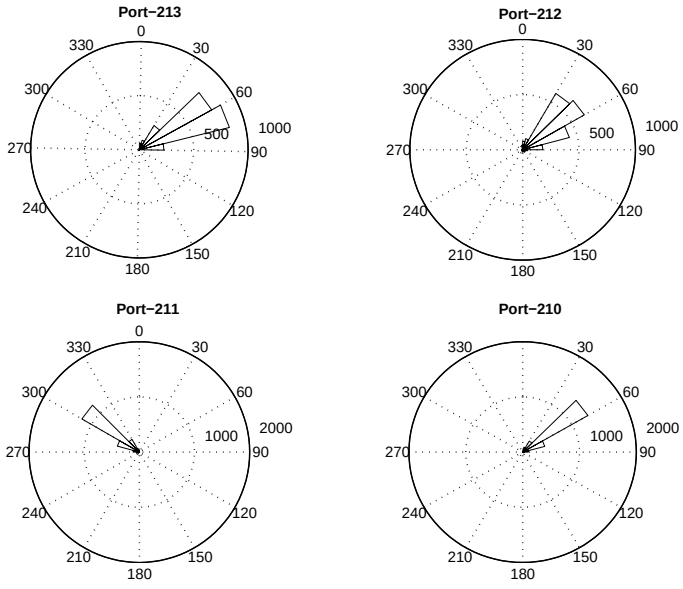

Figure 5.14: Wind rose at 4 stations conditioned incoming winds from 0 to 90° at Port 213.

the values measured with sonic anemometer. Turbulent intensity remains below 10% and gust factor inferior to 1.3. Port 212 presents larger velocity and turbulent intensity values while downstream and downslope Port 211 station present as expected the lowest mean velocity and higher turbulent intensity values. Note that the gust factor in all stations is

close to 1.3. Besides the wind direction discrepancy at Port 211, the turbulence intensity in table 5.8 is within normal operation range for wind turbines.

Table 5.8: Mean and turbulent field statistics for February 2003 for northeast quadrant. Turbulence intensity and gust factor are presented for velocities above 5 ms^{-1}.

Station	v [ms^{-1}]	$\sigma(v)$ [ms^{-1}]	it	G
Port 213	9.56	2.42	0.099	1.26
Port 212	10.39	4.02	0.119	1.25
Port 210	9.01	2.42	0.099	1.26
Port 211	8.69	2.37	0.139	1.31

The velocity measured in 4 locations was compared to this particular northeast sector (table 5.9) using station Port-213 as a reference because it was the station where sonic measurements were done. Table 5.9 also includes the distance and altitude difference from Port 213.

Table 5.9: Mean velocity linear regression results $y = a + bx$ and correlation coefficient R^2 for northeast wind from 0 to 90° at station Port 213. Distance from Port 213 d and altitude difference h.

Station	a	b	R^2	d [m]	h [m]
Port 210	0.448	0.889	0.848	4276	108
Port 212	0.207	1.056	0.565	2932	-91
Port 211	1.385	0.753	0.655	4965	-159

Port 212 is the station where the correlation slope is nearer to the 1:1 ratio; it is the closest station but with wider data dispersion, R^2 =56.5%, which is likely related to the fact that it is located almost 100 m downslope on the plateau. The best linear fit is given by station Port 210, located over 4 km southeast of Port 213. This station is also close to the limit of the plateau where its exposure from northeast to north winds is unaffected as Port 213 and where extrapolations with sonic measurements are likely to agree.

Station Port 211 is the one further apart, almost 5 km and 159 m below the reference station. However, R^2 is higher than Port 212 located in the center of the plateau, showing that Port 211 is not affected as much as Port 212 by the 5 km downslope terrain.

Note that station Port 211 is downslope and downstream of Port 212 and R^2 should be inferior to Port 212 due to effects induced by the terrain. However, the wind rose (figure 5.14) shows that station Port 212 is being subjected to a different wind, probably terrain induced effect, and this hypothesis is consistent with 2 facts: wind rose discrepancies and higher correlation coefficient when comparing to Port 212.

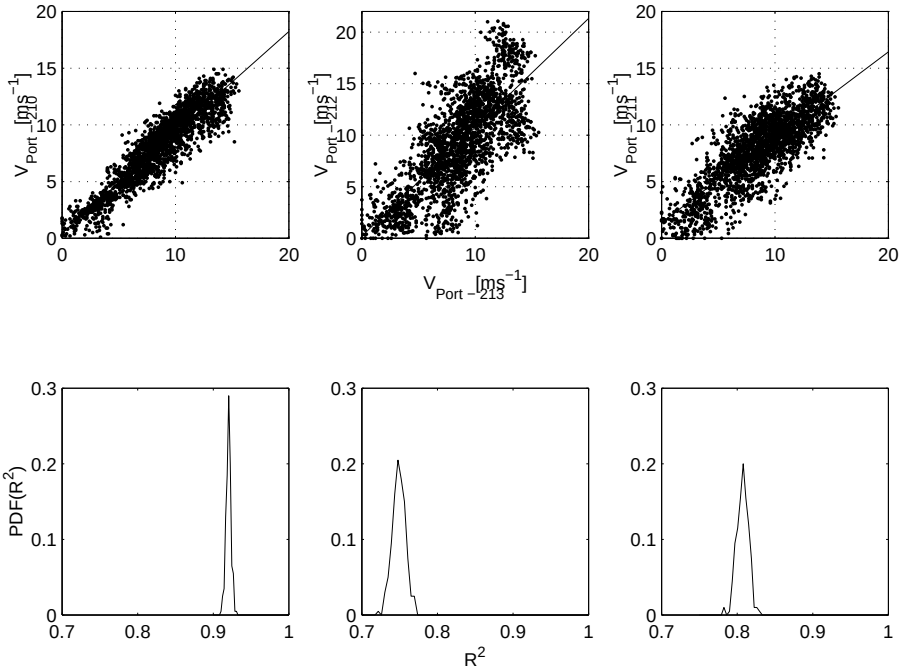

Figure 5.15: Velocity comparison for incoming wind from 0 to 90°.

5.3.3.2 Southwest quadrant flow

The methodology of previous subsection was repeated for an incoming wind from 90 to 270°, a 180° interval centered in wind flow approaching from south direction, by conditioning the data of station Port 211 (it was the station further south). However, the comparisons maintain station Port 213 as a reference. The number of events was lower than in the northeast flow (subsection 5.3.3.1), corresponding to 3 days records, and the wind rose from all 3 stations maintain a direction shift of 75° against Port 211 (figure 5.16). Note that for northeast flow the mean direction difference was 115°.

The mean velocity, standard deviation, turbulent intensity and gust factors are presented in table 5.10 for all stations. The mean velocities were higher than in the previous case, with larger differences between stations. Stations at higher altitudes (Port 213 and 210) had stronger winds, lower turbulence intensity and gust factor. In spite of best exposure to the incoming wind from this wind direction, the mean wind flow at station Port 211 was the lowest and with higher turbulence intensity and gust factor. Station Port 212 presented values slightly lower than Port 211, with mean flow and turbulent statistics similar to Port 211.

The comparison of estimators between stations assuming Port 213 as reference for southwest wind indicates that the best correlation for velocity lies in stations closer to each other, Port 213 and 212, with R^2 of 83.2%, table 5.11. The slopes vary from 40.8%

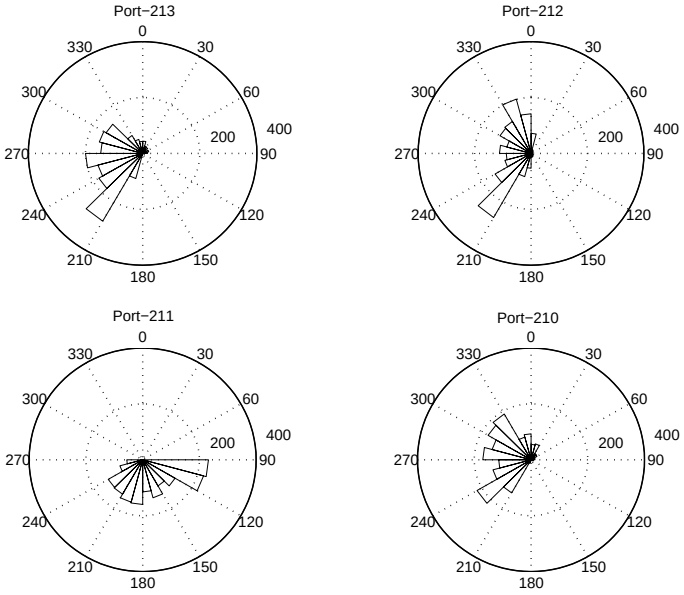

Figure 5.16: Wind rose at 4 stations for incoming wind from 90 to 270° at Port 211.

Table 5.10: Mean and turbulent field statistics for February 2003 for southwest quadrant. Turbulence intensity and gust factor are presented for velocities above 5 ms^{-1}.

Station	v [ms^{-1}]	$\sigma(v)$ [ms^{-1}]	it	G
Port 213	13.97	6.42	0.131	1.35
Port 212	9.65	2.72	0.161	1.38
Port 210	11.23	3.53	0.129	1.35
Port 211	9.45	3.07	0.167	1.40

to 60.5%, and wind velocity offset is quite large, ranging from 1.28 to 2.99 ms^{-1}. Figure 5.17 present the comparison with the bootstraped correlation coefficient.

Table 5.11: Mean velocity linear regression results $y = a + bx$ and correlation coefficient R^2 for south quadrant wind (90 to 270°) at Port 211. Station Port 213 was maintained as reference and distance d and height differences h are included for reference.

Station	a	b	R^2	d [m]	h [m]
Port 210	2.99	0.408	0.493	4276	108
Port 212	2.31	0.605	0.832	2932	-91
Port 211	1.28	0.534	0.784	4965	-159

The wind rose (figure 5.16) for the period and the comparison of estimators at table

5.10 and 5.11 show that southerly winds (between 90 and 270°) at station Port 211 are associated with westerly winds occurring 2 km away in a central area of the plateau, Port 212, and in the north and west end of Paul da Serra. Being located in a well exposed spot for southwest winds it was the first thought that Port 211 would show lower turbulence intensity and gust factors. In fact we may assume that the choice of using Port 211 for direction selection was unsuccessful because it is subjected most likely to local terrain induced effects that need clarification.

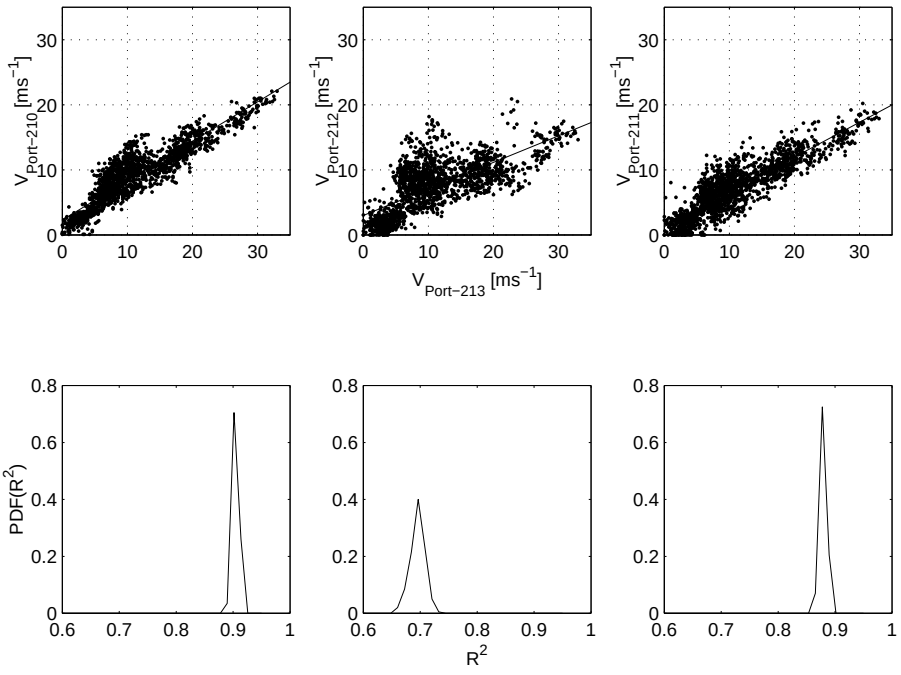

Figure 5.17: Velocity comparison for incoming wind from 90 to 270° at Port 211.

Selecting from data series all records from station Port 210 that are in an interval between 90 and 270° we obtain a wind rose that still present a mean direction shift of 72°, figure 5.18.

The best correlations are obtained for this flow direction, table 5.12. Station Port 211, in spite of the mean direction difference of 72° maintains a velocity correlation against Port 213 of 88.0%, higher than the correlation 83.8% for the central station of Port 212. Again, Port 213 wind speed is much higher than measured at stations Port 211 to 212, benefiting from flow acceleration uphill.

The selection of station 210 for southwest quadrant flow showed that the direction shift of 72° at station 211 is persistent although the correlation estimates improved, showing that the flow over the plateau is strongly related from southwest direction. The different shift in direction for Port 211 for northeast and southwest wind is a clear indication that the measurements are right and there are terrain induced effects that are shifting the flow

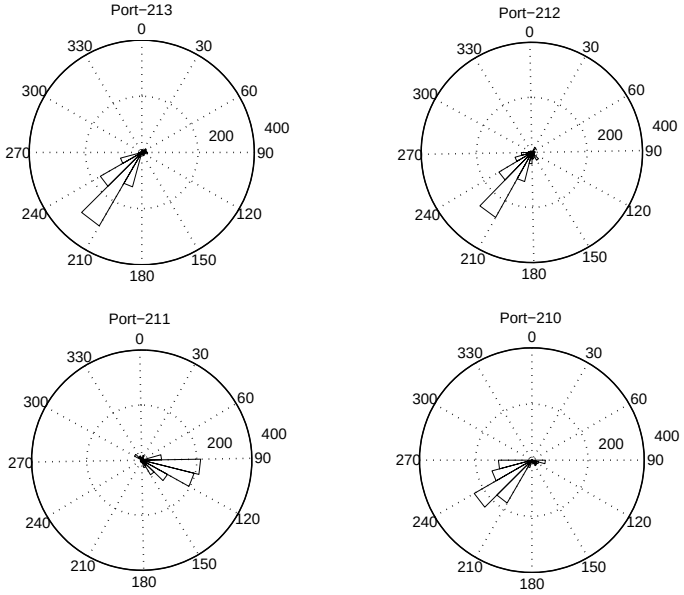

Figure 5.18: Wind rose at 4 stations for incoming wind from 90 to 270° at Port 210.

Table 5.12: Mean velocity linear regression results $y = a + bx$ and correlation coefficient R^2 for south quadrant wind (90 to 270°) at Port 210. Station Port 213 was maintained as reference station and distance d and height differences h are included for reference.

Station	a	b	R^2	d [m]	h [m]
Port 210	0.86	0.626	0.964	4276	108
Port 212	0.84	0.447	0.838	2932	-91
Port 211	1.07	0.515	0.880	4965	-159

at Port 212.

Cup anemometer long-term measurements show that correlations between stations are strongly related to wind direction (tables 5.11 and 5.12) and sonic anemometer measured no wind from this direction thus we recommend no extrapolation from sonic measurements.

Turbulent intensity and gust factor were also compared for both situations, northeast and southeast flow. However no correlation was achieved and for this reason we refrain from presenting the results.

5.3.3.3 Turbulence intensity and gust factor

Turbulent intensity and gust factor were also compared for 10-min and 30-min averages. The shortest averaging period showed no correlation between stations either for turbulence intensity and gust factor. That is an expected feature once it was found in subsection 5.3.1.1 that for 30-min averages the series could be treated as stationary.

Figures 5.19a to 5.19f present the comparison for 30-min averaging intervals for northeast and southwest wind. For northeast wind, station 210 presents a correlation of R^2=42.3% against Port 213, figures 5.19a. Although with similar evolution in figure 5.19c, Port 211 correlation is very poor, R^2=13.4%. All other figures show that there is no correlation for Port 212, where turbulence intensity is larger either for northeast or southwest winds. For this last wind direction, Port 210 and 211 present no correlation.

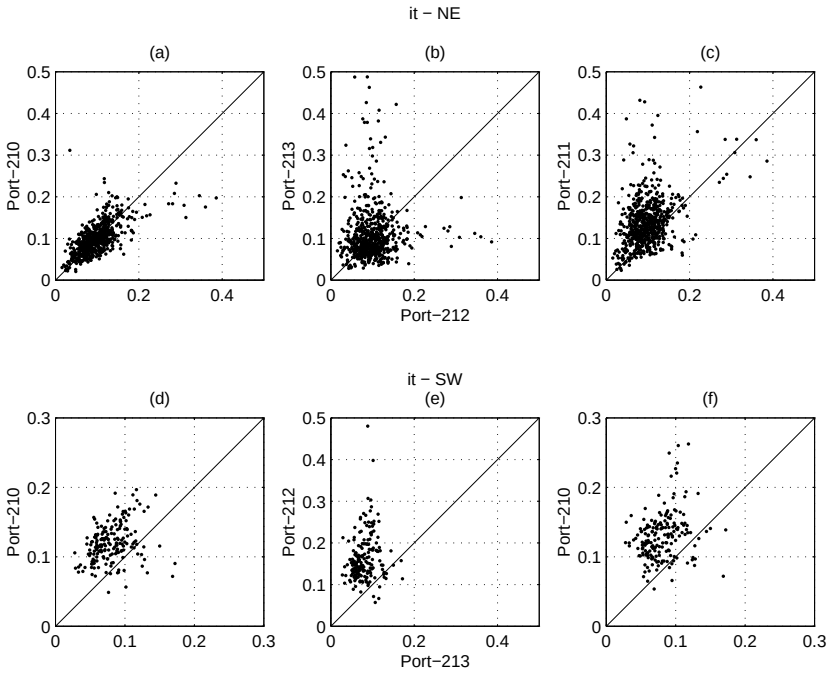

Figure 5.19: Turbulent intensity comparison for 30-min averaging intervals for northeast and southwest flows, figures (a) to (c) and (d) to (f). 1:1 line is plotted for reference.

Gust factor was also compared and is presented in the same way as the comparison of turbulence intensity, figures 5.20a to 5.20c for northeast winds and figures 5.20d to 5.20f for southwest winds. Again, station Port 210 presents the same result for northeast wind for gust factor as turbulent intensity, with R^2=42.5%. For southwest wind the correlation drops to 11.0%. For the other stations in both wind directions the correlation is very poor.

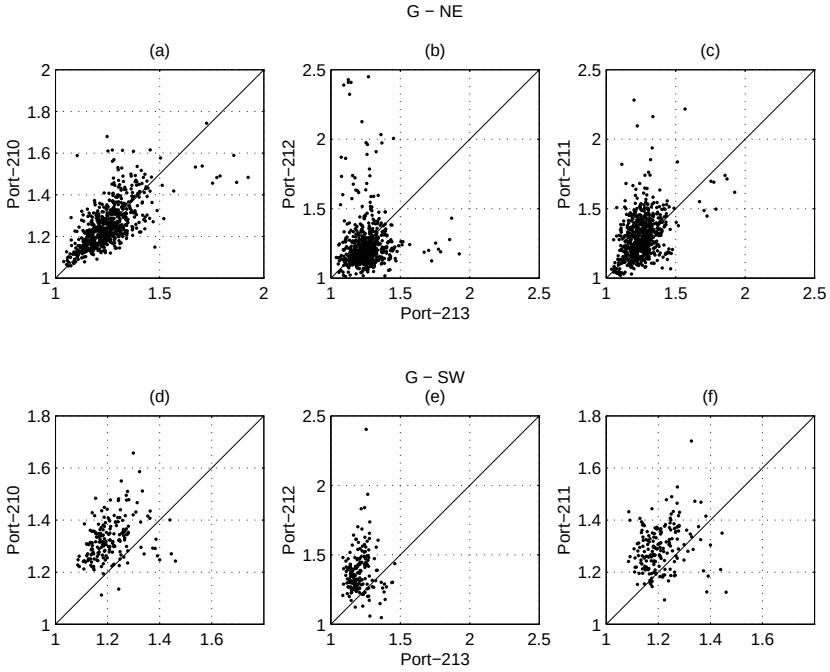

Figure 5.20: Gust factor comparison for 30-min averaging intervals for northeast and southwest flows, figures (a) to (c) and (d) to (f). 1:1 line is plotted for reference.

5.4 Conclusions

The measurements at station Port 213 showed that mean vertical velocity of the flow was ascending with 0.24 ms^{-1} and did not compromise wind turbine operations. Mean turbulence intensity was 8% and turbulence ratios of $\sigma(v)/\sigma(u)$ and $\sigma(w)/\sigma(u)$ were 91 and 60%, the latter being slightly higher than flat terrain reference values. Velocity spectra of all wind components did not show any special feature and resembled flat terrain spectra.

Comparisons of sonic against cup anemometer for mean velocity showed a 99.2% correlation with an overestimation from cup anemometer measurement of 1%. This difference was 3 times lower than at Caniçal wind farm and was a consequence of the minor overspeeding due to lower gust factor and vertical components. Turbulence intensity and gust factors were also compared to a high degree of correlation, 94.2 and 91.2%. Instruments deviation were larger for turbulent intensity, 11% due to higher sampling rate of the sonic. Gust factor deviations were null.

Comparisons of long-term cup anemometer measurements showed that the flow suffered deviation in the lowest part of the plateau due to terrain induced effects. For northeast wind there was a direction shift of 115° while for southwest it was 72°.

Paul da Serra plateau is apparently not a very complex terrain, but only stations Port 213 and 210 are highly correlated, $R^2 = 84.8$ and 96.4% for northeast and southwest flows.

Velocity correlations for Port 211 and 212 are poorer but increase to values over 80% for southwest winds. Turbulent intensity and gust factor of stations Port 213 and 210 are also correlated by 42.3 and 42.5% only for northeast wind.

Due to similarity on surrounding terrain and correlation results of mean velocity, turbulent intensity and mean gust factor, it is most likely that the flow presents at station Port 210 the same characteristics measured at Port 213 with the sonic anemometer.

Chapter 6

Closure

This chapter presents the main conclusions of the present work and provide suggestions for future work.

6.1 Conclusions

This work presents the results of 4 experiments that have in common the use of sonic anemometers under diverse conditions: homogeneous terrain with high roughness, humidity and temperature changes, wind tunnel, and two complex terrain cases, one in a coastal region and other in a mountain plateau, both for wind energy purposes.

A sonic anemometer is an absolute measuring instrument that requires particular care due the sophisticated electronics and array configuration. All instruments used in EBEX00 presented non-orthogonal configuration thus the performance comparison refers to the response and robustness of each instrument electronics. EBEX00 roughly open to rough site (z_0 =15 cm) was characterized by light winds and large temperature gradients, with stable stratification during night and great part of the day. Temperature gradients tended to damp the turbulent mixing mechanism forcing the flow into laminar regime. Under those circumstances sonics from 3 different manufacturers were compared with the following results:

- First statistical moments comparison of velocity and temperature measurements indicated that NUW, Campbell CSI and Gill HS agree with correlations of 0.986 and 0.999, regardless of spacial separation.

- Second statistical moments were also independent of spacial separation: $\overline{w'w'}$, u_* and $\overline{w'T'}$ correlations were respectively 98.6%, 93.3% and 98.1%. Temperature variance, $\overline{T'T'}$ (R^2 = 91.6%), was the only parameter with worse mean correlation and

dependent on the instrument distance.

- Mean correlation of $\overline{u'u'}$ and $\overline{u'w'}$ spectra were 99.4 and 99.2%. Mean correlation for unstable stratification of $\overline{w'T'}$ was 92.7% decaying to 81.5% for stable stratification. That occurred because thermal effects dampened the mixing of the flow into laminar regime contaminating instruments comparison. All results were in agreement with previous studies by Christen et al. (2000) for grass covered terrain or Högström and Smedman (2004) for ocean and agricultural sites.

- Gill HS unit proved to be temperature dependent with measurement drift that may compromise its use for long-term flux measurements.

- NUW sonic overestimates the sensible heat flux, $H = \rho c_p \overline{w'T'}$, by 12% against CSAT-3 models or the Gill HS unit.

- The sonic that presented more stable estimators was Campbell Scientific (model CSAT-3).

All instruments showed high accuracy and precision but caution is needed for measurements that require 2nd statistical moments. Nevertheless, for wind energy purposes these differences between instruments may be negligible.

Flow distortion by sensors is known as a major source of errors, which depends on the array configuration that differ among manufacturers. The Metek (model USA-1) sonic anemometer was calibrated in a large wind tunnel, before field measurements. We found no need for corrections in case of temperature measurements, contrary to velocity measurements, where we obtained:

- Map for the transducer shadow effect for a complete rotation and inclination ranging from -25 to 25°. This map indicated:
  - Flow acceleration areas that are bounded by the acoustic path from each pair of transducers associated with the transducer array. True velocity overestimation reach up to 5%.
  - Flow deceleration areas where velocity defect may reach 12% of the true velocity due to transcuder array blockage of the flow.
  - Measurements at 4 velocities produced correction maps that differ less than 2%.
  - Only one correction map is needed and the mean error drops in the worse case to 0.1%.

The Metek (model USA-1) sonic anemometer measurements made at 40 m high on a wind turbine nacelle at Caniçal wind farm detected in the airflow:

- The existence of eddies with a 2.9-min period confirmed from PDF intermittency, spectral and wavelet analysis, in agreement with VENTOS® software results from Palma et al. (2002).
- Important vertical components (with an excess of 20 ms^{-1}) most likely associated with *sweeps*, *gusts* and *ejections* that coexisted with the eddies.
- The wind flow was classified into 3 types of flow:

  Type A The steadier flow (comparable with simulation) with events of 1.4, 2.9 and 6-min.

  Type B The most frequent flow type, with similar periodicity as flow Type A where flow ejections larger than $5 \times H$ were responsible for 25% of the turbulent flux transport.

  Type C The most unsteady flow type where turbulent transport is from sweeps and gusts with scales inferior to $5 \times H$.
- Cup anemometer difference of 2.3% resulted from overspeeding due to gusty conditions and severe vertical components of the flow. The results were in agreement with cup anemometer flow inclination sensitivity from Papadopoulos et al. (2001).

Measurements made at 40 m high close to the northern cliff of Paul da Serra plateau show that:

- Mean vertical component was ascending but will not compromise wind turbine operations (0.24 ms^{-1}).
- Turbulence is also reduced, 8%, and measured values close to flat terrain reference values and no special flow feature was detected with spectral analysis.
- Cup and sonic anemometer measurements agree quite well for such flow conditions, with cup anemometer overestimation by 1% and sonic anemometer overestimation of turbulence intensity by 11%.
- Comparisons of long term cup anemometer measurements against 3 other stations in the same plateau showed that central tower present larger turbulence estimators and the southest station airflow is shifted due to terrain induced effects.

The detection of terrain induced coherent structures at Caniçal wind farm would be possible from cup anemometer measurements by maintaining the instantaneous values from those measurements. Turbulence in this case is poorly described by standard turbulence indicators: turbulence intensity it and gust factor G. However, these estimators should not be ignored when presenting large values. They are the first evidence of unusual turbulence for wind turbine operations.

Turbulence intensity and gust factor at Paul da Serra where within flat terrain reference values and performance differences from cup against sonic anemometer reduced. However, by performing measurements only with cup anemometers, vital information on vertical component of the wind flow will be lost with consequences for turbine energy output and loads.

6.2 Future work

In Portugal, the predicted wind power installation increase by 10 times from 2005 to 2010 that result from compromises with European Union may lead wind farm promoters and manufacturers into unexpected difficulties. Although large developments were encountered in wind power technology since the 80's, we believe that installing megawatt wind turbines in complex terrain is a risky decision if based in poor estimators of the turbulent field and recurring to experimental techniques and methodologies that, though suitable for flat terrain, are questionable for complex terrain.

There is a clear path to bring both wind turbine manufacturers, wind farm promoters and research groups to common research and development projects:

Turbulence and stratification in complex terrain. Turbulence vertical profile over complex terrain and the role of stratification are mechanisms yet to be fully understood. Kelley (1999) pointed the way demonstrating that diurnal variation of Ri and u_* are important parameters of the turbulent field over complex terrain. How turbulence changes with the distance above ground level and the identification of local phenomena such as low-level jets or temperature inversion will be achieved via measuring towers, with velocity and temperature sensors.

Sodar measurements. Complementary information on wind and temperature profiles from 50 m up to 1 km height in the boundary-layer may be obtained from Sodar measurements. Although their precision and data availability still depends on the weather and *in situ* measuring conditions, it provides information that is estimated nowadays by spectral methods from ground measurements. The domain of the experimental technique and its adequacy for use in complex terrain is a current research area.

Turbine load measurements in complex terrain. Turbine manufacturers do not easily provide information on turbine load limits due to large vertical components. A close link between atmospheric flow research and turbine designers is required, and lack of information on wind turbine limits are likely to rise fatigue loads and reduce their operation life. In complex terrain such concerns are even more pertinent. Such research would require instrumenting the turbine with strain gages and vibration

sensors to be correlated with turbulence measurements from a fully instrumented wind and temperature profile tower.

These are some of the open questions in research, which may represent a contribution towards a greater knowledge of wind flow over complex terrain, and the increased use of wind energy.

Appendix A

Fourier Techniques

A.1 Introduction

In this appendix we discuss some practical questions of signal processing techniques based in Fourier transform. We assume the reader to be familiarized with Fourier based signal processing and a more fundamental consult may be encountered in Papoulis (1962).

A.2 Periodogram performance

The performance of the periodogram with regard to for instance leakage and resolution will be discussed with the help of the following example: $x(t)$ is a periodic sine series with two main frequencies, 140 and 150 Hz, and different amplitudes represented in figures A.1a and A.1c, where the difference lies just on the record length. The signal-to-noise ratio of the series is 40 dB simulated by a random number superposition.

Spectral leakage corresponds to a continuum of the power signal around the discrete signal frequency peak and is solely a contingent on the length of the data record. This can be observed from the following example depicted in figure A.1b, where the energy centred in the frequency peak is represented by a wide energy distribution, from 100 to 200 Hz, instead of a narrow distribution, in a 5 Hz interval, as in figure A.1d. Another similar problem is the *bias of the periodogram* but now in terms of average power. Again, it can be minimized with long records or with special windowing techniques.

Resolution is the ability to discriminate spectral features. In order to resolve two sinusoids that are close in frequency, it is necessary for the difference between the two

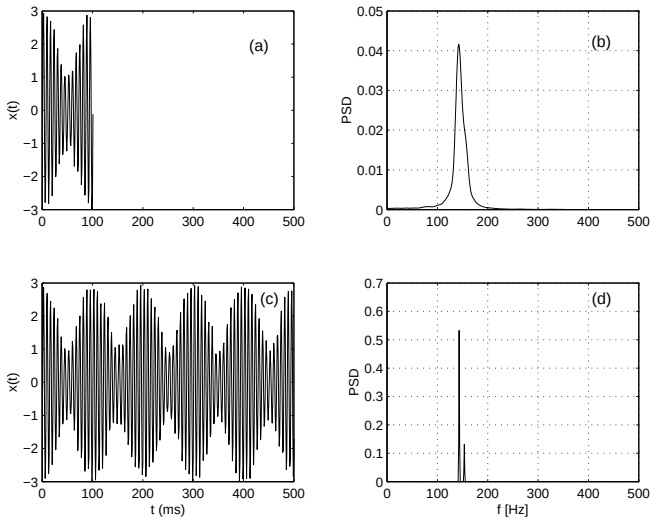

Figure A.1: Series $x(t)$ truncated (a). PSD of the truncated $x(t)$ (b). The same series $x(t)$ with longer time for stability of statistic estimators (c). PSD of the longer series, where the main frequencies are clearly identified, figure (d).

frequencies to be greater than width of the main lobe on the leaked spectra for either one. For the resolvability condition to be complied it is required that:

$$\Delta f = f_1 - f_2 > \frac{f_0}{Q} \tag{A.1}$$

Figure A.1c represents only half of the signal length for clarity. Thus, the resolvability condition is satisfied once we have more than 100 samples in the record length thus both frequencies are identified.

Both leakage and resolution can be reduced artificially reduced by several techniques:

1. Increasing the number M of elementary data segments improves the statistical stability of the results and provides better estimates. In practical applications, M must be greater that 10. Typical values range from 50 to 400. As N is increased to obtain finer resolution, the number of segments used in the averaging operation should also be increased to obtain statistical stable estimates. The reduction of N reduces the low frequency resolution, leading to a compromise between resolution and statistical stability of the PDS estimates.

2. While the series falls short of the length required for the spectrum analysis program on hand, a common practice is to add zeros to the data sequence, equally in both ends, to make up the required number of points. (Generally power of 2 if an FFT is used). Kaimal and Finnigan (1994) warns for the consequences of improper use of this technique because the reduction of estimates by a factor of $(N - N_z)/N$ where

N_z is the number of zeros added. It is essential that means and trends be removed from the time series before adding zeros

3. The Welch method which corresponds to overlapping the elementary data segments. It has been shown that unbiased estimates are obtained with an overlapping of segments corresponding to a half-segment length. This method increases the number of available segments and improves the statistical stability of the results. For noisy series Welch method is recommended. The disadvantage lies on the fact that the overlapping segments are shorter than the series length, therefore the estimator will be biased when compared to the periodogram.

4. Practical Fourier transforms cannot be estimated from a infinite data segments. The finite length of each elementary segment induces the truncation effect. This effect may be attenuated by using a weighting function such as triangular, Hanning, Hamming or Blackman windows. In this case, each data sample is multiplied by a window function w before computing the periodogram.

Table A.1: Classical window functions used in power spectral analysis. N is the number of available samples and the range of k is in the following interval: $0 \leq k \leq N-1$

Type	Sample Values $w(k)$
Rectangular	1
Triangular	$1 - \left\|1 - \frac{2k}{N-1}\right\|$
Hanning	$\frac{1}{2}\left[1 - \cos\left(\frac{2k\pi}{N-1}\right)\right]$
Hamming	$0.54 - 0.46\cos\left(\frac{2k\pi}{N-1}\right)$
Blackman	$0.42 - 0.50\cos\left(\frac{2k\pi}{N-1}\right) + 0.08\cos\left(\frac{4k\pi}{N-1}\right)$

The most classical window functions are summarized in table A.1 and figure A.2 while the performance of the window functions for the example of figure A.2a is depicted in figure A.3. Extracting information from the short signal in figure A.2a is more demanding than case A.2c, where the longer record length would make the correct identification of the peak frequencies for the no window case as well for all window functions. The example only show how different window functions perform differently. Here, only half of the window functions in figure A.3 where able to identify the peak frequencies: rectangular, triangular and Hamming. In this example, the most successful were the rectangular and Hamming, though still disagreeing on the maximum power spectra. Note that for such severe example, where we will not evaluate the general merit of each window function performing, we observe that leaking and power bias is present in all examples.

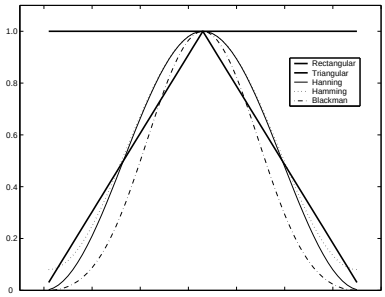

Figure A.2: Classical window functions w, see table A.1.

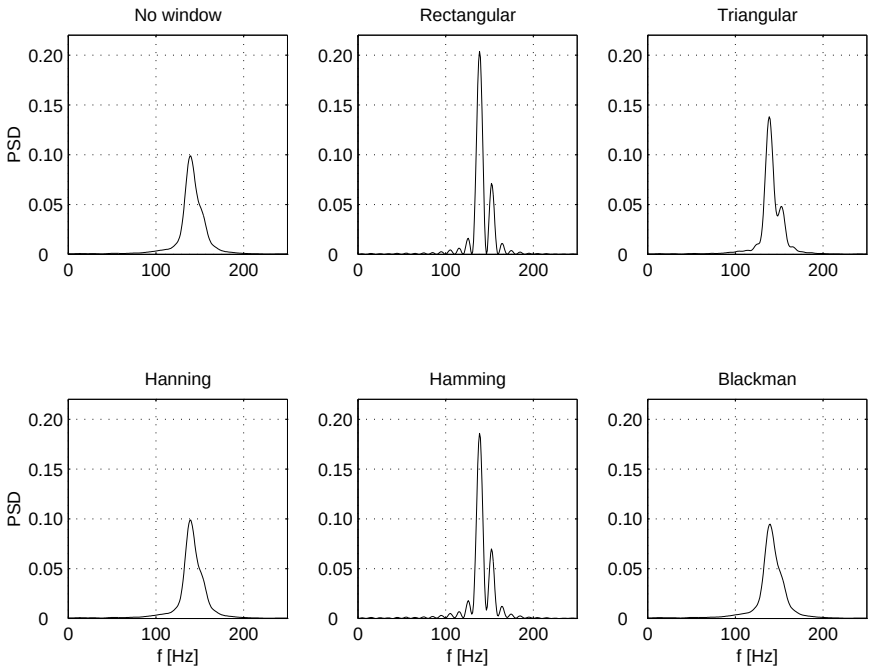

Figure A.3: Application of window function for the example series from figure A.1 (a).

A.3 Obtaining an atmospheric energy spectrum

The example that follows represent a 150 minute time series of a vertical velocity w measurement over flat terrain. Prior to the spectral representation of the signal, we verified the stationarity of the series by the analysis of cumulative mean and variance depicted in figure A.4. The convergence value is the mean and variance for the whole series. The mean converges just after 6 minutes. Variations on 1% of the convergence value are observed thoungh dumped as the time interval increases. In spite of reaching the convergence value after 2, 6 and 20 minutes, the variance diverges to values over 15% in between these time intervals. We observe that the convergence of the variance is consequent from 50 minute intervals where it closes to 5% of the reference value. As for 2nd moment statistics for flux analysis a 60 minute interval should be used. In the application of the spectral procedure to this example, we will disregard this fact and present for 30 minute subsets.

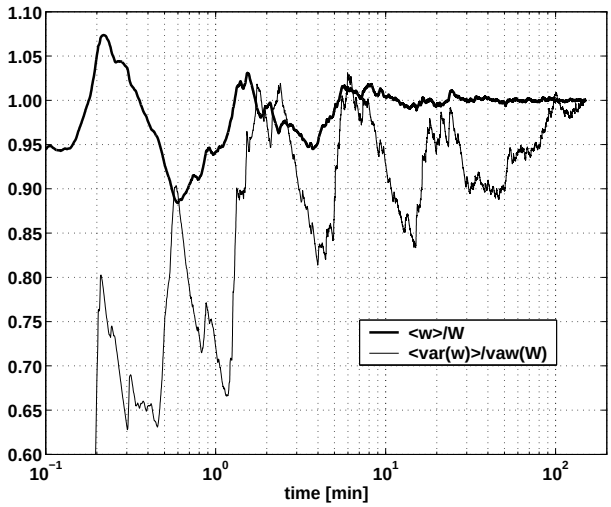

Figure A.4: Cumulative mean and variance, respectively represented by the thicker and thinner lines of the vertical velocity w time series of 150 minute length.

Figure A.5 illustrates the spectral procedure presented in this section. The original time series was transformed directly from the FFT algorithm after demeaning, figure A.5a. The time series was divided into 5 equally spaced sub-series of 30 min each, where a single spectrum for each one was obtained, figure A.5b. Each sub-spectrum information was classified into 20 bins equally spaced in the logarithmic abscissa. The jagged look was reduced by the averaged values for each spectra, and the result could be improved if the number of bins would be reduced. Figure A.5c presents the composite of the low and high-frequency ends. The high-frequency spectra in A.5c arises from the average of the 5 spectra depicted in A.5b. The low-frequency region was obtained directly from the FFT algorithm smoothed by windowing the whole series with a Hamming window, Kaimal and Finnigan (1994). This is a variation of resampling the series at lower rate once there was no computer time limitations. The overlap region in this example, figure A.5c, was obtained

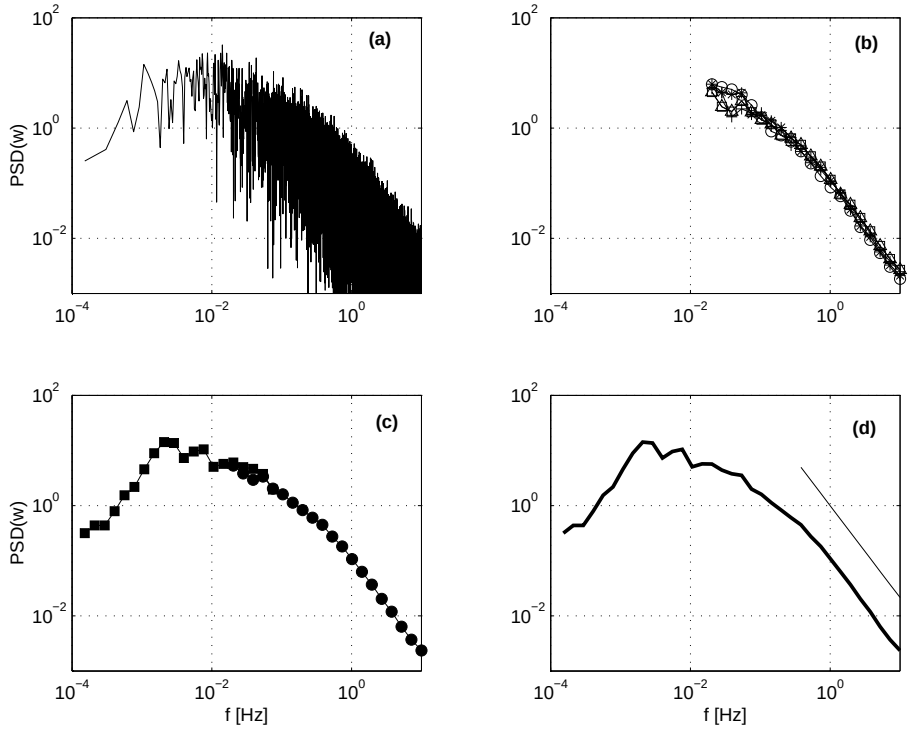

Figure A.5: (a) Raw spectrum of 2.5 hours of data for the vertical velocity w. (b) The data was divided in 5 non-overlapping parts from which 5 high-frequency spectra was obtained. Each high-frequency spectrum was divided into 20 equally log spaced bins where the mean value of each bin is the average power density. (c) Composite spectra of the high and low-frequency ends. The high-frequency curve, circles, was obtained from an average of each 5 spectra. The low-frequency curve, squares, was filtered by a Hamming window then averaged over 20 bins, where 5 overlap the high-frequency curve. (d) Final spectrum: a composite from high and low-frequency curves. An $f^{-5/3}$ inertial decay is included for reference.

by the spectra combination of 5 bins over one decade from the mean high and low-frequency spectrum. The overlap region may be wider, Kaimal and Finnigan (1994) recommends a 2 decade overlap, depending on the time series length or the spectral splicing. The final spectrum is depicted in figure A.5d, plotted side-by-side with the $f^{5/3}$ inertial decay for reference. This procedure can be repeated to different wind conditions by recurring to longer time series and applying both axis normalization.

Appendix B

Wavelet analysis

B.1 Introduction

A *wavelet* is a small wave, which has its energy concentrated in time to give a tool of time varying phenomena. It has the ability to allow simultaneous time and frequency analysis with a flexible mathematical foundation. Figure B.1 shows both a sinusoid wave oscillating with amplitude over $-\infty \leq t \leq +\infty$ and, therefore, having infinite energy and with the wavelet having its finite energy concentrated around a point.

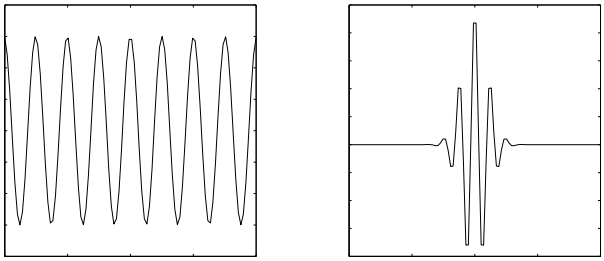

Figure B.1: A sine wave and a Morlet wavelet.

Wavelets are used in terms of series expansion of signal or functions much the same way a Fourier series uses the sinusoid to represent a signal or function. The signals are functions of a continuous variable, which often represent time or distance. From the series expansion, a version similar to the discrete Fourier transform is developed where the signal is represented by a string of numbers.

The statistical description of a turbulent signal is fundamental to retrieve its physical information, being limited thought in revealing periodic or non-periodic features of the signal. In a turbulent signal, it provides a clear view of scales of turbulent motion, namely the energy, shear-stress or concentration distribution in the wavenumber space.

Spectral analysis based in Fourier transforms is the tool of choice for handling stationary time series (Pope, 2000) though presenting limitations for non-stationary processes (Bendat and Piersol, 2000). Wavelet transform is founded in a compact basis and therefore it is more robust than the periodic decomposition of a Fourier transform (Farge et al., 1996). The continuous wavelet transform is an attractive tool for decomposing a time-series into time-frequency space, which gives the opportunity to determine both the dominant modes of variability and how these modes vary in time. The Fourier transform is strictly located in frequency thus not well-suited to investigate intermittent process like atmospheric turbulence because all temporal information is lost. It can be assumed as a 'global' when compared to the 'local' transform features of the wavelet. Justified by the fact that the transformed coefficients are only influenced by a portion of the point defined by the translation parameter.

The wavelet analysis is a relatively recent technique. Wavelets were developed independently in the fields of mathematics, quantum physics, electrical engineering, and seismic geology. Interchanges between these fields during the last 10 years have led to many new wavelet applications including turbulence (Graps, 1995). The early work wavelets applied to turbulence started in the 90's, summarized by the review paper from Farge et al. (1996). Li (1998) classifies the published literature into two categories: extracting the characters of the turbulent or eddy structure from the wavelet analysis of experimental data and simulation data; and developing turbulence modeling and numerical methods based on wavelet bases. Our study fits into the first category. A helpful guide in wavelets for signal processing analysis is presented by Torrence and Compo (1998), where practical issues on wavelet transforms are addressed.

B.2 Wavelet basics

The continuous wavelet transform $W(s,\tau)$ of a real square integrable signal $f(t)$ with respect to an analysing wavelet $\psi(t)$ can be defined as:

$$W(s,\tau) = \frac{1}{s}\int_{-\infty}^{+\infty} f(t)\psi\left(\frac{t-\tau}{s}\right)dt = \frac{1}{s}\int_{-\infty}^{+\infty} f(t)\psi_{s,\tau}(t)dt \tag{B.1}$$

where s is the scale dilatation and τ is a position translation. In Fourier space, using Parseval's theorem equation (B.1) can be written:

$$W(s,\tau) = \frac{1}{s}\int_{-\infty}^{+\infty} \hat{f}(\omega)\hat{\psi}^{*}(s\omega_{\tau})d\omega = \frac{1}{s}\int_{-\infty}^{+\infty} \hat{f}(\omega)\hat{\psi}^{*}(\omega)d\omega \tag{B.2}$$

where * indicates the complex conjugate and $\hat{}$ is the Fourier transform of a function given by:

$$\hat{f}(t) = \frac{1}{2\pi} \int_{-\infty}^{+\infty} f(t) \exp(-i\omega t) dt \tag{B.3}$$

The wavelet representation is much like a musical score where the location of the notes tells when the tones occur and what their frequency are. In fact, it is the convolution of $f(t)$ with a scaled and translated version of a wavelet function $\psi(t)$, Burrus et al. (1998).

A wavelet is defined as a real or complex value function of a real variable that have zero mean and be localized in both time t and frequency spaces ω. The energy of a function $f(t)$ is given by:

$$E = \int_{-\infty}^{+\infty} |\psi(t)|^2 \, dt \tag{B.4}$$

$$C_\psi = 2\pi \int_{-\infty}^{+\infty} \frac{\left|\hat{\psi}(\omega)\right|^2}{\omega} d\omega \tag{B.5}$$

Equation (B.4) implies that ψ has finite energy and equation (B.5) that ψ has zero mean if the Fourier transform ψ is in the vicinity of the detection frequency. This is the admissibility condition, Burrus et al. (1998), and C_ψ is the admissibility parameter, which is scaled independently and constant for each wavelet function.

Thus the wavelet function is a bandpass filter with known response function, the wavelet function, and is invertible and it is possible to reconstruct the signal with the following equation:

$$f(t) = \frac{1}{C_\psi} \int_{-\infty}^{+\infty} \int_{-\infty}^{+\infty} W(s,\tau) \frac{1}{s^2} \psi(s\omega t) ds d\tau \tag{B.6}$$

The wavelet is also energy preserving so the total energy E_f of a function $f(t)$ can be written as:

$$E_f = \int_{-\infty}^{+\infty} |f(t)|^2 \, dt = \int_{-\infty}^{+\infty} \left|\hat{f}(\omega)\right|^2 d\omega \tag{B.7}$$

$$= \frac{1}{C_\psi} \int_0^{+\infty} \frac{ds}{s} \int_0^{+\infty} |W(s,\tau)|^2 \, d\tau \tag{B.8}$$

Equation (B.7) correlates the spectral density energy, also referred as Fourier or energy spectrum, $E_f(\omega) = \left|\hat{f}(\omega)\right|^2$ to the wavelet variance:

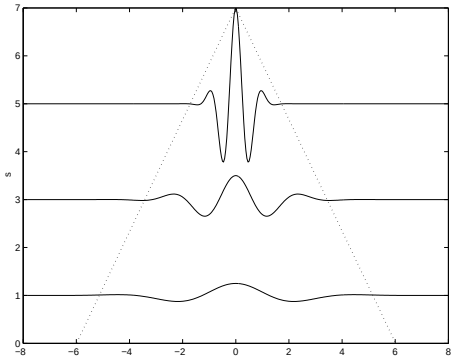

Figure B.2: Morlet wavelet - The x-axis corresponds to a non-dimensional time. The y shows the shape changes due to the scaling factor s.

$$E_W(s) = \int_{-\infty}^{+\infty} |W(s,\tau)|^2 \, d\tau \tag{B.9}$$

Thus, $E_W(s)$ is the energy of a function $f(t)$ at scale s and is referenced as wavelet scalogram. The coherence between Fourier and wavelet spectrum is given by:

$$E_W = 2 \int_{-\infty}^{+\infty} E_f(\omega) E_{\psi_s}(\omega) d\omega \tag{B.10}$$

i.e., $E_W(s)$ is the Fourier spectrum of $f(t)$ averaged by the Fourier spectrum of the wavelet function ψ_s at scale s.

In this study we use the Morlet wavelet (figure B.2) to decompose each scale according to Kelley et al. (2000). A mother wavelet, from were all the others to be scaled - in a expanding and shrinking process according to the s scaling parameter - followed by a convolution with the time series along the time wise direction, figure B.2. That corresponds to a filtering process where filter changes the shape (scale) according to several proprieties presented in Burrus et al. (1998). The degree of similarity between one scaled wavelet and the oscillation in the signal can be represented in a 2-D scalogram, where the x-axis corresponds to the time-wise evolution of the series, and the y-axis corresponds to the scale or frequency. A more comprehensive discussion on the differences between wavelet and Fourier spectra is found at Perrier et al. (1995) and an example is presented in section B.3.

B.3 Scalogram and wavelet spectrum

The example that follows illustrates the applicability of the scalogram wavelet autocorrelation. Figure B.3a presents a statistically unstationary signal with two frequencies in the

time-amplitude domain. The signal is null at the beginning and end of the series to exclude all edge effects, starting to oscillate in the amplitude range of ± 1 changing the frequency as time evolves. Both existing frequencies, 10 and 40 Hz, do not exist simultaneously. This information is not present in the Fourier density spectrum at figure B.3b or in the wavelet spectrum, figure B.3d. The wavelet scalogram, presents a more complete information of the evolution of the signal. The time scale is needed because the signal is time-dependent . A 10 Hz frequency oscillation starts at 0.25 s, changing to 40 Hz at 0.75 s, and this pattern is repeated at 1.25 s. The whiter areas in the scalogram represent the similarity between the signal period and the wavelet scale, where the lighter colors stand for the maximum similarity darkening as the similarity coefficients decrease (black for no similarity).

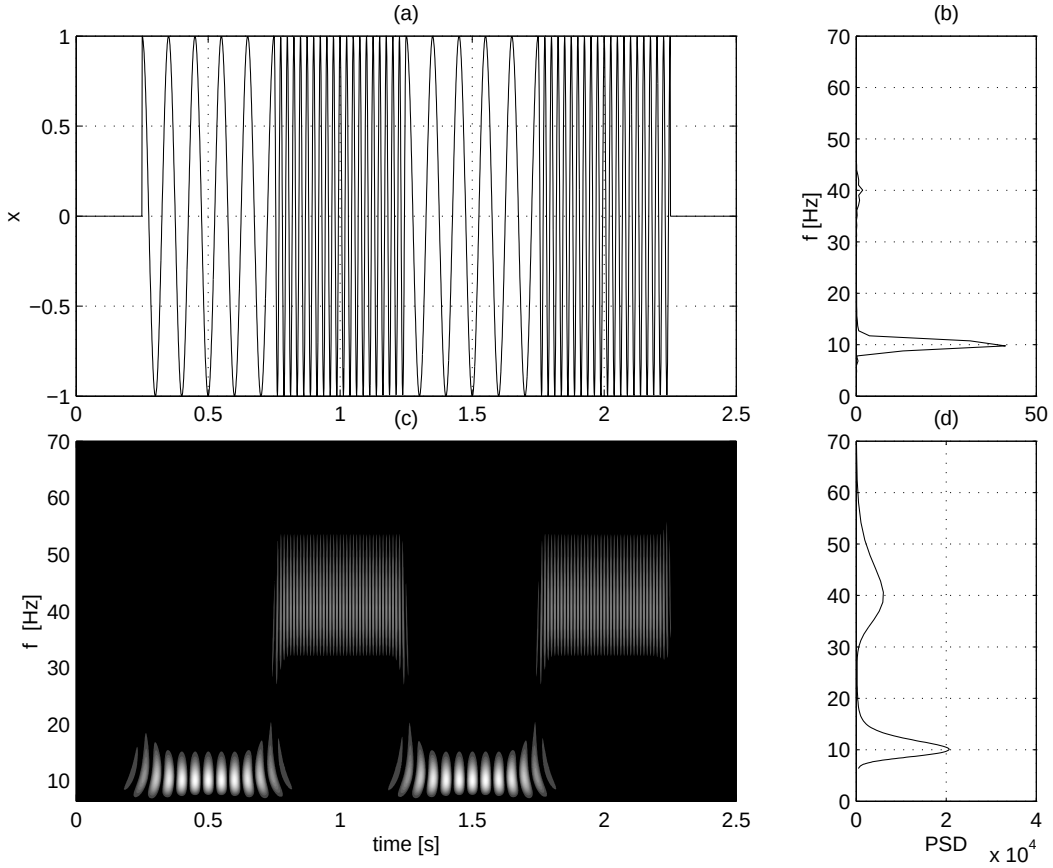

Figure B.3: A statistical unsteady signal with two frequencies and the respective Power Spectral Density.

The clear advantage of this tool lies on the detection of the frequency, or period change, pin-pointing in the time domain where these changes had occurred. In a simple signal such as in this example, a visual observation of the time series will suffice. However, for a unstationary turbulence signal, the frequency change is not so clearly identified due to the superposition of several frequencies at distinct times. Other clear advantage is the identification of the frequency (or period) of oscillation in the scalogram y-axis. A third

advantage of this method is also observed in figure B.3c for the frequency transition between no signal and 10 Hz, or in the transition from 10 to 40 Hz. The scalogram detects a new frequency by prolonging the wavelet coefficients in the time and frequency domain. At times where a frequency transition occur, 0.25, 0.75, 1.25, 1.75 and 2.25 s, the wavelet coefficients are spreader along the maximum than the no transition case.

The wavelet spectrum is obtained by squaring the wavelet coefficients and averaging in the time domain. Basically it is the projection of the average of the square wavelet coefficients in the frequency-power plane. In the example of figure B.3c the wavelet coefficients were normalized to ± 1 thus the spectra of figure B.3d was obtained prior to the scalogram normalization.

By observing figures B.3b and B.3d we verify that the wavelet spectrum is a bias estimator of the spectral power. Although the maximum peaks coincide, the wavelet is wider along each peak than the Fourier spectrum. That is an embedded feature of this tool and is related to the discretization of the time-frequency domain, which will not be discussed in this section. This discussion may be consulted in Burrus et al. (1998).

B.4 Scalogram autocorrelation

The signal of figure B.3 presented two distinct frequencies, although they are repeated in time. If we consider the scalogram as any ordinary time evolving signal, the set of common frequencies and how they are repeating themselves as time evolves may be obtained by the autocorrelation of the scalogram itself. Considering any constant frequency of the scalogram of figure B.3c, were obtain a time evolving wavelet coefficient. When the signal frequency resembles the wavelet shape, the coefficient will close to 1. If that same signal frequency appears latter on in time, the autocorrelation will indicate the time-shift for the same frequency, τ. By applying the autocorrelation for all frequencies, or scales, of the scalogram, we will obtain the repetition time of the frequency set present in the scalogram.

Figure B.4a is the autocorrelation of the scalogram of the example at figure B.3c. In this case, the wavelet coefficient was not normalized between 0 and 1 so the phase shift is also present in the example. The best correlation is clearly, as expected, for a null time shift, $\tau = 0$. As the time shift increases, the autocorrelation between the wavelet coefficients decreases until there is no correlation for $\tau = 0.5$s. As τ increases, the autocorrelation also increases until $\tau = 1$s. This time-shift corresponds exactly to the repetition time of the frequency set of the time series, *i*.e. the two sets of frequencies at 10 and 40 Hz are repeated at every second, figure B.3a. Applying this procedure for all frequencies at figure B.3c we will obtain a time-shift-frequency-autocorrelation plane as depicted in figure B.4b.

We observe if B.4b that both frequencies are correlated for a time-shift from 0 to 0.5 s, although the quality of this correlation decreases until no correlation for $\tau = 5$ s. Increasing the time shift, both frequencies correlation start increasing reaching a new maximum at

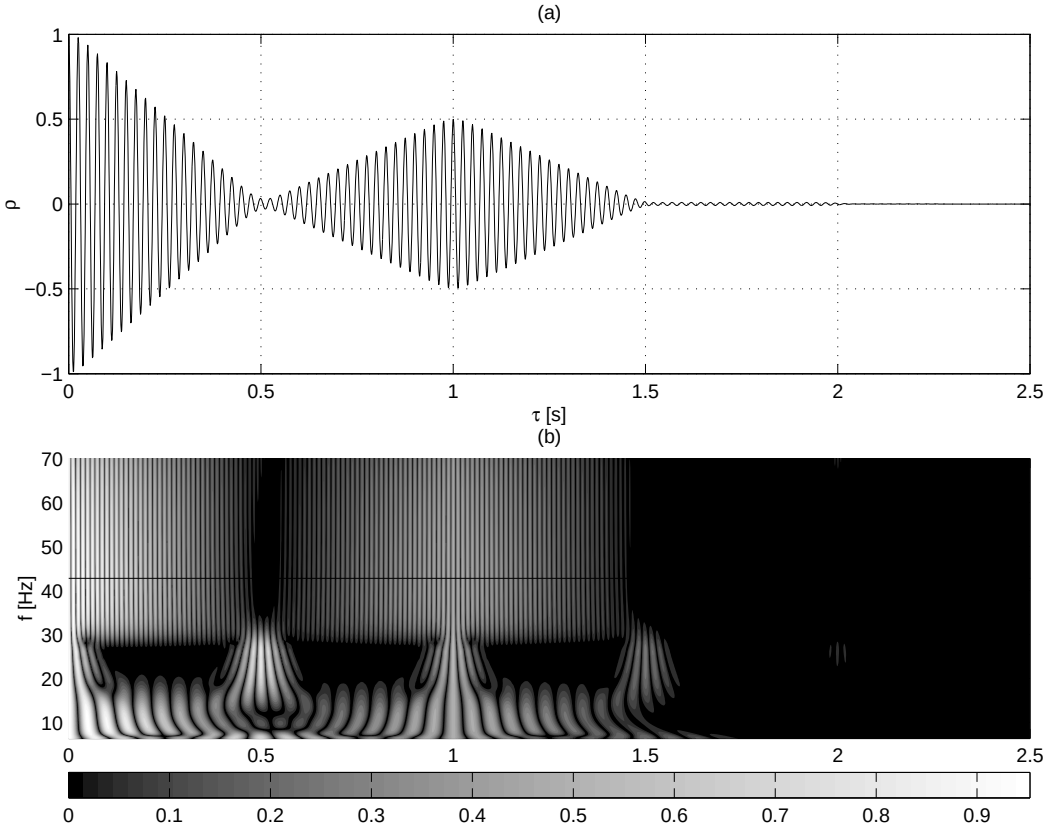

Figure B.4: Scalogram autocorrelation of the signal in figure B.3c.

1 s. Again, the pattern is repeated. As the time-shift increases, the autocorrelation of the wavelet spectrum decreases until 1.5 s. The edge effects of the signal transition from on frequency to another, or from one frequency to no oscillation are also correlated and observable each 0.5 s.

Appendix C

Quadrant analysis

Quadrant analysis is an event detection technique used in fundamental fluid mechanics and micrometeorological research. A comprehensive review on the method may be consulted at Pope (2000) or Krogstad and Skåre (1995) regarding the wall region of boundary layer or duct flows. Quadrant analysis is also widely used in micrometeorology where contributions by Shaw et al. (1983) on canopy flows become standard in fluid mechanics research (Krogstad and Skåre, 1995; Krogstad and Kaspersen, 2002). Feigenwinter (1999) presents a comprehensive list of publications on both urban and canopy flows. Results for flows with lower roughness and complexity (tall grass and bare soil) are found in Katul et al. (1997) while Shiau and Chen (2002) characterizes a complex site in a coastal area.

The $u-w$ decomposition technique has been used to access the importance of ejections and sweeps visually in the wall region of boundary-layer (Wallace et al., 1972). The mean rate of downward diffusion of longitudinal momentum is represented by the kinematic Reynolds stress, $-\overline{u'w'}$. Additional information about the diffusion process is provided by sorting the instantaneous values of u' and w' into four categories according to the sign of the fluctuating components. The quadrants in the (u, w)-plane are numbered as follows (Shiau and Chen, 2002):

- Quadrant 1 - Q_1: $u' > 0$, $w' > 0$ outward interaction.
- Quadrant 2 - Q_2: $u' < 0$, $w' > 0$ ejection or burst.
- Quadrant 3 - Q_3: $u' < 0$, $w' < 0$ inward interaction.
- Quadrant 4 - Q_4: $u' > 0$, $w' < 0$ sweep or gust.

Quadrants 1 and 3 represent upward transfer while quadrants 2 and 4 represent contributions to downward diffusion of momentum. The small scale frequent contributions to the Reynolds stress can be excluded from the analysis by introducing the hyperbolic hole,

H, Lu and Willmarth (1973), which is an excluding criteria in the covariance plane. It wipes out the information from small to large scales by comparing $H|\overline{u'w'}|$ with the $u'w'$ instantaneous values product. The fraction of flux outside the hyperbolic hole H in the quadrant i is defined as:

$$S_{i,H} = \frac{\langle u'w' \rangle_{i,H}}{\overline{u'w'}} \tag{C.1}$$

where the $\langle \ldots \rangle$ denotes a conditional averaging:

$$\langle u'w' \rangle_{i,H} = \lim_{T \to \infty} \frac{1}{T} \int_0^T u'(t)w'(t)I_{i,H}(t)dt \tag{C.2}$$

where I is a quadrant flag defined to be 1 outside the hole and 0 inside

$$I_{i,H} = \begin{cases} 1 & \text{if } u'w' \text{ is in quadrant } i \text{ and } |u'w'| \geq H|\overline{u'w'}| \\ 0 & \text{otherwise} \end{cases} \tag{C.3}$$

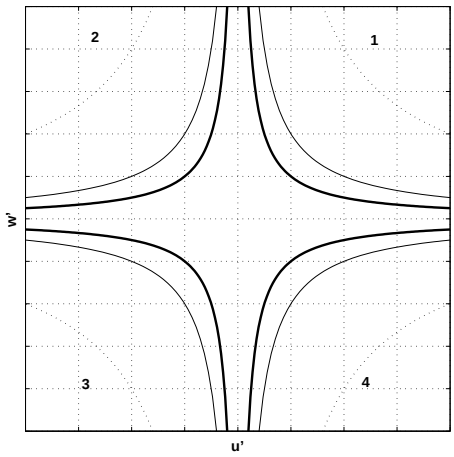

Figure C.1: The hyperbolic hole concept for quadrant analysis. Thicker to thinner lines represent the increase in the hyperbolic hole excluding smaller $u'w'$ products from the analysis.

From the flux fraction definition, equation (C.1), the total flux for the no-hole situation will be the unit, $\sum_{i=1}^{4} S_{i,0} = 0$. We define alternatively the time fraction for any contribution $S_{i,H}$ as

$$T_{i,H} = \lim_{T \to \infty} \frac{1}{T} \int_0^T I_{i,H}(t)dt \tag{C.4}$$

where $T_{2,H}$ or $T_{4,H}$ are the total sweep and ejection duration for the hole size H.

The hyperbolic hole analysis can lead us further with a quadrant to quadrant comparison. On the vertical plane, the ejection and sweeps on quadrants 2 and 4 can be categorized into organized in opposite to 'random' turbulence, that occurs in quadrants 1 and 3.

The exuberance, Ex (Shaw et al., 1983), is defined as the ratio of uncorrelated to correlated of the total momentum flux:

$$Ex = \frac{S_{1,0} + S_{3,0}}{S_{2,0} + S_{4,0}} \tag{C.5}$$

For the organized turbulence on the vertical plane, we can measure the relative importance of sweeps over ejections by the difference

$$\Delta S_H = S_{4,H} - S_{2,H} \tag{C.6}$$

or by their ratio

$$\gamma = \frac{S_{2,H}}{S_{4,H}} \tag{C.7}$$

Appendix D

Combining short-term to longer term statistics and bootstrap technique

D.1 Combining short-term to longer term statistics

Due to data storage limitations, high-rate flux measurements are often stored in 5-min average statistics because this is the shortest time that most users recur to compute second-order moments. Usually, averages over much longer periods, 15-30 minutes, are used to include low-frequency variations associated with, for example, convection.

For two time series $x(t)$ and $y(t)$, the mean and covariance are defined by:

$$\overline{x} = \frac{1}{N}\sum_{i=1}^{N} x(i) \tag{D.1}$$

$$\overline{x'y'} = \frac{1}{N}\sum_{i=1}^{N}[x(i) - \overline{x}][y(i) - \overline{y}] \tag{D.2}$$

Equations (D.1) and (D.2) expands in 4 terms, but the last 3 collapse into one.

$$\overline{x'y'} = \frac{1}{N}\sum_{i=1}^{N} x(i)y(i) - \overline{xy} \tag{D.3}$$

The above definitions are true for any averaging period.

Suppose we subdivide a period N into m segments of length N_j (for example, a 30-min period into 6×5-min periods). In order to find $\overline{x'y'}^N$ in terms of values computed from

periods of length N_j, we need to find $\overline{x}^N$ and $\sum_{i=1}^{N} x(i)y(i)$. Then:

$$\overline{x}^N = \frac{1}{N}\sum_{j=1}^{m}\sum_{i=1}^{N_j} x_j(i) \tag{D.4}$$

$$= \frac{1}{N}\sum_{j=1}^{m} N_j \overline{x}^j \tag{D.5}$$

Similarly

$$\sum_{i=1}^{N} x(i)y(i) = \sum_{j=1}^{m}\sum_{i=1}^{N_j} x_j(i)y_j(i) \tag{D.6}$$

$$= \sum_{j=1}^{m} N_j(\overline{x'y'}^j + \overline{x}^j\overline{y}^j) \tag{D.7}$$

Thus

$$\overline{x'y'}^N = \frac{1}{N}\sum_{j=1}^{m} N_j(\overline{x'y'}^j + \overline{x}^j\overline{y}^j) - \frac{1}{N}\sum_{j=1}^{m} N_j\overline{x}^j \frac{1}{N}\sum_{j=1}^{m} N_j\overline{y}^j \tag{D.8}$$

If all N_j are equal this simplifies to:

$$\overline{x'y'}^N = \frac{1}{m}\sum_{j=1}^{m}(\overline{x'y'}^j + \overline{x}^j\overline{y}^j) - \frac{1}{m}\sum_{j=1}^{m}\overline{x}^j \frac{1}{m}\sum_{j=1}^{m}\overline{y}^j \tag{D.9}$$

Similar expressions my be derived for higher-order moments

D.2 Bootstrap

Bootstrap is a technique based in a new body of statistics named resampling methods, which is tied to the Monte Carlo simulation where the data is 'rearranged' and conclusions are drawned based on many possible scenarios, Lunneborg (2000). The bootstrap technique was developed with inferential purposes, where one available sample gives rise to many others by samples of the original data set with replacement of the original data set, Yo (2003).

The procedure involves choosing random samples with replacement for a data set and analysing each sample the same way. Sampling with replacement means that every sample is returned to the data set after sampling. So a particular data point from the original data set could appear multiple times in a given bootstrap sample. The number of elements in each bootstrap sample equals the number in the original data set and the range of sample estimates we obtain allow us to establish the uncertainty of the quantity we are estimating.

Table D.1 illustrate the bootstrap technique. From an original data set with m observations, $y_1, y_2, \ldots, y_m$, we produce as many new samples of the original set by resampling the original set obtaining thus n virtual samples. Each virtual sample has the same length of the original data set, from were we may obtain an individual estimator, *e.g.* mean, standard deviation, R^2, etc. A probability distribution is build upon the n group of estimators where we can make inference tests based on this empirical distribution.

Table D.1: Bootstrap example.

original data set	virtual set 1	virtual set 2	...	virtual set n
y_1	y_3	y_2		y_5
y_2	y_5	y_6		y_3
y_3	y_4	y_6		y_3
y_4	y_2	y_6		y_m
y_5	y_5	y_4		y_4
y_6	y_3	y_3		y_2
$\vdots$	$\vdots$	$\vdots$		$\vdots$
y_m	y_5	y_1		y_m

Bootstrapping could treat a small sample as the virtual population to generate more observations. Although there is no specific sample size requirement in resampling, the only limitation is the CPU time, there should be enough observations to adequately approximate the universe of possibilities. If the original sample size is 2, then all bootstrap samples will be of size 2. The purpose of resampling is to simulate chance. Needless to say, a sample size of 2 will not illuminate the research question in the perspective of chance simulation, Yo (2003).

Bibliography

Wind turbine generator systems - Part 1: Safety requirements. International Standard, 1999. Reference number IEC 61400-1:1999(E).

Technical Descripton of a Sonic Anemometer/Thermometer. Applied Technogolies, Inc, 1120 Delaware Avenue, Longmont, Colorado, USA, 2002.

A. C. Araujo, A. D. Nobre, B. Kruijt, A. D. Culf, P. Stefani, J. A. Elbers, R. Dallarosa, C. Randow, A. O. Manzi, R. Valentini, J. H. C. Gash, and P. Kabat. Comparative measurements of carbon dioxide fluxes from two nearby towers in a central Amazonian rainforest: the Manaus LBA site. *Journal of Geophysical Research*, 107:359–382, 2002.

M. Aubinet, A. Grelle, A. Ibrom, Ü. Rannik, J. Moncrieff, T. Foken, A.S. Kowalski, P.H. Martin, P. Berbigier, C. Bernhofer, R. Clement, J. Elbers, A. Granier, T. Grunwald, K. Morgenstern, K. Pilegaard, C. Rebmann, W. Snijders, R. Valentini, and T. Vesala. Estimates of the annual net carbon and water exchange of forests: the EUROFLUX methodology. *Adv. Ecol. Res.*, 30:113–175, 2000.

P.G Baines. *Topographic Effects in Stratified Flow*. Cambridge University Press, 1995.

C. B Baker, R. E Eskridge, P. S. Conkin, and K. R. Knoerr. Wind tunnel investigation of three sonic anemometers. NOAA Technical Memorandum ERL ARL-178, Air Resoures Laboratory, Silver Spring, Mariland, 1989.

J. Bendat and A. Piersol. *Random Data - Analysis and Measurement Procedures*. John Wiley & Sons, third edition edition, 2000.

F. Beyrich, S. Richter, U. Wiesensee, W. Kohsiek, F. Bosvelt, H. Lohse, H. de Bruin, O. Hartogensis, J. Bange, and Vogt. R. The Litfass-98 experiment: Fluxes over heterogeneous land surface. In *14th Symposium on Boundary Layer and Turbulence*, 2000.

C. Biltoft. Momentum flux: Gross, scalar, alongwind, or net? Technical report, Adiabat Meteorological Services, 2003a. 0303.

C. Biltoft. Some thoughts on in-situ flux measurement in the atmospheric surface layer. Technical report, Adiabat Meteorological Services, 2003b. 0303.

C. Burrus, R. Gopinath, and H. Guo. *Introduction to Wavelets and Wavelet Transforms – A Primer*. Prentice Hall, 1998.

T. Burton, D. Sharpe, N. Jenkins, and E. Bossanyi. *Wind Energy Handbook*. John Wiley and Sons, 2001.

J. Businger, W. Dabberdt, A. Delany, T. Horst, C. Martin, S. Oncley, and S. Semmer. Aster - the atmosphere-surface turbulent exchange research facility at NCAR. *Bul. Amer. Meteor. Soc.*, 71(7):1006–1011, 1990.

3-D Sonic Anemometer. Campbell Scientific, Inc, Logan, Utah - 84321-1784, 2004.

Carrier and Carlson. A true air speed indicator. NDCR Report, Cruft Laboratories, Harvard University, 1944.

A. Christen, E. van Grosel, M. Andretta, P. Calanca, M. Rotach, and R. Vogt. Intercomparison of ultrasonic anemometers during the Map-Riviera project. In *9th AMS Conference on Mountain Meteorology*, 2000.

P. A. Coppin and K. J. Taylor. A three-component sonic anemometer/thermometer system for general micrometeorological research. *Boundary-Layer Meteorology*, 27, 1983.

A. Cuerva. Steps to reach a safe scenario with sonic anemometer as a standard sensor for wind measurement in wind energy. In *1999 European Wind Energy Conference*, pages 649–652, 1999.

A. Cuerva and Sanz-Andrés. On sonic anemometer theory. *Journal of Wind Engineering and Industrial Aerodynamics*, 88:25–55, 2000.

European Wind Energy Association. The European Wind Industry strategic plan for research and developement - first report: creating the knowledge for a clean energy era. Technical report, European Wind Energy Association, 2004.

M. Farge, N. Kevlahan, V. Perrier, and E. Goirand. Wavelets and turbulence. *Proceedings of IEEE*, 84(4):639–668, 1996.

C. Feigenwinter. *The Vertical Structure of Turbulence above an Urban Canopy*. PhD thesis, Basel University - Swisserland, 1999.

J. W. Finch and R. J. Harding. A comparison between reference transpiration and measurements of evaporation for a riparian grassland site. *Hydrol. Earth System Sci.*, 2: 129–136, 1998.

J. Finnigan. Averaging, integrating and filtering in non-stationary inhomogeneous flows. In *Indiana Workshop on Nightime CO_2 Fluxes*, 1999.

J. J. Finnigan, R. Clement, Y. Malhi, R. Leuning, and H. A. Cleugh. A reevaluation of long-term flux measurements techniques. Part I. Averaging and coordinate rotation. *Boundary-Layer Meteorology*, 107:1–48, 2003.

T. Foken and S. Oncley. A report on the workshop: Instrumental and methodical problems of land-surface flux measurements. *Bull. Amer. Met. Soc.*, 76:1191–1193, 1995.

T. Foken and B. Wichura. Tools for quality assessment of surface-based flux measurement. *Agric. For. Meteorol.*, 78:83–105, 1996.

A. Fragoulis, F. Avia, E. Binopoulos, M. Cruz, A. Cuerva, D. Foussekis, D. Koulouvari, V. Lopez, I. Marti, F. Morfiadakis, F. Mouzakis, S. Petersen, A. Vazquez, and P. Voelund. Site characterization and wind structure on complex terrain. Technical Report 1, Center for Renewable Energy Sources-Wind Energy Department, 19th km Marathonos Avenue, Pikermi, 19009, Greece, 1996.

J. R. Garrat. *The Atmospheric Boundary Layer*. Cambridge University Press, 1994. ISBN 0 521 46745 4.

J. H. C. Gash and A. J. Dolman. Sonic anemometer (co)sine response and flux measurement. i. the potential for (co)sine error to affect sonic anemometer-based flux measurements. *Agricultural and Forest Meteorology*, 119:195–207, 2003.

Research R3, R3A and HS. Gill Instruments, Ltd, Saltmarsh Park, 67 Gosport Street-Lymington - Hampshire - England, 2004.

A. Graps. An introduction to wavelets. *IEEE Computational Science and Engineering*, 2 (2), 1995.

T. Hanafusa, T. Fujitani, Y. Kobori, and Y. Mitsuta. A new type of sonic anemometer-thermometer for field operation. *Pap. Meteorol. Geophys.*, 33:1–19, 1982.

T. Hanafusa, Y. Kobori, and Y. Mitsuta. Single head sonic anemometer-thermometer. Instruments and Observing Methods 3, World Meteorological Organization, Geneva, Switzerland, 1980.

D. Heinemann, D. Langner, U. Stabe, and H.-P. Waldl. Measurement and correction of ultrasonic anemometer errors and impact on turbulence measurements. In *Proceedings of the European Wind Energy Conference, Dublin*, pages 409–412, 1997.

U. Högström and A. S. Smedman. Accuracy of sonic anemometers: Laminar wind-tunnel calibrations compared to atmospheric *in situ* calibrations against a reference instrument. *Boundary-Layer Meteorology*, 111:33–54, 2004.

T. Horst. Sonic tilt angles. Technical report, NCAR, 2001.

T. Horst and C. Weil. How far is far enough?: The fetch requirements for micrometeorological measurement of surface fluxes. *Journal of Atmospheric and Oceanic Technology*, 11(4):1018–1025, 1994.

International Energy Agency. Recommended practices for wind turbine testing and evaluation. International Energy Agency, 1990.

J. C. Kaimal. Sonic Anemometer Measurement of Atmospheric Turbulence. In *Proceedings of the Dynamic Flow Conference, 1978*, pages 551–565, 1978.

J. C. Kaimal. Basic tests for checking validity of field data. Technical report, Aplied Technologies, 1990a.

J. C. Kaimal. Effects of spatial filtering, prefiltering, and aliasing in measurements from Applied Technologies' sonic K-Probe. Technical report, Applied Technologies, 1990b.

J. C. Kaimal. Transducer Shadow Correction for Applied Technologies' Sonic K-Probe. Technical report, Aplied Technologies, 1990c.

J. C. Kaimal and J.J. Finnigan. *Atmospheric Boundary Layer Flows - Their Structure and Measurement*. Oxford University Press, 1994.

J. C. Kaimal, J. Gaynor, H. A. Zimmerman, and G. A. Zimmerman. Minimizing flow distortion errors in a sonic anemometer. *Boundary-Layer Meteorology*, 53:103–115, 1990.

J. C. Kaimal and J.E. Gaynor. Another look at sonic thermometry. *Boundary-Layer Meteorology*, 56:401–410, 1991.

J.C. Kaimal and J.A Businger. A Continuous Wave Sonic Anemometer-Thermometer. *Journal of Applied Meteorology*, 2:156–164, 1963.

G. Katul, G. Kuhn, J. Schieldge, and C. Hsieh. The ejection-sweep character of scalar fluxes in the unstable surface layer. *Boundary-Layer Meteorology*, 83:1–26, 1997.

N. Kelley. A Case for Including Atmospheric Thermodynamic Variables in Wind Turbine Fatigue Loading Parameter Identification. In *2nd Symposium on Wind Conditions for Wind Turbine Design - IEA Annex XI*, 1999.

N. Kelley, R. Osgood, J. Bialasiewicz, and A. Jakubowski. Using Time-Frequency and Wavelet Analysis to Assess Turbulence/Rotor Interactions. In *19th American Society of Mechanical Engineers - Wind Energy Symposium*, 2000.

L. Kristensen. Measuring Higher-Order Moments with a Cup Anemometer. *Journal of Atmospheric and Oceanic Technology*, 17:1139–1148, 2000.

L. Kristensen, O.F. Hansen, and J Høstrup. Sampling bias on cup anemometer mean winds. *Wind Energy*, 6:321–331, 2003.

P-A. Krogstad and J. H. Kaspersen. Structure Inclination Angle in a Turbulent Adverse Pressure Gradient Boundary Layer. *Journal of Fluids Engineering*, 124:1025–1033, 2002.

P-A. Krogstad and P.E. Skåre. Influence of strong adverse pressure gradient on turbulent structure in a boundary layer. *Physics of Fluids*, 7(8):2014–2024, 1995.

Hui Li. Identification of coherent structure in turbulent shear flow with wavelet correlation analysis. *Journal of Fluids Engineering*, 120:778–785, 1998.

S.S. Lu and W.W. Willmarth. Measurements of the structure of the Reynolds stress in a turbulent boundary layer. *Journal of Fluid Mechanics*, 60(481), 1973.

C. E. Lunneborg. *Data analysis by resampling: Concepts and Applications*. Duxbury, 2000.

L. Mahrt, D. Vickers, J. Sun, H. Jensen, H. Jorgensen, E. Pardyjak, and H. Fernando. Determination of the surface drag coefficient. *Boundary-Layer Meteorology*, 99:249–276, 2000.

I. Marti, M. Marchante, J. Navarro, M. Cruz, and F. Martin. Wind turbulent length scale analysis, comparison of Taylor and von Kármán methodologies. In *1999 Wind Energy Conference*, pages 1029–1031, 1999.

W. Massman. Summary and synthesis of recommendations of the AmeriFlux workshop on standartization of flux analysis and diagnostics. Technical report, AmeriFlux, 2003.

W. Massman and X. Lee. Eddy covariance flux corrections and uncertainties in long-term studies of carbon and energy exchanges. *Agricultural and Forest Meteorology*, 113: 121–144, 2002.

J.M Militzer, M.C. Michaelis, S. R. Semmer, K. S. Norris, T. W. Horst, S. P. Oncley, A. C. Delany, and F. V. Brock. Development of the prototype PAM III/Flux PAM surface meteorological station. In *9th AMS Symposium on Meteorological Observations and Instrumentation, Charlote, N. C.*, 1995.

N. Mortensen, S. Oncley, T. Horst, and J. Høojstrup. Flow distortion by sonic anemometers. Unpublished report, 1995.

S. Oncley. Summary of flipped and rotated sonic anemometer tests. Personal Communication, 1996.

S. Oncley, T. Foken, R. Vogt, C. Bernhofer, X. Ping, Z. Sorbjan, A. Pitacco, D. Grantz, and L. Ribeiro. The EBEX field experiment. In *14th Symposium in Turbulence and Boundary Layer*, 2000.

S. P. Oncley. *Flux Parametrization Techniques in the Atmospheric Surface Layer*. PhD thesis, University of California, 1989.

S.P. Oncley. *Air-Sea Exchange: Physics, Chemistry and Dynamics*, chapter The Leading Edge of Turbulence Instrumentation, pages 1–28. Kluwer Academic Press, 1999.

J.M.L.M. Palma, F.A. Castro, and L.M.F. Ribeiro. Análise do escoamento atmosférico na Região do Caniçal e no Paúl da Serra, na Ilha da Madeira. Protocolo de cooperação com a empresa electricidade da madeira, Faculdade de Engenharia da Universidade do Porto, 2002.

K. H. Papadopoulos, N. C. Stefanatos, U. S. Paulsen, and E. Morfidiakis. Effects of turbulence and flow inclination on the performance of cup anemometers in the field. *Boundary-Layer Meteorology*, 101:77–107, 2001.

A. Papoulis. *The Fourier Integral and Its Applications*. McGraw-Hill, 1962.

B. Pedersen, T. Pedersen, H. Klug, N. Borg, N. Kelley, and J. Dahlberg. Recommended practices for wind turbine testing - 11. wind speed measurement and use of cup anemometry. Technical report, Executive Committee of the International Energy Agency Programme for Research and Development on Wind Energy Conversion Systems, 1999.

T. F. Pedersen. On wind turbine power performance measurements at inclined airflow. *Wind Energy*, 7:163–176, 2004.

V. Perrier, T. Philipovich, and C. Basdevand. Wavelet spectra compared to fourier spectra. *J. Math. Phys.*, 36:1506–1519, 1995.

E.L Petersen, N.G. Mortensen, L. Landberg, J. Højtrup, and H. Frank. Wind power meteorology. Part I: Climate and Turbulence. *Wind Energy*, 1:25–45, 1998.

J Pope. *Turbulent Flows*. Cambridge University Press, 2000.

G. Raithby, G. Stubley, and P. Taylor. The askervein hill project: A finite control volume prediction on three-dimensional flows. *Boundary-Layer Meteorology*, 1996.

A. Restivo and E.L. Petersen. Wind measuring and modelling in mountainous regions of portugal. preliminary results. In *European Wind Energy Conference*, 1993.

L.M.F. Ribeiro. Utilização da anemometria sónica no estudo de escoamentos atmosféricos. Master's thesis, Faculdade de Engenharia da Universidade do Porto, 1998.

L.M.F. Ribeiro. Calibration report of 81000 rm young sonic anemometer serial number 00344. Technical report, Instituto Politécnico de Bragança, Bragança, Portugal, 2001.

S. K. Robinson. Coherent motions in the turbulent boundary layer. *Annual Review Fluid Mechanics*, 23:601–639, 1991.

A.H. Rodrigues. Estudo de caracterização do potencial eólico da região norte de portugal (para fins energéticos). Technical report, INEGI, 2000.

M. Rotach, P. Calanca, R. Vogt, D. Steyn, S. Galmarini, and J. Gurtz. The turbulence structure and exchange processes in an alpine valley: The map-riviera project. In *14th Symposium on Boundary Layer and Turbulence*, 2000.

P. Schotanus, F.T.M. Nieuwstadt, and H.A.R. De Bruin. Temperature measurement with a sonic anemometer and its application to heat and moisture fluxes. *Boundary-Layer Meteorology*, 26:81–93, 1983.

R.H. Shaw, J. Tavangar, and D. P. Ward. Structure of the Reynolds stress in a canopy layer. *Journal of Climate and Applied Meteorology*, 22:1922–1931, 1983.

B. Shiau and Y. Chen. Observation on wind turbulence characteristics and velocity spectra near ground at the coastal region. *Journal of Wind Engineering and Industrial Aerodynamics*, 90:1671–1681, 2002.

T. Shimizu, M. Suzuki, and A. Shimizu. Examination of a correction procedure for the flow attenuation in orthogonal sonic anemometer. *Boundary-Layer Meteorology*, 93:227–236, 1999.

H. Siebert and U. Teichman. Behaviour of an ultrasonic anemometer under cloudy conditions. *Boundary-Layer Meteorology*, 94:165–169, 2000.

Roland B. Stull. *An Introduction to Boundary-Layer Meteorology*. Klewer, 1984.

Roland B. Stull. *Meteorology for Scientists and Engineers*. Brooks/Cole Thomson Learning, 2000.

V.E Suomi. *Exploring the Atmosphere's First Mile*, chapter Sonic Anemometer, pages 356–366. Pergamon, New York, 1957.

C. Torrence and G. Compo. A practical guide to wavelet analysis. *Bulletin of the American Meteorological Society*, 79(1):61–78, 1998.

G. Treviño and E. Andreas. Averaging intervals for spectral analysis of nonstationary turbulence. *Boundary-Layer Meteorology*, 95:231–247, 2000.

I. Troen and E.L. Petersen. *European Wind Atlas*. RisøNational Laboratory, 1989.

R. Vogt. *Theorie, Technik und Analyse der experimentellen Flussbestimmung am Beispiel des Hartheimer Kiefernwaldes*. PhD thesis, Basel University - Swisserland, 1995.

R. Vogt, C. Feigenwinter, K.T. Paw U, and A. Pitacco. Intercomparison of ultrasonic anemometers. In American Meteorology Society, editor, *Preprints of the 12th Symposium of Boundary Layers and Turbulence*, pages 354–355, 1997.

J. M. Wallace, H. Eckemann, and R. S. Brodkley. The wall region in turbulent shear flow. *Journal of Fluid Mechanics*, 59(39), 1972.

C. Wamser, G. Peters, and V. N. Lykossov. The frequency response of sonic anemometers. *Boundary-Layer Meteorology*, 84:231–246, 1997.

K. Wesson, G. Katul, and M. Siqueira. Quantifying organization of atmospheric turbulent eddy motion using nonlinear time series analysis. *Boundary-Layer Meteorology*, 106: 507–525, 2003.

J. Wilczak, S. Oncley, and O. Stage. Sonic anemometer tilt correction algorithms. *Boundary Layer Meteorology*, 99:127–150, 2001.

G. Willis and J. Deardorff. On the use of Taylor's translation hypothesis for diffusion in the mixed layer. *Quart. J. Roy. Meteor. Soc.*, 102:817–822, 1976.

K Wilson, A. Goldstein, E. Falge, M. Aubinet, D. Baldocchi, P. Berbigier, Bernhofer C., R. Ceulemans, A. Dolman, C. Field, A. Grelle, A. Ibrom, B. E. Law, A. Kuwlaski, T. Meyers, M. Moncrieff, R. Monson, W. Oechel, J. Tenhunen, R. Valentini, and S. Verma. Energy balance closure at FluxNet sites. *Agricultural and Forest Meteorology*, 113:223–243, 2002.

J. C. Wyngaard. *Workshop in Micrometeorology - On Surface Layer Turbulence*, chapter 3, pages 101–149. Amer. Met. Soc., Boston, MA, 1973.

J.C. Wyngaard. Cup, propeller, vane, and sonic anemometer in turbulence research. *Annual Review of Fluid Mechanics*, 13:399–423, 1981.

J.C. Wyngaard and S.F. Zhang. Transducer-shadow effects on turbulence spectra measured by sonic anemometers. *Journal of Atmospheric and Oceanic Technology*, 2:548–558, 1985.

S. Yahaya and J. P. Frangi. Spectral response of cup anemometers. Technical report, Laboratoire Environnement et Dévelopment - Université Paris 7, 2003.

Chong Ho Yo. Resampling methods: concepts, applications, and justification. *Practical Assessment, Research and Evaluation*, 8(19):1029–1044, 2003.

S.F. Zhang, J. Wyngaard, J. Businger, and S. Oncley. Response characteristics of the U.W. sonic anemometer. *Journal of Atmospheric and Oceanic Technology*, 3(2):315–323, 1996.